Al-Ghamdi, Khalaf (2011) *An investigation of heterogeneous base catalysed acetone conversion.*
PhD thesis.

http://theses.gla.ac.uk/2878/

An investigation of heterogeneous base catalysed acetone conversion

Khalaf Al-Ghamdi

Submitted in fulfilment of the requirements for the Degree of Doctor of Philosophy

School of Chemistry
College of Science and Engineering

2011

Abstract

A series of materials have been compared for their activity in the base catalysed condensation of acetone. Activities have been compared after extended times on stream (18 h) and under a H_2 containing atmosphere at elevated pressure which is designed to mimic conditions applicable for the single stage transformation of acetone to MIBK. In general, catalysts without a strong hydrogenation function have been screened and so mesityl oxide is the dominant reaction product. However, 1%Pd5%MgO/SiO$_2$ does exhibit high selectivity towards MIBK, demonstrating that single-stage conversion is possible under the conditions investigated.

Catalytic activity is found to be a strong function of the material tested. However, when the influence of surface area is taken into account, a spectrum of area normalised conversion rates is evident. These rates were found to vary in the order 36.5% KNO_3/Al_2O_3 > Li/MgO > 36.5% KNO_3/ZrO_2 > 36.5% $KNO_3/Zr(OH)_4$ > MgO derived from $Mg(OH)_2.MgCO_3$ > 14% KNO_3/Al_2O_3 > MgO derived from $Mg(OH)_2$ > 14% $KNO_3/Zr(OH)_4$ > ZrO_2 > 14% KNO_3/ZrO_2 > Y-$Zr(OH)_4$.

When comparing materials produced from different precursors, differences in catalytic behaviour are apparent implying structure-sensitivity and/or the influence of different impurity contents. The role of dopant, additional phase level and precursor phase has also been examined demonstrating that all these parameters are important.

Table of contents

Chapter 3 Catalyst precursor and doping effects upon MgO

Declaration

I declare that, except where explicit reference is made to the contribution of others, that this dissertation is the result of my own work and has not been submitted for any other degree at the University of Glasgow or any other institution.

Signature:

Name: Khalaf Jamaan Alghamdi

Acknowledgment

Firsty, I woud like to thank my supervisor Dr. Justin Hargreaves for his great support, help, guidance and enthusiasm during my study at the University, he always tries to provide a help not only in my study but also in my life in the UK.

Gratitude is extended to Prof. David Jackson for his kind help and support.

I also would like to thank Prof. C. Wilson for his advice and support during my study.

Thank you to Dr. Joe Gamman and Dr. Dan Rosenburg for their help in my experimental work.

I also wish to say thank you to Mr. Ron Spence for his kind help and support in my Lab work.

Thank you to Mr. Andy Monaghan for his kind help and support.

Thank you to Mr. J. Gallagher for his help in SEM experiments.

Thank you to Mrs. Kim Wilson for her help with the CHN analysis.

Thank you to every person who provided me or my family any kind of help in the UK and I wish them every success.

Thanks to my parents, wife and kids.

Thank you very much to all.

Khalaf

Publications

K. Alghamdi, J. S. J. Hargreaves, and S. D. Jackson, *Base catalysis with metal oxides.* In: S. D. Jackson, and J. S. J. Hargreaves (eds.) Metal Oxide Catalysis. Wiley-VCH, Weinheim, Germany, ISBN 9783527318155 (2009).

Figures

Tables

Chapter 1
Introduction.

1. **Introduction.**

2. **1.1 Catalysis.**

A catalyst is defined as a substance which alters the rate of chemical reactions without being changed or substantially consumed in the process [1]. In some cases, a catalyst may increase the rate of only one reaction out of many competing reactions [2]. A chemical combination between the catalyst and reactants may take place but the catalyst will be ultimately regenerated by the end of reaction.

A catalyst hastens reaction by providing an alternate path with lower activation energy. In the reaction cycle, the active centre of the catalyst initially combines with at least one reactant and is then regenerated with the appearance of the product. The resultant vacant centre then further combines with the reactant to produce another cycle in a continuous process. Small quantities of catalytic centres can be sufficient to produce a large amount of products. Catalysts have no impact on equilibrium conversion as catalyst similarly affects forward as well as reverse reactions in an equilibrium system.

Catalysis is generally sub-divided into homogeneous catalysis and heterogeneous catalysis. Homogeneous catalysis is the process where the catalyst and the reactants/products are in the same physical phase (most generally the liquid phase) and heterogeneous catalysis is the process where the catalyst and reactants/products are in different physical phases (e.g. a solid catalysing the conversion of gas-phase reactants). Whilst homogeneous catalysts are generally more selective than their heterogeneous counterparts, problems of separation limit the application on the large-scale, making heterogeneous catalysed processes the preferred option. When consideration is made of the fact that more than 80% of industrial processes involve catalysis, the scale and economic importance of this area becomes evident. This thesis concentrates on heterogeneous catalysis and, in particular, heterogeneous base catalysis.

The catalyst can radically influence selectivity since, as mentioned above, the rate of only one reaction out of a number of completing reactions may be increased in some instances. Solid catalysts are normally porous and most solid catalysts have surface areas in the 5 - 1000 m^2/g range. The geometrical properties of the pores of these materials can affect the global reaction rate. The surface area of a solid has a significant effect on the amount of gas adsorbed and on catalytic activity.

Heterogeneous catalytic processes can be generally classified as redox reactions or acid-base reactions. Solid catalysts are in high demand for acid-base catalysis due to their

advantageous non-corrosive, environmentally benign nature, and low disposal problems. Their re-use is possible and they can be easily separated from products. Acid-base reactions contain all the reactions where the reactants form heterolytic bonds with the catalyst by using the free electron pair of the catalyst or reactants, or the free electron pair formed in the course of reaction by heterolytic rupture of bonds in the reactant molecules [3].

Solid base catalysts were originally defined as catalysts for which the colour of an acidic indicator changes when it is chemically adsorbed. Solid acid catalysts were defined as those catalysts giving rise to a colour change upon adsorption of a basic indicator. According to Brønsted and Lewis definitions [4], a Brønsted acid is a proton donor and Brønsted base is a proton acceptor; a Lewis acid is an electron-pair acceptor and Lewis base is an electron-pair donor.

Solid acid catalysts have traditionally been widely applied in reactions related to the petrochemical industry over the past 40 or more years. However, little attention has been directed towards the study application of base catalysts which can behave in a complementary, but different, manner to their acid counterparts. An illustrative example of the difference in behaviour is the alkyl aromatic side chain alkylation reaction where it is observed that the side chain of the alkyl groups is alkylated with bases rather than the aromatic ring which is the region alkylated by acid catalysts. Tanabe and Hölderich [5] have reported an estimation of the application of acid and base catalysts in industrial processes up to 1999. The use of these types of catalysts are in the order solid acid > solid base > solid acid-base bi-functional catalysts. These were applied to catalyse 103, 10, and 14 processes respectively.

Pines et al [6] first studied a heterogeneous base catalyst of sodium metal dispersed on alumina for double bond migration of alkenes in the 1950s. Studies of solid base catalysts encompass a wide variety of solid bases, solid base catalysts can be categorised as into several different types as shown in Table.1.1.1 below:

Type of soild base	Catalyst	Example
Single metal oxide	Alkaline earth oxides	MgO, CaO, SrO, and BaO
	Rare earth oxide	La_2O_3, and YbO_2
	Transition melt oxide	ZrO_2
Mixed oxide	Mg-Al mixed oxide	$MgO-Al_2O_3$
	Mg-Ti mixed oxide	$MgO-TiO_2$
Supported catalyst	Catalyst: Na, K, KF, KNO_3, and K_2O	KF/Al_2O_3, $Na/NaOH/Al_2O_3$
	Support: C, Al_2O_3, SiO_2, ZrO_2, and MgO	Na/MgO
Mesoporous material	Modified mesoporous material	MgO/SBA-15
	Functionalsied mesoporous	MCM-41 functionlised with amino groups
	Mesoporous silicon oxynitride	
Zeolite	Alkali ion-exchanged zeolite	Cs-exchanged zeolite X, Y
	Alkali metal or metal oxide occluded Zeolite	Cs-occluded zeolite X, Y
Clay and modified Clay	Hydrotacite, calcined, and rehydrated Hydrotacite	Mg-Al hydrotalcites
	Chrysolite	
	Sepiolite	Magnesium silicate
Oxynitride	Silicon oxynitride	SiON
	Aluminophosphate oxynitride	AlPON
	Zirconophosphate oxynitride	ZrPON
Other	Modified natural phosphate (NP)	Calcined $NaNO_3/NP$

Table. 1.1.1 Type of solid base catalysts [8].

Solid bases can catalyse reactions by abstraction of protons, by activation of reactants without proton abstraction, or by Cooperative action of Acidic and Basic Sites [7]. Base catalysts are mostly used in the form of oxides where the basic sites are generally O^{2-} ions with different environments. The formation of the basic site by species other than O^{2-} alters catalytic properties [8]. A suitable solid base catalyst must have appropriate strength for the reaction that needs to be catalysed. For example, for condensation reactions of aldehydes and ketones the base is required to remove protons of pKa $19.7 - 20.0$. There are few solid base materials available with this strength (see Fig.1.1.1). The base strength can be determined by measuring the ability of basic solution to abstract a proton from an acidic neutral solution which is represented by H_- acidity function [9]:

$$H_- = pK_a - \log([AH]/[A^-]) \qquad (1.1)$$

H_- value of a solution can be determined by accurate measurement of AH and A concentrations. If half of a solute, AH, is deprotonated in solution, *i.e.,* $[A^-] = [AH]$, the H_- value of the solution is equal to the pK_a value of AH. When a neutral molecule of larger pK_a value is deprotonated this indicates stronger basicity. The base strength of solid bases

is expressed by means of the *H-* value, associated with the highest pK_a value of the adsorbates from which the basic site is capable to abstract a proton.

The *H-* value of solid bases is used as a parameter to identify the nature of individual basic sites assuming that there are a certain number of basic sites on solid surfaces and that each of the sites have its specific basic strength.

The measurement of base strength by the indicator method is based on the change of colour of indicator molecules upon adsorption, as described previously. Changing of the indicator colour reveals that the *H-* value of the basic sites is higher than the pK_a value of the indicator. However, if the indicator colour is not changed during adsorption, the *H-* value of the sites is less than the pK_a value of the indicator. Thus the *H-* value of the basic sites can be determined by using indicators of different pK_a values. The colour change of the indicator is due to proton abstraction by basic sites and should not relate to other types of interactions such as charge-transfer between the adsorbate and the surface. Catalytic reactions can provide an accurate measurement of basic strength especially reactions that initiate by formation of carbanions by abstraction of a proton from the reactant. The formation of carbanion depends on the pK_a value of reactant.

Base catalysts have been historically been classified according to the value of the acidity function (*H-*) as shown in Fig. 1.1.1:
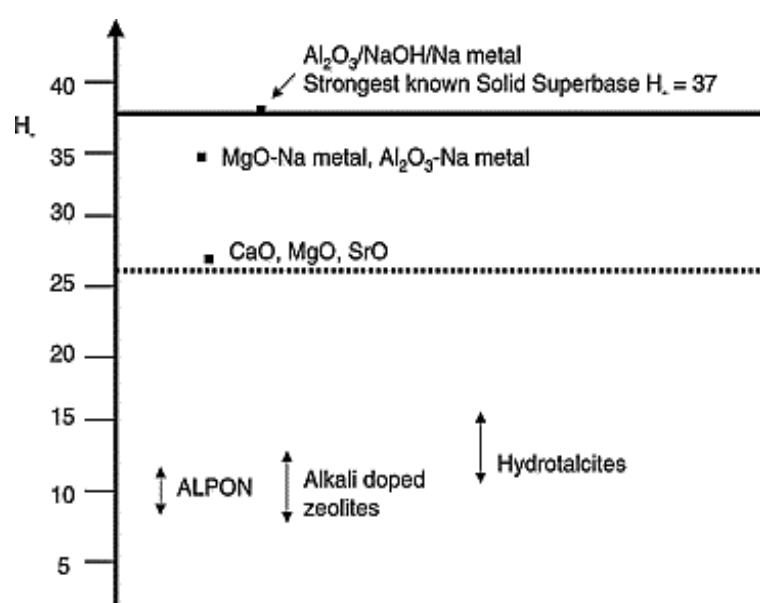
Fig. 1.1.1 Base catalysts types according to the acidity function *H-* value [9].

Despite the fact that the application of indicator methods is still common, it is usually backed up by the use of additional methods, due to their severe limitations [10]. For example, colour changes could only be visible to the naked eye when about 10% of the desorbed layer of indicator is adsorbed thus UV-visible spectroscopic methods should be adapted. Further limitations related to solvent effects, equilibrium time effects, and colour changes induced simply by adsorption can be raised. For such reasons, additional methods which give site strength distribution are therefore recommended even though these methods do not directly generate the value of H_-. Base site strength distribution is traditionally measured by titration methods. However, alternative methods such as probe molecules [11], CO_2 chemisorption [11], microcalorimetry [12], spectroscopy [13] and thermal analysis have been used in recent years. A good method for the characterisation of surface acid-base is the combination of thermal methods and spectroscopy, especially FTIR spectroscopy.

Some catalysts have both acidic and basic properties and contain suitable acid-base pair sites. The acid-base catalysts can possess remarkable activity even though the strength of their acidic and basic sites is much weaker than that of acid or base catalysts. Zirconia was found to have both acid-base sites and can act as an acid as well as a base catalyst. Table 1.1.2 shows examples of materials that comprise both acid-base bi-functional sites.

Type	Catalyst	Example
Single metal oxide	Rare earth oxide	La_2O_3
	Transtion melt oxide	ZrO_2
Mixed oxide	Mg-Al mixed oxide	$MgO-Al_2O_3$
Oxynitride	Aluminophosphate oxynitride	AlPON

Table. 1.1.2 Catalysts that expected both acid-base bi-function properties

Superbase catalysts are catalysts which possess base sites stronger than $H_- > 26$ [14]. Base strength is directly related to the ability of bases to abstract a proton from a C-H bond and form carbanion ions. Ushikubo et al [15] developed a superbase catalyst by the addition of metallic sodium to MgO by decomposing NaN_3 precursor to evolve metallic sodium vapour. The catalyst was investigated over the decomposition of methyl formate to CO and methanol. Pines and co-workers [16, 17] have also prepared superbase catalysts from alkali metals on supports by deposition of the metal vapour and have applied them for the isomerisation of alkenes and related compounds. Another superbase catalyst derived from

sodium metal deposited on MgO (Na/MgO) with base strength $H_- = 35$ for the isomerisation of alkenes has been reported [18, 19]. Sun and Klabunde [20] observed that nanocrystalline MgO doped with potassium metal was highly active for alkene isomerisation and alkene alkylation, including the conversion of propylene–ethylene mixtures to pentene and heptene. Suzukamo et al [21, 22] used Na/NaOH/Al$_2$O$_3$ superbase catalyst which has basic sites stronger than $H_- = 37$ to catalyse various reactions such as side chain alkylations of alkylbenzenes at reaction temperatures of 20–160 ^{o}C, double bond migrations of 5 vinylbicyclo[2.2.1]hept-2-ene to 5-ethylidenebicyclo[2.2.l]hept-2-ene at (-30–100 ^{o}C), and 2, 3-dimethylbut-l-ene to 2, 3-dimethylbut-2-ene at 20 ^{o}C, and safrole to isosafrole at 20 ^{o}C. Previous work described a superbase catalyst generated from K(NH$_3$) and Al$_2$O$_3$ by loading potassium onto alumina in liquid ammonia and heating the resulting material under vacuum at 250–300 ^{o}C [23, 24]. When applied to the isomerisation of alkenes, the catalyst exhibited much higher activity than that of Al$_2$O$_3$ loaded with alkali metals by vapour deposition. Al$_2$O$_3$ loaded with KNH$_2$ was more active than K(NH$_3$)/Al$_2$O$_3$ for the isomerisation of 2, 3-dimethylbut-1-ene. The KNH$_2$/Al$_2$O$_3$ suberbase catalyst has been used to catalyse the reaction of toluene with silanes at 56 ^{o}C [25]. The basic strength of both catalysts was found to be at least $H_- = 37$. Yamaguchi et al [26] prepared superbases by dispersing potassium salts such as KNO$_3$, K$_2$CO$_3$, KHCO$_3$ supported on alumina [27] or zirconia [28] and the catalysts possessed a base strength of at least $H_- = 26.5$. Some superbase catalysts with their preparation methods and basicities are listed in Table. 1.1.3.

Catalyst	Precursor/Preparation method	Pr-treatment temperature (K)	Base strength (H_-)
KNH$_2$/Al$_2$O$_3$	(KNH$_2$ impregnated)	573	>37
K(NH$_3$)/Al$_2$O$_3$	(Ammoniacal K impregnated)	523-573	>37
Na/NaOH/Al$_2$O$_3$	(Na vaporised)	623	35
Na/Al$_2$O$_3$	(Na vaporised)	923	35
KNO$_3$/Al$_2$O$_3$, KNO$_3$/ZrO$_2$	(Dry ground)	873	26.5
NaOH/MgO	(NaOH impregnated)	823	26.5
SrO	Sr(OH)$_2$	1123	26.5
CaO	CaCO$_3$	1173	26.5

Table. 1.1.3 Illustrates some superbase catalysts and their precursors, pre-treatment temperatures, and base strengths [26].

The primary focus of this thesis is the application of solid base catalysts to the conversion of acetone. Comparisons are made between the activities/selectivities of a wide range of

different materials. Accordingly, it is of relevance to summarise the base catalysed conversion of acetone.

1.2 Aldol condensation reaction of acetone and synthesis of methylisobutylketone (MIBK) – industrial consecrations.

Reactions of carbonyl condensation are very important in industrial processes for the production of a number of materials. Aldol condensations in combination with subsequent hydrogenations can yield a variety of key compounds including branched, higher alcohols, polyalcohols as well as branched ketones. Methyl isobutyl ketone (MIBK) and 2-ethylhexanol are the most important compounds synthesised from aldol condensations.

Aldol self-condensation of acetone to diacetone alcohol can be effectively catalysed by a variety of solid bases such as La_2O_3, ZrO_2, $Ba(OH)_2$, and alkaline earth oxides [8]. This reaction can also be catalysed by meixnerite-like hydrotalcite-based catalysts with high selectivity towards the desired product [29].

Production of MIBK from the aldol condensation of acetone is commonly undertaken via three essential steps. Initial acetone self-addition is homogeneously catalysed by acids or bases in the liquid phase to give di-acetone alcohol (DAA) which will be then dehydrated in the second step to form the α, β-unsaturated mesityl oxide (MO). The final stage is the hydrogenation of mesityl oxide in the gas phase over nickel or cupper chromite or noble metal catalysts to produce MIBK. However, this process has numerous disadvantages including corrosion, disposal of inorganic salts, and equilibrium limitation. Therefore, a single-stage process of MIBK synthesis is currently used in industry as an alternative way to deal with some of these disadvantages. The process is conducted in the liquid phase using a trickle bed reactor with typical operation conditions of 10 - 100 bar and temperatures ranging from 120 to 160 ^{o}C [30, 31].

Carrying out the reaction at relatively high pressure around 100 bar is favoured in order to enhance the mass transfer of hydrogen from the gas to the liquid phase. Hydrogenation of mesityl oxide can be considered to be irreversible under these conditions and thus inhibits equilibrium limitation of the formation of DAA and MO.

Some heterogeneous catalysts have been reported for application in the three-phase process. These include $CaO\text{-}MgO\text{-}SrO\text{-}Al_2O_3$ [32], Nb_2O_5 [33-35], $Pd\text{-}Nb_2O_5/SiO_2$ [36], Ti, Zr, and Cr doped oxide or hydroxide with carbon [37], Ce, Hf, and Ta oxide or hydroxide with Al_2O_3 [38]. Several of these catalysts enable high MIBK selectivities, e.g.

more than 90%, at acetone conversions ranging from 25 to 35%. In addition, remarkably long lifetimes are reported [36]. Nowadays, gas phase processes proceeding in simple fixed-bed reactors have attracted attention and are of more interest than the three phase operation. Single stage conversion of gaseous acetone to MIBK has been recently performed using bi- or multifunctional materials [39, 40]. This recent process is usually performed in fixed bed tubular reactors at atmospheric pressure and reaction temperatures exceeding 200 $^{\circ}$C. The molar ratio of hydrogen/acetone is variable and normally in the range from 0.2 to 10. The stoichiometric value of the ratio required for the direct formation of MIBK from acetone is 0.5.

Methyl isobutyl ketone (MIBK) (4-methyl-2-pentanone) is an industrially important solvent, chemical intermediate, and the third largest tonnage product obtained from acetone after methyl methacrylate and bisphenol. It has been commercially produced for more than 60 years. MIBK is medium boiling, clear colourless liquid, which is slightly soluble in water and freely miscible with common organic solvents [41]. It is used in the purification and extraction of antibiotics and for further pharmaceutical applications, and in the manufacture of agricultural chemicals. It is extensively used in nitrocellulose lacquers, epoxy, acrylic, polyurethane paints, and in vinyl resin based coating systems. MIBK is used in solid coatings since it has superior solvent properties. MIBK is a well-known solvent in adhesive, ink and dye formulations as well as in textile and leather finishing. MIBK is widely used as extraction/separation agent for metals such as in separation of niobium from tantalum [42], plutonium from uranium, and zirconium from hafnium [43]. MIBK is used as a raw material in the manufacture of rubber antiozonants, such as N-(1,3-dimethylbutyl)-N-phenyl-p-phenylenediamine.

It can be used as a versatile extraction agent [44] to dewax mineral oils, purify stearic acid, and refine tall oil. Reaction of MIBK with acetylene yields acetylenic surfactant glycols used in ink, paint, and pesticide formulations. MIBK is also used in the manufacture of MIBC. Additional applications of MIBK include an ethanol denaturant, as a synthetic flavouring adjuvant, in food contact packaging materials, and in dry cleaning preparations.

MIBK is a very stable compound under ordinary storage and use conditions but it can undergo a variety of reactions when mixed with other reagents and subjected to suitable reaction conditions. The reactivity of MIBK derived mostly from the acidity of the α-hydrogen and electrophilicity of the carbonyl group. Despite MIBK being involved in a number of chemical reactions that are typical of carbonyl-containing compounds, its

chemical properties more closely resemble that of other aliphatic ketones. The reactivity of MIBK is altered by the presence of an additional isopropyl substituent. The alkyl substituent has both electronic and steric effects on the reaction rate of MIBK and also creates another reactive site, the tertiary C–H bond, which is more easily activated than a primary or secondary C – H bond in reactions that involve radical intermediates.

Synthesis of MIBK in industry can be undertaken by four different routes. Firstly, a three-step process involves acetone and hydrogen as feeds and proceeding via di-acetone alcohol and mesityl oxide intermediates. Secondly, a one-step synthesis from acetone and hydrogen. The third method is a one-step mixed-ketone process from isopropyl alcohol, and finally a single or multistep mixed-feed process in which other products are co-produced. The three-step process was the conventional technology until the late 1960s then the simpler one-step synthesis from acetone was developed by Veba-Chemie and Deutsche Texaco in Germany and Tokuyama Soda in Japan. Despite the improvements offered by the direct route, many of the older three-step methods such as the Shell plant in Deer Park, Texas, are still used [45]. The three-step process has an ability to produce other acetone derivatives such as diacetone alcohol and hexylene glycol (2-methyl-2, 4-pentanediol). The one-step process from 2-propanol co-produces di-isobutyl ketone and acetone are widely practiced in the United States by Union Carbide [46] and in The Netherlands by the Shell Chemical Company. The mixed-feed process co-produces products such as methyl n-amyl ketone [47]. Eastman operates a proprietary unpatented mixed-feed process that produces these co-products [45].

The three-step MIBK process has been descried previously by Hibernia Scholven [48]. This process operates in the way that allows the intermediate recovery of refined di-acetone alcohol and mesityl oxide. Figure. 1.1.2 illustrates a three step MIBK process system designed by Chemische Industrie [48].

 In the first step, acetone and dilute sodium hydroxide were continuously fed to a reactor under low temperature and for 1 h. The product was then stabilised using phosphoric acid and stripped of unreacted acetone to yield a crude di-acetone alcohol stream. The di-acetone alcohol dehydrated to mesityl oxide in a distillation column when more amount of phosphoric acid was added. Mesityl oxide was recovered overhead in this column and was fed to a further distillation column where residual acetone was removed and recycled to yield a product containing 98–99% of mesityl oxide. The mesityl oxide was then hydrogenated to MIBK in a reactive distillation proceeded at 110 ^{o}C under atmospheric

pressure. Simultaneous hydrogenation and rectification were occurred in a column fitted with a palladium catalyst bed and exhibited yields of mesityl oxide to MIBK exceeded 96%. Other three step processes have also been described in literature [49].
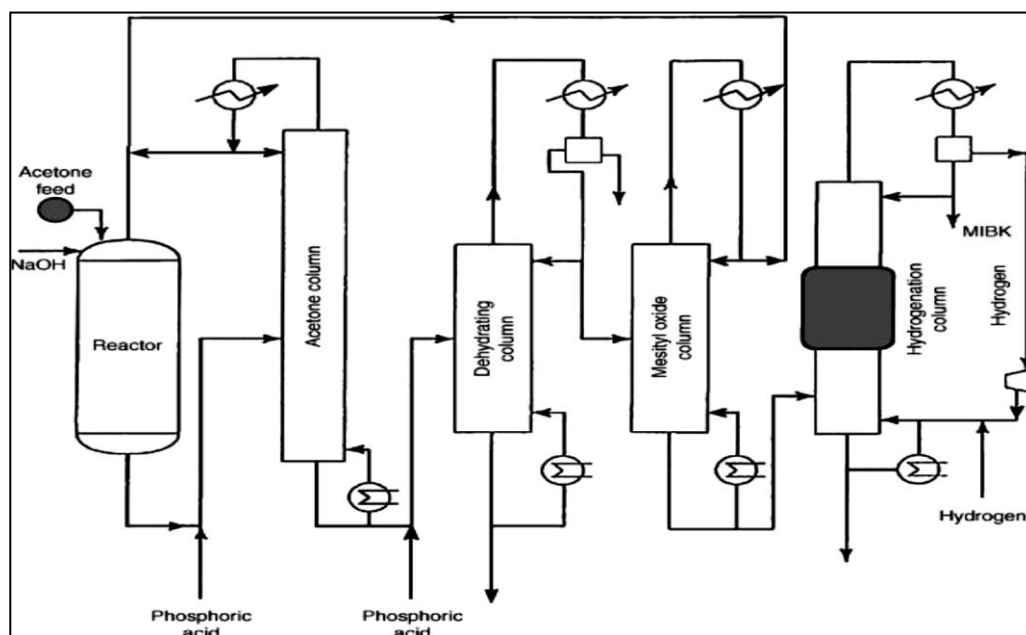
Figure. 1.1.2 A schematic of a three step MIBK process built by Chemische Industrie [48].

The single-step manufacture of MIBK was developed to limit or even prevent some disadvantages that are experienced in the three stage process. It provides lower operating costs, higher acetone conversions, and it prevents the reversion of mesityl oxide to acetone. Direct synthesis is essentially achieved using a multifunctional catalyst to carry out acid aldolisation, dehydration, and hydrogenation reactions [50]. The process has been studied over cation-exchange resin loaded with 0.05% palladium and 2:1 mol feed ratio of H_2/acetone at 135 ^{o}C reaction temperature and 6.1 MPa pressure [51, 52]. Acetone conversion of 35% and 96% selectivity of MIBK were obtained. The light hydrocarbons and second recycled unconverted acetone were removed via the first column and the refined MIBK was then recovered from a four column refining train.

A decanter is located in the final two columns and is used to separate an aqueous phase. Removing the 2-propanol–water mixture was carried out by the third column and the final column produces refined MIBK overhead and heavies (diisobutylketone). A similar process is operated by Deutsche Texaco at reaction temperatures in the range between 130 – 140 ^{o}C and 3 MPa. This process is schematically described in Fig.1.1.3. Acetone

conversion of 40% has been observed and a consumption of acetone was 1.4 kg per kilogram of MIBK.
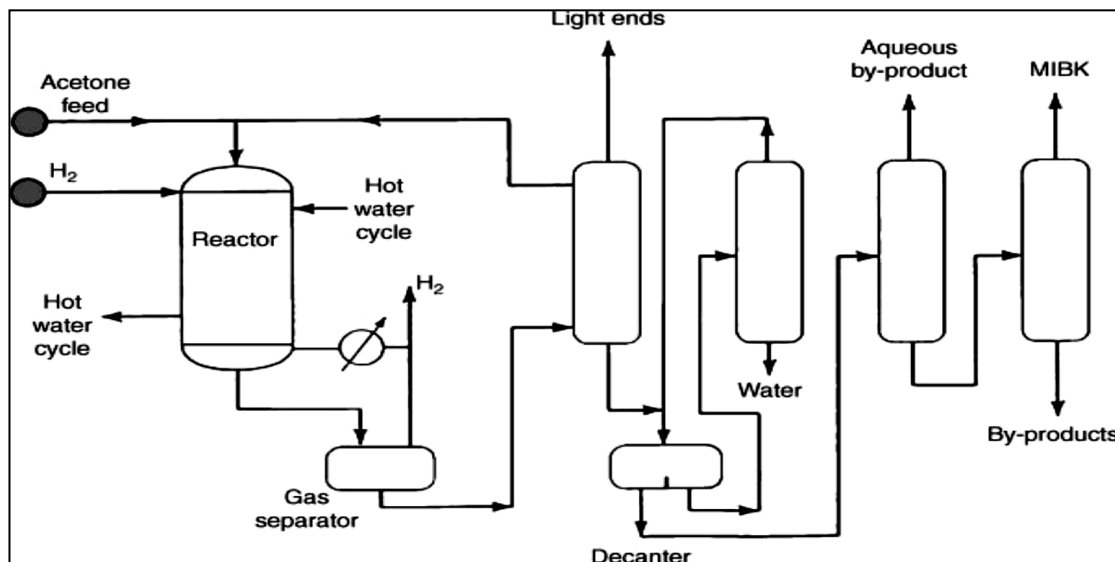
Fig.1.1.3 The Deutsche Texaco one step MIBK process [53].

Previous work reported MIBK selectivity of 95% at acetone conversion of 95% under reaction conditions of 140 ^{o}C, 3 MPa, and a 0.2 mole ratio of H$_2$/acetone [54]. Light methyl pentanes compounds were not formed under these conditions but MIBK recovery has been allowed in a three-column train with a phase separator between the first and second columns. Application of a different catalyst named Tokuyama Soda single-step which consists of a zirconium phosphate catalyst loaded with 0.1–0.5 wt% palladium has also been documented [55]. A palladium doped ion-exchange resin catalyst (Pd/KU-2) was investigated at 120 ^{o}C reaction temperature [56] and the result revealed a selectivity of 94.5% at an acetone conversion of 50%. Mitsubishi Kasei Co. [57] and Sumitomo Chemical Co. [58] have patented single-step catalysts containing palladium and niobium. A Sumitomo catalyst was tested at 160 ^{o}C reaction temperature under 2 MPa of pressure and exhibited 93.5% MIBK selectivity at 41.8% acetone conversion while the Mitsubishi catalyst investigated at 140 ^{o}C and 2 MPa accomplished 92.5% selectivity at 39.5% conversion. Other processes were conducted by different companies such as Allied Corporation [59], BASF [60], BP Chemicals [61], Catalytic Distillation Technology [62], Commercial Solvents Corporation [63], Distillers Co. [64], Industrial Technology Research Institute, Taiwan [65], Japan Bureau of Industrial Technology [66], Sumitomo

Chemical Co. [67], Mitsubishi[68], Showa Denko [69], Scholven-Chemie [70], Mobil [71], and Union Carbide [72].

In the one-step process of MIBK synthesis, numerous products are formed as a result of combining all three steps. The crude product from pilot plant production of MIBK contains at least 17 main [73] A previous study reported that water released during reaction reduces the reaction rate of sulfonic acid resin–Pd catalyst [74]. Numerous reports indicate that catalyst preparation [75], catalyst testing [76], and other investigation [77] have been extensively explored.

The production of MIBK also known as dimethyl ketone (DMK) from acetone and hydrogen as feed materials is initiated by aldol reaction of acetone to diacetone alcohol followed by dehydration of DAA to mesityl oxide (MO), and hydrogenation of MO to MIBK/MIBC. Isolation of DAA and MO intermediates depends on the type of process. In the three-step process these three reactions are performed separately and the crude DAA and crude MO intermediates are isolated. A number of side reactions occur in each of the reaction steps. In the aldol condensation being catalysed by a base catalyst, DAA can undergo further reaction with DMK to produce tri-acetone alcohol (TAA) as a by-product. Partial dehydration of DAA can take place to produce MO, which can then condense with DMK to produce a trimer. The trimer can also be formed by partial dehydration of the unsymmetrical TAA isomer. The trimer could be dehydrated to the pyran compound. The dehydration of DAA over acid catalyst yields MO and isomesityl oxide (Iso-MO) as a major side reaction. The trimers produced in the aldol condensation step also can undergo dehydration and cyclisation reactions.

The hydrogenation process could be conducted to produce MIBC in addition to MIBK depending on the catalyst used. The dehydrated trimers (eg, phorone and isophorone) likewise undergo hydrogenation to saturated C9 ketones and alcohols. Reversible reactions can possibly occur.

Hydrogenation of the olefinic bond in mesityl oxide can be performed over a fixed-bed catalyst in both the vapour and liquid phase. In a liquid-phase hydrogenation reactor the catalyst can be applied as slurry and the reaction can be conducted at a temperature of 150 $^{\circ}$C at 0.69 MPa pressure. The vapour phase reaction occurs at a temperature between 150 – 170 $^{\circ}$C. The reaction is highly exothermic (-30 kcal/mol) and a large yield can be achieved. By limiting the conversion per pass in the liquid phase reaction, high selectivity can be obtained. Inert gases usually use in the gas phase process to dilute the reactants [78].

Various catalysts can be used in on both phase reaction including nickel [79], Raney nickel [80, 81], Ni–Cr [82], palladium [83], copper–alumina [84], copper–chromium oxide [78], copper–zinc oxide [85], cobalt complexes [86], rhodium [87], and rhodium hydride complexes [88]. Complete conversion of mesityl oxide can be obtained at selectivities of 95 – 98% [86]. The kinetics of the hydrogenation process of MO has been investigated over a Pd–Al$_2$O$_3$ catalyst [89].

Alkali metal salts have been reported as promoters for the activity and selectivity enhancement of palladium catalyst in MO hydrogenation and a maximum MIK selectivity of 99.9% could be attained [90]. In addition, water can effectively improve the selectivity of Pd catalyst used for the hydrogenation of MO. High selectivities of 89.3 and 99.5% have been reported in the absence and presence of water [91].

Previous work has observed that treating crude MO, by the dehydration of di-acetone alcohol by sulfuric acid catalyst, with hydrogen peroxide can extend catalyst lifetime [92]. Hydrogen peroxide was used as a promoter for a rhodium complex catalyst in the same reaction [93]. Sec-butyl alcohol [94], formic acid [95], and MIBC [96] have been described as hydrogen donors for the hydrogenation of MO. Use of sec-butyl alcohol as the hydrogen donor results in the simultaneous production of methyl ethyl ketone and MIBK. Other studies on polymer-supported Pd [97], palladium complex polymer [98], Ni–Cu–Cr [99], copper complex [100], and Ni–M [101] catalysts have been reported.

Di-acetone alcohol DAA is a colourless and mild-smelling liquid that is entirely miscible with water and most organic solvents even although DAA is classified as a solvent and is used in many applications. It has ketone and alcohol functionalities hence it has special utility in the coatings industry to dissolve cellulose acetate to give solutions with high tolerance for water [102]. DAA is also used as feed material for the production of hexylene glycol.

DAA is an essential product in the three step process by the low temperature liquid-phase condensation of acetone in the presence of a base catalyst [103]. Solutions of base catalysts and water or water–alcohol solvent mixtures can be used but the catalyst has to be completely neutralised with a suitable acid before the crude product is worked up [104]. However, solid base catalysts placed in a fixed bed are desirable due to ready separation of the product from the catalyst. The reaction is exothermic (ΔH = -5.5 kcal/mol) and is equilibrium controlled [105]. The equilibrium constant influences by increasing

temperature [106]. The equilibrium concentration of di-acetone alcohol is 23.1 wt% at 0 ^{o}C, and reduced to 9.1 wt% at 30 ^{o}C [107].

Despite the formation of di-acetone alcohol being preferred at low temperature, kinetic considerations require commercial operation to be conducted at $10 - 20\ ^o$C. Either single or multistage catalyst beds can be used: single-stage conversion requires lower inlet temperatures, multistage conversion can cascade to gradually lower inlet temperatures [108]. Reaction times of 20–60 mins are typically required. Conversion across the reactors typically ranges from 8 to 15%. At low conversions, separation of acetone from DAA required distillation to allow recycle of unreacted acetone to the reactors. The crude DAA product may contain 85–95% DAA and 5–15% acetone as well as other impurities. The distillation process can be carried out in a single unit [109].

Different catalysts for the aldol condensation reaction include the hydroxides of alkali metals [110, 111] and oxides or hydroxides of alkaline earth metals [112-114] have been reported.

Most solid base catalysts are vulnerable to dissolution by the reaction medium and thus yield a crude product that contains traces of catalyst. Stabilisation of DAA against reversion to acetone during the acetone recycle distillation can be attained by neutralising the solution with acids such as CO_2 [115], phosphoric acid [116], carboxylic acid type ion-exchange resin [117], and phenolic resin [118]. Acetone can then be stripped overhead in a distillation column most, likely under vacuum conditions, and recycled.

Commercial catalysts can remain active for 1 yr and can be reactivated by washing with hot water and acetone [119]. A long catalyst lifetime can be obtained by limiting the concentration of aldehydes in the acetone feed [120].

Previous work showed that [121] aging of a calcium oxide catalyst can be prevented by the addition of $0.2 - 2$ wt% 2-propanol, methanol though aldehydes are considered to be a poison [121].

High mechanically stable anion-exchange resin catalysts have been also reported [122, 123]. These catalysts were found to be beneficial for reactions with the addition of 3–10% weight of C1–C3 alcohols to the acetone feed [124]. Early patents indicated that because water inhibits the aldol condensation mechanism, it was necessary to dry recycle acetone to < 1% water [125]. More recent reports demonstrate DAA production from waste acetone contained 10–50% water [126], and enhanced DAA production over anion-exchange resins using acetone feeds that contain 3–10% water [127]. Alkylene oxide– salt complexes [128]

can be used as catalysts for aldol reactions and as co-catalysts [129] for enhancing the rate of base-catalysed aldol reactions. Hydrotalcite-type catalysts were reported to be highly active for the formation of DAA from acetone [130]. DAA selectivity between 90 and 95% can be achieved in industry [45]. Mesityl oxide and acetone trimmers are mainly the major by-products. Further condensation of acetone with di-acetone alcohol can be conducted to yield sym-tri-acetone di-alcohol which may dehydrate to (6-hydroxy-2,6-dimethyl-2-hepten-4-one) that may cyclise to 2, 2, 6, 6-tetramethylpyrone, or dehydrate to phorone (2, 6-dimethyl-2,5-heptadien-4-one) [131]. An unsymmetrical acetone trimer can also be produced which can be dehydrated to 2,4-dimethyl-2,4-heptadiene-6-one and then cyclised to form 2,2,4,6-tetramethylpyran [132]. Subsequently, impurity and yellow discoloration of DAA can result from these by-products. Purification of the crude DAA can be accomplished by vacuum topping and tailing in a set of distillation columns [133]. Nitrogen containing carboxylic, or phosphoric acids are used as stabilising agents [134].

Mesityl oxide is an oily colorless liquid, toxic, and has unpleasant odour. It is a versatile and highly reactive due to the conjugated α, β-unsaturated carbonyl compounds [135]. Mesityl oxide can slowly react with air and convert to bis(3,5,5-trimethyl-1,2-dioxolanyl)-3-peroxide [136]. Mesityl oxide can contain 5 – 20% of isomesityl oxide (4-methyl-4-penten-2-one) [137], the β, γ-unconjugated isomer. However, at equilibrium the mixture consists of 91% of the α, β-mesityl oxide and 9% of the β, γ-isomer [138]. Acid or alkali can catalyse the equilibration of the isomers [139] and techniques that used to isolate the isomers have been reported [138]. Mesityl oxide is used as an intermediate in MIBK and isophorone [140] production.

Mesityl oxide can be prepared by using a distillation column in which acetone is removed overhead and water saturated mesityl oxide is produced from a side-draw over sulfuric acid [125] and phosphoric acid [141]. Reaction kinetics has been extensively studied [142]. The reverse of DAA to acetone is a major side reaction and acetone remained from dehydration step involves re-cyclisation to the aldol condensation step. The dehydration process is highly selective and strongly depends on the quality of crude DAA, and on the conditions of reaction. A majority of the by-products derived from acetone trimers can be formed. Crude mesityl oxide obtained from the dehydration step could be a suitable feed material for the hydrogenation step.

Mesityl oxide can be formed by the liquid-phase dehydration of di-acetone alcohol over acidic catalysts at $100 – 140$ ^{o}C under atmospheric pressure in an endothermic process (5

kcal/mol). Moreover, mesityl oxide can also be produced from the vapour phase direct condensation of acetone at higher temperatures over copper chromite [143], zinc oxide [144-146], zinc oxide–zirconium oxide [147], and borate–phosphate [148] or in the liquid phase over cation-exchange resin [149] or zirconium phosphate [150] magnesium–aluminium complex compound [151] and heat-treated anionic clays [152] are also known to condense acetone to mesityl oxide.

1.3 Mechanism of aldol condensation reaction of acetone over base catalyst.

Aldol condensation of over base catalyst is initiated by abstraction of acidic α-hydrogen by the base catalyst to form reactive enolate. The nucleophilic enolate then attacks another acetone at the electrophilic carbonyl in a nucleophilic addition type process giving an intermediate alkoxide. Finally, the alkoxide deprotonates a water molecule creating hydroxide and β-hydroxyketone which is the di-acetone alcohol (DAA).

Subsequently, the base catalyst removes an acidic α-hydrogen from di-acetone alcohol (DAA) giving reactive enolate The electrons associated with the negative charge of the enolate are eventually used to form the C=C and displace the leaving group to regenerate hydroxide and a conjugated ketone called mesityl oxide (MO) (Fig. 1.1.4).
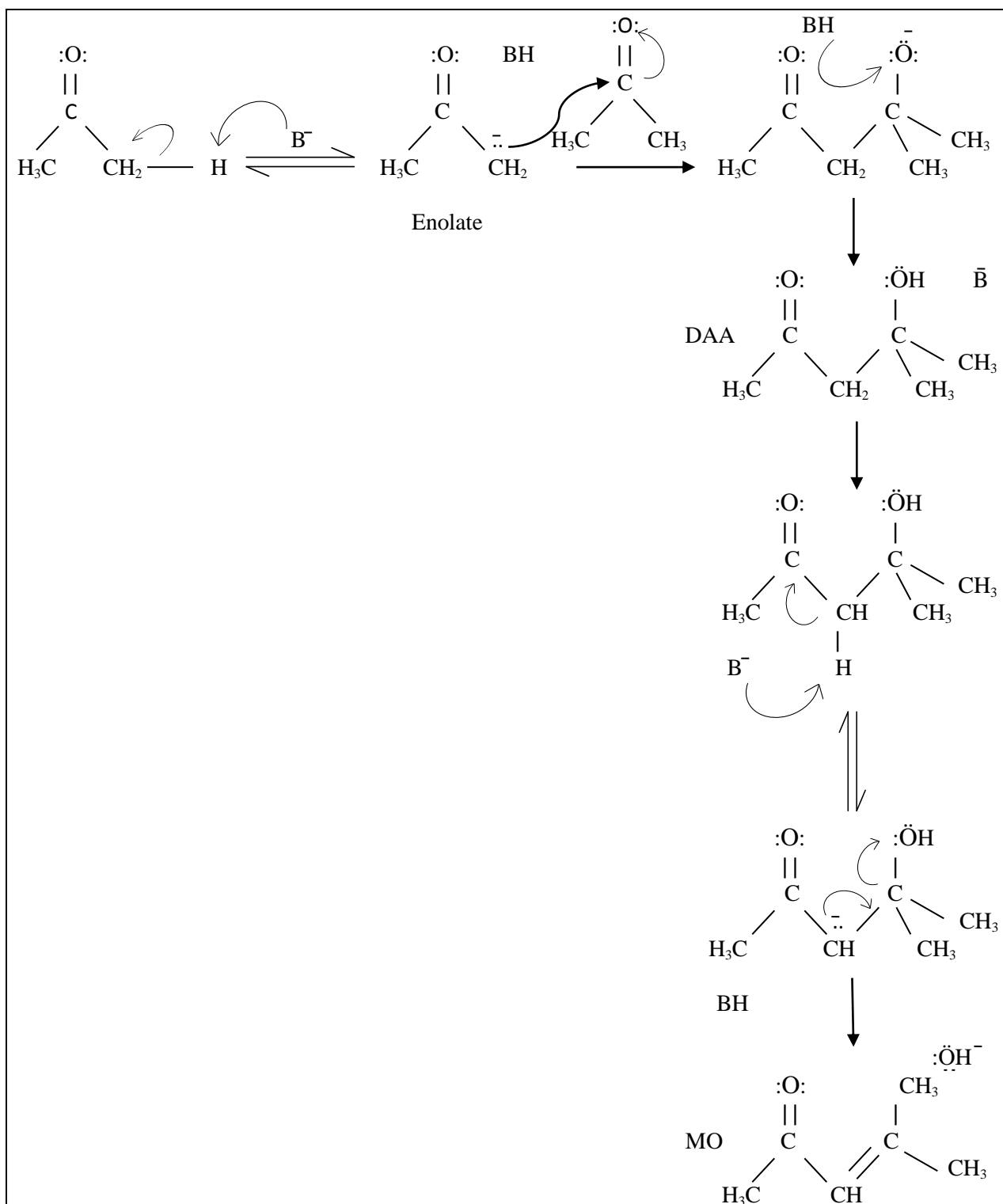
Fig. 1.1.4 Main mechanism of the aldol condensation reaction of acetone over base catalyst.

Various mechanisms have been suggested for the aldol condensation reaction of acetone over base catalysts. Flego and Perego [153] have proposed a mechanism for the acid catalysed condensation of acetone by molecular sieves Fig. 1.1.5. The mechanism involves

a combination between acetone (in enolic form) and another acetone molecule (in protonated ketonic form after bonding with hydroxyl groups), forming di-acetone alcohol (DAA) as a primary product. The di-acetone alcohol is consequently dehydrated to mesityl oxide (MO) and the later undergoes interaction with another acetone molecule to form phorone which is finally cyclised to isophorone. However, the mechanism over the base catalyst is slightly different since the production of isophorone is only occurred via the 1, 6-aldol of 4, 4`-dimethylhepta-2, 6-dione.
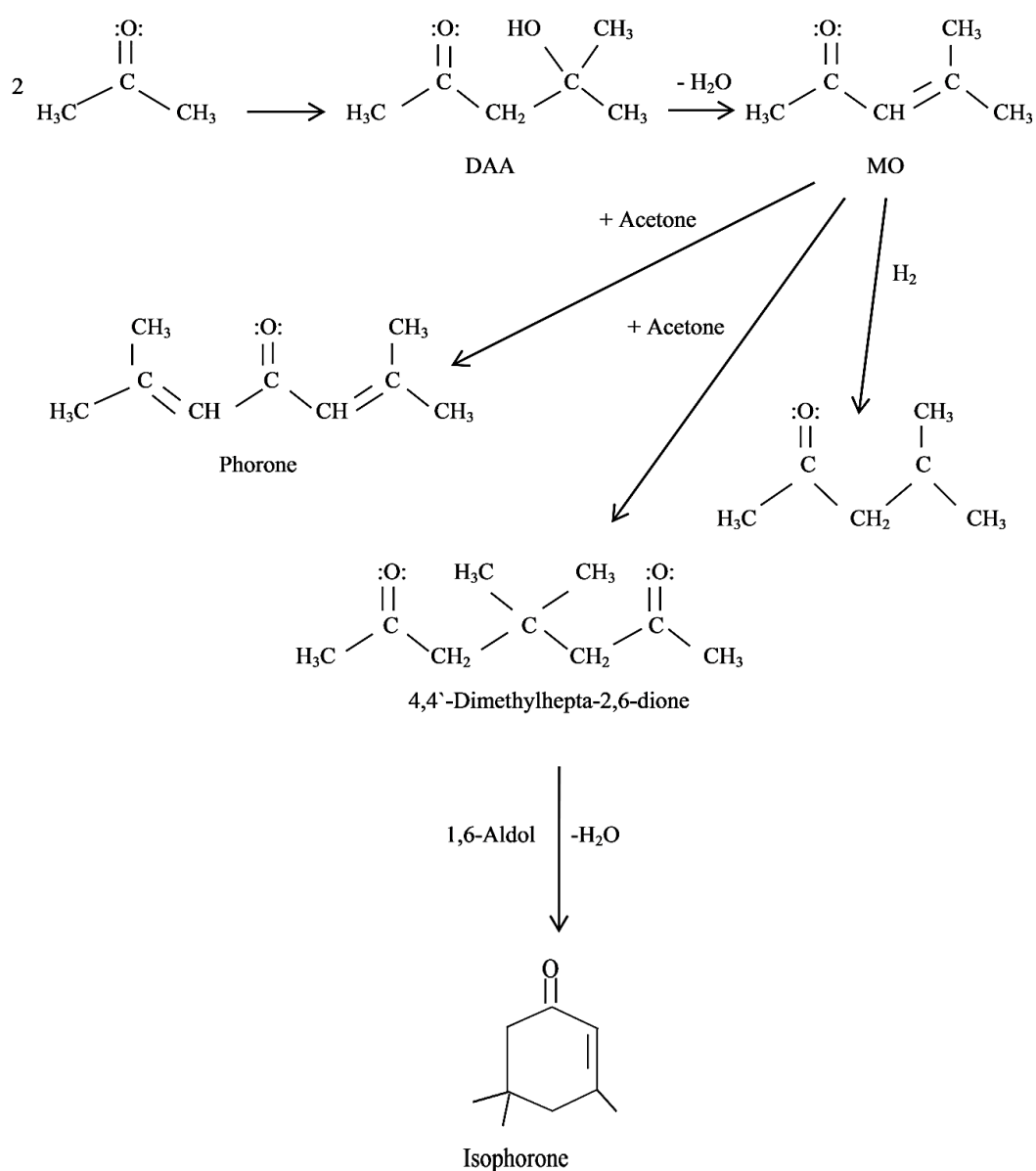
Fig. 1.1.5 Flego and Perego mechanism of the aldol condensation reaction of acetone over acid catalyst [153].

Reichle et al [154] revealed that isophorone is formed via three intermediate species either via a 1, 6-Michael addition of 2, 4- dimethylhepta-2, 4-diene-6-one or phorone, or by a 1, 6-aldol condensation reaction of 4, 4-dimethylhepta-2, 6- dione Fig. 1.1.6.
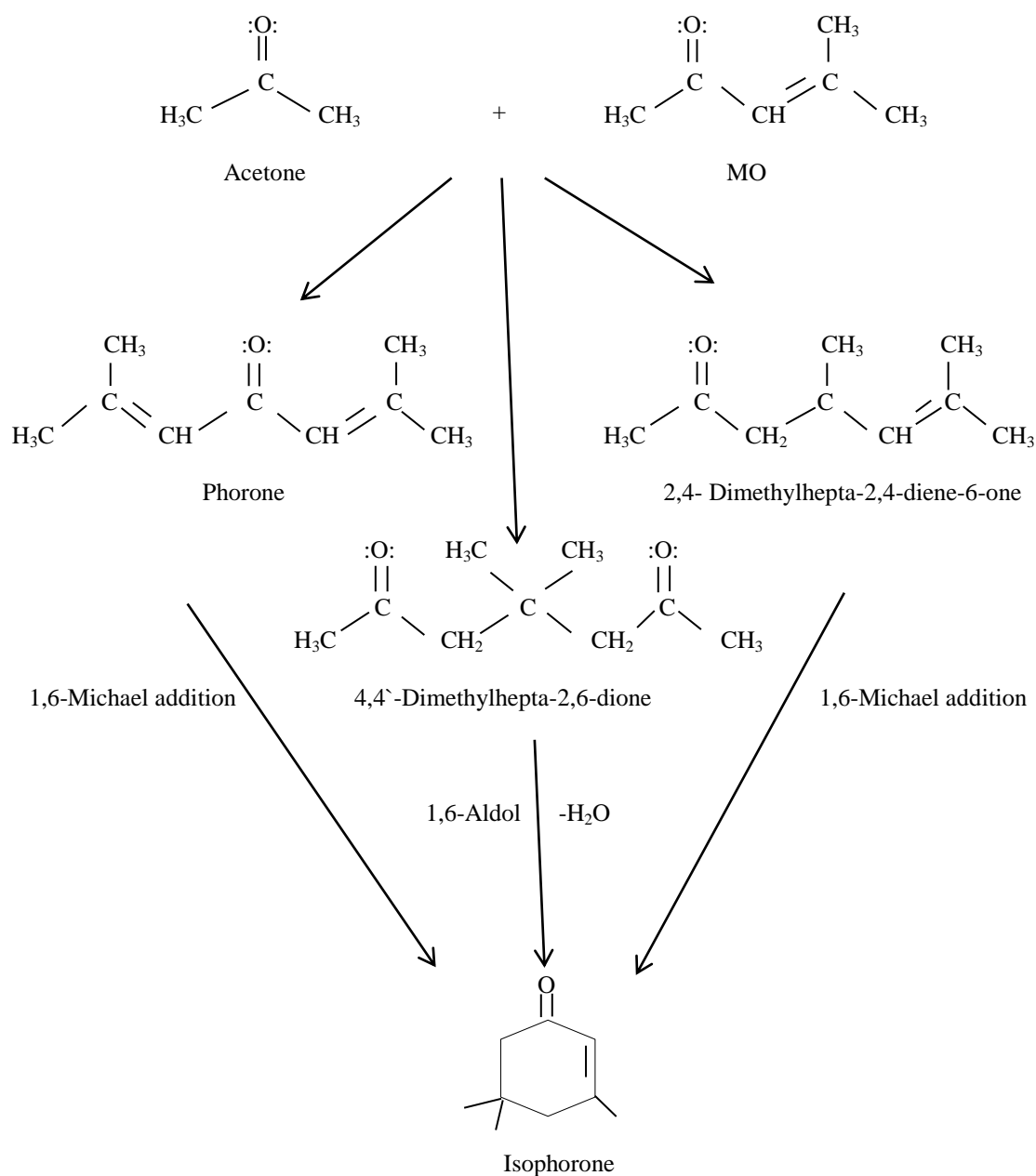
Fig. 1.1.6 Production of isophorone via intermediate steps [154].

Other route of isophorone formation using isoptopes has been also documented [155].

1.4 Aims

In this thesis a series of solid base catalysts have been applied to acetone conversion with the aim of determining catalytic activity and selectivity and determining structure-function relationships. Reactions have been run over extended periods with respect to many other academic studies and comparison is generally made on the basis of product sampling following 18 h on stream. Elevated pressure has been applied to more closely mimic possible industrial practice and hydrogen is included in the reactant stream to be of relevance for one stage MIBK production.

1.5 References.

[1] B. Cornils, W. A. Herrmann, R. Schlögl and C. H. Wong, "Catalysis from A to Z", Wiley-Vch, (2003).

[2] C. Adams, *Chem. Indus*. 740 (1999).

[3] J. Haber, in "Catalysis: Science and technology", (Eds. J. R. Anderson and M. Boudart), Springer-Verlag, (1981).

[4] K. Tanabe, M. Misono, Y. Ono and H. Hattori, "New solid acids and base", Kodansha-Elsevier, Tokyo- Amsterdam, (1989).

[5] K. Tanabe and W. F. Hölderich, *Appl. Catal.* 399 (1999).

[6] H. Pines, J. A. Veseley and V. N. Ipatieff, *J. Am. Chem. Soc*. **77**, 6314 (1955).

[7] Y. Ono and T. Baba, *Catal.* 15 (2000).
[8] H. Hattori, *Chem. Rev.* **95**, 537 (1995).

[9] C. H. Rochester, *Academic Press*, 72 (1970).

[10] K. Alghamdi, J. S. J. Hargreaves, and S. D. Jackson, "Base catalysis with metal oxides". In: S. D. Jackson, and J. S. J. Hargreaves (eds.), Metal Oxide Catalysis. Wiley-VCH, Weinheim, Germany, ISBN 9783527318155 (2009).

[11] D. Martin and D. Duprez, *J. Molec. Catal.* A, **118**, 113(1997).

[12] A. Auroux and A. Gervasini, *J. Phys. Chem.* **94**, 6371 (1990).

[13] H. Vinek, H. Noller, M. Ebel and K. Schwarz, *J. Chem. Soc*., **1**, 73 (1977).

[14] H. Matsuhashi, and K. Arata, *J. Phys. Chem.* 9, 11178 (1995).

[15] T. Ushikubo, H. Hattori and K. Tanabe, *Chem. Let.* 649 (1984).

[16] W.O. Haag and H. Pines, *J. Am. Chem. Soc*. **82**, 387 (1960).

[17] H. Pines and W.M. Stalick, "Base-catalysed reactions of hydrocarbons and related compounds", New York (1977).

[18] J. Kijienski and S. Malinowski, *Reac. Kinet. Catal. Let.* **3**, 343 (1975).

[19] J. Kijienski and S. Malinowski, *Catal. RSC*, **4**, 130 (1981).

[20] N. J. Sun and K. J. Klabunde, *J. Catal.* **185**, 506 (1999).

[21] G. Suzukamo, M. Fukao and M. Minobe, *Chem. Let.* 585 (1987).

[22] G. Suzukamo, M. Fukao, T. Hibi and K. Chikaishi, "Acid-Base catalysis", (1989).

[23] T. Baba, H. Hand and Y. Ono, *J. Chem. Soc.* **90**, 187 (1994).

[24] T. Baba, *Catal. Surveys Jpn.* 17, (2000).

[25] T. Baba, H. Yuasa, H. Handa and Y. Ono, *Catal. Let.* **50**, 83 (1998).

[26] T. Yamaguchi, Y. Wang, M. Komatsu, and M. Ookawa, *Catal. Surveys Jpn.* **5**, 81 (2002).

[27] Y. Wang, J.H. Zhu and W.Y. Huang, *Phys. Chem. Chem. Phys.* **3**, 2537 (2001).

[28] Y. Wang, W.Y. Huang, Y. Chun, J. R. Xia and J. H. Zhu, *Chem. Mater.* **13**, 670 (2001).

[29] D. Tichit, M. N. Bennani, F. Figueras, R. Teissier and J. Kervennal, *Appl. Clay Sci.* **13**, 401 (1998).

[30] J. I. Di Cosimo, G. Torres and C. R. Apesteguia, *J. Catal.* **114**, 28 (2002).

[31] M. Guisnet, A. Mitschker, R. Wagner and P. M. Lange, *Elsevier Sci. Publish.* (1988).

[32] T. Yasuhiko, *Japanese Patent JP62258335* (1987).

[33] Y. Higashio and T. Nakayama, *Catal. Today*, **28**, 127 (1996).

[34] M. Takao, Japanese Patent JP63068538 (1988).

[35] M. Takao, Japanese Patent JP63068539, (1988).

[36] Y. Z. Chen, B. J. Liaw, H. R. Tan and K. L. Shen. *Appl. Catal.* **205** (2001).

[37] M. Takao, *Japanese Patent* JP63096147 (1988).

[38] M. Takao, *Japanese Patent* JP63096146 (1988).

[39] L. Melo, G. Giannetto, F. Alvarez, P. Magnoux and M. Guisnet, *Catal. Let.* **44**, 201 (1997).

[40] L. Melo, G. Giannetto, L. Cardozo, A. Llanos, L. Garcia, P. Magnoux, M. Guisnet and F. Alvarez, *Catal. Let.* **60**, 217 (1999).

[41] R. W. Gallant, **47**, 127 (1968).

[42] Methyl Isobutyl Ketone, Environmental Health Criteria 117, World Health Organization, (1990).

[43] G. T. Austin, *Chem. Eng.* 149 (1974).

[44] Unocal Corp., Hydrocarbon Proc. 211 (1992).

[45] Topical Reports, *Chem Systems Inc.*, Tarrytown, N.Y., (1989).

[46] S. N. Bizzari, Chemical Economics Handbook, CEH Data Summary, SRI International, Menlo Park, (1999).

[47] D. Muthusamy, C. Wang, R. D. Swain, D. B. Litzen and W. R. Pledger, US. Pat. 5583263 (1996).

[48] K. Schmitt, *Chem. Ind.* **18**, 204 (1966).

[49] Kyowa Hakko Kogyo Co., Hydrocarbon Proc. **48**, 205 (1969).

[50] V. N. Ipatieff, V. Haensel, *J. Org. Chem.* **7**, 189 (1942).

[51] J. Disteldorf, DE Pat. 1643044, 131 (1972).

[52] K. Schmitt, *Chem. Ind.* **33**, 632 (1981).

[53] P.M. Lange, F. Martinola and S. Oeckl, Hydrocarb. Proc. 51 (1985).

[54] Y. Onoue, Y. Mizutani, S. Akiyama, Y. Izumi and Y. Watanabe, Chem. Tech. **7**, 36 (1977).

[55] Y. Watanabe, M. Okada, Y. Izumi and Y. Mizutani, Bull. Chem. Soc. Jpn, **50**, 1539 (1977).

[56] S. I. Guseva, A. A. Grigoreva and T. G. Proxorovskaya, N. Neftekhim, **6**, 30 (1978).

[57] T. Maki, T. Yokoyama and Y. Sumino, JP63068539 (1988).

[58] Y. Higashio and T. Nakayama, *Eur. Pat.* 227,868 (1989).

[59] F. J. Gerfri, D. Masilamani, Murthy and K. S. Andiappan, *US Pat,* 4,704,480 (1987).

[60] A. Nissen, G. Heilen, E. Sapper, W. Fliege, A. Wittwer, *US Pat.* 4,212,825 (1980).

[61] S. Lane, *Brit. Pat.* 1,226,029 (1971).

[62] K. H. Lawson and B. Nkosi, *U.S. Pat.* 6,008,416 (1999).

[63] S. E. Foy, *U.S. Pat.* 2,499,172 (1950).

[64] W. J. Fox, D. A. Lawton, L. E. Cooper, and M. Sutcliffe, *DE Pat.* 1,232,942 (1967).

[65] S. J. Chu, K. C. Wu and W. C. Lin, *U.S. Pat.* 5,684,207 (1997).

[66] M. Dokiya, *Jpn. Pat.* 47-020,112 (72-020,112) (1972).

[67] K. Takagi and M. Murakami, *DE Pat.* 1,936,203 (1970).

[68] N. Isogai, T. Okawa and N. Wakui, *U.S. Pat.* 4,289,911 (1981).

[69] T. Imai, M. Yukimitsu, H. Ebisawa, T. Kametaka, and T. Minoura, *Jpn. Pat.* 46-002,009 (71-002,009) (1971).

[70] Scholven-Chemie, *Fr. Pat.*1,579,809 (1969).

[71] T. J. Huang and W. O. Haag, *U.S. Pat*. 4,339,606 (1982).

[72] K. D. Olson, *U.S. Pat.* 4,704,478 (1987).

[73] Z. Hejda, *Chem. Prum.* **29**, 26 (1979).

[74] A. A. Grigoriev, S. I. Guseva, E. A. Katzman and P. Himicheskii, **7**, 392 (1988).

[75] A. Nissen and W. Fliege, *U.S. Pat.* 4,049,571 (1977).

[76] T. M. Khannanov, *U.S. Pat.* 445,263 (1978).

[77] B. R. Serebryakov and N. A. Smirnova, Neftekhim. Sintezy, **3**, 153 (1976).

[78] S. Kudo, Y. Mihara and S. Yada, *U.S. Pat.* 3,449,435 (1969).

[79] B. Turnquest and O. H. Thomas, *Fr. Pat.* 1,478,704 (1967).

[80] C. Weizmann, *Brit. Pat.* 574,446 (1946).

[81] A. Heykoop and F. V. A. Dijk, *U.S. Pat.* 3,374,272 (1968).

[82] 93. V. Sh. Mirzazyanov, *S.U. Pat.* 891,625 (1981).

[83] V. Macho, *Czech. Pat*. 131,903 (1969).

[84] M. Voicu, J. Herscovici, T. Bota, I. Gros, and A. Lupescu, *Rom. Pat.* **64**, 150 (1978).

[85] K. Takagi and K. Manabe, *Jpn. Pat.* 47-015,808 (72-015,808), (1972).

[86] G S R S. Rao, J Rajaram, S Rathnamala and R Sivaramakrishnan, *Proc. Indian Acad. Sci. Sect.* **86**, 435 (1977).

[87] E. Uccian, L. Tanguy, R. Lai, *Fr. Pat.* 2,247,445 (1975).

[88] K. C. Dewhirst, *U.S. Pat.* 3,480,659 (1969).

[89] V. Macho, *Chem. Prum*. **21**, 9 (1971).

[90] M. Otake and Y. Koike, *Jpn. Pat.* 61-030,545 (86-030,545) (1986).

[91] Y. To and T. Nakayama, *Jpn. Pat.* 61-085,343 (86-085,343) (1986).

[92] A. Heykoop and A. F. Van Dijk, *DE Pat.* 1,243,665 (1967).

[93] W. Strohmeier and E. Hitzel, *J. Organomet. Chem*. **102**, 37 (1975).

[94] T. Takahashi, F. Matsuda, and T. Abe, *Jpn. Pat.* 48-034,727 (73-034,727) (1973).

[95] M. A. Aramendia, V. Borau, M. C. Gomez, C. Jimenez and J. M. Marinas, *Appl. Catal.* **8**, 177 (1983).

[96] V. S. Mirzazyanov, *US. Pat.* **649**,702 (1979).

[97] L. Hong, *Chin. J. React. Polym.* **5**, 26 (1996).

[98] Y. Fang, S. Zhang,W. Zhao, Y. Zhang, and L. Yang, **4**, 325 (1988).

[99] Y. Qi, R. Wang, and Z. Wang, **9**, 1 (1988).

[100] W. S. Mahoney and J. M. Stryker, *J. Am. Chem. Soc.* **111**, 8818 (1989).

[101] J. Zhang, J-Z Zhao, X-L Zhang, Y-L Jiang, X-L Ma, Y-X Sun, W-P Jiang, Y-X Li, and Z-L Xu, *Chem. Res. Chin. Univ.* **14**, 125 (1998).

[102] S. K. Datta, *Indian Chem. J.* **9**, 535 (1975).

[103] P. W. Sherwood, *Pet. Refin.* **33**, 144 (1954).

[104] A. Grigor'ev, I. Berger, L. Ivanova, and O. Ostapenko, *Khim. Prom.* **47**, 647 (1971).

[105] S. Kudo, s. Yada, S. Tsuruki, Y. Mihara, R. Nozawa, M. Makino,*Chem. Eng. Jpn.* **30**, 1124 (1966).

[106] J. P. Guthrie, *Can. J. Chem.* **56**, 962 (1978).

[107] E. C. Craven, *J. Appl. Chem.* **13**, 71 (1963).

[108] C. Hawkins and B. Yeomans, *Brit. Pat.* 1,527,033 (1978).

[109] C. Huang, L. Yang, F. Ng and G. Rempel. *Chem Eng Sci*. 53, 3489 (1998).

[110] W. T. Reichle, *U.S. Pat.* 4,086,188 (1978).

[111] P. Godet and L. Adam, *U.S. Pat.* 2,889,369 (1959).

[112] A. G. Raso, J. V. Sinisterra and J. M. Marinas, *React. Kinet. Catal. Let.,* 18, 33 (1981).

[113] K. Inui, *Jpn. Pat.* 07-256,102 (95-256,102) (1995).

[114] F. Araya, Mitsubishi Chem. Ind. Co., *Jpn. Pat.* 57-128,650 (1982).

[115] A. Knorr and W. Albert, *U.S. Pat.* 1,714,378 (1929).

[116] J. Przondo, E. Bielous and I. Franek, *Przem. Chem.* **59**, 436 (1980).

[117] Y. Murata, N. Miyake, N. Ueki, and O. Hotta, *Jpn. Pat.* 02-015,042 (1990).

[118] Y. Murata, N. Miyake, N. Ueki, and O. Hotta, *Jpn. Pat.* 02-015,042 (1990).

[119] S. H. McAllister and F. E. Bullard, *Brit. Pat.* 504,337 (1939).

[120] K. Seishiro, *Mitsui Petrochem. Ind. Ltd*, *Jpn. Pat.* **55**, 436 (1980).

[121] S. Kubota, *Mitsui Petrochem. Ind. Ltd*, *Jpn. Pat.* 55, 831 (1980).

[122] V. A. Navrotskit, *USSR Pat.* 963,983 (1983).

[123] R. Nozawa, *Kyowa Yuka Co. Ltd*,   *Jpn. Pat.* 58-059,936 (1983).

[124] R. Nozawa, *Kyowa Yuka Co. Ltd*, *Jpn. Pat.* 58-059,935 (1983).

[125] H. D. Burgess, *Brit. Pat.* 881,918 (1961).

[126] B. Jover, T. Mandy, J. Soos, G. Gati, I. Juhasz, I. Fischer, and L. Nemeth, *H.U. Pat.* 38,089 (1986).

[127] R. Nozawa, *Kyowa Yuka Co. Ltd*, *Jpn. Pat.* 58-059,936 (1983).

[128] M. L. Deem, U.S. Pat. 4,102,930 (1978).

[129] M. L. Deem K. C. Stueben, *U.S. Pat.* 4,101,586 (1978).

[130] R. Teissier, D. Tichit, F. C. O. Figueras and J. Kervennal, *U.S. Pat.* 5,672,764 (1997).

[131] E. E. Connolly, *J. Chem. Soc.* 338 (1944).

[132] A. Hinnen, J. Dreux, and M. DelCpine, *Compt. Rend.* **255**, 1747 (1962).

[133] Y. Murata, N.Miyake, N. Ueki, K. Nagayama, *Jpn. Pat.* 62-190,141 (1987).

[134] Y. Ueda, *Mitsui Petrochem. Indu., Ltd., Jpn. Pat.* 59-222,435 (1984).

[135] M. Hauser, *Chem. Rev.* **63**, 311 (1963).

[136] A. Rieche, E. Schmitz and E. Gründemann, *Chem. Ber.* **93**, 2443 (1960).

[137] Y. Mizutani, *DE Pat.* 1,922,755 (1970).

[138] H. Stross, J. M. Monger and H. de V. Finch, *J. Am. Chem. Soc.* **69**, 1627 (1947).

[139] D. S.Noyce and M. Evett, *J. Org. Chem.*, 87, 397 (1972).

[140] A. Reiche, E. Schmitz and E. Grunderman, *Chem. Ber.* **93**, 2443 (1960).

[141] H. Guinot, *U.S. Pat.* 1,913,159 (1933).

[142] S. Denko, *Jpn. Pat.* 45-041566 (70-041566)45-041566 (70-041566) (1970).

[143] Y. K. Kim and J. D. Hatfield. *J. Chem. Eng. Data*, 30, 149. (1985).

[144] L. V. Robbins and W. J. Porter, *Brit. Pat.* 1,181,416 (1970).

[145] L. J. Sirois and F. J. Herrmann,M. E. Oldweiler, *Brit. Pat.* 1,116,037 (1968).

[146] L. V. Robbins, Jr. and W. J. Porter Jr., *U.S. Pat.* 3,361,828 (1968).

[147] W. J. Porter and E. E. Benjamin, *U.S. Pat.* **3**,153,068 (1964).

[148] R. J. Piccolini and M. J. Smith, *U.S. Pat.* 4,490,476 (1984).

[149] F. G. Klein and J. T. Banchero, *Ind.Eng.Chem.*, 48, 1278. (1956).

[150] Y. Mizutani, Y. Izumi, Y. Watanabe, *U.S. Pat.* 3,946,079 (1976).

[151] H. Guinto, *U.S. Pat.* 1,913,159 (1933).

[152] W. T. Reichle, *US Pat.* 4,458,026 (1984).

[153] C. Flego and C. Perego, *Appl. Catal.* **192**, 317 (2000).

[154] W. T. Reichle, *J. Catal.* **63**, 295 (1980).

[155] A. Canning, S. Jackson, E. McLeod, and E. Vass, *Appl. Catal.* **289**, 59 (2005).

Chapter 2
Experimental methods.

2.1 Catalyst preparation and characterization.

2.1.1 X-ray diffraction (XRD).

Since many substances have known crystal structure, powder XRD can be used as a fingerprint technique [1]. This technique uses powder or polycrystalline materials to create patterns arising from all possible crystalline orientations for each material. A powder diffractometer essentially consists of an x-ray source, a sample holder, a detector and a data storage device. XRD data can be analysed to give information such as the identification and proportion of the constituent phases, the degree of their stoichiometry and the formation of solid solutions. X-ray diffraction measurements are based on the generation of an x- ray beam when high speed electrons collide with a metal target. The electrons are usually generated from a hot tungsten filament cathode which is at high accelerating voltage with respect to the anode which is a water–cooled target metal. They are directed from the cathode toward the anode to produce the x-ray source. The x-ray beam generated is energy filtered and is then directed onto the sample of interest, creating diffraction for crystalline substances as shown in Fig. 2.1.1. The intensities of the diffracted beams are recorded by the detector and reported in terms of 2θ angle [2]. When used as a fingerprint technique, patterns are matched by comparison to the JCPDS or ICDD databases, although it is possible to perform more detailed structural analysis using techniques such as Rietveld refinement [3].

The resultant peaks are related to planes of lattice points within the analysed materials. Each diffraction plane of the material of interest is designated by Miller indices (h, k, l). Phase analysis and more detailed characterization can be then performed [4].
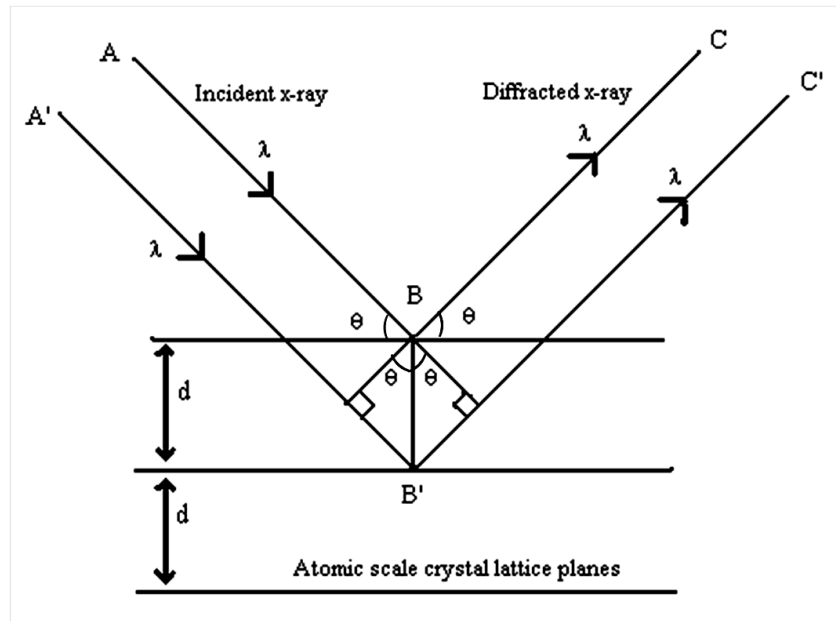
 Fig. 2.1.1 X-ray diffraction. The two parallel incident rays, A and B are at an angle (θ) with respect to the diffracting planes. A reflected beam of maximum intensity will result if the waves are in phase, represented by A' and B'. The difference in pathlength between A to A' and B to B' must be an integral number of wavelengths (λ).

Diffraction of the x-ray beam only occurs when Bragg's law is satisfied for constructive interference from two lattice planes with spacing d, according to [Eq. 2.1.1] [5]:

$$n \lambda = 2 \, d \sin \theta \quad (\text{Bragg's law}) \tag{2.1.1}$$

where d is the interplanar spacing, n is an integer, λ is the x-ray wavelength and θ is the diffraction angle.

The preparation and handling of XRD samples is an important consideration and care must be taken not to introduce any artefacts such as inducing structural changes upon sample grinding and/or neglecting the influence of preferred orientation.

All the x-ray diffraction measurements reported in this thesis were conducted using a Siemens D5000 diffractometer supplied with a graphite monochromator using Cu Kα radiation ($\lambda = 0.15406$ nm), at a generator setting of 40 kV and 40 mA with a 2 θ range between 5 $^{\circ}$ and 85 $^{\circ}$ using a 0.02 $^{\circ}$ step size and a scanning speed of 1s per step.

The powders were ground to ensure random orientation of the crystallites and were packed into a sample holder with a glass slide.

2.1.2 Thermal Analysis (TGA, DSC, DTA).

Thermal analysis is a general term for a group of analytical techniques which are used to monitor the behaviour of materials as a function of temperature, or time at a specific temperature [6]. A general definition describes the thermal analysis as the change in a property of a sample which is related to an imposed temperature alteration [7]. Thermal analysis techniques are used for many purposes such as to identify particular materials or to measure a property of interest, such as the heat of reaction, specific heat capacity, latent heat, flow stress, viscosity, elastic modulus and damping, thermal expansion and weight at a specified temperature pre-treatment region. It is applied to detect phase transformations, to assess the high-temperature stability of materials or to perform fundamental studies of reaction kinetics [8, 9]. Evolved gas analysis can be undertaken to determine the identity of gases lost from the sample under investigation as a function of temperature. No single thermal analysis technique works best in all situations. The key features for any thermal analysis technique comprise a furnace, a sample holder containing thermocouples, a recording system and a temperature programmer [10]. The atmosphere in the system can be varied for the parameter of interest. For most applications, thermal analysis is experimentally carried out by scanning a temperature range and measuring changes in mass (TGA) or heat flow (DSC or DTA).

TGA (thermogravimetric analysis) is one of the most commonly applied techniques. The change of mass of the sample of interest is measured as a function of temperature and time, in a controlled system [11, 12]. It is also possible to vary the reaction atmosphere to determine the "reactivity" of the material. The change in weight can be correlated to the thermal stability of a material, which is directly related to the material's volatility or thermal degradation. Commercial TGA instruments contain a furnace where the temperature is increased with time, often to temperatures exceeding 1000 $^{\circ}$C. Temperature calibration can be performed using Curie point analysis of reference standards [13, 14].

Calorimetry such as differential scanning calorimetry (DSC), measures the change of the difference in the heat flow rate to the sample and to a reference sample while they are subjected to a controlled temperature programme [15]. In adiabatic systems, the change in temperature can be translated into the enthalpy or energy content of a material by using the

heat capacity of the system. The experimental measurement is usually carried out on a closed system where determination of the heat, Q, associated with a change in temperature, ΔT, yields the heat capacity of the material C_p [Eq. 2.1.2.1]:

$$C_p = Q/\Delta T \hspace{5cm} (2.1.2.1)$$

There are two types of DSC thermal technique, heat-flux DSC and power-compensated DSC [16]. Heat flux DSC is the most practical and comprises an instrument where both sample and reference are in one furnace and connected by a low-resistance heat-flow path. Resultant heat flow is proportional to temperature difference. In power-compensated DSC the sample and reference are in different furnaces with separate heater coils and thermocouples. The difference in temperature between sample and reference is converted to a differential thermal power, or Δq, that is supplied to the heaters to maintain the temperature of both the sample and reference at the programmed value. Temperature is the independent parameter which is varied at a controlled rate. The feed heat to the sample and reference is controlled. The obtained data is heat flux per time or power as a function of temperature at a fixed rate of change of temperature. The heat flux can be converted to C_P [Eq. 2.1.2.1] by dividing by the constant rate of temperature change. The heat flux increases with temperature ramp rate, therefore, higher heat presents more sensitive spectra but the high heat lowers the resolution of the temperature of transition and can have consequences for transitions which display kinetic features. Differential thermal analysis (DTA) [17] is a technique which is related to DSC. The basic instrument for DTA is composed of two identical cells in which the sample and the reference (often an empty pan) are placed. The thermocouples are directly placed into the samples. Both cells are heated with a constant heat flux, using a single heater, and the temperatures of the two cells are measured as a function of time. A difference in temperature between the sample and reference is observed when a thermal transition occurs and can be calculated by [Eq.2.1.2.2]:

$$\Delta T = T_{sample} - T_{reference}. \hspace{4cm} (2.1.2.2)$$

The output from a DTA is temperature difference (ΔT) between the reference and sample cells. A negative value of ΔT indicates an endothermic process whereas a positive value is indicative of an exothermic process.

In DTA, heat is provided at a constant rate and temperature is a dependent parameter. Although the determination of transition temperatures is accurate in this technique, estimates of enthalpies of transition are generally not accurate. Quantitative analysis of DTA data is complicated which is why DSC is usually preferred, although improvements have been made to DTA instruments in this respect. These improvements include a good heat flow path between the sample and the reference minimising the resulting heat flow.

All thermal analysis measurements reported in this thesis were performed using a SDT-Q600 V 8.3 build 101, Standard DSC-TGA model equipped with an ESS quadrupole mass spectrometer. The DSC reference was an empty sample pan. Generally, analysis was performed on ca. 20 mg of sample, employing a 10 °C/min temperature ramp rate up to 900 °C.

2.1.3 TPD.

Temperature programmed desorption (TPD) is sometimes called thermal desorption spectroscopy (TDS) [18, 19]. It is used to measure the desorption rate of adsorbed molecules as a function of temperature. It also can be used in the study of strength of adsorption, adsorption states, surface concentration and desorption kinetics [20]. Atoms or molecules in the gas phase are adsorbed onto a surface at a low temperature (sometimes sample cooling is employed) and then desorbed by heating. Heating is generally performed in vacuum and a mass spectrometer and/or thermal conductivity detector is employed to detect desorbed species. Upon increasing the temperature, species can desorb as a function of their binding strength, and rate of desorption reflects the dependence of desorption activation energy on surface coverage. The measurement is mainly performed by cleaning the sample surface followed by adsorbing gas-phase species of interest and finally monitoring the desorption of adsorbate as temperature is increased in a controlled process.

For acid-base catalysts, the basic and acidic properties of solid catalysts are usually measured by the method of desorbing ammonia (NH_3 –TPD) [20, 21] and carbon dioxide (CO_2 –TPD) probe molecules for acidic and basic sites respectively [22, 23]. A more recent method is termed the acid-base simultaneous TPD method [24] which involves three sequences of adsorption of CO_2 and NH_3 followed by a linear increase of the system

temperature. The TPD technique can be used for the determination of the quantity and strength of the active catalytic sites located on catalysts. This idea is based on the principle that the strength of gas adsorption is strongly dependent upon the strength of the active sites on the surfaces. It is important to recognise that a potential limitation to the technique is that the probe molecules may interact with the surface in a different manner than that envisaged. For example, it has been documented that NH_3 dissociation can occur on CaO leading to high desorption temperatures and associated erroneous conclusions that CaO is a strong acid [25]. In this respect, where possible, independent spectroscopic investigation of the probe molecule –surface interaction should be undertaken.

The CO_2 –TPD reported in this thesis was performed using a pulse-flow microreactor system supplied with an on-line GC-14A Shimadzu gas chromatograph with a thermal conductivity detector and an ESS mass spectrometer (Fig. 2.1.3).
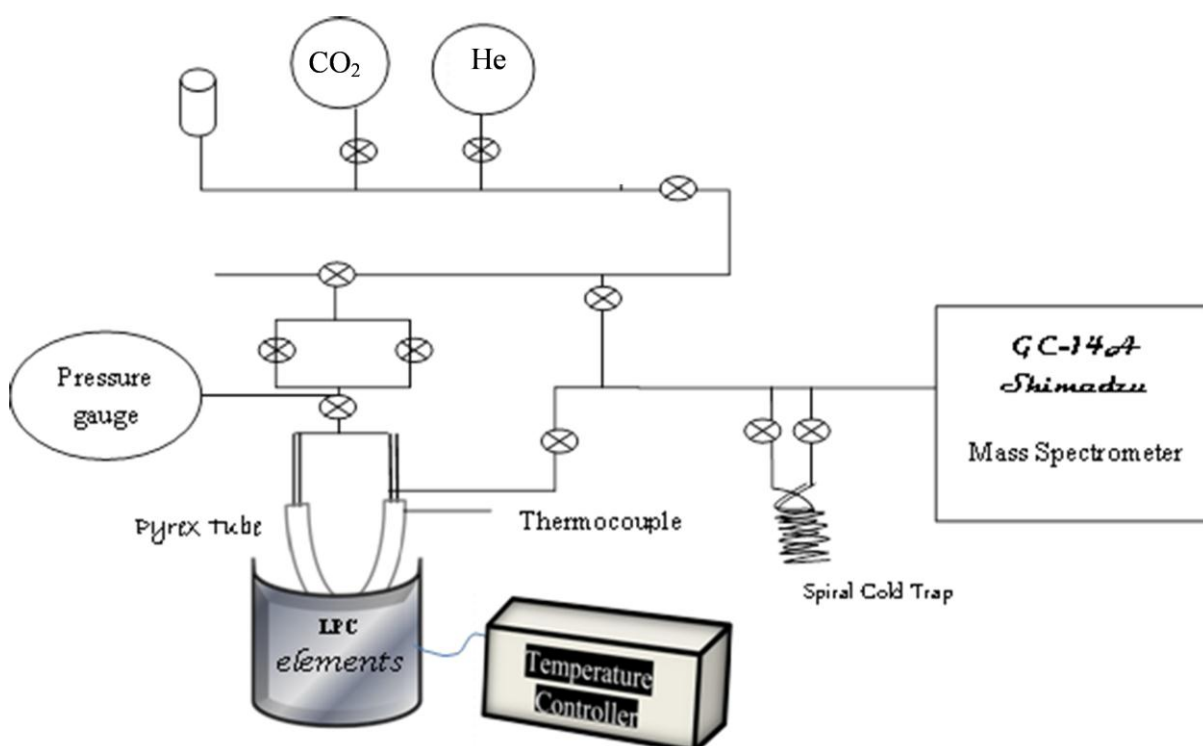
Fig. 2.1.3 Glass rig CO_2-TPD system used in this work.

The required amount of catalyst (generally in the range 0.2 - 0.5 g) was placed in the Pyrex reactor tube and housed on a CPC elements heater and heated in a 30-40 mlmin^{-1} flow of helium to 450 ^{o}C (10 K min^{-1}) for 2 h. The sample was then cooled to room temperature and the helium flow maintained. A gas pulse (15 μmol) of high purity >99.9%

CO_2 was then introduced from the sample loop into the carrier gas. Once the catalyst was saturated with carbon dioxide as determined by no further uptake of CO_2, TPD was applied by heating the sample to 600 ^{o}C in helium using a ramp rate of 10 K min^{-1}. The mass spectrometer was used to simultaneously detect and monitor the desorbed CO_2 (m/z = 44).

2.1.4 BET.

The determination and control of the surface areas and porosities of materials are very important in heterogeneous catalysis since they have a strong influence upon catalytic activity. The most widely technique for surface area measurement is the BET (Brunauer, Emmett and Teller) technique [26, 27]. The BET method is based upon the Langmuirian physisorption of molecules of precisely known size on the surface of interest. The monolayer capacity can then be determined and the surface area extracted by application of the following relationship:

$$\frac{P}{V_s(P_o - P)} = \frac{1}{V_m C} + \frac{(C-1)}{V_m C}\frac{P}{P_o} \qquad (2.1.4)$$

where V_s is the volume of the vapour adsorbed at equilibrium pressure P, V_m is the monolayer volume, P_o is the saturated vapour pressure for the adsorbate at the temperature of the experiment, and C is equal to $\exp[(L-L_o)/RT]$ where L refers to the latent heat of adsorption of the first layer of molecules and L_o represents the heat of evaporation of the adsorbate. Plotting $P/V_s(P_o-P)$ against P/P_o yields a straight line with slope $[(C-1)/(CV_m)]$ and intercept $[1/(CV_m)]$ and V_m can be determined by taking the reciprocal of the addition of their values. It is important to note that BET analysis should only be applied to type II and type IV isotherms in the BDDT classification [28] as well as in the P/P_o range of 0.05 – 0.3^{o}. Nitrogen is usually used as the adsobate due to its inert nature, well defined molecular cross-sectional area (16.2 $A^{o\,2}$) and because liquid nitrogen is a convenient coolant which is widely available.

In this thesis BET surface area measurements were performed using a Micromeritics Gemini 2360 Surface Area Analyser. The required amount of the sample (usually around

0.3 g) was placed in a sample holder and degassed at 110 ^{o}C overnight to remove any adsorbed moisture prior to analysis. The sample was then re-weighed to obtain the exact mass for analysis. The BET surface area measurement was then carried out by nitrogen adsorption at liquid nitrogen temperature using an automated programme.

2.1.5 SEM.

The scanning electron microscope (SEM) is a development of the light microscope which uses electrons instead of light to produce an image of materials by focusing a high energy beam of electrons onto the surface of a solid sample [29, 30]. The main features of the SEM instrument are a filament for the generation of electrons, lenses to direct the electrons toward samples, a beam deflector and a detector [31]. The operational process is performed by applying a voltage between the filament and the conductive sample in a vacuum environment (10^{-4} to 10^{-10} torr). A voltage is applied to heat up the filament causing the generation of electrons which are accelerated toward the anode. The beam is subsequently condensed by a condenser lens and the electrons then focused as a spot on the sample by the objective lens. The SEM contains various types of electromagnetic lens which have different functions. The lenses are also used to adjust the beam and the final spot size. They also shape the beam to prevent or limit the effect of the astigmatism, chromatic aberration, spherical aberration and diffraction. After electrons strike the sample they are emitted either as backscattered or secondary electrons. Secondary electrons are most widely applied for studying surfaces and are used to form a three dimensional image. The back scattered electrons are formed by the interaction of the beam electrons with the nucleus of the sample and are scattered back by the sample. The secondary electrons can be used to form the image. X-rays are also produced by interaction with the sample. The energies of such x-rays are sensitive to the elemental composition of the samples and this forms the basis of Energy Dispersive X-ray Spectroscopy (EDS or EDAX). SEM measurements in this thesis were performed using Philips XL30E-SEM. Samples were placed in a sample holder and inserted into the instrument. Some samples were coated with gold to prevent distortion of images by the build-up of charge on insulating materials. All images were magnified 1000 times under a 20 kV accelerating voltage.

2.1.6 GC.

Chromatography is a very important analytical technique that is used to separate mixtures of chemicals into individual components which then can be individually identified and

quantified [32-34]. The separation between components is based upon the difference in their partitioning behaviour between stationary and mobile phases. The partitioning behaviour has a temperature and column interaction dependence and mixtures of components can be resolved by passage through a column containing the stationary phase which may be held isothermally or subjected to a temperature programme. The time required for a compound to elute through the column depends upon the strength of its interaction with the stationary phase.

Gas chromatography (GC) consists of a carrier gas (the mobile phase) which is usually an inert gas such as helium, argon or nitrogen, a pressure regulator to control the flow rate of the gas through the chromatograph, a flow meter to measure and the flowrate of carrier gas, an injection port with a syringe needle to inject the sample, a column with a stationary phase, a heating system, a detector and a recorder. The injection port is maintained at a higher temperature than the boiling point of the sample components. The temperatures of the column, the injector and the detector are usually controlled independently. The injection of the sample is performed either by an automated device, or manually. If necessary, the sample is vapourised and mixed into the carrier gas where the sample vapour is then partitioned between the mobile and stationary phases. The choice of the carrier gas depends on the operation of the detector, as well as the efficiency and speed of separation required. There are two different general types of column, capillary and packed. Capillary columns comprise a thin fused silica coil of around 10-100 m length with the stationary phase coated at the inner surface. A packed column is a glass or stainless steel coil typically 1-5 m length filled with the stationary phase. The capillary column, as used in this study, provides perfect separation efficiency but it is easily overloaded. The separation occurs according to two factors, the solubility of the compounds in the stationary phase and the vapour pressure of the compounds. The more volatile compounds that have higher vapour pressure and lower boiling point require less energy to reach the equilibrium therefore they pass through the stationary phase faster than the less volatile compounds. Other factors such as the flow rate of the carrier gas, the type of stationary phase and the length of the column can also affect the separation process. The separated compounds are then detected by the detector to creating an output in proportional to their quantity. Various detectors can be used such as flame photometric (FPD), electrolytic conductivity (Hall/ELCD), mass spectral (CI/EI), flame ionization (FID), nitrogen-

phosphorus (NPD), electron capture (ECD), photo ionization (PID) and thermal conductivity (TCD) detectors.

Gas chromatography has been applied in this thesis as a means of product / reactant analysis. GC analysis was conducted on liquid samples (diluted in 1:10 ratio with HPLC grade Fisher Scientific acetone) using a Thermo Quest Trace GC, trace MS fitted with a AS2000 auto sampler. The column used in this instrument was a SGE sol gel wax 30 metre, 0.25 mm ID, 0.25 mm film run at a pressure of 14.5 p.s.i. The injector was heated to 200 ^{o}C and split ratio was 50:1. The initial oven temperature was 40 ^{o}C. After 5 minutes it was increased at 10 ^{o}C /min to 170 ^{o}C where it was held for 41.5 minutes. GC calibration and method setting were performed by preparing various standard solutions of the expected reaction products. Four different concentrations 0.1, 0.5, 0.75 and 1 M of methylisobutylketone (MIBK, Fluka, 99%), mesityl oxide (MO, Fluka, 99%), diacetonealcohol (DAA, Aldrich), 2,6-dimethylheptan-4-one (DH, Aldrich), Isophorone (Isoph, Aldrich, 97%), phorone (Phor, Aldrich, 97%) and 4-methyl-2-pentanol (4M2P, Aldrich) were prepared. Each component was run individually using acetone as a solvent, and area for each concentration was recorded and saved. Calibration curves were obtained by plotting area against concentration for each component and the gradient and intercept were determined to use in further calculations such as conversion and selectivity (Fig. 2.1.6). Traces of the GC analysis were included in the appendix.
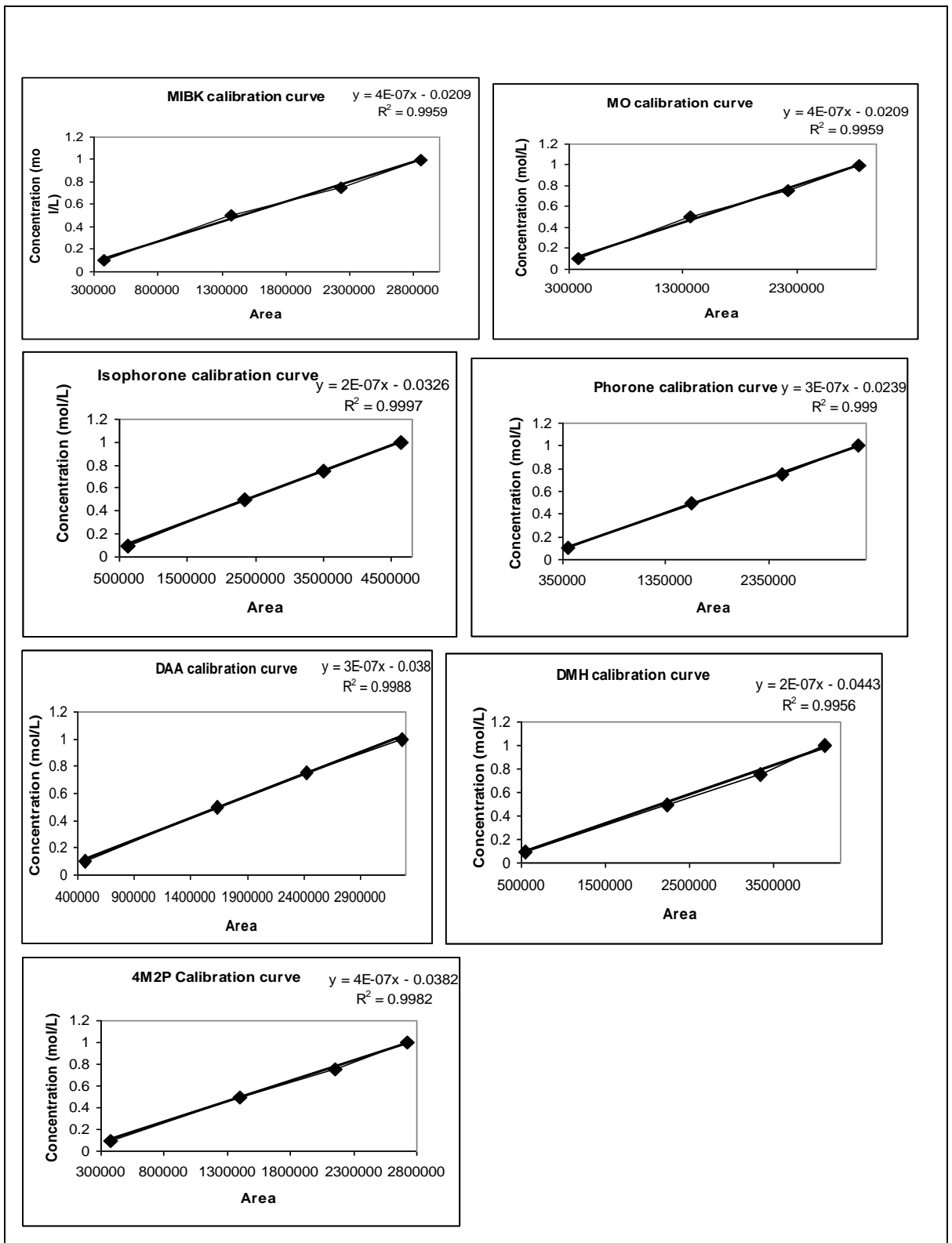
Fig. 2.1.6 Standard component GC calibration curves.

2.1.7 Reactor.

Catalytic reactors are designed according to the nature of the reactions of interest. They may be operated in batch, semi-batch, or continuous modes [35-37]. Therefore the difference in their shapes, sizes and operating conditions are strongly based on the nature of the reaction system and how it is influenced by pressure, temperature, catalyst properties, and other factors. Laboratory reactors which are usually used to gather information and perform activity screening require careful design to obtain well defined reaction temperatures and pressures and hence reliable reaction kinetics. They differ from large scale industrial reactors which are typically designed to achieve efficient production. In addition, the phase in which the reaction takes place also strongly influences the design of reactor applied. For homogeneous reactions, particular reactors such as plug flow, continuously stirred tank reactors (CSTR) and batch reactors are used. Heterogeneous reactions are carried out in either packed or fluidised bed reactors and bubbled fixed bed, tickle bed, CSTR slurry, bubble slurry and 3-phase fluidized reactors.

The reactor that was used in the current work was a continuous flow microreactor consisting of an HPLC pump connected to a vapouriser which was connected to a 15 inch reactor tube housed in a tube furnace. The exit of the tube was connected to a knock-out pot. Gas flow rates were maintained by Brooks 5850 TR mass flow controllers (MFCs), the reaction pressure was maintained by a Tescom back pressure regulator and thermocouples were used to monitor temperature. A schematic of the reactor is presented in Figure 2.1.7.

Reaction conditions were chosen to mimic those of interest for application to the development of single stage processes for the production of MIBK. This involves running the reaction at elevated pressure in a H_2-containing atmosphere. Extended times on stream were investigated in order to determine the rates of reaction following initial deactivation processes.
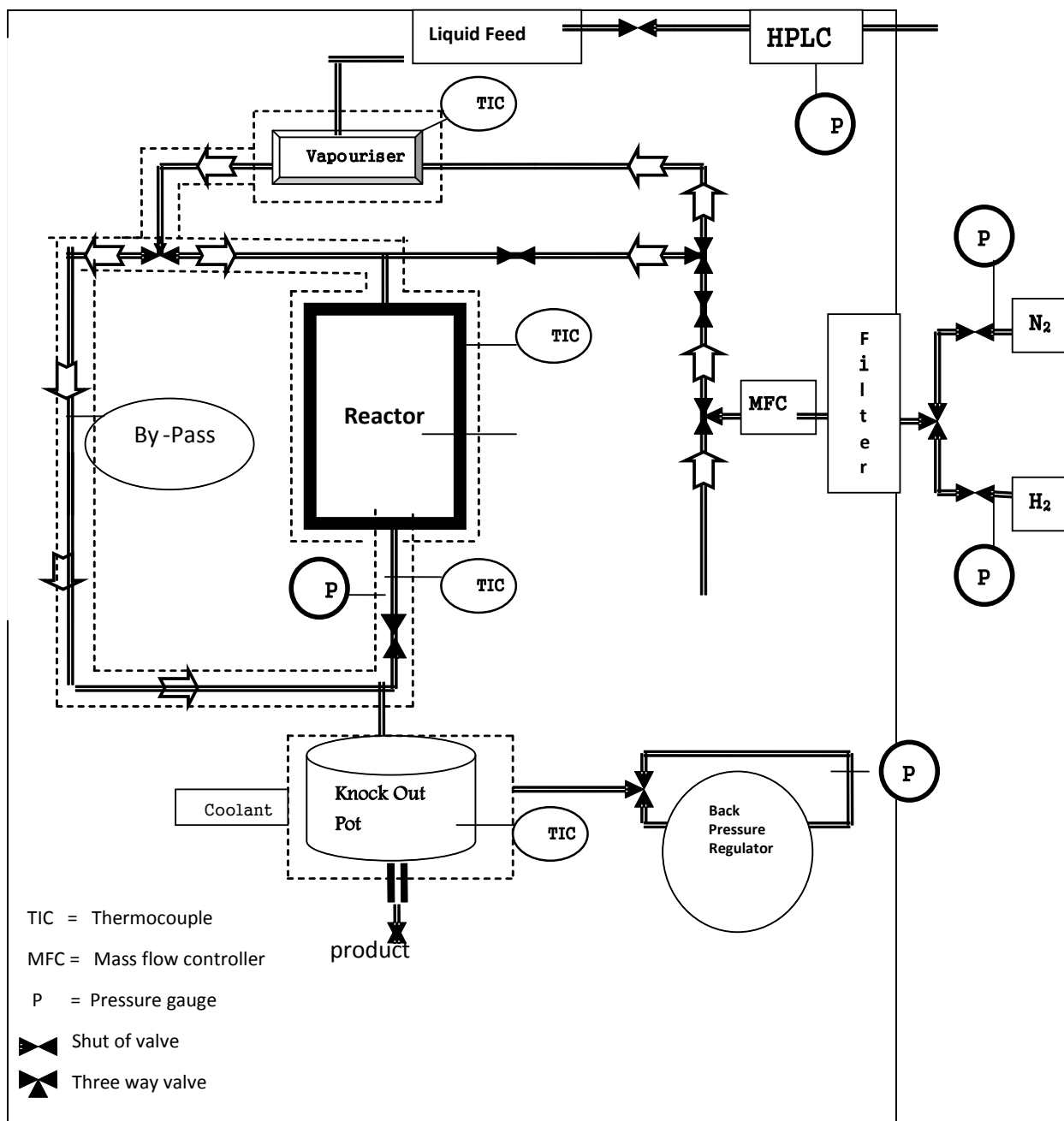
Fig. 2.1.7 A schematic of the microreactor used for the studies presented in this thesis.

All catalysts were activated and pre-treated before reaction. The pre-treatment process was conducted by heating the catalyst at 450 °C for 2 h in a 50 ml min⁻¹ flow of nitrogen at 5 bar pressure. Aldol condensation reactions of acetone were performed in the continuous flow microreactor and the acetone (Fisher Scientific HPLC grade 99.99 %) flowrate was

Fig. 2.1.7 A schematic of the microreactor used for the studies presented in this thesis.

All catalysts were activated and pre-treated before reaction. The pre-treatment process was conducted by heating the catalyst at 450 $^{\circ}$C for 2 h in a 50 ml min^{-1} flow of nitrogen at 5 bar pressure. Aldol condensation reactions of acetone were performed in the continuous flow microreactor and the acetone (Fisher Scientific HPLC grade 99.99 %) flowrate was

maintained at 0.0415 ml min^{-1} (liquid) using a Gilson HPLC 307 pump. H$_2$ (BOC high purity) was used to volatilise the acetone with a flow rate of 50 ml min^{-1}. Acetone and hydrogen were continuously fed to the reactor where the reaction was conducted using 0.5 g of catalyst at 400 ^{o}C and a total pressure of 5 bar. Products were collected in the cooled knock-out pot and analysed using GC.

2.1.8 CHN Analysis.

Elemental analysis techniques are used to identify elements in compounds quantitatively by determining the weight percentages of the elements of interest. They provide important information which can help in determining unknown structures and the purities of materials. Quantitative analysis can be performed by gravimetry or by optical atomic spectroscopy including graphite furnace atomic absorption, flame atomic absorption and inductively coupled plasma atomic emission. Qualitative analysis can also be performed using atomic spectroscopy, x-ray photoelectron spectroscopy, Auger electron spectroscopy, particle induced x-ray emission and x-ray fluorescence .

The most commonly applied technique is CHNS analysis. The technique is used to determine the percentages of carbon, hydrogen, nitrogen, and sulfur. The method is destructive and involves burning a sample in an excess of oxygen to yield various combustion products in the form of CO$_2$, H$_2$O, NO$_x$ and SO$_2$ that are detected and identified. This information can be then used to calculate the composition of an unknown sample. The theory of the CHNS analyzer is based on Duma's method which involves total oxidation of the sample by flash combustion. Appropriate reagents are used to assist oxidation and to remove unwanted by-products such as halogens. The combustion products are then passed into a chromatographic column by a carrier gas where they are separated and NO$_x$ is reduced to N$_2$ prior to analysis. The products are then detected by a thermal conductivity detector (TCD) to produce output signals. These signals indicate the quantity of each component in the sample by reference to calibration standards [31, 32]. CHN analyses reported in this thesis was performed with the kind assistance of Mrs Kim Wilson using an Exeter Analytical CE- 440 elemental analyser instrument.

2.2 Catalyst preparation.

The main purpose for catalyst preparation is to form a material which has high productivity and efficiency [38-40]. This can be achieved by generating catalysts comprising small particles (high dispersion) and high surface areas. Various important factors such as regenerability, stability, activity and selectivity should be taken into account in catalyst preparation. These features are controlled by physical and chemical properties of the catalyst. Catalyst properties are essentially dependent upon different parameters. Supported catalysts are usually prepared in two stages [41]. Firstly, a dispersion process which consists of the interaction of metal-salt components in a highly dispersed form is achieved via co-precipitation, impregnation, deposition or adsorption from solution. In the second stage a calcination or reduction process which involves the generation of a metallic or oxidic form of the supported metal salt which can be achieved by a thermal treatment in an inert atmosphere or an active atmosphere of hydrogen or oxygen [42]. In the preparation of supported base catalysts, impregnation and precipitation procedures can be applied. To generate strongly basic sites, high temperature calcination or activation procedures are necessary but care must be taken to ensure the maintenance of surface area, prevention of inactive phase formation and maintenance of the most active morphology. With respect to the latter point, surface ions of different co-ordination number environment will have different acid-base site strengths.

Impregnation occurs when the metal is loaded onto the support via filling the pores of the support with a metal salt solution in which the solvent is subsequently evaporated [43]. This can be achieved either by adding the support material to a solution of a metal salt or by spraying the support by the metal salt solution. The mixture is then dried and decomposed at elevated temperature by reduction or thermal decomposition to generate the active phase. In the initial stage of impregnation, the interaction between metal salt and the support in solution can be controlled by pH. This requires a determination of the point of zero charge (PZC) of the oxide which defined as the pH where the net surface charge of the oxide is equal to zero. When the pH is less than the PZC, the oxide surface is positively charged (protonated) and will adsorb anions. When the pH is higher than the PZC, the oxide surface is negatively charged (deprotonated) and will adsorb cations (Fig. 2.2.1) [44]. The strength of electrostatic interaction between the metal precursor species and the support is therefore crucially dependent upon the impregnation pH, and generally not enough attention is paid to this aspect.
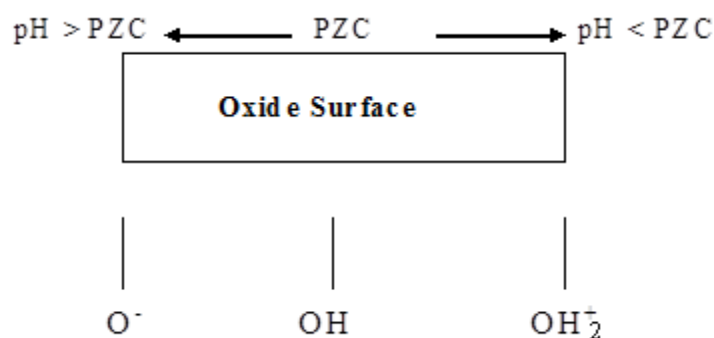
Fig. 2.2.1 The point of zero charge (PZC) on an oxide surface.

The pH of the impregnating solution may also have an influence upon the chemical species adsorbed, e.g.

$$7 \, MoO_4{}^{2-} \quad + \quad 8H^+ \quad \rightleftharpoons \quad Mo_7O_{24}{}^{6-} \quad + \quad 4H_2O \quad (2.2.1)$$
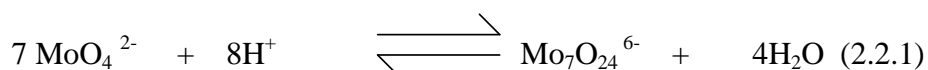
is a pH dependent equilibrium , with low pHs favouring $Mo_7O_{24}{}^{6-}$ over $MoO_4{}^{2-}$.

Properties and designed parameters of the resultant catalyst are based on the chemistry of the impregnated solution and the chemical and physical properties of the support. Thermal treatments are applied via two regimes: (i) at low-temperatures ($< 150 \, ^{o}C$) to remove water and some decomposition species, and (ii) high temperatures (often between 150 and 500 °C) to produce the metal or metal oxide. Different factors can influence the impregnation process such as the type of ion exchange and the ionic character and the capacity of the support surface. These factors are directly related to the chemical structure of the supports. Modern methods, mostly adapted from electronics industry, have recently been used for catalyst preparation. These include atomic layer deposition, chemical and physical vapour deposition.

The co-precipitation process [45] is a simultaneous precipitation of more than one component to achieve an intimate mixing of the catalyst and support and produce a stoichiometrically defined precursor with homogeneous distribution of catalyst components that are difficult to obtain by other preparation methods. The process is

performed via two alternative routes, either by dropping the salt solutions into an alkaline solution or the opposite way round. However, in multicomponent catalyst preparation, heterogeneous product can be obtained under inappropriate conditions due to the differences of the solubility of the product components. An example of this technique is the co-precipitation of metal ions with aluminium ions to produce a precipitated alumina gel containing the metal hydroxide. This is can be achieved via calcination which produces a support with active component dispersed throughout the bulk as well as at the surface. Co-precipitation is generally a simple method which does not require sophisticated instrumentation and low cost raw materials can be used. Very fine particles with high chemical homogeneity and high reactivity can be obtained. Calcination and sintering temperatures can be relatively low.

The deposition precipitation (DP) [46, 47] method is an alternative procedure which involves placing the support in contact with an aqueous solution of metal compound, the pH of which can be raised by the addition of a base, so that upon heating, oxidic precursor particles are formed on the support. Alternatively, it can also be performed by laying down the active components on the exterior surface of a support. One means by which this process may be performed is the preparation of catalysts by sputtering, which involves condensing the metal vapour onto an finely dispersed support. However, as this process requires a high vacuum, the technique is probably only useful for the preparation of 'model' catalysts. In liquid phase, the process can be achieved by the deposition of a metal sol onto a suspended support. Particle size and density on the substrate can be controlled by various factors including the concentration of metal compound, the type of support, the base, the reaction pH, the temperature and the time of reaction.

Most of the catalysts used in this thesis were prepared by the impregnation. All catalysts were calcined in a flow of N_2 (BOC, O_2 free N_2) at 50 ml min^{-1} for 2 h at 450 $^{\circ}$C prior to reaction.

CaO/SiO_2, $Pd/MgO/SiO_2$ catalysts (kindly supplied by Dr. Joe Gamman) were prepared by dissolving the exact amount in the minimum amount of distilled water before addition to the silica support. The amount of the nitrate precursors added was calculated in order to give a 5 wt% metal loaded catalyst. The catalyst was then dried in an oven overnight at 373 K.

MgO catalysts were prepared from two different precursors since the morphology, and hence resultant catalytic activity is known to be strongly dependent upon preparation route

[48, 49]. Magnesium hydroxide and magnesium hydroxycarbonate precursors were used as described elsewhere in the literature [48, 49].The magnesium hydroxide (Merck) derived catalyst was prepared by calcination in static air at 450 °C for 24 h and at 800 °C for a further 24 h. The magnesium hydroxycarbonate (Merck) derived catalyst was prepared by suspending in 750 ml distilled water, stirred at 70 - 90 °C for 30 min, and then filtered and dried at 150 °C for 16 h and calcined at 450 °C for 24 h in static air, and at 800 °C for a further 24 h.

5% Li-MgO catalyst was prepared by dissolving 4.5 g LiCl (Aldrich, 99%) in water (720 ml). The solution was then impregnated onto MgO, dried at 150 °C for 16 h and finally calcined at 800 °C for 3 h.

KNO_3/Al_2O_3 and KNO_3/ZrO_2 were prepared by grinding the support γ-Al_2O_3 (Synetix) with KNO_3 (Hopkin & Williams, 99%) at a given weight ratio in a mortar to mix them. 0.5 ml g^{-1} distilled water was then added to the mixture. The resulting paste was then kneaded for 10 min, dried at 383 K for 12 h and finally crushed to particles. Commercial catalysts including ZrO_2 (Alfa Aesar, 99.7%), $Zr(OH)_4$ (kindly supplied by MEL Chemicals) and Y-$Zr(OH)_4$ were also used.

2.3 Catalytic studies.

The initial stage of the target process is the base-catalysed aldol condensation of acetone to DAA (diacetone alcohol). In the second stage, the acid-catalysed dehydration of DAA to MO (mesityl oxide) and finally a metal-catalysed hydrogenation of MO to MIBK (methyl isobutyl ketone) occurs in the ideal case [50, 51]. The target product MIBK is the intermediate of a consecutive reaction in which it is both formed and consumed by hydrogenation. Apart from that, a parallel reaction path is possible representing the direct hydrogenation of acetone to 2-propanol. Two different functional groups are subjected to hydrogenation. The hydrogenation of the highly reactive carbon double bond of mesityl oxide (MO) is necessary for MIBK production which is favourable. On the other hand, hydrogenation of any carbonyl group negatively affects MIBK selectivity. However, a metal site is essential for MIBK production. [52, 53]. The reaction is described in Figure. 2.3.1:

Fig. 2.3.1 Aldol condensation reaction of acetone over base catalyst indicating reaction products.

Various base catalysts have been used to catalyse the reaction including 5% CaO/SiO_2, 1% Pd 5% MgO/SiO_2, 14% KNO_3/ZrO_2, 36.5% KNO_3/ZrO_2, 5% $KNO_3/Zr(OH)_4$, 14% $KNO_3/Zr(OH)_4$, 36.5% $KNO_3/Zr(OH)_4$, ZrO_2, Y-$Zr(OH)_4$, 5% KNO_3/Al_2O_3, 14% KNO_3/Al_2O_3, 36.5% KNO_3/Al_2O_3, Li/MgO, MgO derived from $Mg(OH)_2$ and MgO derived from $Mg(OH)_2.MgCO_3$. Catalysts initially underwent a pre-treatment process at 450 ^{o}C under a 50 mlmin^{-1} flow of N_2 as an inert gas for 2 h to remove molecules such as water and generate the active sites. Reaction and pre-treatment procedures were normally conducted at 5 bar, unless stated otherwise.

Reactions were generally performed using a feed mixture of acetone and hydrogen and were carried out in the continuous flow micro-reactor previously described at a range of temperatures (100 ^{o}C, 200 ^{o}C, 300 ^{o}C, and 400 ^{o}C) under a 50 ml min^{-1} flow rate of H_2 gas and 5 bar pressure for 24 h. The pump rate of acetone was 0.0415 ml min^{-1}. The first sample of the product was collected after 18 h of the reaction. Subsequent samples were taken every hour, and the composition and time on stream for the collected samples were recorded. The collected samples contained a range of products namely: DAA (diacetone alcohol) as an initial product formed by the base-catalysed aldol condensation of two molecules of acetone, mesityl oxide (MO) produced from an acid-catalysed dehydration of DAA and MIBK (methylisobutylketone) formed by a metal-catalysed hydrogenation of MO. Further by-products could be formed depending upon reaction conditions. These include 4-methyl-2-pentanol, 2,6-dimethylheptan-4-one and the trimeric species phorone and isophorone. Samples were then analysed using GC and GCMS. Conversions and selectivities were calculated using the calibration curves for standard compounds (see GC section) obtained from GC analysis. From the calibration curves, the concentration of each component can be calculated from the GC peak area as follows:

Concentration (mol/L) = Area * (Calibration Chart x co-efficient) + (Calibration Chart y-int). Concentration was then used to calculate moles of product:

Moles of product = (Sample volume (mL) /1000) * Concentration (mol/L).

Moles of C atoms in product = Moles of product * Number of carbon atoms in product molecule.

Conversion (%) = Sum (Moles of C atoms in product) / carbon feed.

Selectivity (%) = Moles of product of interest/ Sum (Moles of all products).

Reaction rate = ((Acetone feedrate * Conversion) / Catalyst weight)/100. Similar equation was used to calculate the surface area normalised conversion using the total surface areas.

The reaction was significantly influenced by a number of variables. The catalyst pre-treatment process is important in order to activate the catalyst and consequently attain reliable results. The influence of pre-treatment variables has been investigated and examples of their influence is given below. Examination of the effect of the pre-treatment procedure upon the reaction has been determined by running an experiment without a pre-treatment process over the 5% CaO/SiO_2 catalyst. The result has been compared to that with the pre-treatment process. The comparison demonstrated that the conversion of acetone following pre-treatment was initially higher than that without pre-treatment, although at longer times on stream there was little/no difference between the two values (Fig. 2.3.2).
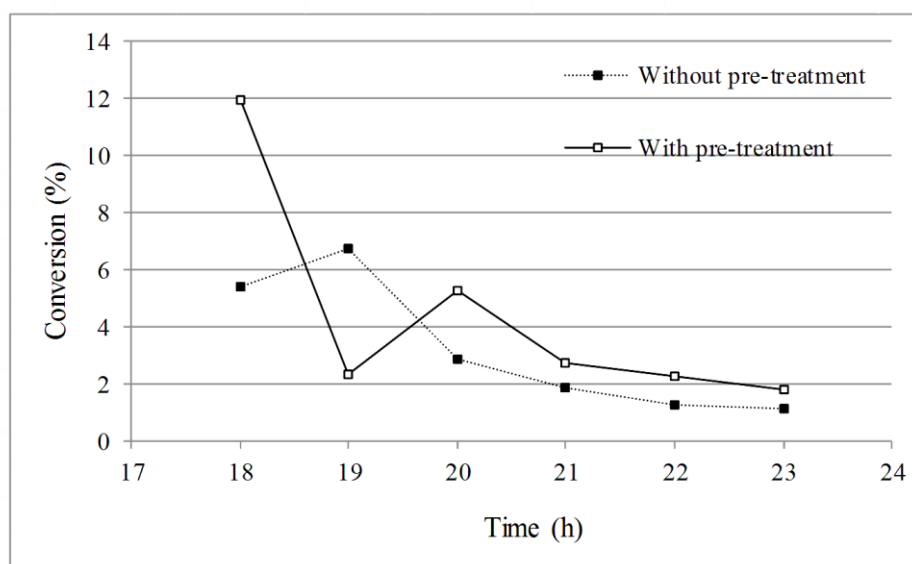
Fig. 2.3.2 The effect of the pre-treatment process upon acetone conversion (300 $^{\circ}$C, 5 bar pressure).

Furthermore, the influence of the temperature of the pre-treatment process has been examined at two different temperatures (350 $^{\circ}$C and 450 $^{\circ}$C) on the 36.5% $KNO_3/Zr(OH)_4$ catalyst. The experiments possibly indicate a very minor enhancement in conversion and higher MO selectivity at 350 $^{\circ}$C than the catalyst pre-treated at 450 $^{\circ}$C (Fig. 2.3.3), possibly due to loss of surface area. However, caution must be applied in making this comparison since the small difference at very low conversions observed may be prone to very large comparative errors.
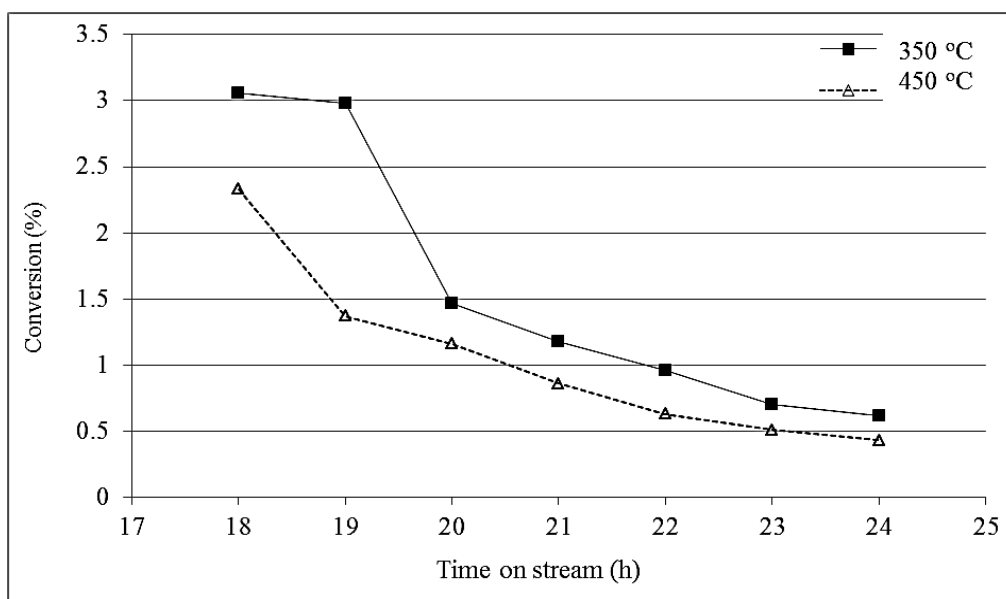
Fig. 2.3.3 The effect of the pre-treatment temperature on acetone conversion at 350 ^{o}C and 450 ^{o}C after 18 h of time on stream.
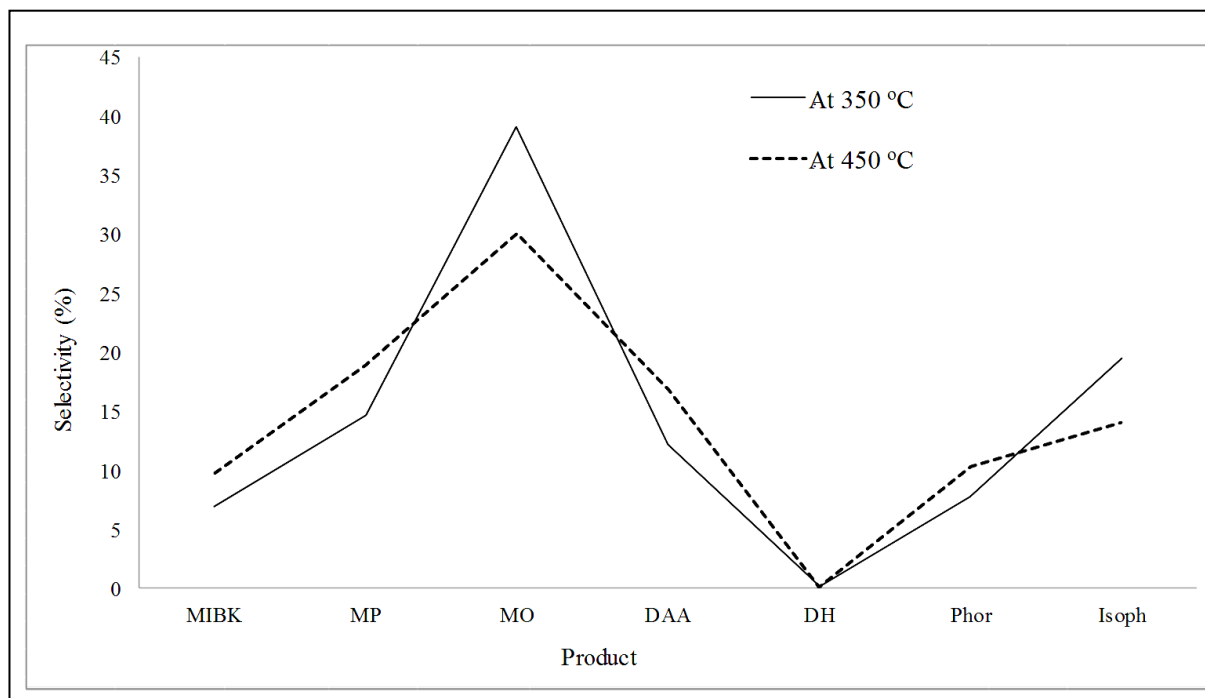
Fig. 2.3.4 The effect of the pre-treatment temperature on product selectivity at 350 ^{o}C and 450 ^{o}C after 18 h of time on stream.

The reproducibilitly has also been demonstrated over a 5% CaO/SiO$_2$ catalyst, at 200 ^{o}C reaction temperature and 5 bar pressure. Predictably, similar conversions values were achieved (Fig. 2.3.5):
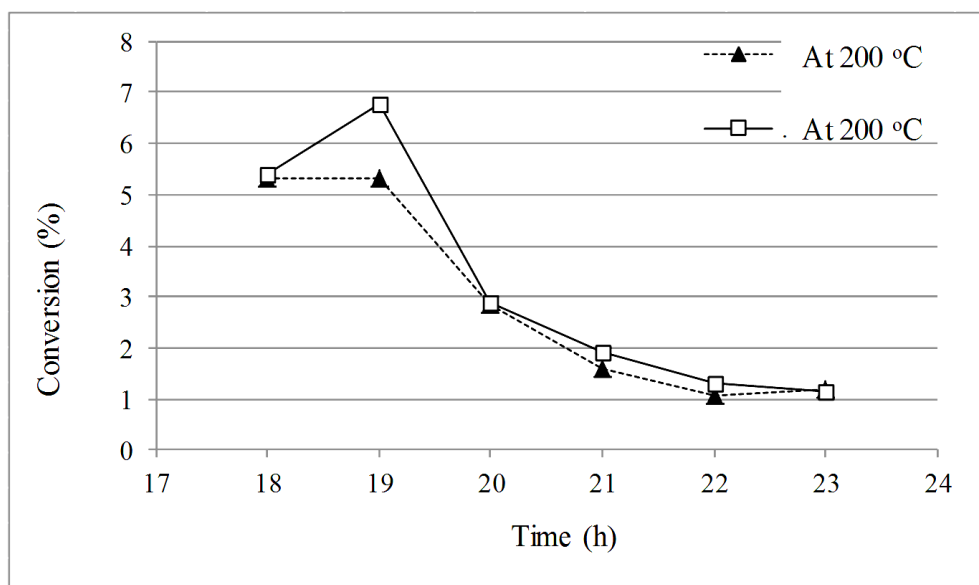
Fig. 2.3.5 Reproducibility test over 5% CaO/SiO$_2$ catalyst, at 200 ^{o}C reaction temperature, 5 bar H$_2$ pressure, TOS > 18).

Upon duplication, conversions were found to be generally reproducible within 12% of the mean and selectivities within 30% of the mean.

2.4 References.

[1] C. Suryanarayana, and M. Gr. Norton, "X-Ray Diffraction: a practical approach", Springer, ISBN: 030645744X, 9780306457449 (1998).

[2] B. D. Cullity, " Elements of x-ray diffraction ", Addison Wesley, (1956) .

[3] J. I. Langford and D. Louer, *Rep. Prog. Phys*. **59**, 131 (1996).

[4] R. J. D. Tilley, "Crystals and crystal structures", John Wiley and Sons, ISBN:0470018216, 9780470018217 (2006).

[5] C. Hammond, "The basics of crystallography and diffraction", 2nd ed., Oxford University Press, ISBN: 0198505523, 9780198505525, (2001).

[6] W. Wendlandt, "Thermal analysis", 3rd ed., Wiley, New York, (1986).

[7] W. Hemminger, and S. M. Sarge, " Handbook of thermal analysis and calorimetry", (Ed. M. E. Brown), Elsevier, Amsterdam, (1998).

[8] C. T. Kresge, M. E. Leonowicz, W. J. Roth, J. C. Vartuli, and J. S. Beck, *Nature*, **359**, 710 (1992).

[9] V. Antoshchuk, and M. Jaroniec, *J. Phys. Chem*. **103**, 6252 (1999).

[10] M. E. Brown, "Introduction to thermal analysis: techniques and applications", 2nd ed., Springer, ISBN: 1402004729, 9781402004728 (2001).

[11] R. C. Mackenzie, *J. Therm. Anal*., **8**,197 (1975).

[12] R. C. Mackenzie, *Thermochimica Acta*, **28**, 1(1979).

[13] P.K. Gallagher, and E. M. Gyorgy, *Thermochimica Acta*, **109**, 193 (1986).

[14] C. M. Earnest, "Compositional analysis by thermogravimetry ", ASTM International, Philadelphia , PA, ISBN: 0803111770, 9780803111776 (1988).

[15] G. Höhne, W. Hemminger, and H.-J. Flammersheim, " Differential scanning calorimetry", 2nd ed., Springer, ISBN: 354000467X, 9783540004677 (2003).

[16] J. W. Robinson, E. M. S. Frame, and G. M. Frame, "Undergraduate instrumental analysis", 6th ed., CRC Press, ISBN: 0824753593, 9780824753597 (2005).

[17] P. J. Haines, "Principles of thermal analysis and calorimetry", RSC, ISBN: 0854046100, 9780854046102 (2002).

[18] J. L. Falconer and J. A. Schwartz, *Catal. Rev. Sci. Eng*. **25**, 141 (1983).

[19] J. Lynch, "Physico-chemical analysis of industrial catalysts: a practical guide to characterisation", Editions Technip, ISBN: 2710808374, 9782710808374 (2003).

[20] M-Y He, *Catal. Today*, **73**,49 (2002).

[21] R. J. Gorte, *Catal. Let.,* **62**,1 (1999).

[22] R. J. Cvetanovic and Y. Amenomiya, *Adv. Catal.* **17**, 103(1967).

[23] P. Malet. *Stud. Surf. Sci. Catal.*, **57**, 333 (1990).

[24] T. Tago, Y. Okubo, S.R. Mukia, T. Tanaka, and T. Masuda, *Appl. Catal.* , **290**, 54 (2005).

[25] M. V. Juskelis, J. P. Slanga, T. G. Roberie, and A. J. Peters, *J. Catal.* **138**, 391 (1992).

[26] J. Rouquerol, F. Rouquerol, and K. S. W. Sing, "Adsorption by powder and porous solids", Academic Press, New York, (1999).

[27] S. J. Gregg, and K. S. W. Sing, "Adsorption surface area and porosity", Academic Press, London, (1982).

[28] K.S.W. Sing, D. H. Everett, R. A. W. Haul, I. Moscou, R. A. Pierotti, J. Rouquerol, and T. Stemieniewska, *Pure Appl. Chem.* **57**, 603 (1985).

[29] G. Cao, "Nanostructures & nanomaterials: synthesis, properties & applications", Imperial College Press, ISBN: 1860944809, 9781860944802 (2004).

[30] P. Echlin, "Handbook of sample preparation for scanning electron microscopy and x-ray Microanalysis", Springer, ISBN: 0387857303, 9780387857305 (2009).

[31] S. J. B. Reed, "Electron microprobe analysis and scanning electron microscopy in geology", 2nd ed., Cambridge University Press, ISBN: 052184875X, 9780521848756 (2005).

[32] W. Ramsey, *Proc. Roy. Soc.* **76**, 111 (1905).

[33] M. Tswett, *Ber. Deutsch. Botan. Ges.* **24**, 316 (1906).

[34] R. P. W. Scott, and J. A. Perry, "Introduction to analytical gas chromatography", 2nd ed., CRC Press, ISBN: 0824700163, 9780824700164 (1998).

[35] P. Trambouze, and J-P Euzen, "Chemical Reactors", Editions. Technip, ISBN: 2710808455, 9782710808459 (2004).

[36] U. Mann, "Principles of chemical reactor analysis and design: New tools for industrial chemical reactor operations", 2nd ed., Wiley-Interscience, ISBN: 0471261807, 9780471261803 (2009).

[37] D. L. Penry, and P. A. Jumars, *Biosci.* **36**, 310 (1986).

[38] R. L. Augustine, "Heterogeneous catalysis for the synthetic chemist", CRC Press, ISBN: 0824790219, 9780824790219 (1996).

[39] J. T. Richardson, "Principles of catalyst development", Springer, ISBN: 0306431629, 9780306431623 (1989).

[40] G. J. K. Acres, A. J. Bird**,** J. W. Jenkins, and F. King, *Catal.* London, **4**, 1 (1981).

[41] B. Delmon, P. Grange, P. A. Jacobs, and G. Poncelet, "Preparation of catalysts", Elsevier, Amsterdam, (1979).

[42] M. Che, and C. Bennett, *Adv. Catal.* **36**, 55 (1989).

[43] J. T. Richardson, "Principles of catalyst development", Springer, ISBN: 0306431629, 9780306431623 (1989).

[44] R. Richards, "Surface and nanomolecular catalysis", CRC Press, ISBN: 1574444816, 9781574444810 (2006).

[45] K. P. de Jong, *Stud. Surf. Sci. Catal.* **63**, 19 (1991).

[46] P. Serp and J. L. Figueiredo, John Wiley and Sons, (2008).

[47] J. R. Regalbuto, "Catalyst preparation: science and engineering", CRC Press, (2007).

[48] J. S. J. Hargreaves, G. J. Hutchings, R. W. Joyner, and C. J. Kiely. *J. Catal.* **135**,576 (1992).

[49] A. Burrows, S. Coluccia, J.S.J. Hargreaves, R.W. Joyner, C.J. Kiely, G. Martra, I.M. Mellor, and M. Stockenhuber, *J. Catal.* **234**, 14 (2005).

[50] C. Fiego, and C. Perego, *Appl. Catal.* , **192**,317 (2000).

[51] J. R. Sowa, "Catalysis of organic reactions", CRC Press, ISBN: 0824727290, 9780824727291 (2005).

[52] J. Baithwaite, "Kirk-othmer encyclopedia of chemical technology", 4th ed, (Eds. J. I. Kroschwitz, and M. Howe-Grant), **14**, 978 (1997).

[53] S. Wilde, and D. Sommer, *Petrol Tech. Quart*. 127 (1998).

Chapter 3

Catalyst precursor and doping effects upon MgO catalysed acetone conversion.

3.1 Introduction.

3.1.1 MgO.

Magnesium oxide is the most widely used alkaline earth oxide as a catalyst [1, 2], catalyst support [3-5], and modifier or promoter [6-8] in heterogeneous catalysis. MgO has strong basic properties that are responsible for base-catalysis in a large number of organic reactions. Nano-crystal MgO powders have potential applications for catalysis owing to strong surface basicity and high surface area [9]. Magnesia is one of the strongest basic oxides due to the presence of low co-ordinate O^{2-} anions [10]. However, it has also been proposed that surface basic hydroxyl groups are the active sites in the liquid phase aldol condensation of acetone over magnesium oxide [11].

MgO has been effectively used as a catalyst in numerous organic reactions, such as self-Michael addition to form methyl diesters [12], the Tishchenko reaction [1], the Meerwein-Ponndorf-Verley reaction [2], dimerisation of ethanol to butanol [13], self-condensation of propanol [14], benzylation of aromatic compounds [15], transesterification [16], aldol reaction [17], and Michael addition of malonates to enones [18].

The surface structure of MgO has been extensively investigated by Coluccia and Tench [19]. Several types of Mg–O ion pairs with different coordination numbers are evident (Fig. 3.1). Ion pairs of low co-ordination number exist at corners and edges of the MgO (100) plane or on high Miller index surfaces [20]. These different ion pairs appeared to be the responsible for the various basic sites that are generated upon heating. The doping of alkali metal with metals of larger cationic radius and lower cationic charge than Mg^{2+} such as Li^+, Na^+, K^+, and Cs^+ imparted high catalytic activity to MgO in acrylonitrile synthesis from methanol [21].
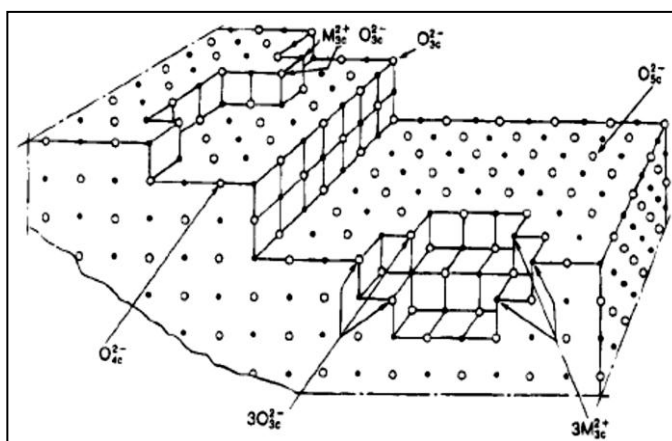
Fig. 3.1 Low coordination ions exhibited on the MgO surface [19].

MgO is often used as a model system as it can be easily prepared in the form of high surface area powders with microcube particles terminated by (100) faces which contain a series of morphological defects including terraces, kinks, and steps [22]. The surface can be described by families of well-defined low coordination sites of Mg^{2+} and O^{2-} ions [23]. Five co-ordinate ions are exhibited on crystallite surface planes, four co-ordinate ions upon crystallite edges and three co-ordinate ions on cube corners. The lowest coordination number ion pairs are reported to be able to promote the heterolytic dissociation of X–H bonds (where X = H, O, N, S, C) [24–26] and they also can be reacted with NO [27], CO [28, 29] and carbonylic compounds [30], whereas 5 co-ordinate ion pairs on the (100) surface are essentially inert. The lowest coordination sites are responsible of the reactivity of MgO towards adsorbed molecules promoting the formation of usual species such as polymeric oxoanions produced from the reaction with CO [31] or the reversibility and irreversibility of some reactions such as the heterolytic dissociation of H_2 (or D_2) [32]. Therefore the presence of multiple cation sites, which result from ensembles of Mg^{2+} ions possibly located on adjacent corners and/or edges, is an essential feature for the formation of adsorbed species [33]

It has been observed that the properties of various coordination sites of MgO strongly depend on the morphology of the microcrystals [34]. MgO can be prepared by simple thermal decomposition of precursors such as $Mg(OH)_2$, $MgCO_3$, $Mg(NO_3)_2$. Morphologies and properties of the synthesised MgO differ and strongly depend on the synthesis route and processing conditions. Therefore preparation conditions including time of pre-treatment, calcination temperature, and gas environment can substantially affect the catalytic behaviour and properties of the resultant MgO. Magnesium acetate and magnesium carbonate precursor are reported to be the most effective sources of MgO [35]. Aramendia et al found that magnesium oxide prepared from a commercial magnesium hydroxide is the most active catalyst for Meerwein-Ponndorf-Verley reaction of cyclohexanone with isopropyl alcohol [2]. Another study documented the application of a nanoscale high surface area MgO prepared from $Mg(OCH_3)_2$ by use of autoclave hypercritical drying (aerogel) procedure [36]. Aerogel prepared MgO exhibited higher reactivity than commercial and conventionally prepared MgO in Wadsworth–Emmons reactions [15]. MgO showed high activity of self-Michael addition of methyl crotonate [12]. In the same study, the authors found that MgO prepared from the decomposition of carbonate had a higher surface area and gave typically 70% greater selectivity than lower

surface area MgO prepared from the oxidation of metal ribbon in air. Lapszewicz and Jiang measured the basicity of some metal oxide catalysts including MgO and γ-Al_2O_3 using the CO_2-TPDE technique and they found that MgO was more basic than γ-Al_2O_3 and several types of basic sites with different strength existed [37]. Negatively charged oxygen anions (such as O^- or O^{2-}) are responsible for enhanced basicity.

MgO is not generally a support of choice in catalysis because of its low surface area as well as its tendency to reduce metal reactivity [38, 39]. Conversely, MgO has shown some interesting support performances in terms of its ability to stabilise some metals, preventing sintering and volatilization, and to improve the reactivity of Au metal in isotopic oxygen exchange and other reactions [40-43]. The favourable support effect of MgO is likely to be related to the formation of a metastable phase formed as a result of phase transformations [44] during catalyst preparation and pre-treatment. MgO is exclusive among common catalyst supports since it can react extensively with water. MgO has been reported as an active catalyst for certain reactions (e. g. H_2 -D_2 exchange) [45] after suitable pre-treatment.

The transformation of MgO (periclase) to $Mg(OH)_2$ (brucite) and its reverse, which are the basis of the synthesis of high surface area MgO powders, have been extensively studied [46]. Thermal expansion data for the layered $Mg(OH)_2$ lattice up to 100 °C has been previously documented [47].The thermal expansion measurements were performed up to and beyond the on-set of the dehydration. The dehydration reaction of brucite, $Mg(OH)_2$, to periclase, MgO, was investigated on both single crystal and poly-crystalline material. The cubic MgO formed as final product is always microcrystalline with grain sizes ranging from 75 Å or less when single crystals are decomposed, to 100 - 600 Å for poly-crystalline material [48].

Bussem and Koberich [49] have reported that the MgO crystallites have some degree of preferred orientation with respect to the original $Mg(OH)_2$ since the (001) plane of $Mg(OH)_2$ was converted to the (111) plane in MgO. The hexagonal [..OH/Mg/OH/OH/Mg/OH...] layer sequence in brucite occupied (001) plane transforms into the cubic [...O/Mg/O/Mg/O...] sequence on periclase along the [111] direction. The (100) direction of $Mg(OH)_2$ becomes the (110) direction in MgO. Both MgO and $Mg(OH)_2$ have close packed structures which can be described as a topotactic relationship that involves an overall arrangement in the stacking sequence of the anion layers and a redistribution of the cations. In industry, transformation from low surface area MgO (15-

30 m^2 g^{-1}) to high surface area MgO (100-300 m^2 g^{-1}) can be substantially undertaken by hydrating MgO and then calcining at temperatures above 400 ^{o}C, whereas catalysts prepared from MgO mostly have lower surface areas comparable to that of the starting material [50].

Brucite has the trigonal CdI$_2$ structure [51] in which each Mg^{2+} ion lies in a plane and ia surrounded by distorted octahedral OH ions in a sandwich arrangement (Fig. 3.2):
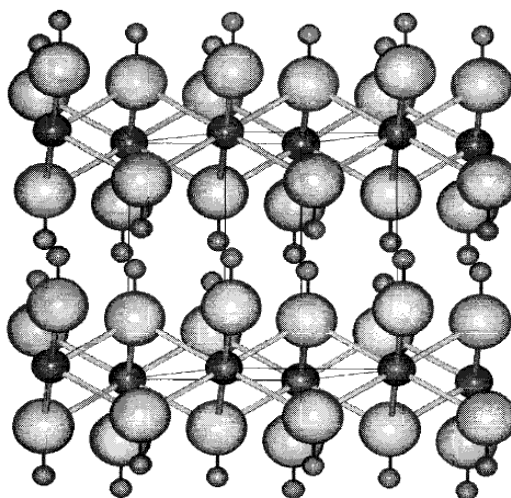
Fig. 3.2 Crystal structure of brucite (small spheres = H, intermediate spheres = Mg, and large spheres = O). The O-H bonds are stacked along the c direction [51].

The O-H bonds are perpendicular to these planes. The layers of brucite are held together by weak interlayer forces and are stacked along the c direction.

Some studies have investigated the morphology of magnesium oxide [52-54]. MgO has the sodium chloride structure and electrostatic considerations dictate that the (100) face, which contains equal numbers of magnesium and oxygen ions, is the only stable exposed face. In some instances higher index mean planes can be exhibited in MgO surfaces. These mean planes comprise aggregates of MgO microcublets which are assembled to form rough surface structures as shown in the figure taken from work by Moodie and Warble [52] and which is shown below (Fig. 3.3):
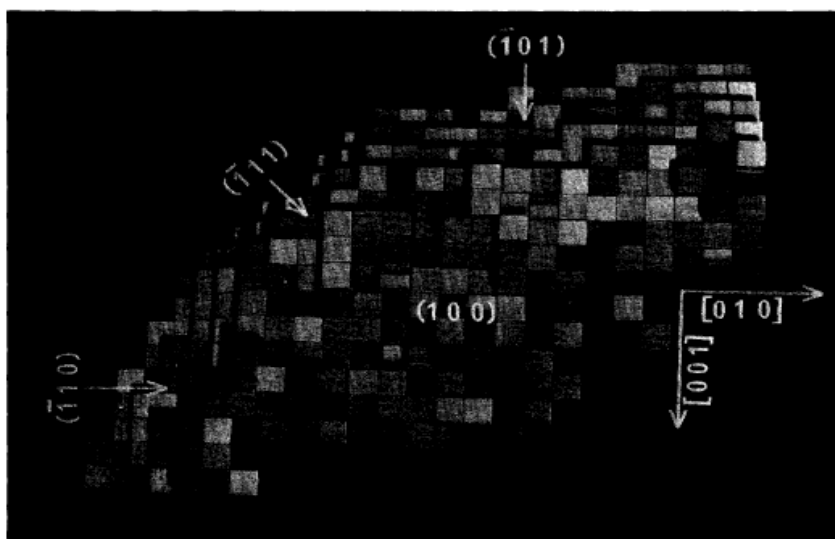
Fig. 3.3 High index plane aggregates of MgO microcublets [52].

In addition to higher index mean planes, it is possible to form metastable higher index planes as intermediates in the decomposition of some precursors. This has most commonly been observed/described when using brucite as the MgO precursor. In such studies, it is found that the morphology of magnesium oxide produced is dependent on the rate and the temperature at which the hydroxide is calcined. Heating of $Mg(OH)_2$ at about 300 ^{o}C results MgO crystallites with small crystal size which exhibit metastable surface planes where the orientation of (111) and (110) planes relate to the basal and prismatic faces of the parent hydroxide lattice respectively [55, 56]. At low heating rates up to low temperatures (300 °C) $Mg(OH)_2$ transforms into an assemblage of undulating sheets consisting of cubes of MgO joined near the edges, and with (111) axes normal to the plane of the sheet. The edges of the cubes are two to three unit cells in length and the overall variation in orientation is about 1°. This type of morphology was mainly generated under the mildest calcination conditions applied. On the other hand, calcination at higher rates of heating up to 600 ^{o}C gave a similar morphology, but with fracture along cube edges which breaks the primary structure into attached rafts made up of many cubes with (111) orientation [57]. The (111) surface termination plane resulting from the thermal decomposition of $Mg(OH)_2$ has been proposed to be stabilised by the presence of residual surface OH groups. A theoretical study has shown the following relationship (Fig. 3.4) [58]:
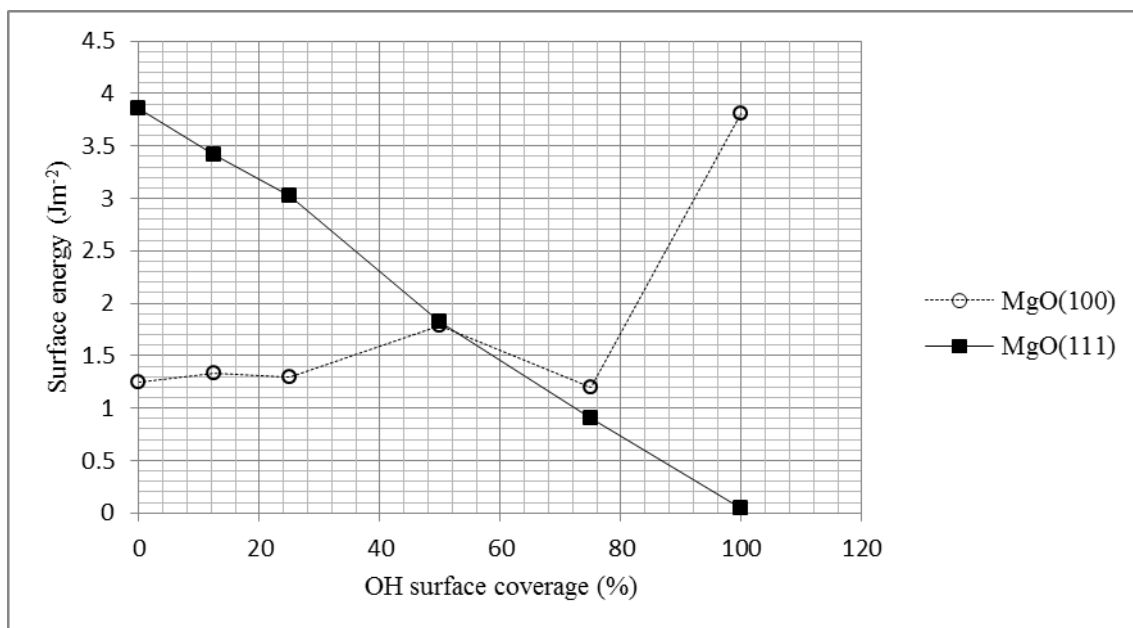
Fig. 3.4 MgO surface energy vs OH surface coverage of MgO(100) and MgO(111) [58].

Electron micrographs of various samples of MgO prepared by different methods from different precursors have been described in the literature [59]. MgO ribbon residue sample after use as a catalyst exhibited cubic morphology and exposed large (100) faces (Fig. 3.5). The side length of the cubes was in the range of 1000-2000 Å and there was a wide size distribution. The corners of crystallite appeared to be rounded, probably as a result of etching with water.
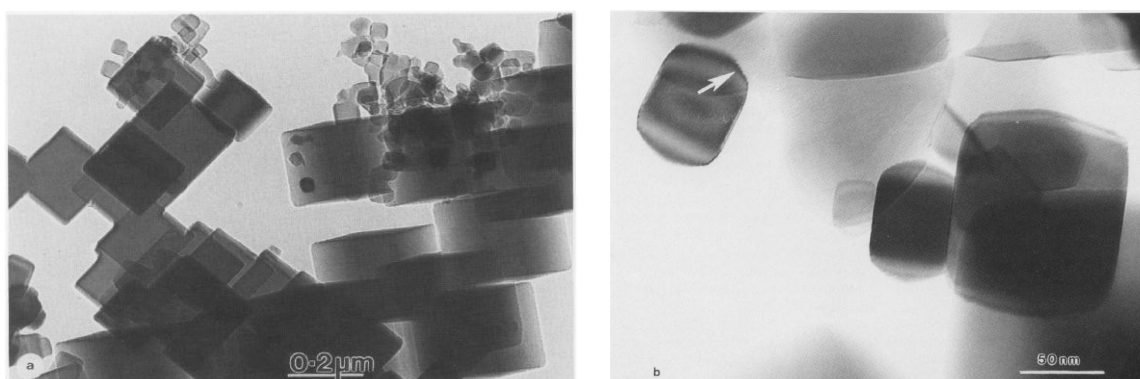
Fig. 3.5 Transmission electron micrograph (TEM) image of non-calcined MgO ribbon residue after use as a catalyst illustrating the predominant cube morphology of the crystallites and the rounded cube corners. (b) Phase contrast electron micrograph of MgO ribbon residue the post-reaction sample. The arrowed area indicates the high index surface structure composed of [100] type microsteps [59].

For MgO prepared from thermal decomposition of hydroxide precursor 800 ^{o}C in air, the size of the crystallites was between 200-400 Å and some crystallite alignment was also observed with the (100) face similar to the ribbon residue sample being exhibited (Fig. 3.6).
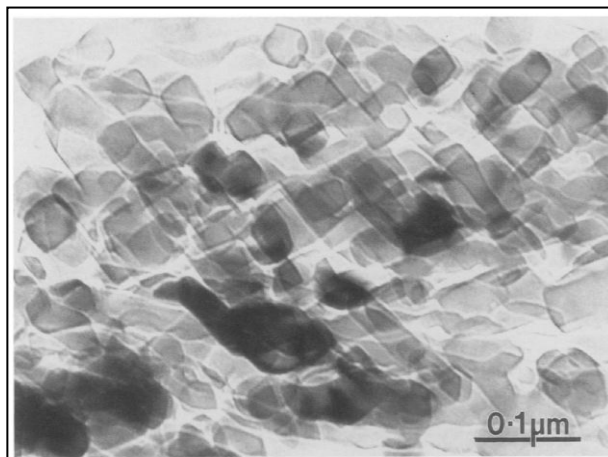
Fig. 3.6 Transmission electron micrograph of MgO prepared from Mg(OH)$_2$ prior to use as a catalyst and the distinctive "blocky" morphology of the individual crystallites is observed [59].

The crystallites of MgO that were prepared by calcining of a magnesium hydroxycarbonate (basic carbonate) precursor at 800 ^{o}C have an average size between 200-400 Å, which is similar to the crystallites of MgO derived from Mg(OH)$_2$ under similar conditions (Fig. 3.7). Nevertheless they were smaller and also they exhibited a less regular shape than those for the MgO ribbon residue (Fig. 3.5). They had a greater preponderance of microfacetted, higher index mean planes such as (111) and (110) than other two samples. These surface structures are similar to those described by Moodie and Warble [52] which were discussed earlier. When the calcination temperature was increased to 1100 ^{o}C, the resultant crystallites presented similar morphology to the ribbon residue sample (Fig. 3.5) and the average crystallite size was substantially enlarged to 2000 – 4000 Å.
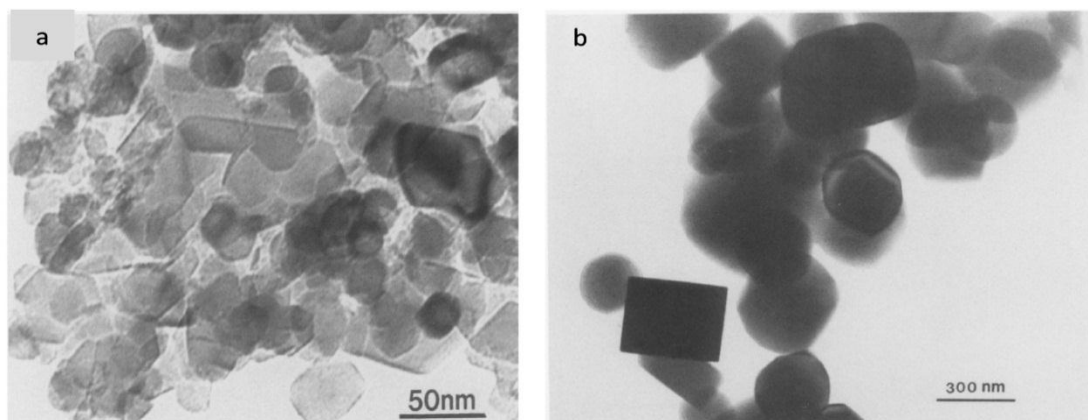
Fig. 3.7 a) High magnification transmission electron micrograph (TEM) image of MgO derived from $Mg(OH)_2.3MgCO_3$ and calcined at 800 ^{o}C in reaction atmosphere. The irregular shapes of the individual crystallites are increased. b) Transmission electron micrograph (TEM) image of MgO prepared from $Mg(OH)_2.3MgCO_3$ and calcined at 1100 ^{o}C prior to use as a catalyst [59].

The addition of water to hydroxide and basic carbonate derived materials can be used to modify MgO catalysts. Impregnation alters morphology and increases surface area. The post-treated material exhibited a higher preponderance of (100) planes (Fig. 3.8).
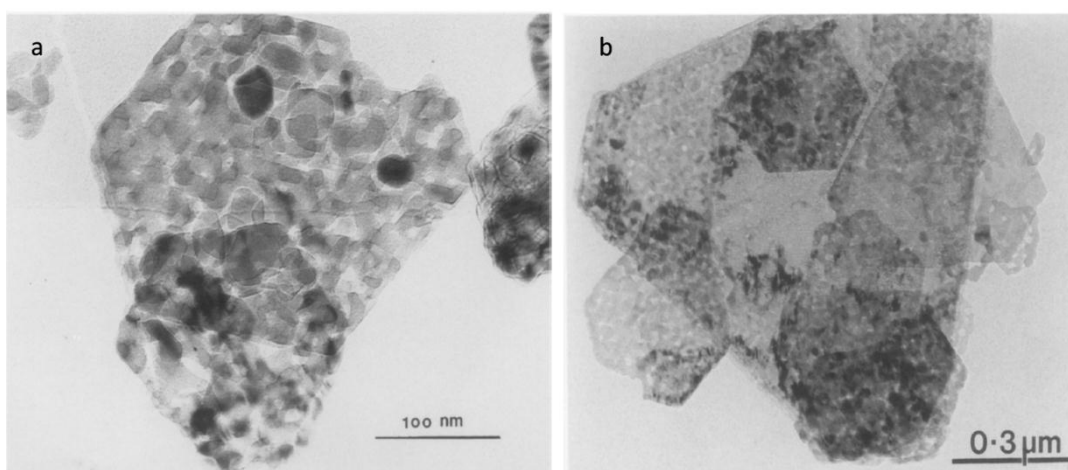
Fig. 3.8 a) Transmission electron micrograph (TEM) image of wet impregnated MgO prepared from $Mg(OH)_2.3MgCO_3$ precursor and calcined at 800 ^{o}C prior to use as a catalyst. b) Transmission electron micrograph (TEM) image of a wet impregnated MgO prepared from $Mg(OH)_2$ prior to use as a catalyst. The crystallites are arranged in hexagonal platelets [59].

Accordingly, although a fairly simple oxide, it is possible to produce MgO with different morphologies with a range of surface area using fairly simple preparation methods. Significant differences in the catalytic behaviour of such materials can be anticipated and have indeed been reported in a number of cases, e.g. [59, 78, 88]. Metastable MgO (111) planes, produced by decomposition of $Mg(OH)_2$ at lower temperatures, may be expected to exhibit especially enhanced reactivity since they are polar and comprise only 3 co-ordinate ions (as opposed to the 5 co-ordinate ions which comprise MgO (100) terrace faces, with the edges being 4 co-ordinate and only corner sites being 3 co-ordinate) as shown in the scheme below (Fig. 3.9):
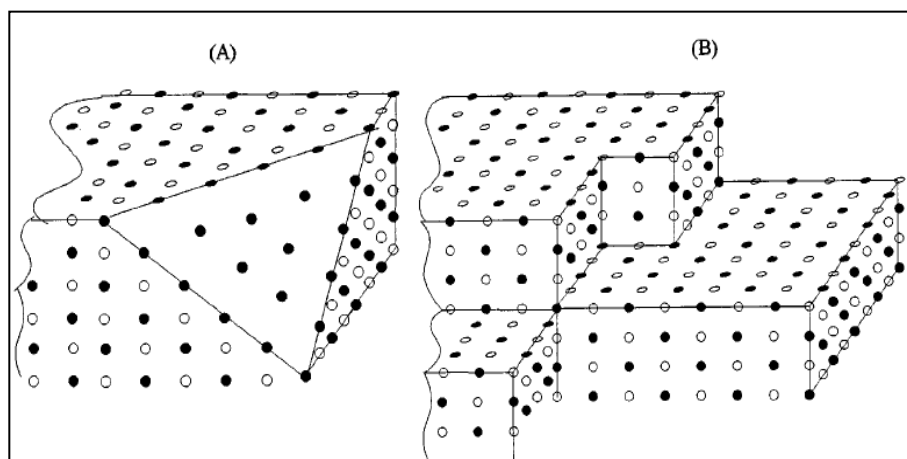
Fig. 3.9 Ideal MgO surface structures (A) (111) surface plane (B) microfacetted (100) planes.

On this basis, it can be anticipated that the preparation variables (and in particular the precursor) used for MgO synthesis may have a significant impact upon its performance as a base catalyst in acetone condensation.

3.1.2 Li/MgO.

In order to improve the catalytic performance of MgO, several workers have promoted the single component metal oxides by adding metal cations. Ueda et al [60] reported that promotion of magnesium oxide with Cu^{2+}, Ni^{2+}, Cr^{3+}, and Fe^{3+} enhances activity for the dehydrogenation of isopropyl alcohol. Other work showed that the addition of Li^+ to MgO creates high-strength basic centres and suggested that and this probably can be attributed to the effect of ion size which causes the structural promotion of the MgO lattice. Kurokawa et al [61] have extensively studied the dehydrogenation of isopropyl alcohol over magnesium oxide promoted by Fe^{3+}, Mn^{2+}, Cd^{2+} or Cr^{3+}, Al^{3+}, Ni^{2+}, and Cu^{2+}. The authors

found that the basicity of magnesium oxide was considerably increased by promoting with metal ions with ionic radius slightly larger than that of Mg^{2+}, such as Ni^{2+} and Cu^{2+}. They explained that such incorporation results in an expansion of the Mg-O bond length and in the localisation of an electron on the oxygen atom which subsequently enhances the solid base property. However, the addition of metal ions with far larger ionic radii, such as Cd^{2+}, did not enhance surface basicity.

Li-promoted MgO was also studied extensively for methane oxidative coupling [62] and $[Li^+O^-]$ centres, which consist of O^- ions adjacent to substitutional lithium ions, were proposed to be the active sites for abstracting a hydrogen atom from methane to form the methyl radical which is the reaction intermediate. The concept behind the Li-MgO system is again based on the effect of the ion size. The ionic radius of Li^+ is similar to that of Mg^{2+} ion and thus easy replacement of Mg^{2+} by Li^+ in the MgO lattice may occur. Substitution of a divalent ion by a monovalent one in the MgO matrix requires the formation of O^- anions in order to maintain electroneutrality, resulting in the formation of $[Li^+O^-]$ species, which are the responsible for the generation of basic sites. The oxygen anion O^- active species may be formed via two ways. In undoped MgO, oxygen active species can be generated from reaction of oxygen molecules with intrinsic vacancies. However, formation of active species in Li-MgO are produced by reaction of Li^+ ions with molecular oxygen [63]. Aparicio et al [64] found that in alkali promoted alkaline earth oxide materials, alkali metals can form stable bulk peroxides, and surface peroxide species produced by adsorption of gaseous diatomic oxygen may dissociate to form the active sites. The cleavage of the O-O bond can determine the overall activity by forming the active O^- ions. Other studies showed that formation of active species on the ionic surface of Li-MgO catalyst occurred by reversible dissociative chemisorption of gaseous $O_{2(g)}$. Oxide O^-, superoxide O_2^-, and $[Li^+O^-]$ were proposed to be the kinetically relevant species on the catalyst [65]. The addition of Li^+ to MgO increases mobility of lattice oxygen and thus decreases the activation energy of bulk oxygen diffusion from 63.50 kcal/mole for pure MgO to 14.60 kcal/mole for Li-MgO in the oxidative coupling reaction of methane [66]. Doping of lower valence cations into bulk oxides may generate lattice defects and increase oxygen mobility. The resultant oxygen vacancies react with gaseous oxygen to form O^- ions. Tanabe et al [67] have studied the influence of the addition of twelve different metal cations to magnesium oxide on the activity in the liquid-phase condensation of acetone at 0 °C and they concluded that Na^+, Zn^{2+}, and Zr^{4+} increased the catalytic activity. Di Cosimo

et al [68] investigated the vapour phase condensation of acetone at 300 °C over magnesium oxide promoted with 0.7 - 1.0 wt% of alkaline (Li^+, Na^+, K^+, and Cs^+) or alkaline earth (Ba^{2+}, Ca^{2+}, and Sr^{2+}) metal cations and they found significant impact of doping on the aldol condensation reaction of acetone and that the reaction was controlled by surface base property. They also observed that α, β-unsaturated carbonyl compounds were formed by consecutive condensation of acetone via aldol and/or Michael addition condensation reactions. In addition to modifying the surface catalytic properties, the inclusion of dopants can also exert physical influences, e.g. modification of surface area, etc. Dopants may also lead to surface modifications in which co-ordination numbers are changed. Martin and Mirodatos revealed that doping 20% mole of Na^+ into MgO caused a remarkable reduction of surface area from 70 m^2/g to 1 m^2/g [69]. Another study conducted by Iwamatsu et al showed also that the addition of alkali to MgO results in sintering and loss of surface area [70]. Parida and Rao have shown that preparation methods had significant impact on the surface area of Li^+-MgO prepared by different methods. They also reported that yield and selectivity for C_2-hydrocarbons, in the oxidative coupling of methane over Li-MgO prepared by precipitation methods, were decreased by increasing surface area, and by decreasing basicity. They proposed that the alkali dopants may lead to an increase of basicity due to the dispersion of univalent alkali ions on the divalent surface which results in formation and stabilisation of O^- ions [71].

Several theoretical studies have considered clusters of Li-MgO [72, 73]. Anchell et al [74] described the clusters of $(MgO)_n$ and $LiMg_{n-1}O_n$ (n= 4 and 6) as models for MgO and Li-MgO surfaces. They found that the lower co-ordinated lattice O species were more reactive and that homolytic fission of the C–H bond occurred on Li-MgO whereas heterolytic fission was achieved on MgO during methane activation. Similar results were reported by Orlando et al [75] that homolytic fission of the C–H bond was particularly favourable on the non-defect Li-doped MgO (001) surface when calculated using a periodic model surface. Relaxation and reconstruction of the lattice on MgO or Li-MgO during adsorption and a surface reaction were not considered, although relaxation of the lattice influences the stabilization of surface-adsorbed species. A significant relation between the co-ordination number of the reaction site and the reactivity has been reported by others [76]. A lower co-ordinated atom is usually more reactive and an extremely high reactivity is often accompanied by a lower selectivity in reaction in which intermediate products are targeted. The co-ordination numbers of reaction sites that can be presented on the surface are three,

four, and five as discussed above for pure MgO. Lintuluoto et al [77] have reported a model for the Li/MgO surface which includes all possible coordination numbers. They took into account the effects of relaxation and reconstruction of the lattice. The cluster has considered the relation between the reactivity and co-ordination numbers of the reaction site and the dopant Li atom. They chose the Mg_9O_9, Mg_8O_9Li clusters as MgO and Li/MgO surface models and the resultant modifications induced by doping are summarised in Figure 3.10 below:
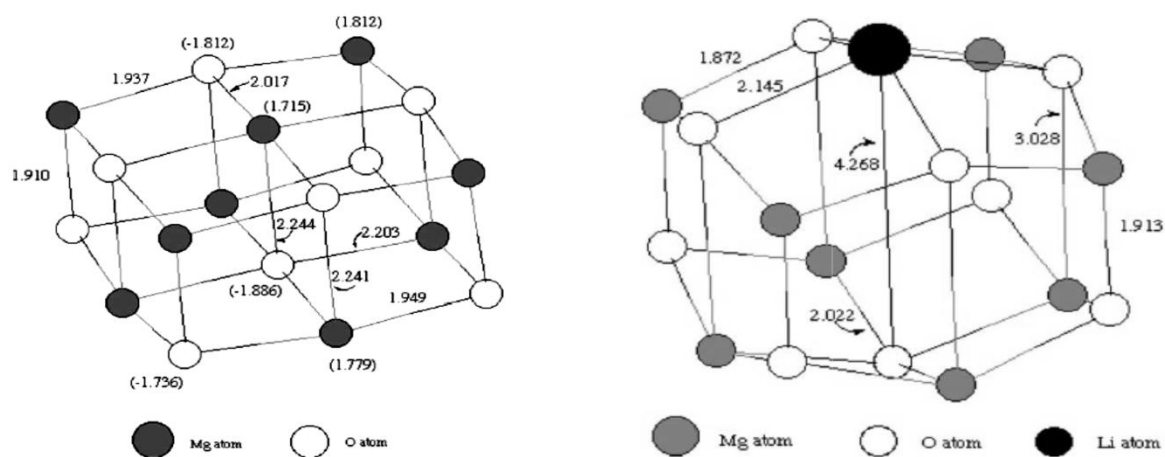
Fig. 3.10 a) Model of MgO and Li-MgO clusters illustrating optimized bond distances (Å) and net atomic charges for a) Mg_9O_9, b) Mg_8O_9Li. Values in parentheses denote net atomic charges [77].

The morphological effect of lithium addition to MgO has been previously discussed in experimental studies. Hargreaves et al [78] have investigated the morphological role of Li^+ doping MgO by transmission electron microscopy. They observed that the addition of lithium dopant to MgO increases the catalyst particle size and thus decreases surface area. Lithium also has a significant effect on the morphology of MgO. The characteristic morphologies resulting from the use of different precursors were lost on lithium doping and extensive dislocation networks were formed as discussed/shown below (Fig. 3.11). The grain growth possibly resulted from the oxygen vacancies that are introduced to maintain charge balance of Mg^{2+} substitution by Li^+. These vacancies assist diffusion within the lattice and thus increase sintering. The original precursor shapes of grains were changed and became almost spherical exposing mean higher index planes. They also found that adding lithium ions to MgO inhibits phase transformation and the main phase is cubic. Irregular grain boundary dislocation arrays also occur. Other dislocations are formed in the bulk as observed by systematic dislocation contrast imaging and these were identified as

the ½(110) type. It was suggested that they are probably caused by the segregation of lithium to the dislocation core since the defects are not annealed out by irradiation with the electron beam in microscope and by calcination at high temperature. They also concluded that lithium oxide did not form since lithium can be distributed throughout the MgO crystallites either by segregating at dislocation cores or by substituting on the surface of MgO. It was stated that is probable that the dislocations formed are related to the active sites for reaction. The termination of the dislocations at the MgO surface is expected to result in a net charged region of higher reactivity.
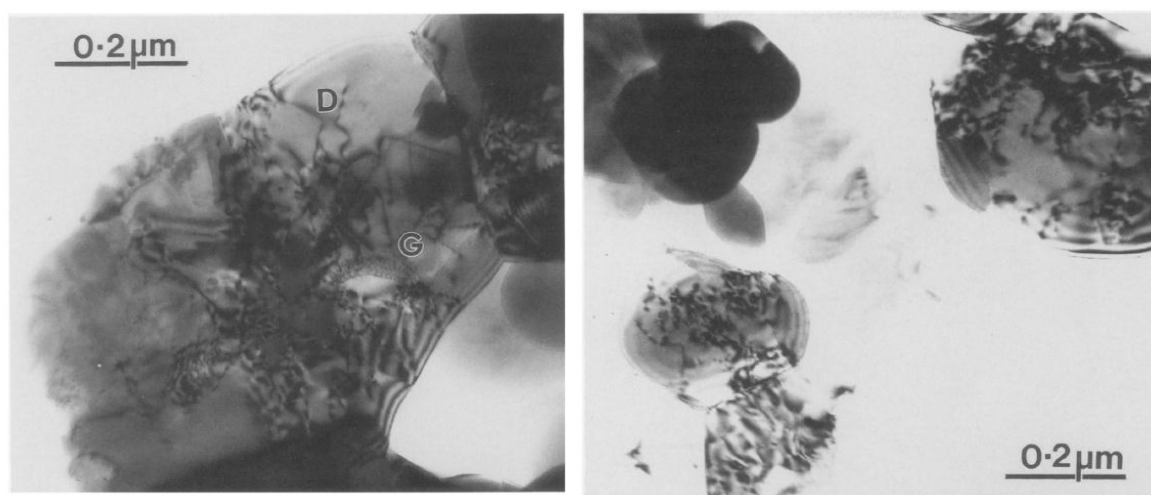
Fig. 3.11 Transmission electron micrograph (TEM) of about 5 wt% Li_2CO_3 doped MgO that prepared from $Mg(OH)_2$ prior to use as a catalyst. Individual dislocations within crystal bulk (area D) and a grain boundary dislocation array (area G) are obviously formed [59].

Since they are found to be immobile, this suggests that the dislocation is pinned by lithium on segregation to the dislocation core. This lithium pinning plays significant part of the formation of [Li^+O] centres which are possibly the active sites of the oxidative coupling of methane since direct relationships can be evidenced between [Li^+O^-] and the rate of methane activation [79].

Other workers [80] demonstrated in their SEM study of Li-MgO catalysts that the morphological properties of MgO were alerted by adding an excess amount of lithium dopant. Undoped MgO particles essentially exhibited a flake structure and after lithium addition (up to 6.1 wt%), the flake structure is preserved with agglomerates being surrounded by a diffuse structure. When the lithium dopant amount exceeded 6.1 wt%, the

surface was highly saturated by alkali metal and became almost heterogeneous with a molten phase being observed although traces of flake structures remained. They concluded that surface di-oxygen species, such as peroxide, would be present in the lithium-doped MgO catalysts. The active species were proposed to be [M^+O^-] centres produced by Li^+ substitution into the lattice and this process was associated with an increase of point defect concentration. At a higher Li^+ amount the outer surface layers are mainly composed of Li_2CO_3. Korf et al observed high active sites of Li-MgO system for the oxidative coupling of methane were formed by the decomposition of the Li_2CO_3 dopant [80]. In a study of different MgO/CaO catalysts, 85% loading of MgO/CaO presented the strongest basicity [81], demonstrating the influence of alkaline earth metal ion addition also.

It is clear that the addition of lithium ion dopant can have a profound effect upon the morphological and defect properties of MgO. As anticipated this results in modified catalytic activity. Whilst, arguably, most attention has been directed towards the oxidative coupling of methane in this regard, effects have been observed for other reactions. Hence, it can be anticipated that the lithium doping would be an area of interest for acetone conversion and also that morpgological features of MgO may play a role.

3.2 Results and discussion.

3.2.1 MgO.

In a view of the pronounced effects of MgO morphology upon its catalytic activity, as detailed in the introduction, catalysts have been prepared by different routes.

The precursors used are $Mg(OH)_2$ and $Mg(OH)_2.3MgCO_3$ which have been shown to yield MgO samples of very different morphology in previous studies [59].

The powder x-ray diffraction patterns of pre-reaction sample derived from the different precursors is presented in Figure 3.12. Prior to reaction, it can be seen that, as expected, MgO is the only phase evident in both samples. Upon comparison of the MgO reflection widths in both pre-reaction samples, it can be observed that those for the $Mg(OH)_2$ derived MgO are significantly broader. The width of reflections in powder x-ray diffraction patterns is governed by a number of potential factors: (i) instrumental broadening, (ii) lattice strain and (iii) coherent diffraction domain size. Given that the samples were run on the same instrument, the potential influence of differing instrumental effects can be ruled out.

The most probable explanation for the apparent difference relates to coherent diffraction domain size. This effect is governed by the Scherrer relationship:

$$d = k\lambda/b \cos \theta \qquad (3.2.1)$$

where d = diffraction domain size.

k = the shape constant.

λ = the x-ray wavelength.

b = the reflection width.

θ = the diffraction angle.

If crystallites are relatively perfect, as may be expected to result from the high calcination temperature applied in this study, the diffraction domain size will be the crystallite size of the material. Hence, narrower reflections relate to larger crystallites. On this basis, it can be suggested that the MgO derived from $Mg(OH)_2$ has a smaller crystallite size, and hence larger surface area, than the sample derived from $Mg(OH)_2.3MgCO_3$. This is indeed found to be the case as shown in Table. 3.1. A similar XRD result has been documented by Gulkova´ and Sˇolcova [82] in their study of MgO prepared by various methods under different conditions.
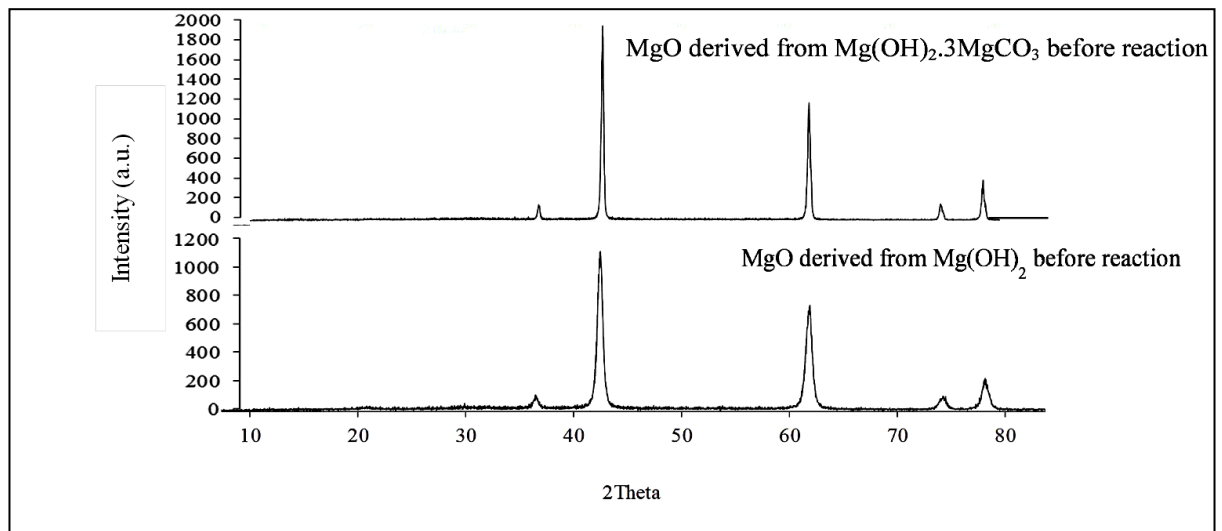
Fig. 3.12 X-ray diffraction patterns of the pre-reaction samples of MgO derived from $Mg(OH)_2$ and $Mg(OH)_2.3MgCO_3$ precursors.

Catalyst	Surface area (m^2g^{-1})
MgO derived form $Mg(OH)_2$	61
MgO derived form $Mg(OH)_2.3MgCO_3$	36

Table. 3.1 BET surface area of $Mg(OH)_2$ and $Mg(OH)_2.3MgCO_3$ catalysts.

The CO_2-TPD pattern of MgO prepared from $Mg(OH)_2.3MgCO_3$ showed three peaks which were observed at 90 ^{o}C, 240 ^{o}C, and 370 ^{o}C and which represent the basicity characteristics of the sample (Fig. 3.14). The CO_2 adsorption isotherms are very sensitive to the presence of polar groups or ions on the surface of the solid, such as hydroxyl groups [83]. The nature of the basic site in MgO at high temperatures could be attributed to low co-ordinate oxygen anions O^{2-} [84]. Different types of OH groups normally exist on magnesium oxide surfaces and they can be retained even after calcination at high temperatures (around 900 ^{o}C) [85] (Fig. 3.13):
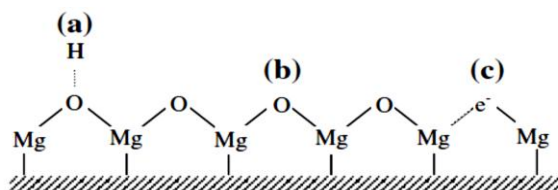
Fig. 3.13 Various structures of MgO contributing to the observed basicity [85].

The occurrence of the three regions of CO_2-TPDE pattern reveals a distribution of types of basic site. These regions are classified based on strength of the basicity [85]. The first region is between 100–300 °C relating to weak basic sites, the 300–550 °C region relates to medium basic sites, and 550–750 °C represents the strong basic sites [86]. On this basis, it can be concluded that only weak and medium basicity could be evidenced on the sample, although caution is necessary in this interpretation since the temperature limitation inherent to the experienced system used, means that it is not be possible to observe CO_2 desorption from any very strong sites present. Accordingly, due to this limitation, and also instrumental problems, no other MgO samples were investigated.
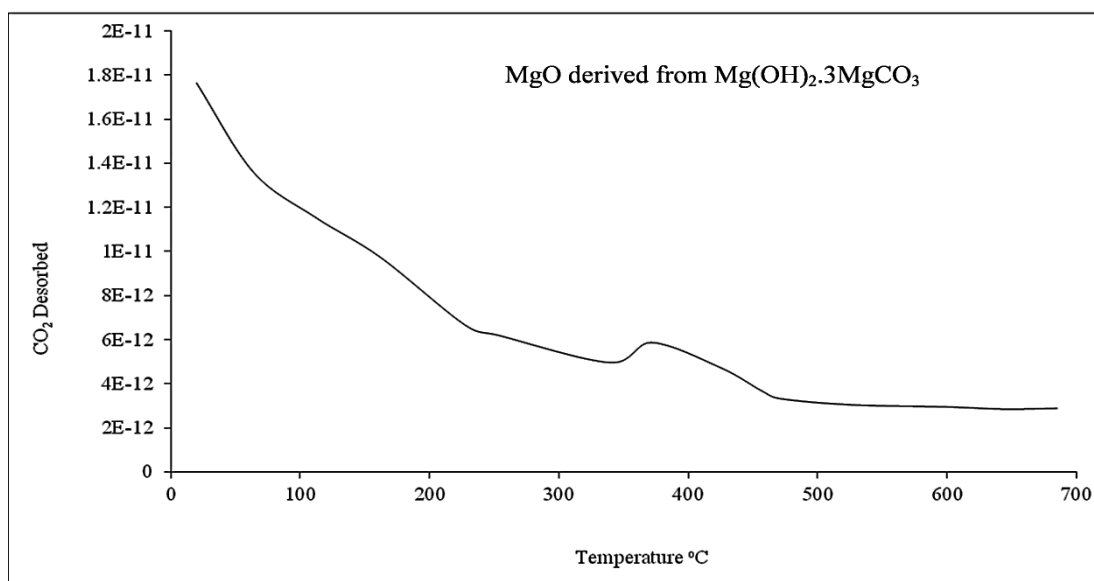
Fig. 3.14 CO_2 temperature programmed desorption (TPD) pattern of MgO prepared from $Mg(OH)_2.3MgCO_3$ catalysts.
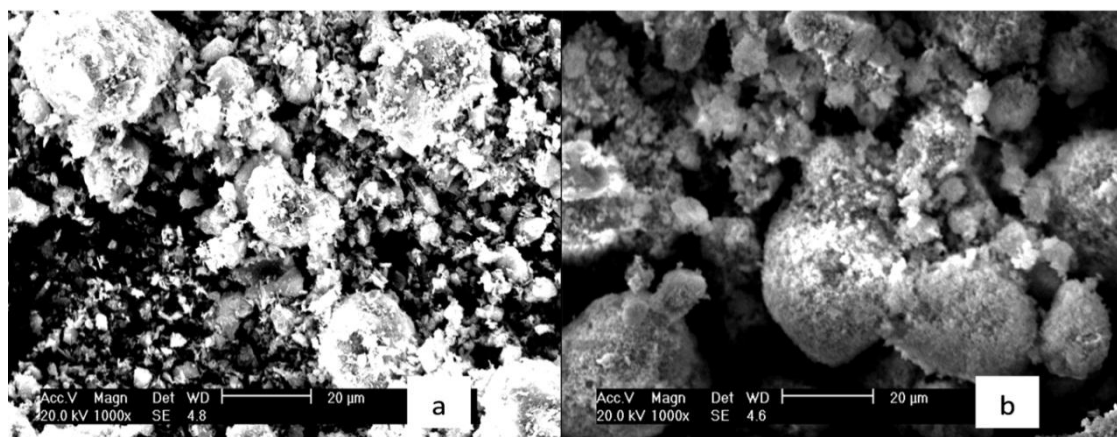
Fig.3.15 Scanning electron microscope (SEM) images of a) MgO produced from $Mg(OH)_2$, b) MgO produced from $Mg(OH)_2.3MgCO_3$ precursors.

SEM images of MgO catalysts prepared from $Mg(OH)_2$ and $Mg(OH)_2.3MgCO_3$ precursors showed unsymmetrical particles randomly distributed within structures having different shapes and sizes (Fig. 3.15). MgO derived from hydroxycarbonate (b) has a more regular morphology with larger particle size than MgO prepared from $Mg(OH)_2$.

The different MgO materials have been evaluated as catalysts for acetone conversion. In Table 3.2, it can be seen that there are differences in conversion evident between the MgO catalysts. However, the differences in surface area need to be borne in mind. Accordingly, surface area normalised conversion data has been calculated for the 18 to 23h time course

of the reaction and the results are presented in Figure 3.16. With the exception of the first point, it can be seen that surface area normalised rates of conversion are very similar over both materials and that the deactivation process also occurs in a similar manner. On this bases, it is tempting to conclude that there is no structure –sensitively in this reaction. However, consideration should also be given to the reaction selectivity, although this parameter is a function of concentration.

Catalyst	Conversion (%)	Selectivity (%)						
		DAA	MO	MIBK	Phor	Isoph	DH	MP
MgO prepraed from Mg(OH)$_2$.MgCO$_3$	85	4.01	87.63	0.54	0.40	1.74	0.11	5.57
MgO prepared from Mg(OH)$_2$	60	3.45	81.79	1.29	1.44	5.05	0.21	6.77

Table. 3.2 Conversions and selectivities for the aldol condensation reaction over MgO prepared from Mg(OH)$_2$, and Mg(OH)$_2$.3MgCO$_3$ precursors at 400 ^{o}C, 5 bar H$_2$ pressure, TOS > 18 h.
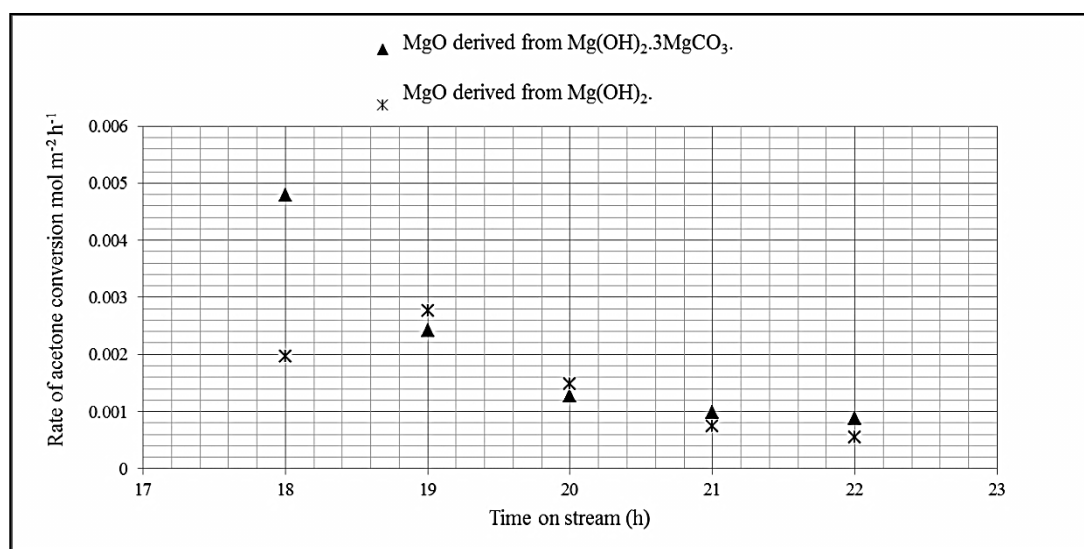
Fig. 3.16 Surface area normalised rates of acetone conversion at 400 ^{o}C and 5 bar as a function of time on stream of MgO catalysts derived from Mg(OH)$_2$ and Mg(OH)$_2$.3MgCO$_3$ precursors.
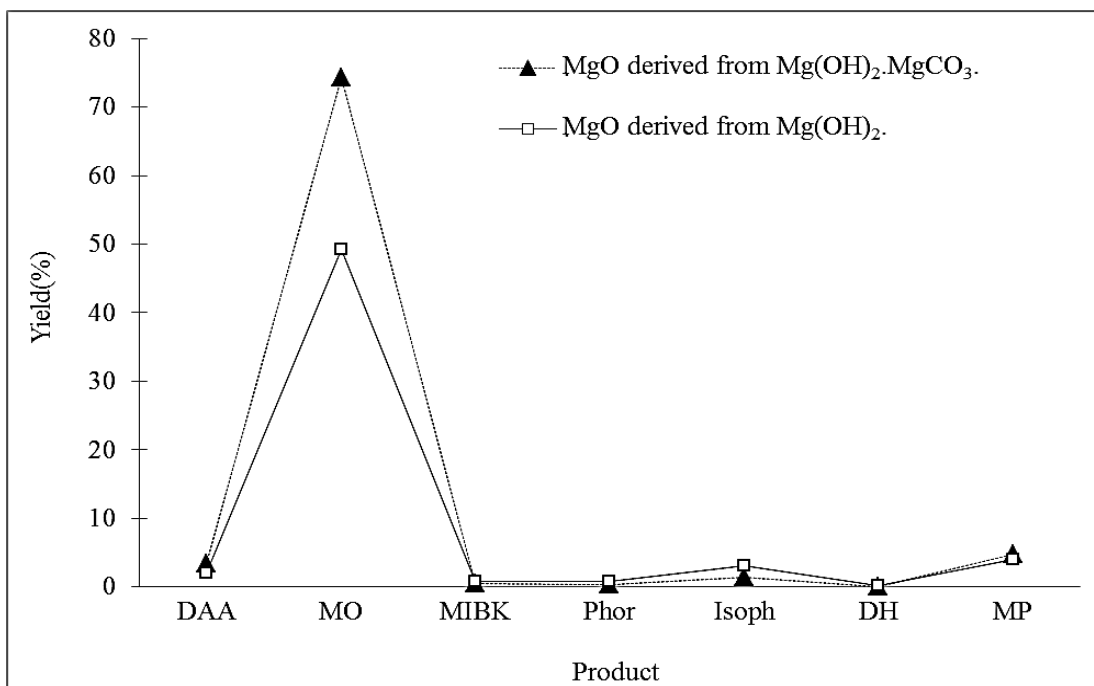
Fig. 3.17 Percentage yields of aldol condensation of reaction of acetone over MgO derived from $Mg(OH)_2$, $Mg(OH)_2.3MgCO_3$ precorsors at 400 ^{o}C, 5 bar H_2 pressure, TOS > 18 h.

The main product was MO with maximum selectivity of ca. 88% over MgO derived from $Mg(OH)_2.3MgCO_3$ and ca. 82% over MgO that derived from $Mg(OH)_2$ (Fig. 3.18). Isoph was a significant product over $Mg(OH)_2$ catalyst but with very low selectivity whereas both catalysts were slightly selective towards MP. Traces of MIBK were detected over both catalysts revealing that the hydrogenation process was limited due to the absence of a hydrogenation function. The reaction was also investigated by Di Cosimo et al [88] over an MgO catalyst at lower temperature and pressure (T = 300 ^{o}C, P = 1 atm) and they reported that MO was the main product with 67% selectivity. The observation that MgO was produced in highest selectivity was also made by Zamora et al [89]. Based on this selectivity result, it can be concluded that the MgO precursor has affected selectivities in the aldol condensation reaction of acetone and that, therefroe, the reaction is possibly structure-sensitive to a small degree. However, it is important to note that there may be different impurty contenets between MgO samples prepared from different precorsuors [59]. It is important to determine whether phase changes have occurred for the MgO catalysts upon reaction. Accordingaly, post-reaction XRD analysis has been undertaken and the results are preseneted in Figure. 3.19.
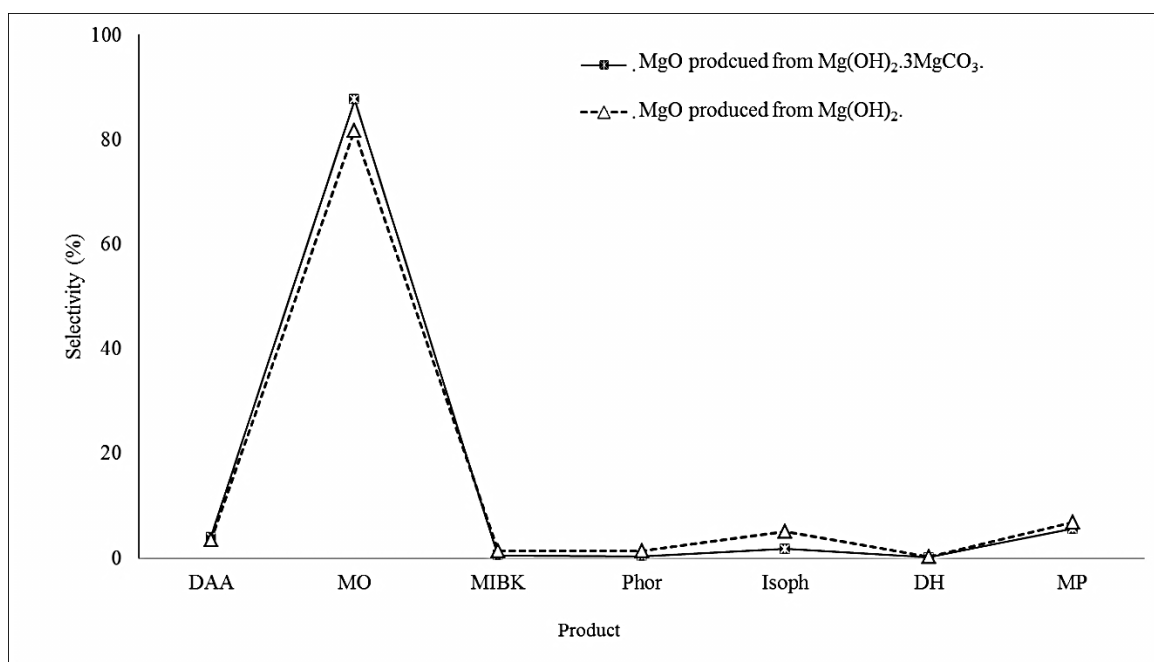
Fig. 3.18 Percentage selectivities of the condensation and hydrogenation products of acetone on MgO derived from $Mg(OH)_2$ and $Mg(OH)_2.3MgCO_3$ precursors at 400 ^{o}C, 5 bar H_2 pressure, TOS > 18h.
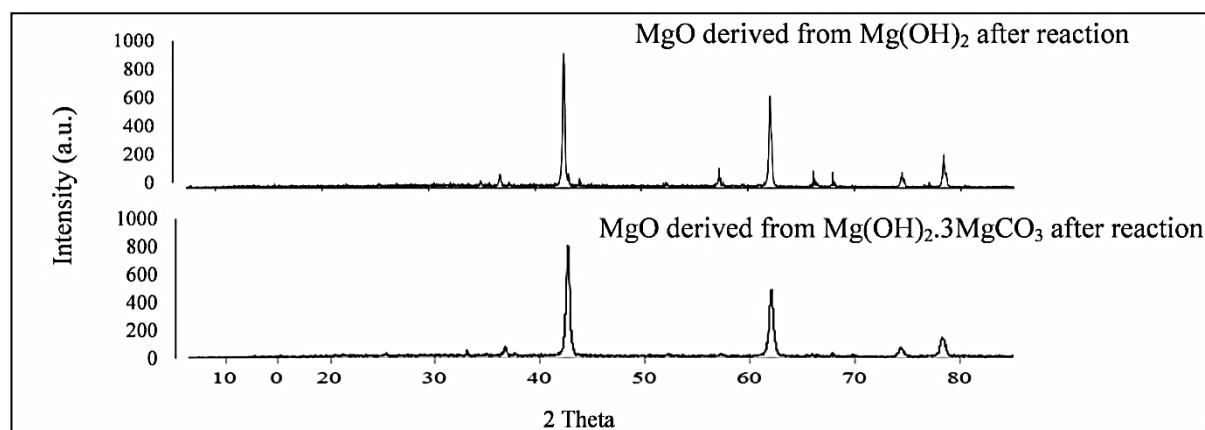
Fig. 3.19 X-ray diffraction pattern of post-reaction samples of MgO catalyst derived from $Mg(OH)_2$ and $Mg(OH)_2.3MgCO_3$ precursors.

Since the MgO phase is still observed on the both XRD patterns of MgO catalysts that prepared from both the $Mg(OH)_2$ and $Mg(OH)_2.3MgCO_3$, it is evident that the MgO phase is generally stable under reaction conditions. However, small additional reflections in the XRD patterns are evident which evidence limited transformation of MgO to brucite $Mg(OH)_2$ upon reaction. Since phase transformation may occur to differing extents in the

two MgO samples, caution must be exercised in ascribing any catalytic differences solely to the role of MgO morphology.

3.2.2 Li-MgO.

Since, as stated in the introduction, doping can increase the catalytic activity of MgO it was undertaken to determine whether there were any effects upon acetone conversion. Accordingly MgO prepared from $Mg(OH)_2$ was doped with 5wt% LiCl. The XRD pattern of the resultant material is shown in Figure 3.20.
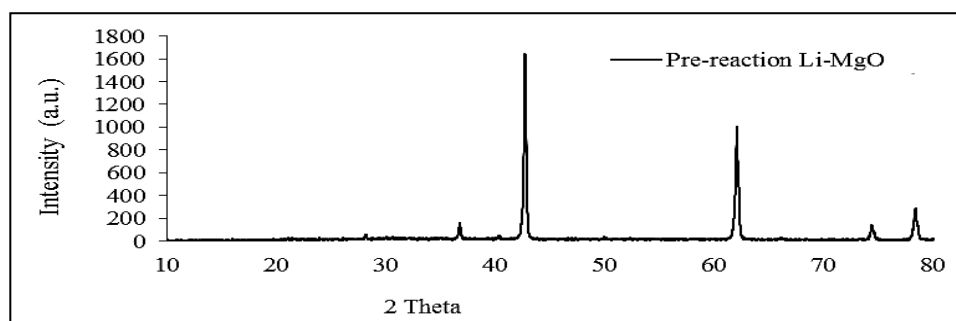
Fig. 3.20 XRD pattern of the pre-reaction sample of Li-MgO catalyst.

XRD pattern of Li-MgO confirmed the presence of the MgO phase with no additional phases being observed. Pre- and post-reaction BET areas were determined for the sample and the results are shown in the table below:

Catalyst	Surface area before reaction (m^2g^{-1})	Surface area after reaction (m^2g^{-1})
Li-MgO	2	3

Table. 3.3 BET surface areas of the Li-MgO catalyst.

The surface area of pre-reacted Li-MgO catalyst was much lower (2 m^2/g) than the MgO precursor and it was observed to increase to 3 m^2/g upon reaction. The loss of surface area upon Li^+ doping is consistent with the literature and may possibly be ascribed to the role of increased oxygen vacancy concentration in enhancing the sintering rate.
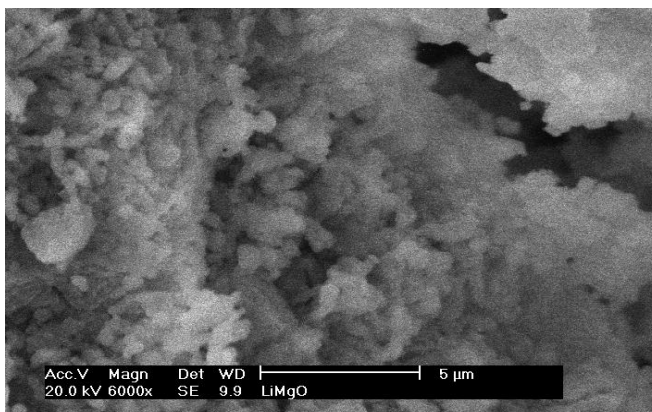
Fig. 3.21 Scanning electron microscopy (SEM) image of Li-MgO.

Scanning electron microscopy revealed that there was a random distribution of particles and they were in variable shapes and sizes (Fig. 3.21).

Catalyst	Conversion (%)	Selectivity (%)						
		DAA	MO	MIBK	Phor	Isoph	DH	MP
Li-MgO	65	1.98	73.59	2.30	1.00	10.16	0.46	10.52

Table. 3.4 Conversions and selectivities, after 18 h of the reaction for the aldol condensation reaction over the Li-MgO catalyst at 400 ^{o}C, 5 bar H_2 pressure, TOS > 18h.

Despite having a much lower surface area, it is apparent that the acetone conversion is comparable to that reported for the undoped MgO samples (Table. 3.2) Surface area normalised conversion rates have been calculated and are plotted as a function of time on stream as shown in Figure 3.22. Upon inspection of the figure, it is apparent that, as expected, the normalised activity of Li-MgO is much higher than that for the MgO sample. Again, deactivation is apparent.
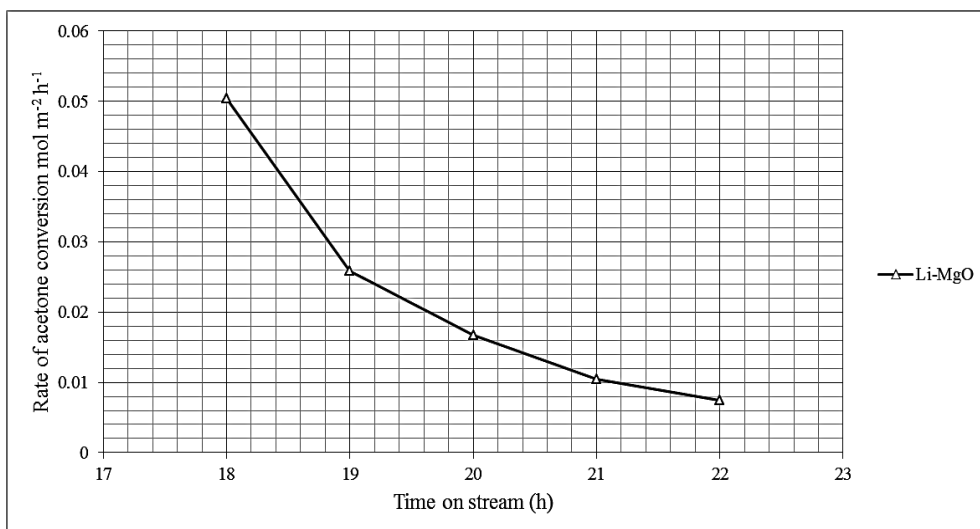
Fig. 3.22 Rate of acetone conversion as a function of time on stream on Li-MgO catalyst at 400 ^{o}C, 5 bar H_2 pressure, TOS > 18 h.

Deactivation was probably caused by coke formation. Previous work reported by Di Cosimo et al [88] on same the reaction conducted over Li-MgO reported a low conversion of 14.2% at 300 ^{o}C and 1 bar pressure and also that lithium negatively affected the catalytic activity of MgO reducing conversion. Product selectivities and yields were determined and the results are shown in Figure 3.23 and 3.24.
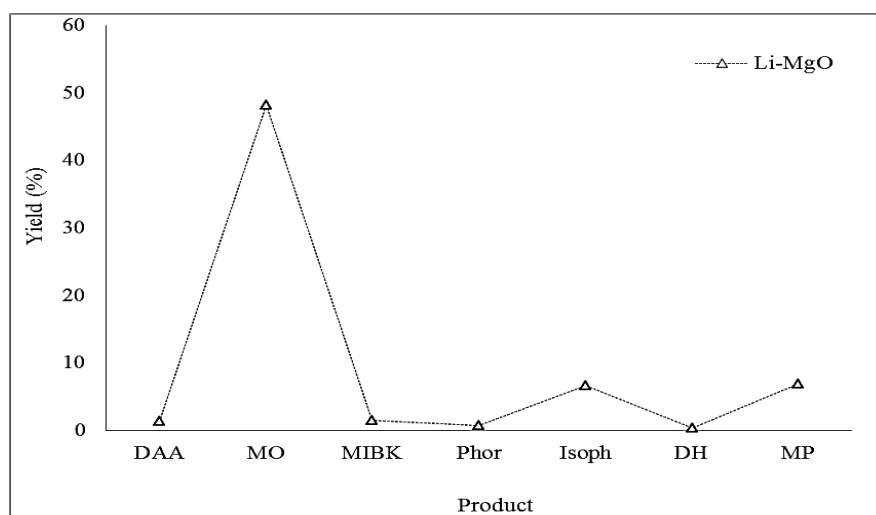
Fig. 3.23 Percentage yields of the condensation and hydrogenation products of acetone over Li-MgO catalyst at 400 ^{o}C, and 5 bar H_2 pressure, TOS > 18h.

The maximum yield was achieved for MO as a major product whereas small quantities of Isoph and MP have been produced (Fig. 3.23). On the basis of these results, as expected, lithium doping does not generate an appropriate hydrogenation site to carry out the conversion of MO to MIBK. Since production of Isoph required strong basic sites its selective be evidence for the strong basicity of the Li-MgO catalyst. The yield of this product is greater than was observed for the non-doped MgO catalysts described earlier, which is a possible indication of the increase in basicity generated by Li^+ doping. The differences in conversion between the doped and non-doped catalysts although small, needs to be borne in mind, however. It should be pointed out that although the conversion of the $Mg(OH)_2$ sample is comparable to the Li-MgO sample, the Isoph selectivity is higher in the latter case.
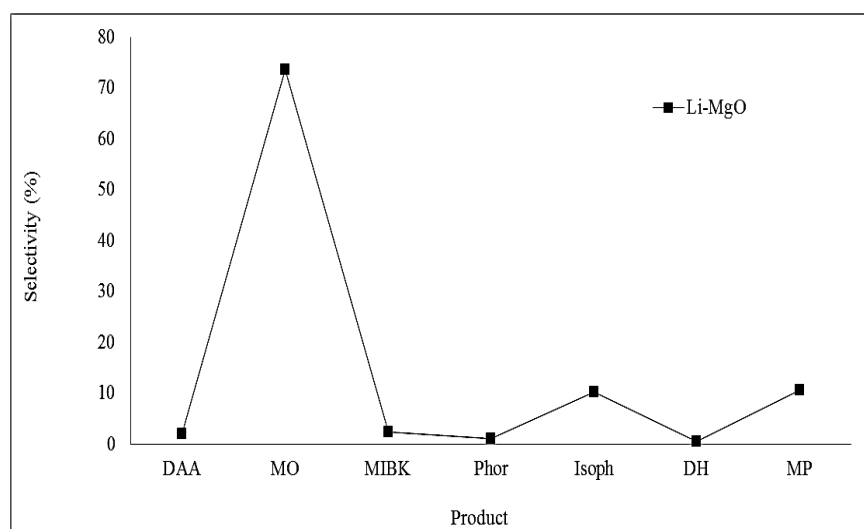
Fig. 3.24 Percentage selectivities of the condensation and hydrogenation products of acetone as a function of time on stream on Li-MgO catalyst at 400 ^oC, 5 bar H_2 pressure, TOS > 18 h.

Although the addition of lithium dopant to MgO catalyst modified selectivity, MO was still the main product. The selectivities over Li-MgO catalyst were 74%, 11% and 10% for MO, MP and Isoph respectively (Fig. 3.24). However, a very low selectivity of ca. 0.5% was observed for DH. This current result is slightly different compared to other workers for the same reaction under similar conditions. For example, Martens et al [90] found selectivities of MO+Isoph products between 69% and 83% over NaX and NaY zeolites at 380 °C, whereas the selectivity toward further heavy products was in the range of 8%-27%.

Veloso et al [91] investigated the condensation of acetone over Faujasite zeolites with different silica/alumina ratios, both in sodium form and exchanged with cesium, at 290 °C and they exhibited 20% to 78% selectivity of MO while the formation of Isoph was negligible in all cases. Large amounts of MIBK and isobutene were observed in the products. Reichle et al [92] have applied thermally activated Mg-Al hydrotalcites to catalyse the vapor-phase oligomerisation of acetone in a continuous reactor and they showed selectivities toward MO+Isoph of 74% and 91% over the temperature range 308-330 °C depending on the preparation method of the catalyst. Finally, Lippert et al [93] studied the self-condensation of acetone over $La(OH)_3$, $Ca(OH)_2$, ZrO_2, and CeO_2 by means of a micro-pulse reactor at reaction temperatures between 200-400 °C. Maximum selectivity of 82% was observed for (MO+IP) products with the $Ca(OH)_2$ catalyst at 200 °C. The other samples exhibited a lower selectivity of 15% over all temperature ranges and further products such as mesytilene and isobutene were observed. Hoodless et al [94] found, in their study of 2-propanol decomposition on MgO, that the selectivity of dehydrogenation was decreased by the addition of lithium dopant.

As for the undoped samples, post-reaction XRD analysis was undertaken in order to confirm the stability of the MgO phase.
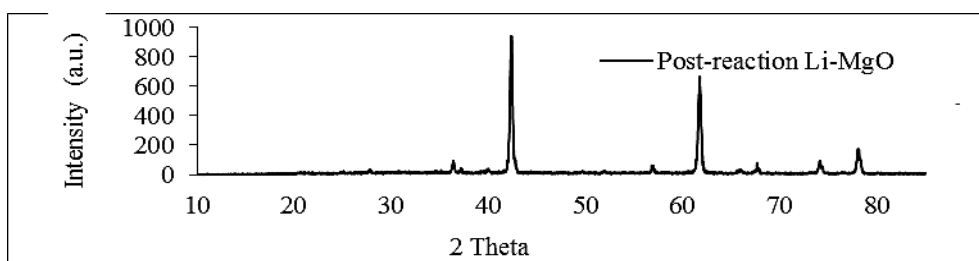
Fig. 3.25 X-ray diffraction pattern for the post-reaction Li-MgO catalyst.

The post-reaction Li-MgO sample displayed characteristic reflections of MgO, although additional low intensity reflections $Mg(OH)_2$ were apparent. This demonstrates that whilst the MgO phase is generally stable, a small degree of hydration does occur. This is possibly consistent with the enhanced surface area evident for the post-reaction sample.

3.3 Conclusion.

The aldol condensation reaction of acetone has been investigated in this thesis over MgO catalysts prepared from $Mg(OH)_2$ and $Mg(OH)_2.3MgCO_3$ precursors. This comparison has been undertaken to elucidate whether structure sensitivity is operative and the precursors used have been chosen because the morphology of the resultant MgO has been extensively characterised [95].
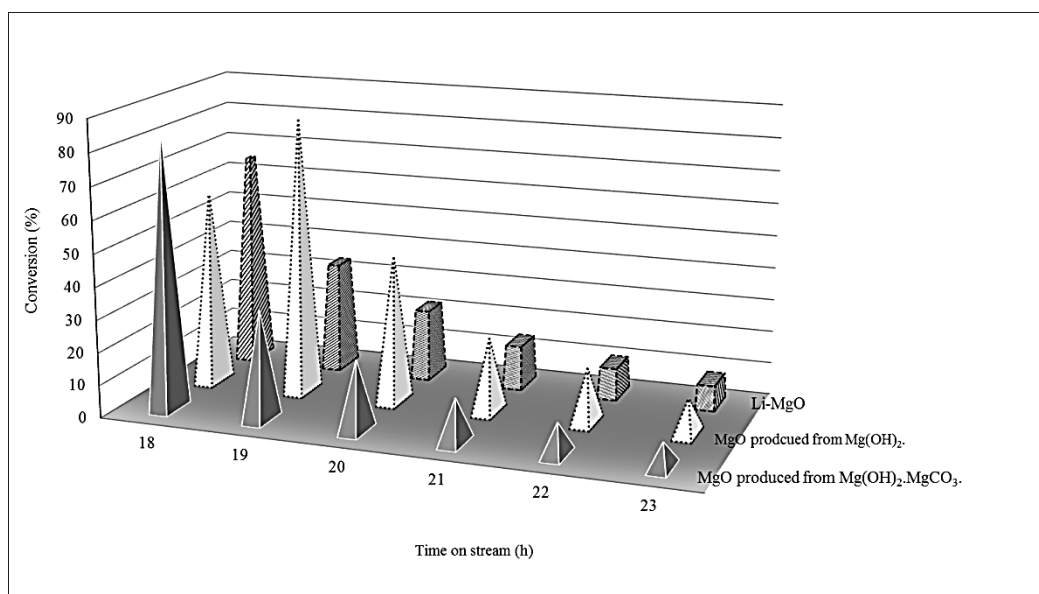
Fig. 3.26 The performance of MgO based catalysts for the conversion of acetone, at 400 ^{o}C and 5 bar H_2 pressure, TOS > 18 h.
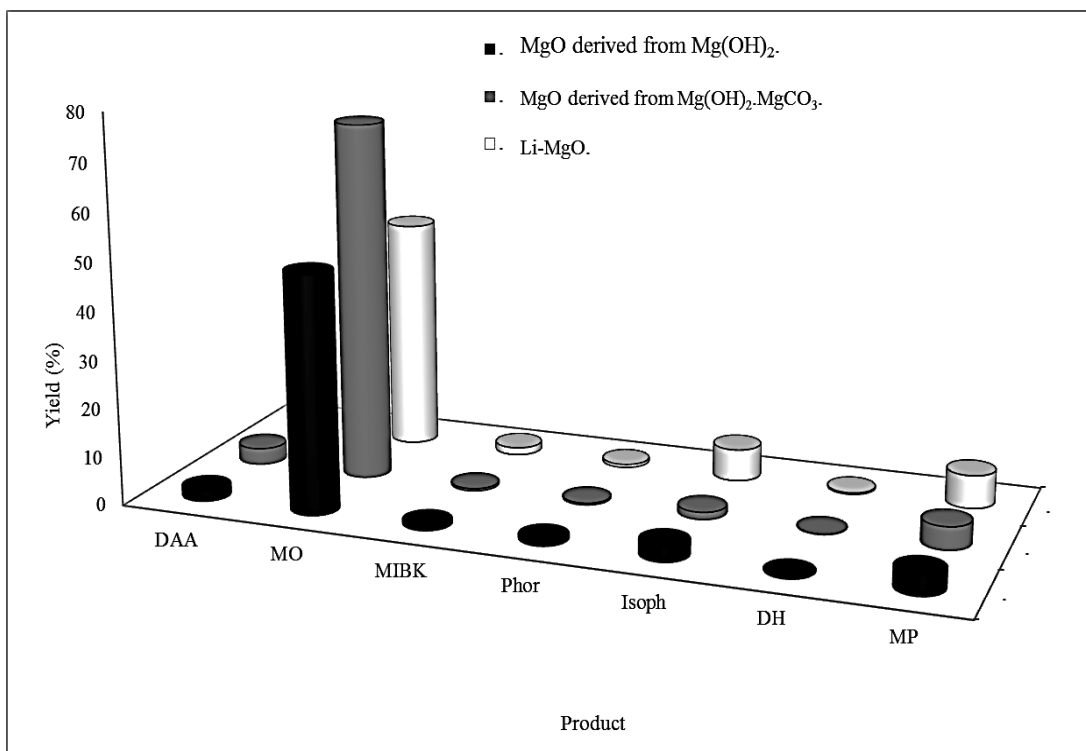
Fig. 3.27 The influence of MgO precursor and Li doping yields of the aldol condensation reaction of acetone at 400 ^{o}C, 5 bar H_2 pressure, TOS > 18 h.
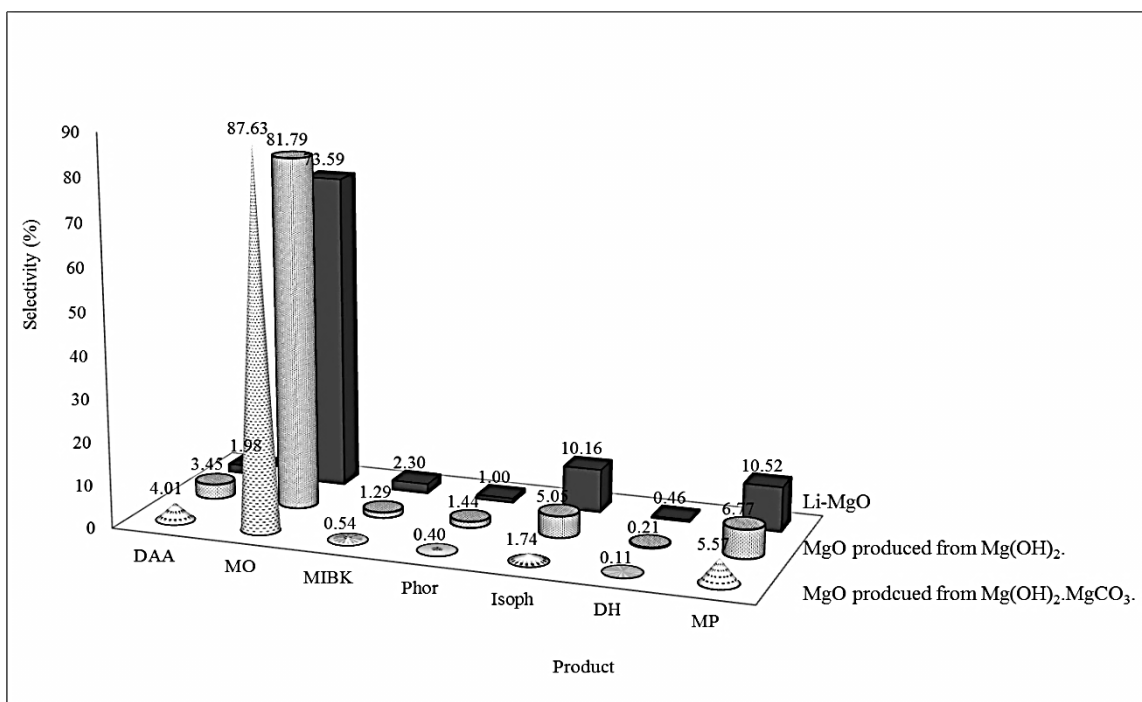
Fig. 3.28 The influence of lithium doped MgO precursor and Li doping on selectivities of the aldol condensation reaction of acetone at 400 ^{o}C, 5 bar H_2 pressure, TOS > 18 h.

It is undoubtedly the case that lithium dopant has reduced the catalytic activity of MgO catalyst and therefore diminished conversion by about 20% compared to MgO prepared from $Mg(OH)_2.3MgCO_3$ (Fig. 3.26). Similarly, yield of MO has also been reduced by at least 20% (Fig. 3.27). A possible explanation for the negative role of Li^+ doping may be related to reduction in surface area as discussed previously. Furthermore, selectivity toward the formation of MO was reduced but production of Isoph became more favourable (Fig. 3.28). It can be concluded that lithium dopant inhibited MgO activity.

Comparison of the surface area normalised conversion data takes the differences in surface area into account and allows the intrinsic effect of Li^+ doping to be determined, on comparing the data for the MgO and Li-MgO samples. On this bases it can be concluded that Li^+ doping significantly enhances the specific activity of MgO. The generation of high-strength basic sites was described by assuming that lithium dopant causes a structural promotion of the MgO sample by replacing the Mg^{2+} ions by Li^+ in the MgO lattice, straining Mg-O bonds, and forming $[Li^+O^-]$ active species which are the main sites responsible of strong basicity. The following reaction is reported to occur on the MgO surface:

$$(Mg_1{}^{2+})(O_1{}^{2-}) + \tfrac{1}{2}\, n\, Li_2O \longrightarrow (Mg_1{}^{2+}\, Li_n{}^+)\, (\, O_1 + \tfrac{1}{2}\, n^{2-}\; \boxed{a}\; \tfrac{1}{2}\, n\,)$$
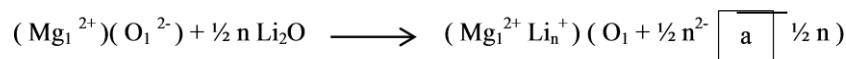
$\boxed{a}$ Anion vacancy

 Doping of lithium is reported to increase anion vacancy concentration, and the effects upon yield therefore may be directly associated and proportional to the vacancy concentration [96].

Surface area normalised conversions of the three catalysts have been considered (Fig. 3.29). As dscussed, lithium dopant significantly increases the rate of acetone conversion on MgO catalysts.

This high modification after MgO being doped with lithium attributes to the surface area effects.
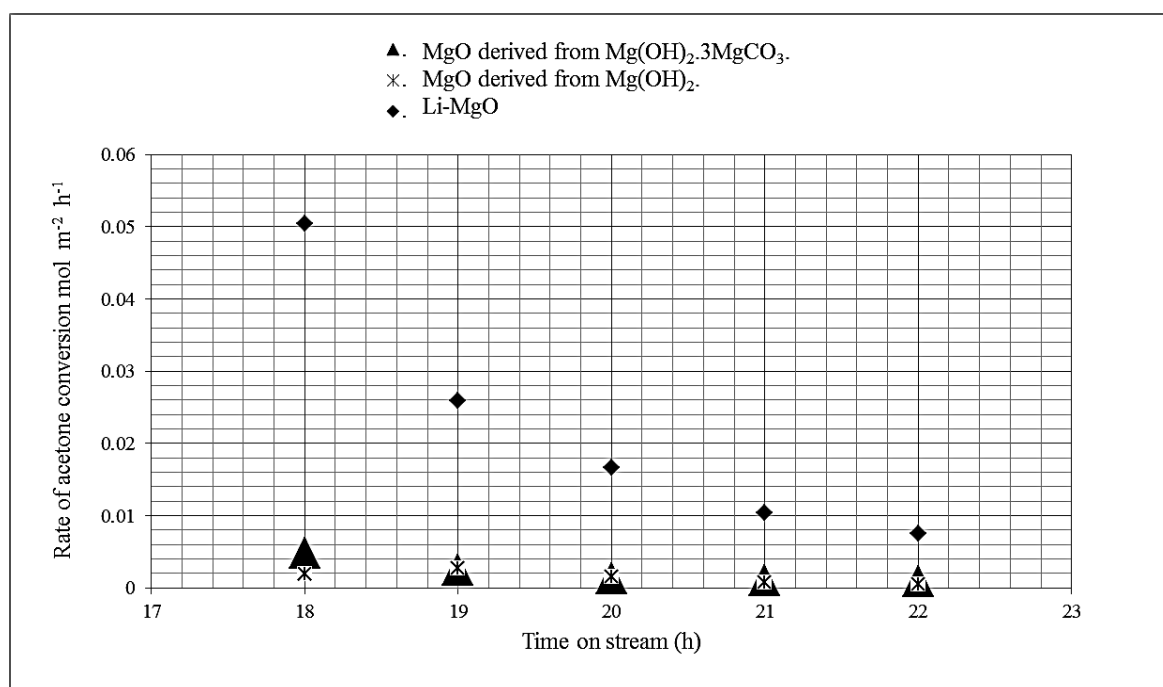
Fig. 3.29 Surface area normalised conversions on different MgO catalysts at 400 $^{\circ}$C, 5 bar H$_2$ pressure, TOS > 18 h.
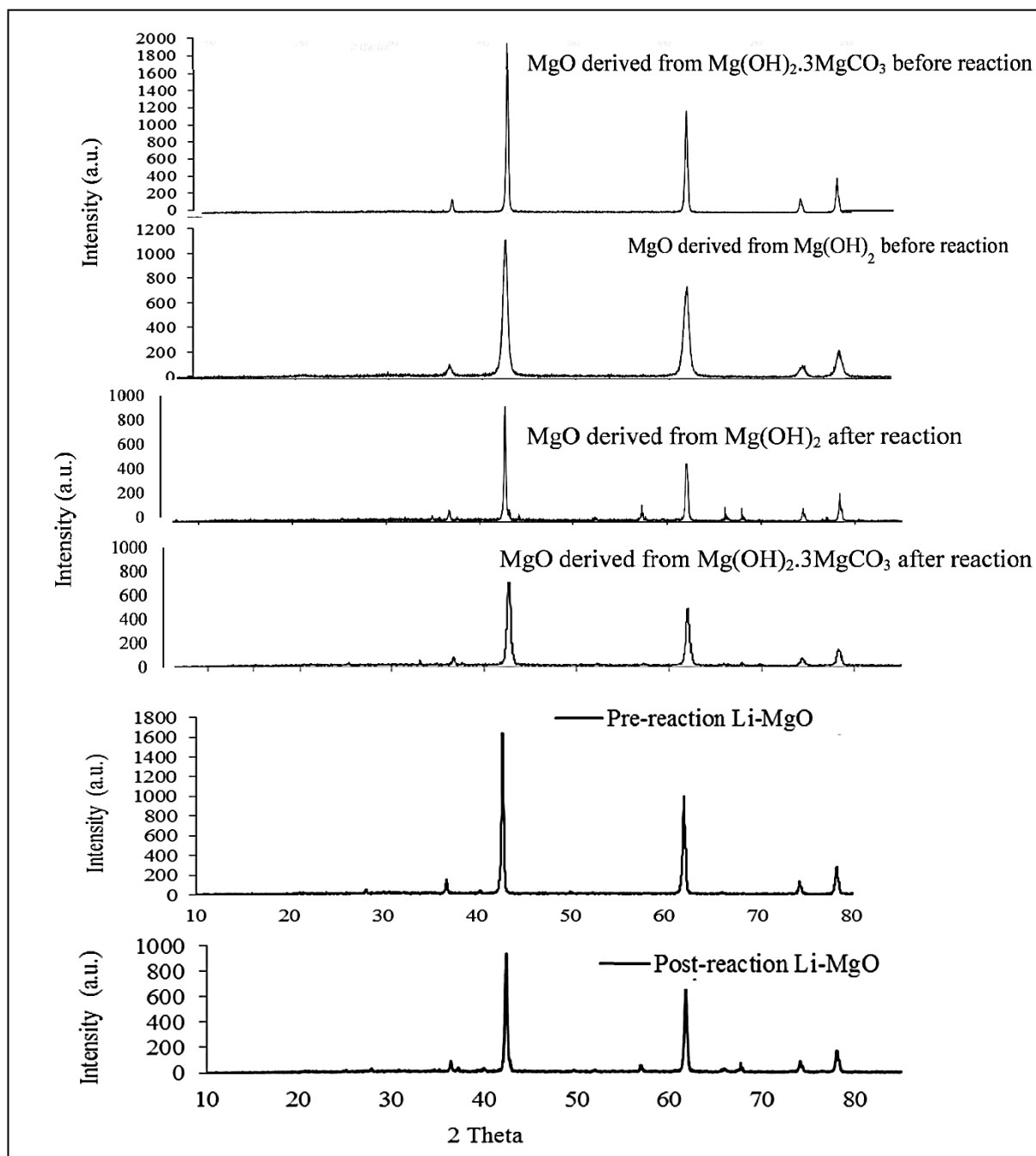
Fig. 3.30 Powder x-ray diffraction patterns of all the MgO materials.

In all cases, MgO is the predominant phase apparent in the XRD patterns (Fig. 3.30). In the case of the materials (both pre- and post-reaction) generated from $Mg(OH)_2$ broader reflection widths are evident which are consistent with the higher surface area, and possibly smaller crystallite size, of this material. Upon reaction, traces of an additional phases are present which indicates that whilst the samples are generally stable, they are not absolutely so.

Catalyst	Surface area (m^2g^{-1})
MgO derived form $Mg(OH)_2$	61
MgO derived form $Mg(OH)_2.3MgCO_3$	36
Li-MgO	2

Table. 3.5 BET surface area of MgO catalyst before and after doping with lithium.

The surface areas of the MgO catalysts are significantly reduced by lithium doping (Table. 3.5). The reduction in surface area is most likely a consequence of facilitated sintering due to the enhanced concentration of oxygen defect sites. Oxide ion mobility is often rate determining in the sintering of oxides and can be facilitated by the presence of oxygen containing atmospheres such as CO_2 and /or H_2O as well as dopants which increase vacancy concentration.
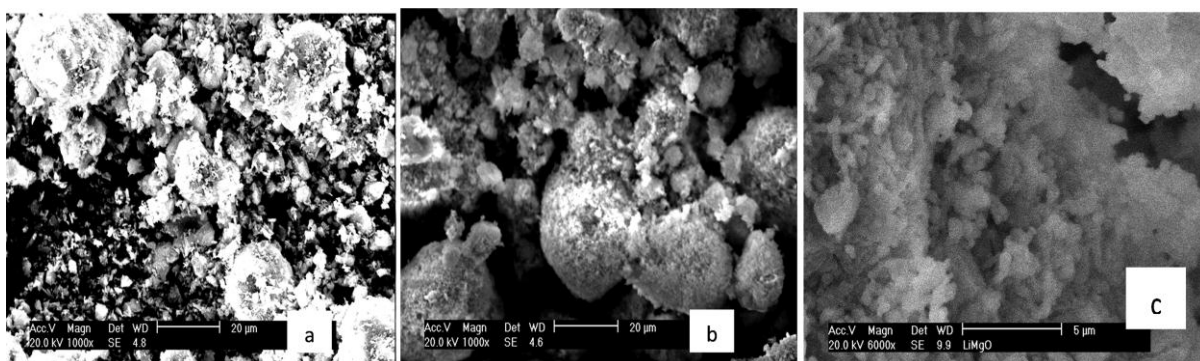
Fig. 3.31 The effect of lithium dopant on MgO morphology: a) MgO derived from $Mg(OH)_2$, b) MgO derived from $Mg(OH)_2.3MgCO_3$ and c) Li-MgO.

Addition of lithium dopant has been documented to produce morphological effects, although these are not readily apparent in the present study in Figure 3.31. In investigating structure-sensitivity and the role of Li^+ doping upon the activity of MgO for acetone conversion, the main focus of this chapter, it is evident that the role of morphology and doping are limited particularly in the case of the undoped MgO sample. Whilst small effects have been observed, these are in contrast to significant effects reported in other reactions such as the oxidative coupling of methane.

In summary, several significant points can be concluded from studying MgO catalysts for the aldol condensation reaction of acetone:

- the surface area normalised conversion rates were comparable for the MgO samples prepared.
- Despite this, significant differences in product distribution were evident, implying that structure-sensitivity is operative.
- Post-reaction XRD analysis of MgO samples evidenced the formation of traces of $Mg(OH)_2$ for both samples.
- Li^+ doping dramatically enhances the surface area normalised conversion rates for MgO in acetone conversion.
- Li^+ doping leads modified product distribution in relation to MgO for acetone conversion, reflecting enhanced basicity.

3.4 References.

[1] T. Seki, H. Kabashima, K. Akutsu, H. Tachikawa and H. Hattori, *J. Catal.* **204**, 393 (2001).

[2] M. A. Aramendia, V. Borau, C. Jiménez, J. M. Marinas, J. R. Ruiz and F. J. Urbano, *Appl. Catal*. A:General, **244**, 207 (2003).

[3] Y. Sakurai, T. Suzaki, K. Nakagawa, N. Ikenaga, H. Aota and T. Suzuki, *J. Catal*. **209**, 16 (2002).

[4] S. Freni, S. Cavallaro, N. Mondello, L. Spadaio and F. Frusteri, *Catal. Commun*. **4,** 287 (2003).

[5] K. D. Jung, O. S. Joo , S .H. Cho and S. H. Han, *Appl. Catal.* A **240**, 235 (2003).

[6] Y. Wang, J. H. Zhu, J.M. Cao, Y. Chun and Q.H. Xu, *Micropor. Mesopor. Mater.* **26, 175** (1998).

[7] D. E. Jiang, G. C. Pan, B.Y. Zhao, G. P. Ran, Y.C. Xie and E. Z. Min, *Appl. Catal.* **201**, 169 (2001).

[8] J. Kijenski and S. Malinowski, *J. Chem. Soc.*, Faraday Trans. **74**, 250 (1978).

[9] E. Lee, K. Jung, O. Joo and Y. Shul, *Chem. J., Korean chem. Soc.* **26**, 281 (2005).

[10] K. Tanabe, G. Zhang and H. Hattori, *Appl. Catal.,* **48**, 63 (1989) .

[11] P. Kovacheva, K. Arishtirova and S. Vassilev, *Appl. Catal.* **210**, 391 (2001).

[12] H. Kabashima, H. Tsuji and H. Hattori, *Appl. Catal*. **165**, 319 (1997).

[13] A. S. Ndou, N. Plint and N. J. Coville, *Appl. Catal.* **251**, 337 (2003).

[14] A. S. Ndou and N. J. Coville, *Appl. Catal.* **275**, 103 (2004).

[15] B. M. Choudary, R. S. Mulukutla and K Klabunde, *J. Am. Chem. Soc.* **125**, 2020 (2003).

[16] T. F. Dossin, M.-F. Reyniers, R. J. Berger and G. B. Marin, *Appl. Catal.* **67**, 136 (2006).

[17] B. M. Choudary, L. Chakrapani, T. Ramani, K. V. Kumar and M. L. Kantam, *Tetrahedron,* **62**, 9571 (2006).

[18] M. L. Kantam, K. V. S. Ranganath, K. Mahendar, L. Chakrapani and B. M. Choudary, *Tetra.Let*.,7646(2007).

[19] S. Coluccia and A. J. Tench, *Proc. 7th Inter. Cong. Catal.* Tokyo, Japan, 1160 (1981).

[20] G. Martra, T. Cacciatori, L. Marchese, J. S. J. Hargreaves, I. M. Mellor, R.W. Joyner and S. Cosuccia, *Catal. Today* **70**, 121 (2001).

[21] J. M. Hur, B. Y. Coh and H. I. Lee, *Catal. Today,* **63,** 189 (2000).

[22] S. Coluccia, A .J. Tench and R. L. Segall, *J. Chem. Soc.*, 1769 (1979).

[23] S. Coluccia, M. Deane and A. J. Thench*, J. Chem. Soc.*, 2913 (1978).

[24] S. Coluccia, F. Boccuzzi, G. Ghiotti and C. Mirra, *Phys. Chem.* 141 (1980).

[25] E. Knözinger, K. H. Jacob and P. Hofmann, *J. Chem. Soc.,* **89,** 1101 (1993).

[26] M. Che, S. Coluccia and A. Zecchina, *J. Chem. Soc.* 1324 (1978).

[27] L. Cerruti, E. Modone, E. Guglielminotti and E. Borello, *J. Chem. Soc.*, 729 (1974).

[28] A. Zecchina, S. Coluccia, G. Spoto, D. Scarano and L. Marchese, *J. Chem. Soc*, **86**, 703 (1990).

[29] A. Zecchina and F. S. Stone, *J. Chem. Soc.*, *Chem. Commun.* 582 (1974).

[30] E. Garrone, D. Bartalini, S. Coluccia, G. Martra, D. Tichit and F. Figueras, in "Proceedings of the International Symposium on Acid–Base Catalysis", 2nd ed., Eds H. Hattori, M. Misono, Y. Ono, Elsevier, 183 (1994).

[31] A. Zecchina, S. Coluccia, G. Spoto, D. Scarano and L. Marchese, *J. Chem. Soc.*, **86**, 703 (1990).

[32] E. Knözinger, K. H. Jacob and P. Hofmann, *J. Chem. Soc.,* **89**, 1101 (1993).

[33] M. Bensitel, O. Saur and J. C. Lavalley, *Mater. Chem. Phy.* **28**, 309 (1991).

[34] A. F. Moodie and C. E. Warble, *J. Cryst. Growth* **10**, 26 (1971).

[35] V. R. Choudary, V.H. Rane and R.V. Gadre, *J. Catal.* **145, 300** (1994).

[36] S. Utamapanya, K. J. Klabunde and J. Schlup, *Chem. Mater.* **3**, 175 (1991).

[37] J. A. Lapszewicz and X. Z. Jiang, *Amer Chem. Soc.* **5**, 102 (1992).

[38] S. R. Morris, R. B. Moyes, P. B. Wells and R. Whyman, in "Metal-support and Metal-Additive effects on Catalysis", Eds B. Imelik, Elsevier, 247(1982) .

[39] A. K. Datye and J. Schwank, *J. Catal.*, **93**, 256 (1985).

[40] M. Boudart, A. Delbouille, J. A . Dumesic, S. Khammouma and H. Topsoe, *J. Catal.*, **37**, 486 (1975).

[41] S. J. Tauster, L. L. Murell and J. P. DeLuca, *J. Catal.,* **48**, 258 (1977).

[42] J. Schwank, S. Galvagno and G. Parravano, *J. Catal.,* **63**, 415 (1980).

[43] G . Parravano, *J. Catal.*, **78**, 320 (1970).

[44] P. J. Anderson and R. J. Forlock, *Trans . Faraday Soc.* 930 (1964).

[45] M. Boudart, A. Delbouille, E. G. Derouane, V. Indovina and A. B. Walters, *J. Amer. Chem. Soc.*, **94**, 6622 (1972).

[46] L. Volpe and M. Boudart, *Catal. Rev. Sci. Eng.*, **27**, 514 (1985).

[47] H. D. Megaw, *Proc. Roy. Soc.* **142**, 198 (1933).

[48] R. Pampuch and Z. Librant, Zest.Nauk. Gorn.-Hutn. Kracovie, *Ceram.* **11**, 45 (1969).

[49] W. Bussem and F. Koberich, *Phys. Chem.* **17**, 310 (1932).

[50] G. Leofanti, M. Solari, G. R. Tauszik, F. Garbassi, S. Galvagno and J. Schwank, *Appl. Catal.,* **3**, 131 (1982).

[51] J. D. Bernal and H. D. Megaw, *Proc. Roy. Soc.*, **151**, 384 (1935).

[52] A. F. Moodie and C. E. Warble, *J. Cryst. Growth,* **10**, 26 (1971).

[53] A. F. Moodie C. E. Warble, and L. S. Williams, *J. Am. Ceram. Soc.,* 676 (1966).

[54] V. E. Heinrich, *Surf. Sci.* **57**, 385 (1976).

[55] L. S. Dent, F. P. Glasser and H. F. W. Taylor, *Quart. Rev.* **16**, 343 (1962).

[56] G. W. Brindley, in "Progress in ceramic science", Vol. 3. Eds. J. E. Burke, 1 (1963).

[57] A. F. Moodie and C. E. Warble, *J. Crystal Growth*, **74**, 89 (1986).

[58] N. H. de Leeuw, G. W. Watson and S. C. Parker, *J. Phys.Chem.* **99,** 17219 (1995).

[59] J. S. J. Hargreaves, G. J. Hutchings, R. W. Joyner and C. J. Kiely, *J. Catal.*, **135,** 576 (1992).

[60] W. Ueda, T. Tokoyama, Y. Moro-oka and T. Ikawa, *J. Chem. Soc., Chem Commun.* 39 (1984).

[61] H. Kurokawa, T. Kato, T. Kuwabara, W. Ueda, Y. Morikawa, Y. Moro-Oka and T. Ikawa, *J. Catal.* **126**, 208 (1990).

[62] J. H. Lunsford, *Catal. Today*, **6**, 235 (1990).

[63] D. J. Driscoll, W. Martir, J-X. Wang and J. H. Lunsford, *J. Am. Chem. Soc.* **107**, 58 (1985).

[64] L. M. Aparicio, S. A. Rossini, D. G. Sanfilippo, J. E. Rekoske, A. A. Trevino and J. A. Dumesic, *Ind. Eng. Chem. Res.* **3**, 2114 (*1991*).

[65] V. T. Amorebieta and A. J. Colussi, *J. Phys. Chem.* **93**, 4576 (1988).

[66] K. P. Peil, J. G. Goodwin and G. Marcelin, *J. Catal.* **131**, 143 (1991).

[67] K. Tanabe, G. Zhang and H. Hattori, *Appl. Catal.,* **48**, 63 (1989) .

[68] J. I. Di Cosimo, V. K. Diez and C. R. Apestegula, *Appl. Catal.* **137**, 149 (1996).

[69] G. A. Martin and C. Mirodatos in " Methane Conversion By Oxidative Processes", Ed. E. E. Wolf, New York, ISBN: 0442006179, 9780442006174, 351 (1990).

[70] E. Iwamatsu, T. Moriyama, N. Takasaki and K. Aika, *J. Chem. Soc. Chem. Commun.* 19 (1987).

[71] K. M. Parida and S. B. Rao, *React. Kinet. Catal. Let.* **44,** 95 (1991).

[72] Y. Aray, J. Rodrı´guez, J. Murgich and F. Ruette, *J. Phys. Chem.* **97**, 8393 (1993).

[73] C. M. Zicovich-Wilson, R. Gonza`lez-Luque and P. M. Viruela-Martı´n, *J. Mol. Struct.* **208**, 153 (1990).

[74] J. L. Anchell, K. Morokuma and A. Hess, *J. Chem. Phys.* **99**, 6004 (1993).

[75] R. Orlando, F. Cora`, R. Millini, G. Perego and R. Dovesi, *J. Chem. Phys.* **105**, 8937 (1996).

[76] M. Lintuluoto, *J. Phys. Chem.* **104**, 6817 (2000).

[77] M. Lintuluoto and Y. Nakamura, *J. Mol. Struct.* **674**, 207 (2004).

[78] J. S. J. Hargreaves, G. J. Hutchings, R. W. Joyner and C. J. Kiely, *Catal. Today*, **10**, 259 (1991).

[79] C. L. Padro, W. E. Grosso, G. T. Baronetti, A. A. Castro and O. A. Scelza, in " New development in selective oxidation", 2nd ed, Eds V. Corte's Corbera'n and S. Vic Bello'n, 411 (1994).

[80] S. J. Korf, J. A. Roos, N. A. De Bruijn, J. G. van Ommen and J. R. H. Ross, *Appl. Catal.* **58**, 131 (1990).

[81] R. Philip, K. Omata, A. Aoki and K. Fujimoto, *J. Catal.* **134**, 422 (1992).

[82] D. Gulkova´, O. Sˇolcova´ and M. Zdrazˇil, *Micropor. and Mesopo. Mat.* 76, 137 (2004).

[83] J. S. Valente, F. Figueras, M. Gravelle, P. Kumbhar, J. Lopez and J. P. Besse, *J. Catal*. **189,** 370 (2000).

[84] J. Li, W.-L. Dai and K. Fan, *J. Phys. Chem.* **112**, 17657 (2008).

[85] J. Puriwat, W. Chaitree, K. Suriye, S. Dokjampa , P. Praserthdam and J. Panpranot, *Catal. Commun.* **12**, 80 (2010).

[86] G. A. Lomić, E. E. Kiš, G. C. Bošković and R. P. Marinković-Nedučin, *Acta, Per. Tech.,* **35**, 67 (2004).

[87] J. Kijenski and S. Malinowski, *J. Chem. Soc. Faraday Trans.* **1**, 74(1978).

[88] J. I. Di Cosimo, V. K. Diez and C. R. Apestegula,. *Appl. Catal.* **137**, 149 (1996).

[89] M. Zamora, T. Lo´pez, R. Go´mez, M. Asomoza and R. Mele´ndrez, *Appl. Surf. Sci.* **252**, 828 (2005).

[90] L. R. Martens, W. J. Vermeiren, D. R. Huybrechts, P. J. Grobet and P. A. Jacobs, *Proc. 9th. Int. Cong. Catal.* 420 (1988).

[91] C. O. Veloso, J. L. F. Monteiro and E. F. Souza-Aguiar, *Stud. Surf. Sci. Catal.* **84**, 1913 (1994).

[92] W. T. Reichle, *J. Catal.* **94**, 547 (1985).

[93] S. Lippert, W. Baumann and K. Thomke, *J. Mol. Catal.* **69**, 199 (1991).

[94] I. M. Hoodless and G. D. Martin, *Can. J. Chem.* **53**, 2729 (1975).

[95] I. M. Mellor, A. Burrows, S. Coluccia, J. S. S. Hargreaves, R. W. Joyner, C. J. Kiely, G. Martra, M. Stockenhuber and W. M. Tang, *J. Catal.* **234**, 14 (2006).

[96] D. A. Dowden, *Chem. Soc.* 242 (1950).

Chapter 4

Zirconia based catalysts for acetone conversion.

4. Introduction.

4.1. Zirconia.

Zirconia (ZrO_2) is the polymorphic ceramic white crystalline oxide of zirconium. It is a promising catalyst and catalyst support due to its high thermal stability, redox properties and amphoteric nature [1]. Thus, ZrO_2 has been reported as an excellent support for metal and transition metal oxide catalysts [2]. It has been used extensively as structural component material because of its phase transformation toughening mechanism [3].

Many of the catalytic applications of zirconia are related to its surface acid-base functionality.

Zirconia commonly exists in three well-known structural forms (Fig. 4.1) namely: monoclinic (α-ZrO_2), tetragonal (β-ZrO_2), and cubic (γ-ZrO_2) [4-10].
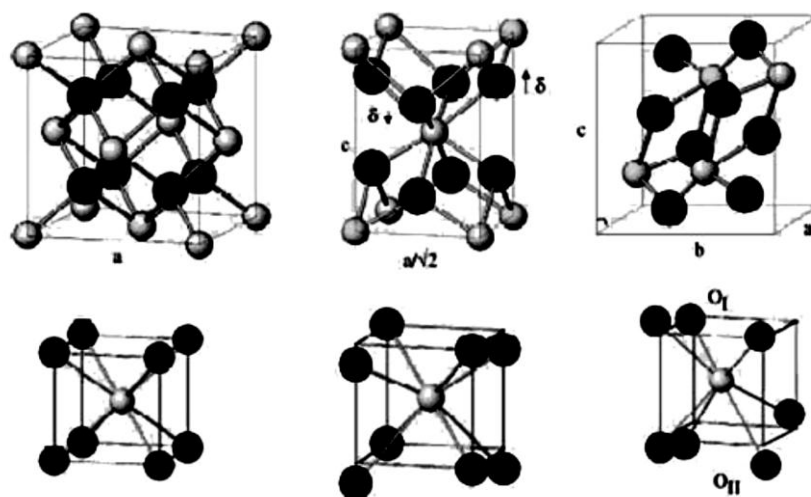
Fig. 4.1 Atomic structure (top) and Zr to O coordination units (bottom) for the three low pressure polymorphs of ZrO_2: cubic (left), tetragonal (middle), and monoclinic (right). Large dark circles denote O atoms, small light circles, Zr [10].

A high-pressure polymorph form of zirconia (orthorhombic) has been reported. This phase is metastable at atmospheric pressure and hence it reverts to the monoclinic form by such a mild treatment as grinding in a mortar [11].

Monoclinic zirconia (m-ZrO_2) is the most stable phase under normal atmospheric pressure at room temperature. Accurate descriptions of the structures are still not clear although a tremendous amount of research has been carried out to elucidate the crystal structures of industrially important zirconia. Mazdiyasni et al [12] reported that a cubic phase could be

obtained by the addition of 6.5 mol% yttria, following an alkoxide preparation route. Davis et al [14] found that the pH at which the precursor gels are precipitated causes the monoclinic or the tetragonal phase to be formed after calcining the material at 400-600 ° C. Accordingly, the tetragonal phase could be obtained either at a low pH (between 3-5) or at a high pH (13-14), and that the monoclinic phase could be obtained in the middle pH range (8-11). Srinivasan et al [15] suggested that the tetragonal phase obtained at pH 13.5 was stable even after calcination at 500 °C for 300 h and later found that both the monoclinic and tetragonal phases can be attained at a pH of 10.5, depending upon the time taken to effect the precipitation [16]. Most recently, Jada and Peletis [17] suggested that the solution chemistry of zirconia precursor materials plays a key role in controlling crystal structure formation, polymorphic transformation, and crystalline growth. Mamott et al [18], using a time resolved dynamic high-temperature XRD technique, have reported on the onset of an ordering within the amorphous starting material, and on the progress of its conversion into crystalline zirconia.

 Assignment of the tetragonal and cubic structures can be misleading due to the similarity of their lattice parameters (a_0 = 0.5124 nm for the cubic, and a_0 = 0.5094 nm and c_0 = 0.5177 nm for the tetragonal structures) [19]. Srivastava et al [20] revealed that the tetragonal and cubic phases can be identified by the presence of the characteristic splitting of the tetragonal phase refelctions, such as (002), (200), (113), (311), (004), (400), (006) as the cubic phase exhibits only single refections at all of these positions. Garvie et al [13] used high-angle reflections to distinguish the tetragonal and cubic structures and to determine their relative proportions. Miller et al [21] used the (400) region of the x-ray diffraction patterns in order to calculate the relative proportions of cubic and tetragonal phase in their study of plasma-sprayed yttria stabilised zirconia coatings. They found that the main peaks in this region change from monoclinic to tetragonal and gradually to the cubic reflections by increasing the loaded amount of yttria. Separation of the tetragonal and cubic peak components in the (400) region was undertaken using "curve resolver" [22] and the *d* values for the (400) and (004) tetragonal peaks were calculated from the curve-resolved peak positions. The cubic phase forms at a very high temperature (over 2370 °C). It transforms into the tetragonal phase at intermediate temperatures (1170 to 2370 °C). At temperatures below 1170 ° C, the material transforms to the monoclinic structure.

Despite of the difficulty in the identification of the zirconia phase structures, the most stable form under normal conditions (Baddeleyite) can be described as a complex

monoclinic structure (m-ZrO_2) with nine internal degrees of freedom and four formula units per primitive cell. Each Zr cation is 7-fold coordinated by oxygen. The structure can be explained as rotating layers of Zr and O with the coordination of the oxygen atoms exchanging between 3 and 4 from one oxygen layer to the next. By increasing temperature, a first-order martensitic phase transition occurs, initiating the transformation into the tetragonal phase (t-ZrO_2).

 The tetragonal form of zirconia (t-ZrO_2) can be viewed as a simple distortion of the cubic fluorite structure, with alternating columns of oxygen atoms along one crystallographic axis shifting upward or downward by an amount. The structure is defined by two lattice parameters, a and c, and it has two formula units per unit cell. Cubic zirconia (c-ZrO_2) occurs at a very high temperature and possesses the fluorite structure. This structure contains only two degrees of freedom, the lattice constant, a, and an internal coordinate, u, reflecting the positions of the oxygen atoms along the body diagonal of the cubic cell. An irreversible transformation from the tetragonal to the monoclinic phase can be induced by mechanical impact such as indentation, fracture, heating and thermal cycles [23]. Zirconia stabilisation is essentially controlled by several factors such as the lattice effect, the particle size, the presence of water vapour, sintering, and the electronic structure.

Doping with suitable aliovalent cations stabilises the cubic and tetragonal forms at room temperature and gives rise to their functional properties. Oxide dopants such as CaO, MgO, CeO, and Y_2O_3 can be used to partially or completely stabilise the tetragonal and cubic structures of zirconia. Partial stabilisation of zirconia (PSZ) occurs by adding insufficient cubic phase-forming oxide to the ZrO_2. Adding a small amount of stabiliser to pure zirconia will transform its structure to tetragonal at a temperature higher than 1,000 ° C and a mixture of cubic and monoclinic or tetragonal at a lower temperature [24]. PSZ is usually formed by addition of 8 mol% (2.77 wt%) MgO, 8 mol% (3.81 wt%) CaO, or 3 - 4 mol% (5.40-7.10 wt%) of Y_2O_3 [25]. The microstructure of PSZ at room temperature generally consists of cubic zirconia as the major phase, with minor precipitation of monoclinic and tetragonal phases [26].

The improvement in the mechanical strength and toughness due to phase transformation in partially stabilised zirconia was first reported by Garvie et al [13]. PSZ is a transformation-toughened material which may be explained by the micro-crack and induced stress. The micro-crack stress depends on difference in the thermal expansion between the monoclinic and cubic particles [27]. The difference in coefficient of thermal expansion between

monoclinic and cubic phase creates micro-cracks that dissipate the energy of propagating cracks. The cubic matrix initiates a compressive force that maintains the tetragonal phase. Stress energies from propagating cracks promote the transition from the metastable tetragonal to the stable m-ZrO_2. The energy used by this transformation is sufficient to slow or even stop crack propagation. However, the addition in an of dopant amount higher than 16 mol% for CaO (7.9 wt%) [28], 16 mol% for MgO (5.86 wt%) [29], or 8 mol% for Y_2O_3 (13.75 wt%) [30], into the zirconia structure forms fully stabilised zirconia which comprises 100% cubic zirconia which is stable from room temperature to 2500 °C.

There are two essential transformations of zirconia phases either from cubic to tetragonal (c-t) [31] or from tetragonal to monoclinic (t-m) [32] which occur upon cooling from the melting point. Phase transformation of cubic to tetragonal in ZrO_2 ceramics is similar to transformations in steel. The transformation involves lattice rearrangement and adjustment of chemical composition toward the equilibrium state [33]. The lattice rearrangement from the cubic to tetragonal structure requires dislocation of oxygen ions in order to increase the parameter of the c-axis and decrease the parameters of a and b axes.

The transformation to monoclinic during the cooling process starts in the temperature range between 1000–650 °C, below this temperature full transformation occurs. On the other hand, during the heating process the transformation initiates at 820 °C whereas the full 100% tetragonal phase will be formed above 1170 °C [8]. Transformation from tetragonal to monoclinic occurs with volume expansion and shear distortion parallel to the tetragonal phase plane. These volume and shear strain developments are substantially exhibited in ZrO_2-based ceramic materials. They cause an increase in strength and toughness of the materials and they also improve their resistance against crack propagation. The impact of volume change and shear distortion resulting from the tetragonal to monoclinic transformation enhances the reliability and lifetime of ZrO_2 derived materials and leads to the high fracture toughness of tetragonal zirconia [13]. Phase transformation from tetragonal to monoclinic is not isotropic. The a and c lattice parameters significantly change, while the b value has a negligible change [34].

Rashad et al [35] have investigated the effects of thermal treatment on the crystal structure and morphology of zirconia prepared by precipitation (CP), citrate gel combustion (CGC) and microemulsion refined precipitation (MRP) using XRD (Fig. 4.2 a, b and c). They revealed that amorphous zirconia was observed for calcination at temperatures up to 120 °C. By increasing temperature to the range between 500 °C and 700 °C, the transformation

of ZrO$_2$ precursors to the crystalline tetragonal phase occurred. The presence of tetragonal phase in the XRD pattern at relatively low temperature was attributed to the fact that the specific surface free enthalpy of the monoclinic form was higher than that of the tetragonal form. The large surface area of the nano-powder became a thermodynamic barrier for the transformation of t-ZrO$_2$ to m-ZrO$_2$.
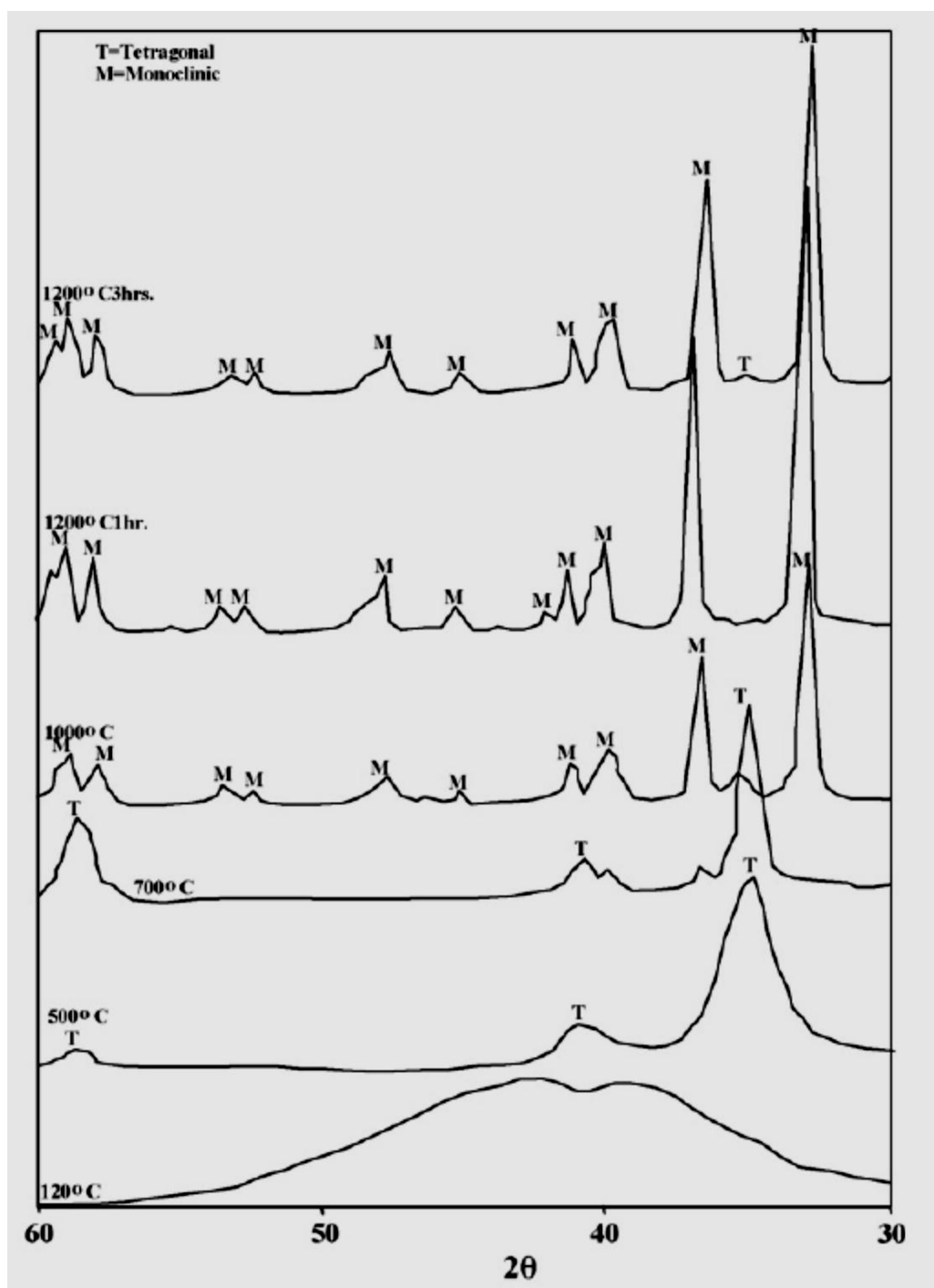
Fig. 4.2 a) XRD patterns of the produced ZrO$_2$ powders by the CGC method at 120, 500, 700, 1000 and at 1200 $^{\circ}$C for 1 and 3h [35].
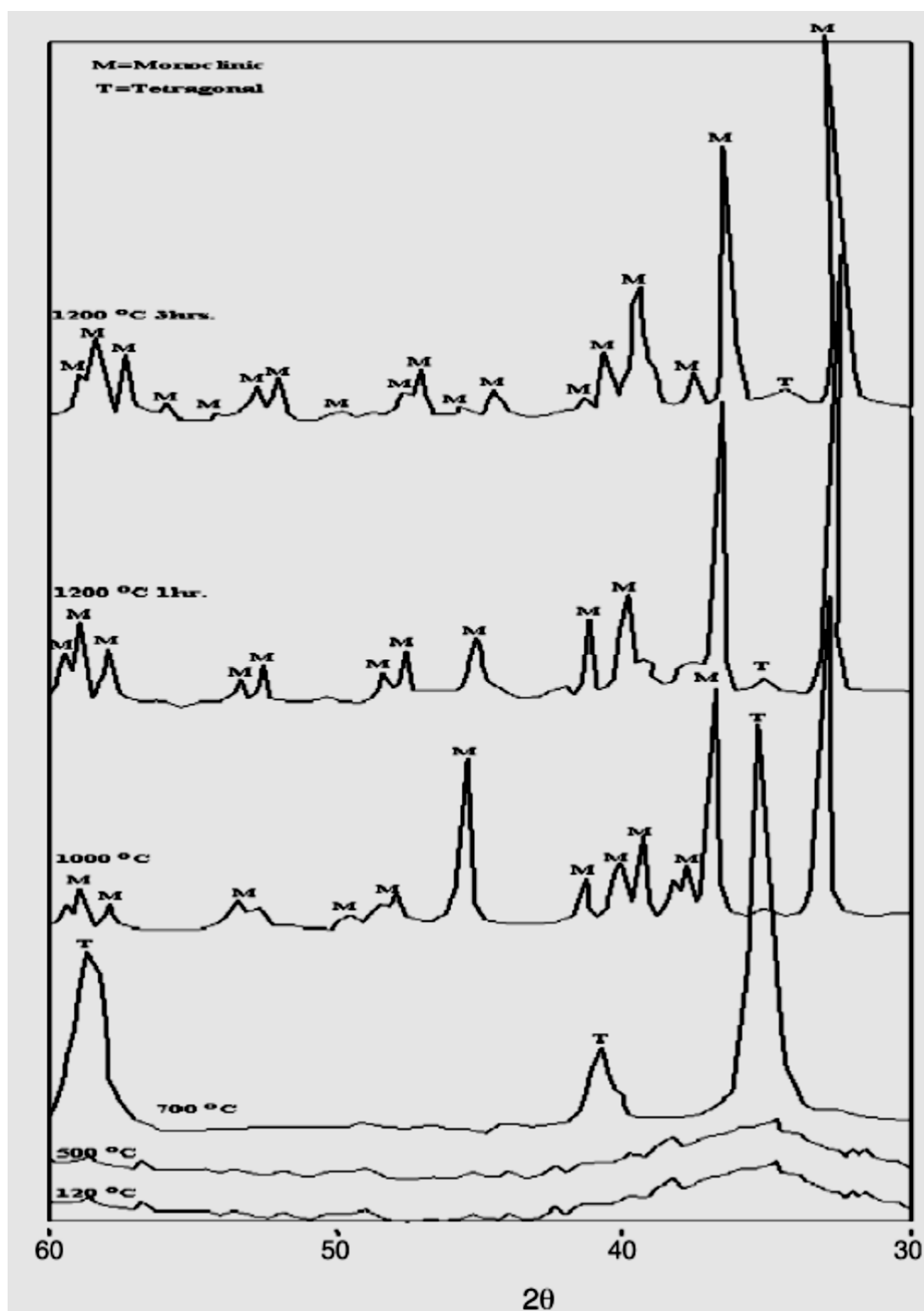
Fig. 4.2 b) XRD patterns of the produced ZrO_2 powders by the CP method at 120, 500, 700, 1000 and at 1200 ^oC for 1 and 3h [35].
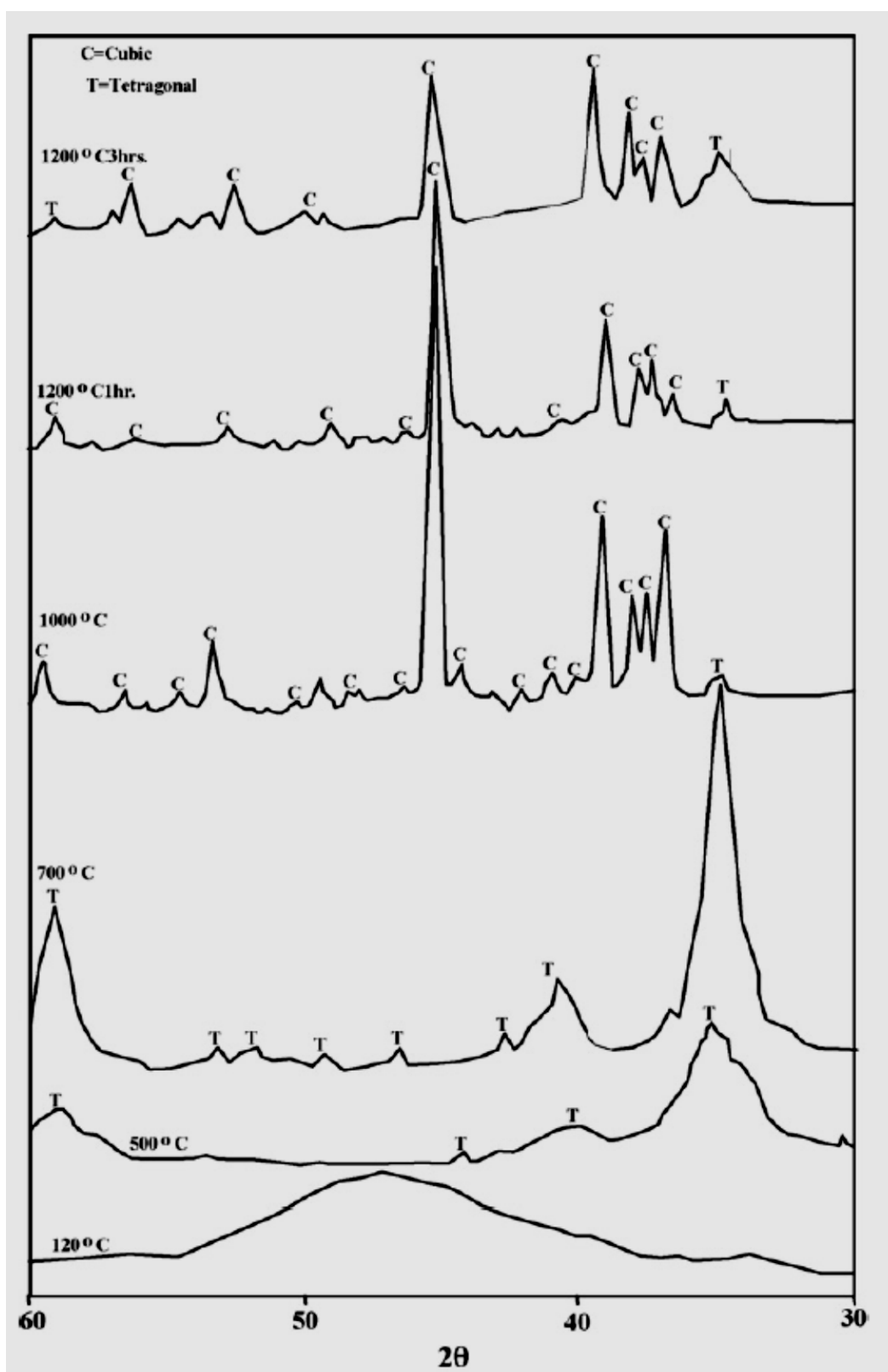
Fig. 4.2 c) XRD patterns of the produced ZrO_2 powders by the MRP method at 120, 500, 700, 1000 and at 1200 ^{o}C for 1 and 3h [35].

The formation of tetragonal phase at low temperature which occurs in some cases was attributed to the presence of hydrous zirconia ($ZrO_2 \cdot nH_2O$) [36], in which each structure unit contains 16 zirconium atoms, 20 non-bridging hydroxo groups, 22 bridging oxide bonds and 20 coordinated water molecules. The conversion process at 700 ^{o}C is described by the following equation:

$$[Zr_{16}O_{22}(OH)_{20}(H_2O)_{20}].xH_2O \xrightarrow{\text{Naturally dried}} [Zr_{16}O_{22}(OH)_{20}(H_2O)_{20}] + xH_2O$$

$$[Zr_{16}O_{22}(OH)_{20}(H_2O)_{20}] \xrightarrow{\text{heat}} 16ZrO_2 + 30H_2O$$
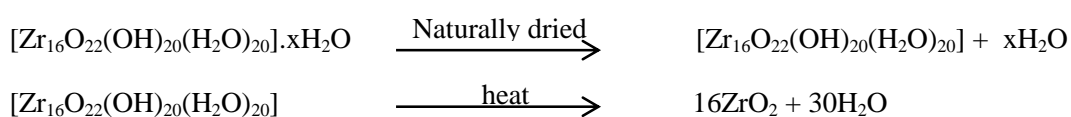
Heating $ZrO_2 \cdot n H_2O$ up to about 300 ^{o}C led to the observation of metastable tetragonal zirconia. The amorphous hydrous zirconia lost water by releasing water of hydration and producing water. Both processes caused a reduction in the BET surface area of the calcined solid and a consequent increase in the average particle size. The crystallite sizes of the produced powders by the CP method increased from 7.00 nm to 32.90 nm upon increasing temperature from 500 ^{o}C to 700 ^{o}C. The surface area of amorphous zirconia at 120 ^{o}C was 250 m^2/g and decreased to 230 m^2/g upon calcining the precursor to 500 ^{o}C. Further calcination to about 700 ^{o}C caused an additional reduction of the surface area to 180 m^2/g which then diminished to 20 m^2/g when the temperature reached 1000 ^{o}C. For the zirconia sample prepared by the CGC method, the BET specific surface area of amorphous zirconia was 280 m^2/g and decreased to 210 m^2/g for the precursor that was heated up to 700 ^{o}C and 60 m^2/g for the sample treated at 1000 ^{o}C. The BET specific surface area of the sample that was prepared from MRP was also 280 m^2/g then declined to 200 m^2/g and 45 m^2/g for the precursors annealed at 700 ^{o}C and 1000 ^{o}C. The tetragonal phase was then converted to pure monoclinic phase by increasing the temperature up to 1000–1200 ^{o}C for 1h in the case of CP and CGC preparation methods. Hydrous zirconia didn't fully convert to t-ZrO_2 since about one percent water remained. Further heating caused transformation to m-ZrO_2 and all traces of hydrous $ZrO_2 \cdot nH_2O$ entirely disappeared, but traces of water persisted to about 1000 ^{o}C. The phase transformation was accompanied by a 9% volume expansion. The crystallite sizes of the produced m-ZrO_2 nanopowders generated from the most intense peaks (111) plane were temperature dependent. The crystallite sizes increased from 64.5 nm to 98.1 nm upon increasing calcination temperature from 1000 ^{o}C to 1200 ^{o}C for

zirconia that prepared by the CP method whereas they were increased from 41.2 nm to 75.9 nm for the ZrO_2 powders that produced by the CGC route under the same conditions. The tetragonal ZrO_2 was converted to the cubic phase by increasing temperature from 700 – 1000 ^{o}C for the zirconia powders that prepared by the MRP technique.

Phase transformation from tetragonal to cubic forms might be attributed to high temperature treatment during preparation which caused an exothermic decomposition of any carbonaceous residue. The formation of cubic phase zirconia prepared in a polyacrylamide matrix was due to the fact that the crystallite size resulting from the polymer co-precipitation method was smaller than that of the aqueous co-precipitation method which created a considerable number of oxygen vacancies in the bulk and on the surface [37]. These oxygen vacancies play a significant role in the stabilisation of metastable tetragonal/cubic phase of ZrO_2. Crystallisation of the produced m-ZrO_2 can be increased by annealing the precursor to 1200 ^{o}C as well as by increasing time of calcination. The c-ZrO_2 phase is stable at all temperatures up to its melting point at 2680 ^{o}C. Scanning electron microscopy (SEM) of the ZrO_2 nanopowders produced by the three different preparation methods (Fig. 4.3) revealed that the precipitated ZrO_2 powders which were heated at 700 ^{o}C exhibited tetragonal structure represented as aggregations of fine to very fine grains. The grains were varied from spherical to elongated and from angular to rounded (Fig. 4.3a). The elongated, angular and spherical shapes were characterized by rounded aggregates of larger size in some instances (Fig. 4.3b). The monoclinic phase demonstrated two grain types obtained by calcining at 1000 ^{o}C. The SEM image of ZrO_2 powder which was prepared by the CGC technique and heated to 700 ^{o}C demonstrated that the tetragonal form appeared as dense, uniform, fine to medium grains which were rounded in general (Fig. 4.3c) while the monoclinic ZrO_2 phase formed at 1000 ^{o}C was observed to be an aggregation of very fine rounded grains (Fig. 4.3d). The SEM micrographs of ZrO_2 powders produced from the MRP method and calcined at 700 ^{o}C showed that the tetragonal phase exhibited elongated and tetragons crystallites. Aggregation of small grain generated larger grains in some instances (Fig. 4.3e). c-ZrO_2 powders calcined at 1000 ^{o}C showed a flower-like texture of flaky grains which were generally larger than that of tetragonal phase (Fig. 4.3.f).
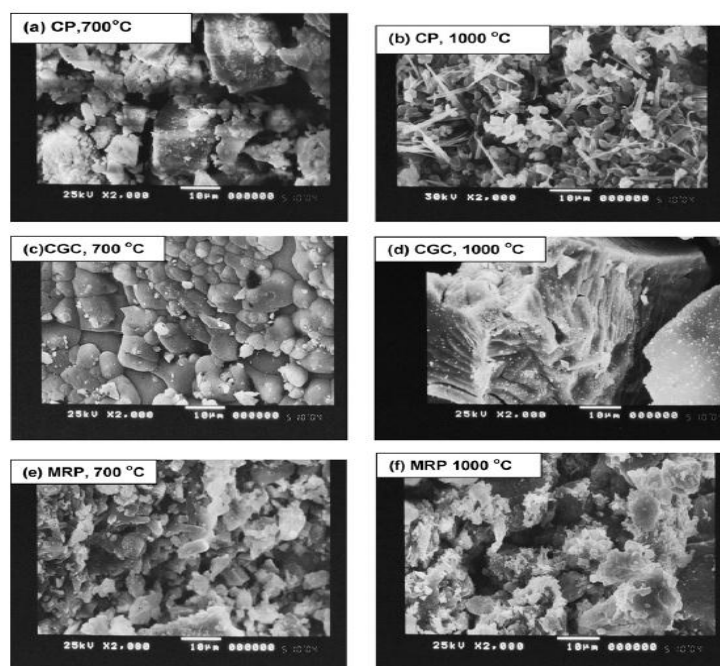
Fig. 4.3 SEM micrographs of ZrO_2 powders produced by CP (a, b), CGC (c, d) and MRP (e, f) methods calcined at 700 and 1000 ^{o}C [37].

Banu´s et al [38] have studied the morphology of zirconia using SEM for samples prepared at different temperatures 500 ^{o}C, 700 ^{o}C (Fig. 4.4 b, c) and at room temperature overnight (Fig. 4.4 a). In general, all SEM images had an arrangement of interconnected surface cracks. The sample that was kept at room temperature and left overnight exhibited a mosaic-type structure (Fig. 4.4 a). Samples that were calcined at higher temperature exhibited flakes and wider cracks due to the shrinkage mechanism which occurred during the drying process (Fig. 4.4 b and c). After calcination at 500 ^{o}C, the samples had black colours which turned eventually to white when the treatment temperature reached 700 ^{o}C indicating the removal of the residual carbon compounds.
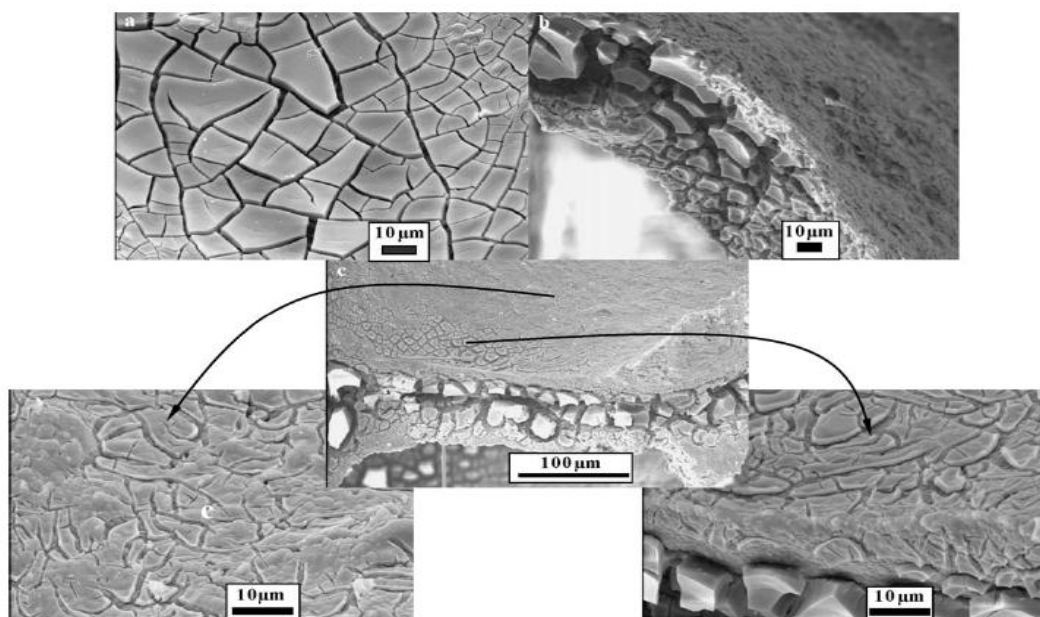
Fig 4.4 SEM micrographs of the ZrO_2 after: (a) drying at 25 ^{o}C, (b) calcination at 500 ^{o}C and (c) calcination at 700 ^{o}C [38].

The SEM images of zirconia after incorporation with Co, Ba and K active elements (Fig. 4.5) showed that the interconnected cracks with flake structure were present in the samples (Fig. 4.5 a, d). High magnification of the flake surfaces (Fig. 4.5 c, f) demonstrated some differences among the morphologies which might be caused by different solvent evaporation rates. A larger size of the flakes was observed after the Co, Ba and K addition compared to the undoped ZrO_2 (Figs. 4.5 c, b and e).
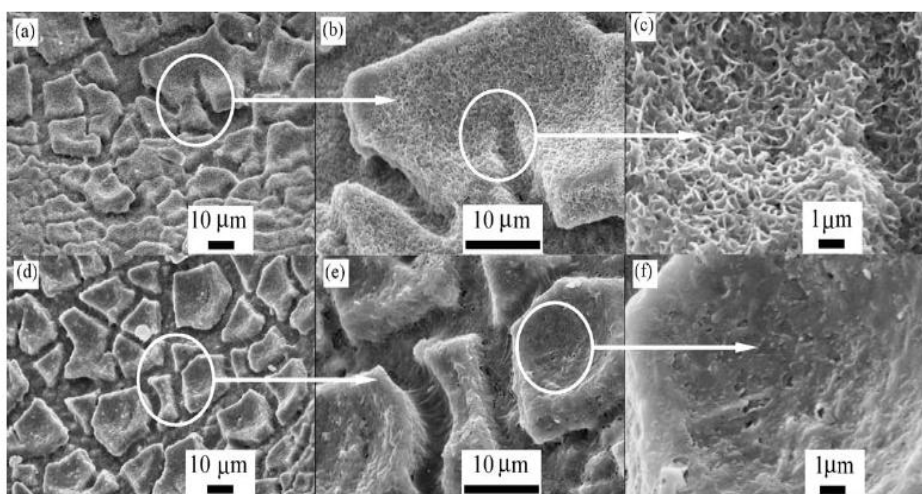
Fig. 4.5 SEM micrographs of Co, Ba, K/ZrO_2 with three different magnifications: (a and d) x 1000, (b and e) x3000 and (c and f) x10,000 [38].

Transformation from the tetragonal to monoclinic phase is usually favoured due to the relative stability of these two phases which depends on the sum of the free energies from the particle surface, bulk and strain contribution [39, 40]. The lower bulk free energy of m-ZrO_2 and the lower surface free energy of t-ZrO_2 promote the stability of tetragonal phase below a critical particle size, which is estimated to be 10 nm at 298 K. In the absence of particle strain, this thermodynamic description can provide the appropriate temperature required for the tetragonal to monoclinic phase transformation for the particles ranging from 9 nm to 10 μm. The phase transformation takes place only if the size of zirconia particles is equal to or greater than the critical size determined from an analysis of the thermodynamic stability of small particles of tetragonal and monoclinic ZrO_2. However, t-ZrO_2 that is larger than the critical particle size can be obtained by taking into account factors such as nucleation embryos, domain boundary stresses, anionic vacancies and adsorbed cations and anions. The effects of external strain and the adsorbed ionic species on the surface free energy of zirconia can be included within the thermodynamic theory for the tetragonal to monoclinic phase transformation. The phase transformation of zirconia is basically initiated from its surface region and then continues progressively into the bulk although the stabilisation of tetragonal phase in the surface region is difficult.

Xin-Me and Zi-Feng [41] have considered the effects of crystallisation temperatures on phase transformation of zirconia. The XRD results showed that amorphous material was obtained when the temperature was lower than 150 ^{o}C, but pure monoclinic phase nano-sized particles were only produced when the temperature was increased to 180 ^{o}C (Fig. 4.6).
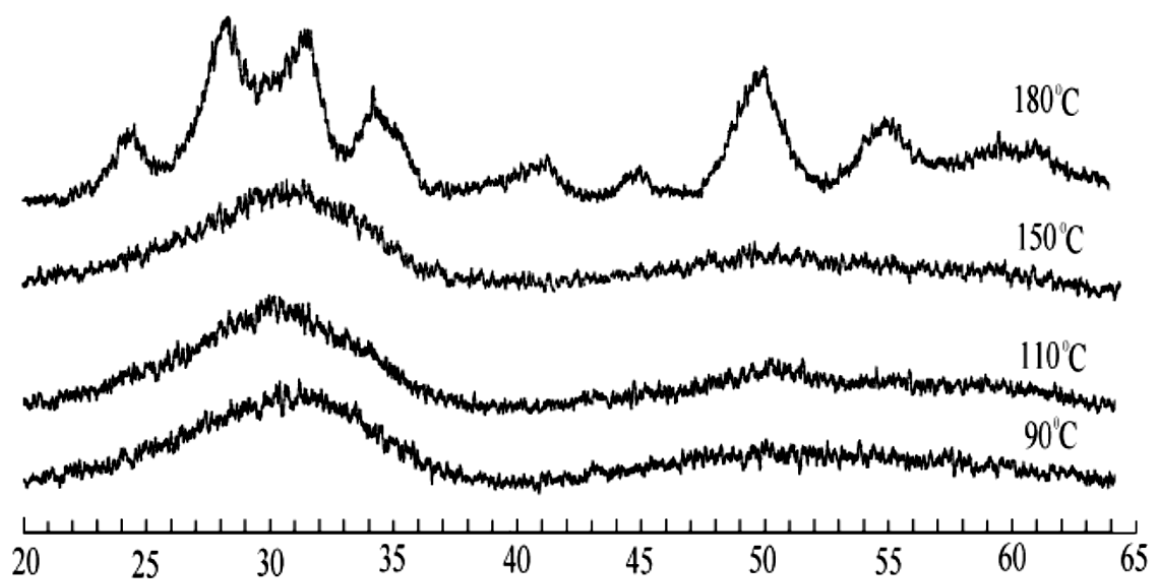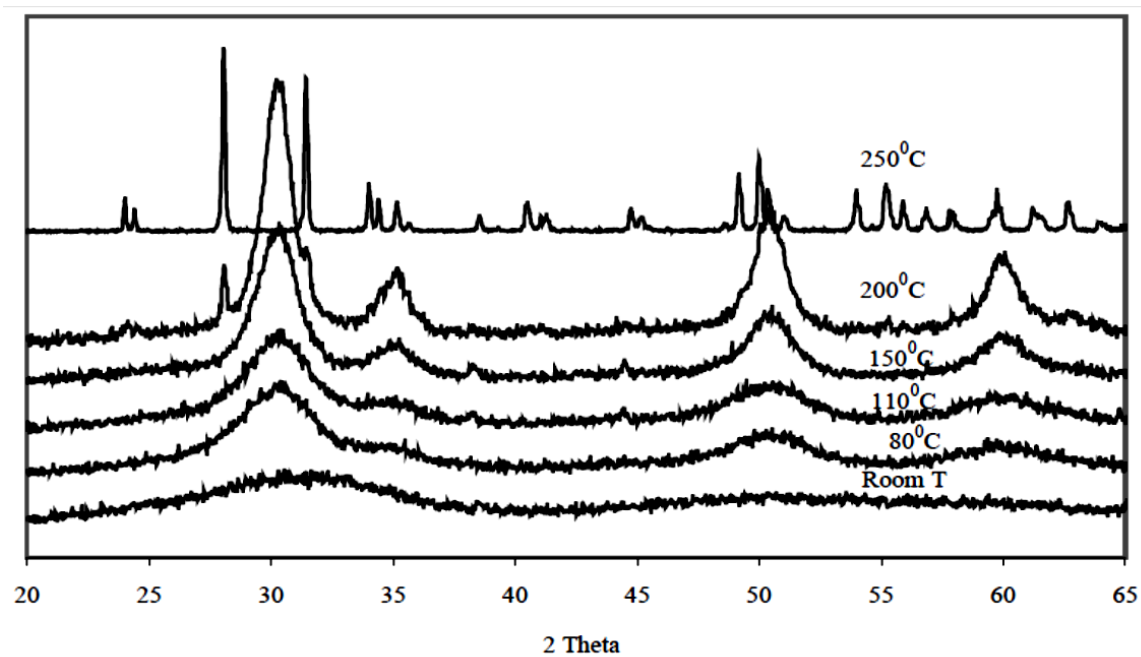
Fig. 4.6 Effect of crystallising temperature on the crystal phase of zirconia: (a) $\overline{OH}$/Zr = 2.0, (b) $\overline{OH}$/Zr = 4.0 [41].

The tetragonal phase gradually initiated upon increasing temperature even though these tetragonal phase particles have obvious structural defects and their crystallinity was relatively low. The diffraction peaks of the tetragonal phase strengthened clearly and crystal particles began to grow when the temperature increased to 150 ^{o}C. But when the temperature was as high as 180 ^{o}C, the monoclinic phase appeared. Beyond 250 ^{o}C, the phase was a perfect monoclinic phase. The crystal size was developed upon calcination from 1.5 nm for the tetragonal phase to 54.2 nm for the monoclinic phase. The influence of crystallizing temperature on the morphology of zirconia was strongly related with its formation mechanism (Table 4.1). Further frequent collision among $ZrO_x(OH)_y$ species occurred due to the increase of crystallising temperature, resulting in the acceleration of surface hydroxyls condensation and increasing corresponded crystallisation rates. Accordingly, mesoporous nano-sized zirconia was changed from an amorphous state to a crystalline state. This transformation was accompanied by conversion of the atomic arrangement from short range order to long range order. Upon the increase in temperature, the crystallite size of the sample was increased and the structure was compacted.

Table 1. Effect of Crystallizing Temperature on Crystal Phase and Size of Zirconia

Surfactant	353 K		383 K		423 K		473 K	
	C.S./nm	C.P.	C.S./nm	C.P.	C.S./nm	C.P.	C.S./nm	C.P.
CTABr	2.7	T	3.5	T	5.1	T	6.8	M/T
PEO	0.9	T	1.5	T	3.4	T	5.0	M/T

C.S.----Crystal size   C.P.----Crystal phase   T--- Tetragonal   M---Monoclinic

Table 4.1 Effect of crystallisation temperature on crystal phase and size of zirconia [41].

The XRD result also demonstrated that higher temperature was beneficial for the formation of monoclinic phase nano-sized zirconia, and zirconia with a smaller crystallite size of 3.8 nm could be attained at lower OH/Zr ratio and at 180 ^{o}C. At higher OH/Zr ratio, calcination encouraged formation of metastable tetragonal phase, as did the presence of the alkali metal ions while surface defects of the sample were decreased and the crystallinity was subsequently increased. Higher crystallisation temperature and lower alkalinity were suitable conditions for the formation of the monoclinic phase whilst tetragonal phase required higher alkalinity. This observation has also been documented by several authors such as Adair et al [42]. Nano-sized zirconia with different phase states and crystal sizes could be synthesized by tuning the crystallising temperature and OH/Zr ratio. SEM

pictures showing the influence of crystallising temperature upon morphology are shown in Figure 4.7.
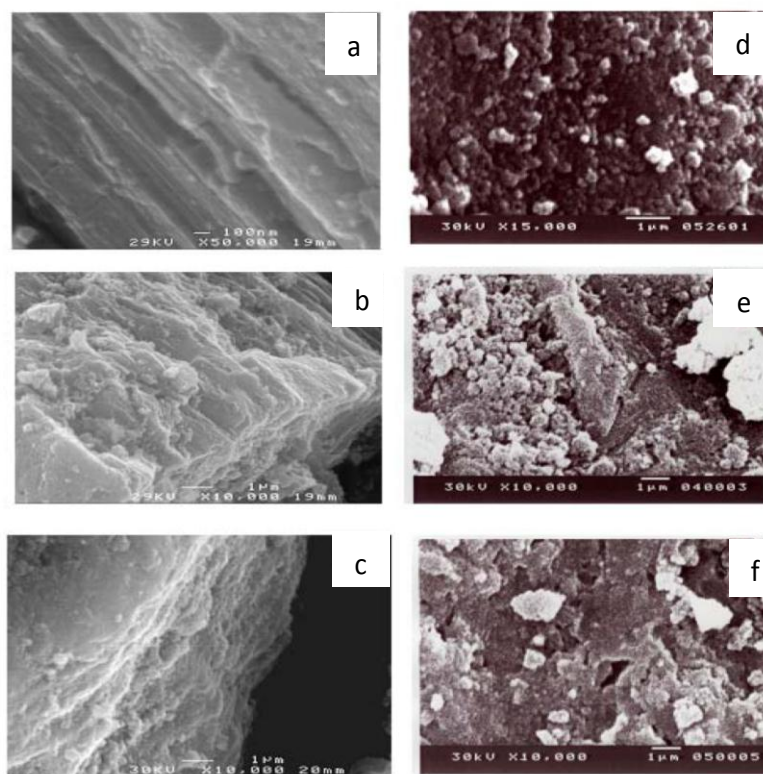
Fig. 4.7 Effect of crystallising temperature on the morphology of zirconia (a, d) 90 ^{o}C, (b, e) 150 ^{o}C, (c, f) 180 ^{o}C [42].

Phase transformations in zirconia have been followed by DTA (differential thermal analysis). A "glow exotherm" can be observed for amorphous samples at about 450 ^{o}C (Fig. 4.8) in comparison with crystalline zirconia [41].
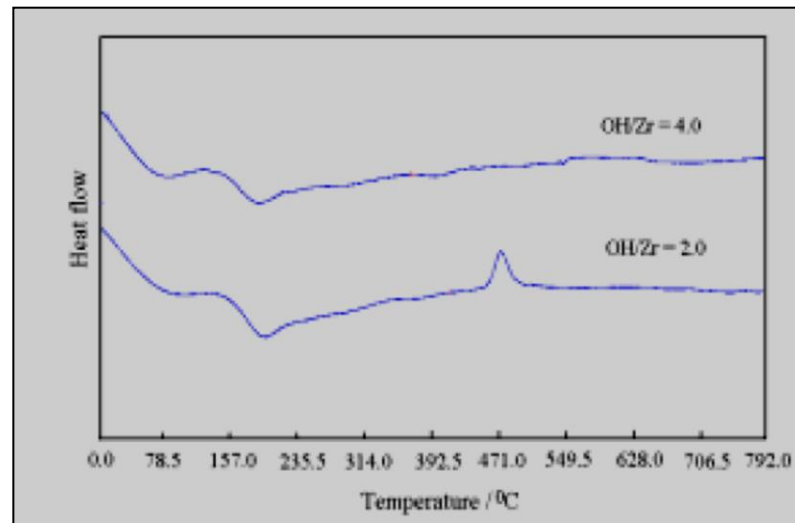
Fig. 4.8 DTA diagram of zirconia prepared with different OH⁻/Zr ratios [41].

The "glow exotherm" was generated due to the transformation from the high energetic amorphous phase to low-energetic crystalline phase which produces energy. The activation energy of this transformation was 183.8 KJ/mol which has been calculated using Redhead equation:

$$r_d/N_s = -d\theta_A/dt = k_0 \exp(-\varepsilon_A/kT) \theta_A^n$$

where:

- r_d is the rate of desorption of species.
- N_S is the concentration of surface adsorption sites.
- θ_A is the coverage of species.
- t is the time.
- k_0 is a pre-exponential factor for the rate constant.
- T is the temperature (K).
- n is the order of the desorption reaction.
- E_A is the activation energy (per mole) for the desorption of molecule, alternatively, ε_A (per molecule).
- k or k_B is the Boltzmann constant (per molecule).
- Alternatively, R ($=N_A k_B$) per mole.
- NA is Avogadro's number.

However, the shrinkage of the structure for mesoporous nano-sized zirconia caused by the increase of temperature might be attributed to the acceleration of the hydroxyl condensation reaction at higher temperature. For the crystalline phases, the deposit rate of $ZrO_x(OH)_y$ solid particles was also accelerated by hydroxyl condensation. The nano-sized zirconia tended to deposit at joints of polymeric particles that generated the pore wall thicknesses. However, enhancement of crystal size of the product occurred by increasing crystallisation rate. The crystal sizes of zirconia prepared at different crystallizing temperatures are shown in Table 4.1. From XRD analysis, the diffraction peaks of the nano-crystalline sample were relatively wide as would be expected. The initial phase was tetragonal with a large amount of defects. When the time of characterisation was increased up to 12 h, diffraction peaks of tetragonal phase because apparent. The strength intensity of diffraction peaks was slightly improved by expectation of the crystallisation time (Table 4.2):

Table 2. Effect of Crystallizing Time on the Nano-size of Zirconia					
Crystalline time/h	0	12	24	72	96
Mesh size/nm	0.47	1.42	1.67	1.67	1.71

Table 4.2 Effect of crystallisation time on the nano-size of zirconia [41].

Although zirconia has been widely used as a strong solid acid catalyst by modification with WO_3 [42], sulfate [43, 44], B_2O_3 [45] and MoO_3 [46], few studies have applied zirconia as a solid base catalyst. Several studies have reported the high activity of alkali-modified zirconia catalysts for the oxidative coupling of methane [47]. Studies of the Knoevenagel condensation of various aliphatic, aromatic and heterocyclic aldehydes with malononitrile over sulfate-ion promoted zirconia solid acid catalysts have also been conducted [48]. Synthesis of methanol from carbon dioxide was carried out over copper-zirconia catalysts [49]. Ga-promoted tungstated zirconia has been used for the isomerisation of *n*-butane [50]. Removal of vehicular exhaust gas pollutants was investigated on zirconia supported copper oxide catalyst [51]. The partial oxidation of methane was performed over yttria-stabilised zirconia catalyst in a dielectric barrier discharge has been investigated [52]. The structure and properties of vanadium oxide–zirconia catalysts were determined for the propane oxidative dehydrogenation reaction [53]. Additionally, it has been reported that

ZrO_2 can be used as acid-base bi-functional catalyst in industrial applications [54]. Zirconia plays an unusual role in the direct synthesis of dimethyl carbonate from CO_2 and methanol. It was documented that zirconia has a surface acidity equivalent to about 100% H_2SO_4 after modifying by SO_4^{2-} and it can be transformed to a strong base by addition of KF [55].

Rinn and Schmidt [56] have detailed the thermal analysis of zirconia. Formation of zirconia was almost free of organics, nitrates and hydroxides at about 450 ^{o}C and no further noticeable weight loss was documented up to 1200 ^{o}C (Fig. 4.9).
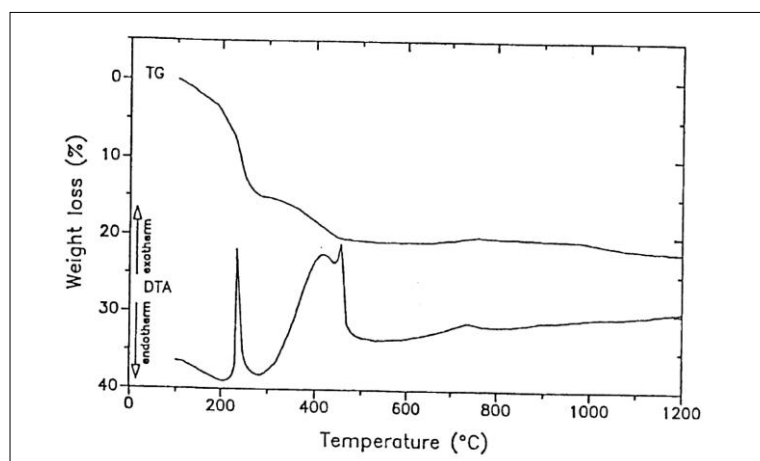
Fig. 4.9 Thermal analysis of the zirconia powder [56].

The x-ray diffraction pattern showed an amorphous material after drying at 100 ^{o}C and tetragonal zirconia at 500 ^{o}C (Fig. 4.10). The broad peaks indicated very small and/or disordered crystals. Further heating resulted in a sharpening and growth of peak intensities, but no monoclinic zirconia formed. The initial phase of the pure amorphous zirconia produced from gels or hydroxides crystallises a metastable tetragonal phase which then transformed into the stable monoclinic form below 1000 ^{o}C.
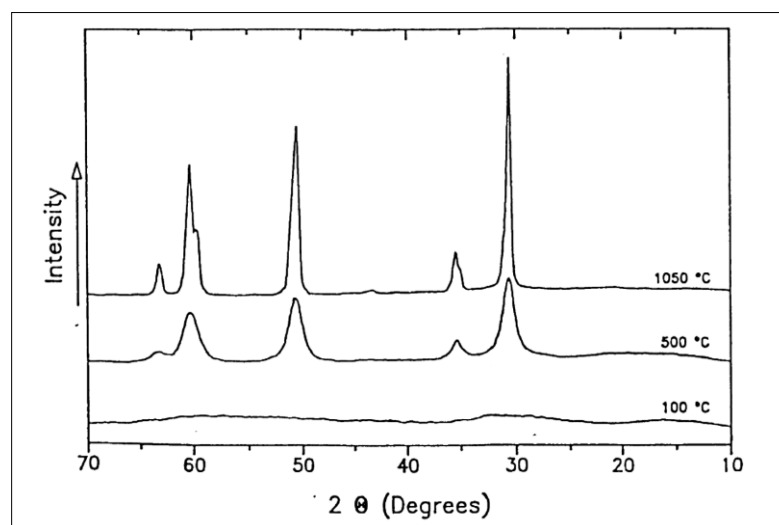
Fig. 4.10 X-ray diffraction pattern of dried and calcined zirconia powders [56].

Scanning electron micrographs of the dried powder showed almost perfect spheres with a size distribution of about 0.3-3 μm (Fig. 4.11 a, b). Calcination up to 850 ^{o}C produced a linear shrinkage of about 50%, but no hard agglomerates were detected (Fig. 4.11 c, d). At temperatures below 400 ^{o}C where OH^{-} groups on the surfaces are lost, sol-gel powders tend to form strong agglomerates by condensation processes. The absence of agglomeration was due to the adsorption of organic molecules. At higher temperatures enhanced crystal growth occurred and caused a sub-structure of the particle surfaces and the formation of some agglomerates.
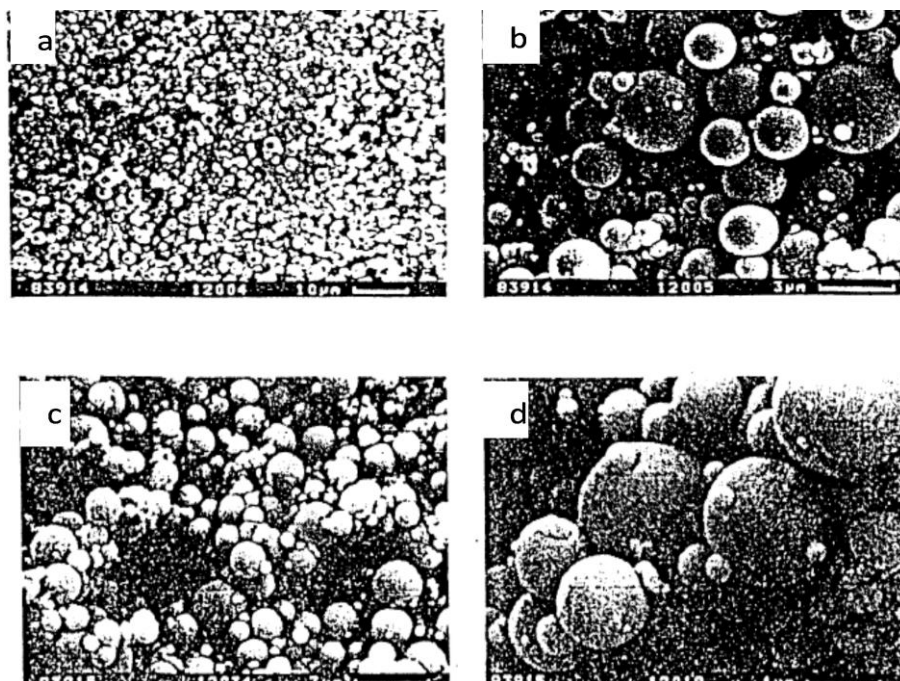
Fig. 4.11 (a, b) SEM-micrographs of the dried zirconia powder. (c, d) SEM-micrographs after calcination at 850 ^{o}C [56].

Modification of zirconia by doping with lower valence cations such as Y^{3+}, La^{3+}, Mg^{2+} and Ca^{2+} can stabilise the cubic or tetragonal phase at room temperature. A solid solution can be obtained in which the replacement of the Zr^{iv} by cations of lower valence produces oxygen vacancies in the ZrO_2 lattice to maintain electroneutrality. The presence of these oxygen defects promotes ionic conductivity.

Bellido and Assaf have investigated the addition of 4%, 8% and 12% mole fractions of Y_2O_3 to ZrO_2 [57]. XRD diffraction studies revealed that ZrO_2 exhibited a mixture of monoclinic phases whereas the addition of Y_2O_3 to ZrO_2 produced only the tetragonal phase due to formation of a solid solution of Y_2O_3 in ZrO_2. This idea was corroborated by a continuous shift of the (111) reflection plane to smaller Bragg angles as a function of the Y_2O_3 loading since the substitution of Zr^{4+} ions (radius 0.80 Å) by Y^{3+} ions (radius 0.93 Å) increased the inter planar distance. A fine dispersion of Y_2O_3 microcrystallites could have occurred but evidence of a segregated Y_2O_3 phase or monoclinic ZrO_2 was not detected. The peaks that resulted from the addition of Y_2O_3-ZrO_2 solid solution became larger and less intense as the Y^{3+} content resulting from reduction of the crystalline particle size. The range of the crystal sizes of the supports calculated from all the reflections is shown in Table 4.3. The particle diameters were all much smaller than 30 nm.

Support	(111)	(200)	(220)	(311)
Z	9.7	6.7	8.8	9.1
4YZ	6.6	6.6	5.0	6.1
8YZ	5.5	4.7	5.0	4.6
12YZ	5.3	4.7	5.0	4.6

Table 4.3 Crystallite sizes (nm) of the supports calculated by Scherrer equation [57].

The BET surface areas (Table 4.4) of the Y_2O_3-ZrO_2 revealed that the surface area of ZrO_2 increased after doping with Y_2O_3 and this was associated with the decrease of the crystal size. However, the BET surface area declined with increasing Y_2O_3 content. Marcos and Gouvea [58] showed a similar behaviour for the MgO-ZrO_2 system, where the addition of MgO up to its level of saturation (8.6% MgO) reduced the surface area. This was due to solubility of Mg^{2+} cations in the ZrO_2 lattice and subsequent generation of oxygen vacancies to balance the charge difference that resulted. Thus, a higher coefficient of diffusion combined with consequent adhesion of the particles was promoted which produced agglomerates that eventually decreased the surface area. Labaki et al [59] reported a remarkable increase in the original ZrO_2 surface area by more than 50% when Y_2O_3 was added to the ZrO_2 lattice, due to structural changes leading to stabilisation of the tetragonal phase.

Support	Composition (mol × 10^{+5})^a		S_{BET} (m^2 g^{-1})
	ZrO_2	Y_2O_3	
Z	40.6	–	19.7
4YZ	37.7	1.6	55.5
8YZ	35.0	3.0	30.0
12YZ	32.5	4.4	25.3

Table 4.4 Composition and BET surface area of supports. a = Sample weight: 50 mg [59].

Yang et al [60] have reported the TG-DTA results for two dried powders of zirconia prepared at different pH values. They were analysed by heating in air at the rate of l0 °C/min. The TG-DTA curves observed that the total weight loss was 34.6% (TG-1) and 35.9% (TG-2) respectively (Fig. 4.12a). The endothermic peak up to 245 °C was due to the dehydration of water and corresponded to a weight loss of 22.0% (TG-I) and 27.8% (TG-2). The exothermic peaks starting at 245 °C and finishing at about 320 °C were attributed to the thermal decomposition and combustion of adsorbed organic materials with a weight loss of 8.5% (TG-I) and 2.9% (TG-2). The weight loss was continued until an exothermic peak resulting from the crystallisation of powder appeared at about 450 °C. However, the

addition of 1.7 and 59 mol% Y_2O_3 to ZrO_2 caused the loss of all the powder crystallisation peaks up to 1000 °C in air (Fig. 4.12b).
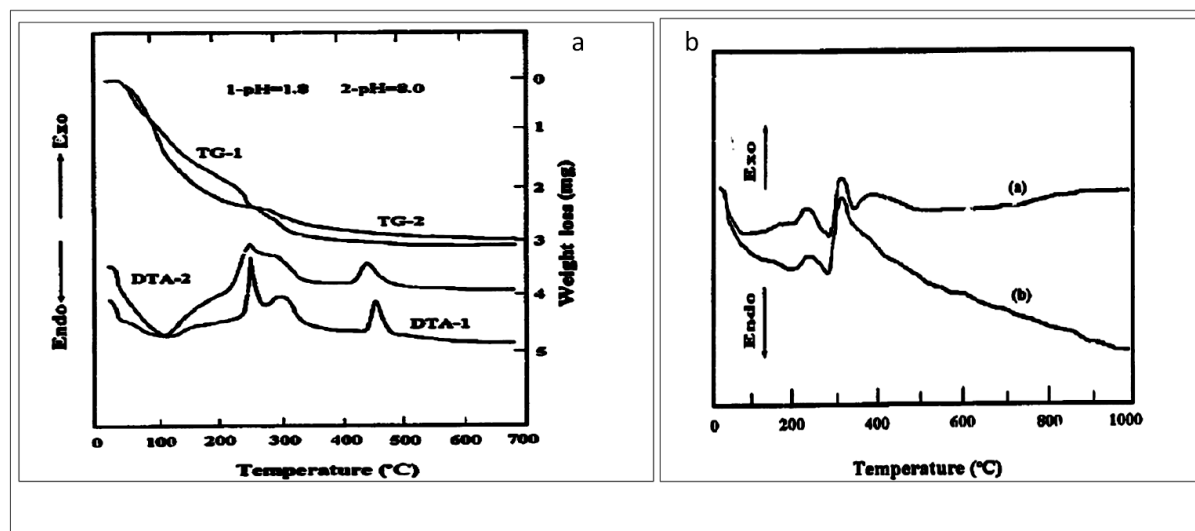
Fig. 4.12 a) TG-DTA curves for prepared ZrO_2 powders. Initial sample weight for analysis: curves 1, 890 mg, curves 2,830 mg. b).DTA curves of Y-doped ZrO_2 powders: (a) 1,7 mol% Y_2O_3; (b) 59 mol% Y_2O_3 [60].

TEM images and a corresponding selected area electron diffraction (SAED) patterns of the prepared ZrO_2 powder (Fig. 4.13b) showed a histogram of the particle size distribution obtained by sampling stochastically 100 particles from the TEM images. The particles were actually well shaped with a narrow size distribution, and the average diameter obtained from (Fig. 4.13a) was about 10 nm. SAED revealed that the powder was polycrystalline. However, the TEM micrograph of the Y-ZrO_2 and the corresponding SAED observed a flocculent morphology with amorphous diffraction pattern of the powder (Fig. 4.13c).
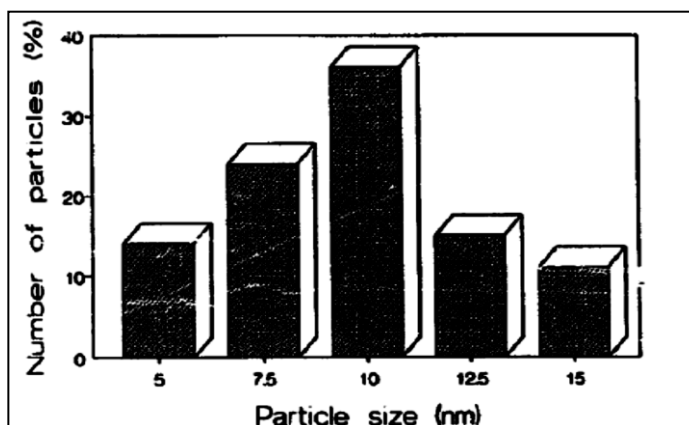
Fig. 4.13 a) Histogram of the particle size distribution of particulate ZrO$_2$ powder [60].

Fig. 4.13 b) Typical TEM image and SAED pattern of particulate ZrO$_2$ powder [60].
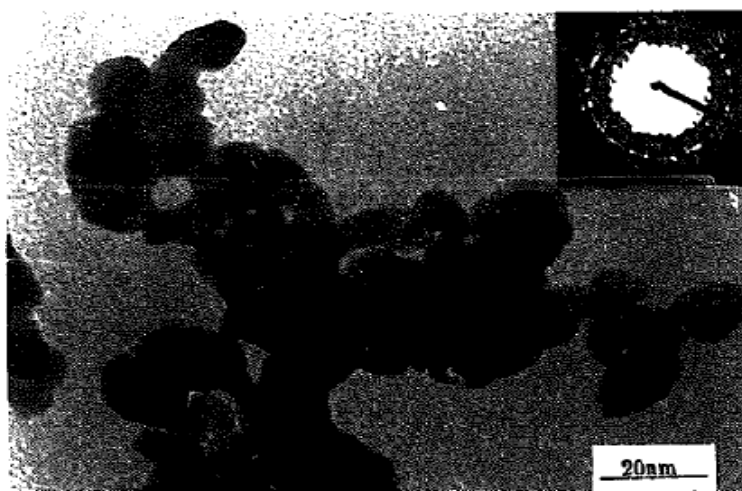
Fig. 4.13 c) Typical TEM image and SAED pattern of the prepared Y-doped ZrO_2 powder [60].

The effects of combining zirconia with other catalysts, either being supported or as a support itself, on its catalytic activity, characterisation and morphology have been widely studied [61-64]. Carrascull et al [65] have studied the effects of supporting potassium nitrate on zirconia on the catalytic activity and surface area. They concluded that the zirconium oxide (ZrO_2) and catalysts containing potassium nitrate at lower concentration ($K0:25ZrO_2$ and $K1:25ZrO_2$) present the largest surface area (Table 4.5). The addition of KNO_3 to ZrO_2 enhances its activity due to enhanced bonding of reactants and catalyst and also because the KNO_3 itself acts as catalyst. Incorporation of potassium ions into ZrO_2 induces a guest-host interaction and is proposed to result in the formation of "superbasic" sites.

Catalyst	S (m^2/g)
ZrO_2	45
0.25% KNO_3/ZrO_2	45
1.25% KNO_3/ZrO_2	52
11.5% KNO_3/ZrO_2	15
20.5% KNO_3/ZrO_2	11

Table 4.5 Specific surface area of the ZrO_2 and different loaded KNO_3/ZrO_2 catalysts. The effect of KNO_3 loaded on zirconia surface area was illustrated. (The precursors were calcined at 600 ^{o}C) [65].

Wang et al [66] have presented a characterisation study of KNO_3/ZrO_2 catalysts. They observed that the XRD pattern of 14% KNO_3/ZrO_2 was identical to that of ZrO_2. Above a 14% loading, the characteristic XRD peaks of KNO_3 appeared in the patterns (Fig. 4.14e, g) and their intensities increased demonstrating the presence of residual KNO_3. They suggested that the spontaneous dispersion capacity of KNO_3 on ZrO_2 was 14% wt since that quantity could be well dispersed and caused no significant distortion in the structure of ZrO_2.

The equivalent surface concentration of K^+ for the capacity was 8.1 nm^{-2} which was reportedly quite similar to that of surface vacant sites on ZrO_2 which was 8.6 nm^{-2}. The K^+ ion of KNO_3 can insert into the surface sites of alumina and consequently accelerate

dispersion and decomposition of KNO_3 to form strong basic sites in the activation process. Two essential crystalline phases of zirconia were observed namely: monoclinic and tetragonal. The peak intensity of the monoclinic phase is weaker than that of the tetragonal phase when the sample was dried at 110 ^{o}C (Fig. 4.14a). It developed quickly while that of the tetragonal phase declined upon calcination. The tetragonal phase disappeared after calcination at 700 ^{o}C which indicated that it was a metastable phase. In contrast, the metastable tetragonal phase of zirconia was strongly evident in the XRD pattern of 20% KNO_3/ZrO_2 despite the fact that it was heated to 700 ^{o}C. K^{+} ions possibly occupy the position of octa-coordinated Zr^{iv} in the tetragonal phase rather than the hepta-coordinated Zr^{iv} in monoclinic phase and thus delay phase transformation of ZrO_2 at high temperature.
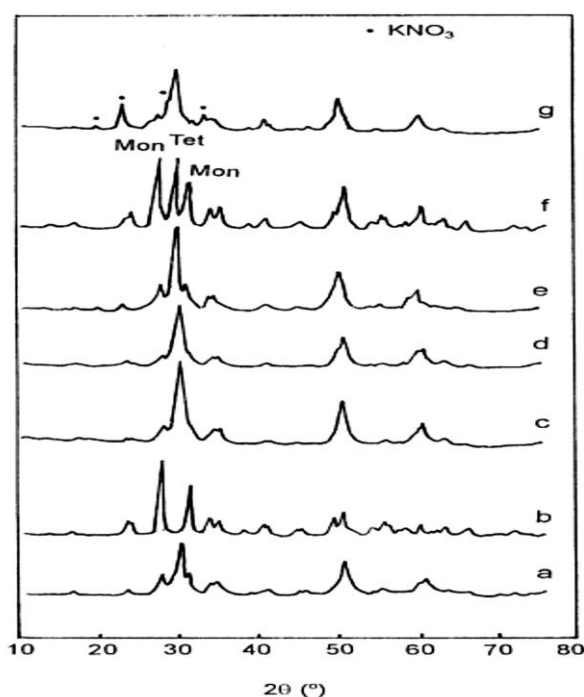
Fig. 4.14 XRD patterns of ZrO_2 (a) before and (b) after calcination at 700 ^{o}C, (c) 14% KNO_3/ZrO_2, (d) 20% KNO_3/ZrO_2, (e) 27% KNO_3/ZrO_2, (f) 20% KNO_3/ZrO_2 calcined at 700 ^{o}C, and (g) 34% KNO_3/ZrO_2 [65].

The authors also discussed the thermal decomposition of KNO_3/ZrO_2 catalyst which was studied using the TPDE-CM technique. KNO_3 generally starts to decompose at 480 ^{o}C which is reduced to 340 ^{o}C after being supported on ZrO_2 [65]. Hence supporting KNO_3 on zirconia hastens the decomposition of KNO_3 (Table 4.6). However, the decomposition temperature is a function of loading, e.g. high loadings of KNO_3 such as 34% KNO_3/ZrO_2

gives rise to decomposition at 410 $^{\circ}$C. Good dispersion of KNO_3 on ZrO_2 weakens the binding of K^+ and NO_3^- ions owing to the interaction between KNO_3 and the surface of zirconia support which is beneficial for decomposition of KNO_3.

Amount of KNO_3 loaded (wt%)	7.5	14	20	27	34
Concetration of K^+ ions (K^+ nm^{-2})	4	8.1	124	18.4	25.6
Initial tempretaure of KNO_3 decompostion	340	349	343	344	410
Amount of KNO_3 decomposed (mmol g^{-1})					
Below 400 $^{\circ}$C	0.01	0.02	0.02	0.01	0
400-500 $^{\circ}$C	0.13	0.14	0.18	0.1	0.05
500-600 $^{\circ}$C	0.03	0.08	0.27	0.09	0.12

Table 4.6 Decomposition of various loaded amounts of KNO_3 on ZrO_2 [65].

The basicity of KNO_3/ZrO_2 has been measured using the CO_2-TPD technique by the same authors [65]. Desorption features for base ZrO_2 were evident at around 76 $^{\circ}$C, 115 $^{\circ}$C and 148 $^{\circ}$C indicating the weak basicity of ZrO_2 (Fig. 4.15).
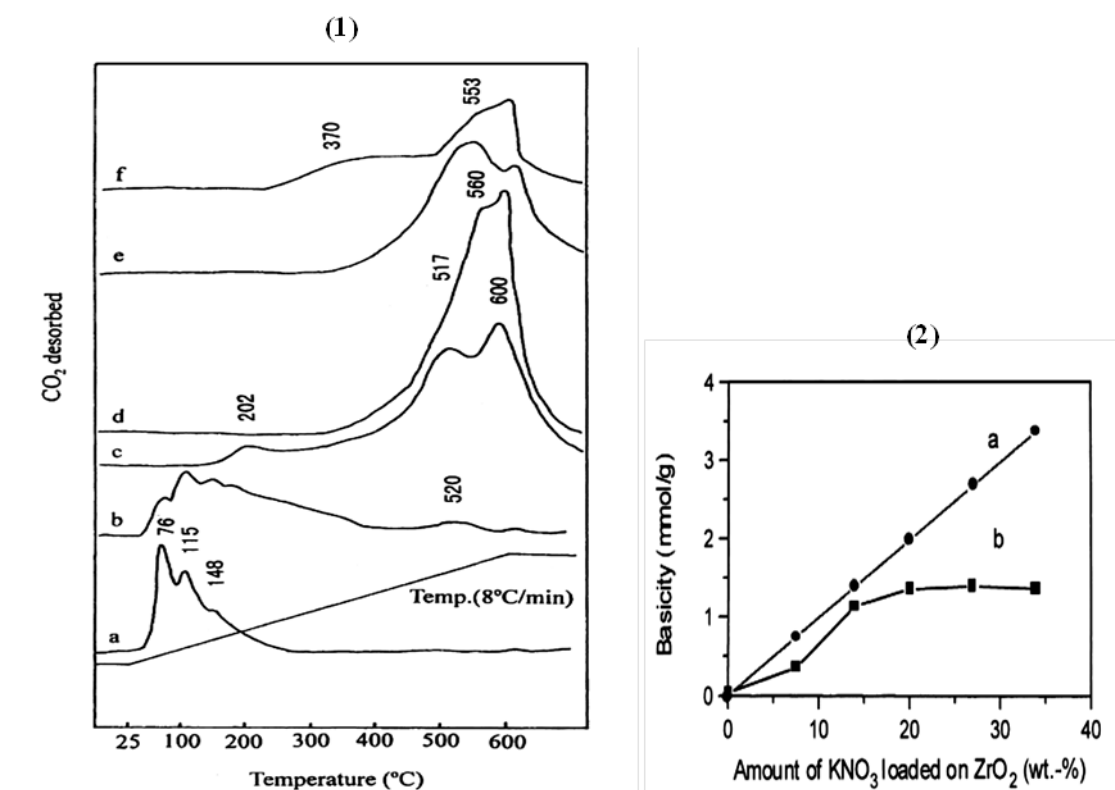
Fig. 4.15 (1) CO_2-TPD profiles of ZrO_2 loaded KNO_3 of a) 0, b) 7.5, c) 14, d) 20, e) 27 and f) 34 wt.%. (2) a) The calculated and b) the measured basicity of KNO_3/ZrO_2 [65].

Loading 7.5 wt.% KNO_3 resulted in a new peak at 520 ^{o}C while three new peaks were generated at 202 ^{o}C, 517 ^{o}C and 600 ^{o}C when the amount of KNO_3 was approximately doubled to 14 wt.%. Further addition of KNO_3 up to 20 wt.% caused a remarkable enhancement to the rate of CO_2 desorption in the range between 320 ^{o}C and 600 ^{o}C which peaked at 600 ^{o}C. Further addition of KNO_3 on ZrO_2, e.g. 27 wt.%, decreased the maximum temperature of CO_2 desorption from 600 ^{o}C to 553 ^{o}C and reduced peak intensity. For the 34% KNO_3/ZrO_2 sample, a new peak of CO_2-TPD was observed at around 370 ^{o}C. The reduction of basicity in such instances is related to the coverage of the strongly basic sites by excess KNO_3.

If the amount of KNO_3 exceeded the spontaneous dispersion capacity which was 14 wt.%, a value of 1.35 mmolg^{-1} of the measured basicity was obtained which is very close to the calculated value that has been estimated to be 1.39 mmolg^{-1}. The catalytic activity of the KNO_3/ZrO_2 catalyst has also been investigated for the decomposition of iso-propanol (Fig. 4.16). A small amount of acetone was detected in the products on the ZrO_2 catalyst accompanied by a high reactant conversion of 99%. Since the reactant was well known to be dehydrated by acidic sites [66], this demonstrated the acidic characteristics of zirconia. The addition of 7.5 wt% of KNO_3 to ZrO_2 increased the selectivity of acetone to 51% and lowered the iso-propanol conversion to 31% due to the suppression of acid sites and hence dehydration of iso-propanol. When the loading amount of KNO_3 reached the spontaneous dispersion capacity of 14 wt% (with a K^+ ion density of 8.1 nm^{-2} on ZrO_2), the acetone selectivity dramatically increased to 99% which evidenced the increase of basic sites formed on the sample while the isopropanol conversion continued to decrease to 28%. Further addition of KNO_3 on ZrO_2 had no further impact on the basic activity. On the 34% KNO_3/ZrO_2 catalyst (with a K^+ ion density of 25.6 nm^{-2}), the conversion of iso-propanol remained constant at 29% although acetone selectivity declined to 80%. The excess amount of KNO_3 was proposed to cover the basic sites on the surface of composite and thus inhibit acetone formation.
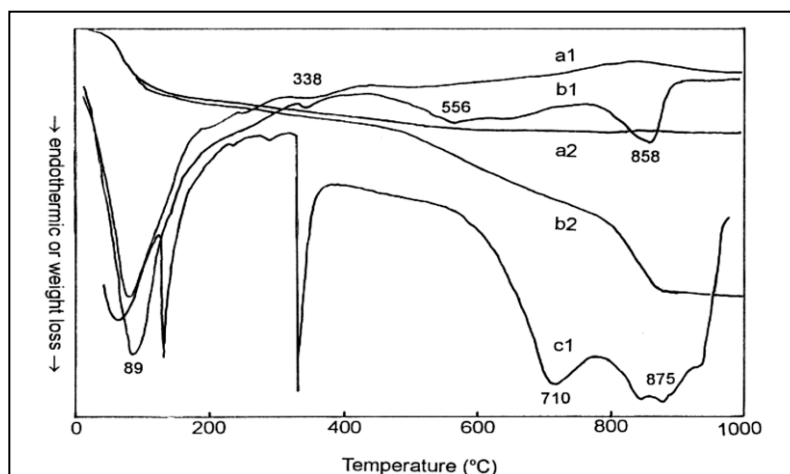
Fig. 4.16 (1) DTA and (2) TG spectra of (a) ZrO_2 , (b) 20% KNO_3/ZrO_2 and (c) KNO_3 [66].

Zhu et al [67] have shown that zirconia catalyst was weakly active for the isomerisation of cis-but-2-ene reaction at 0 °C with an initial reaction rate smaller than 0.001 mmolg^{-1}min^{-1} and that KNO_3 was inactive. On the other hand, supporting KNO_3 on ZrO_2 increased catalytic activity by a hundred times. The activity was proportional to the amount of KNO_3 decomposed at 500 °C (Fig. 4.17).
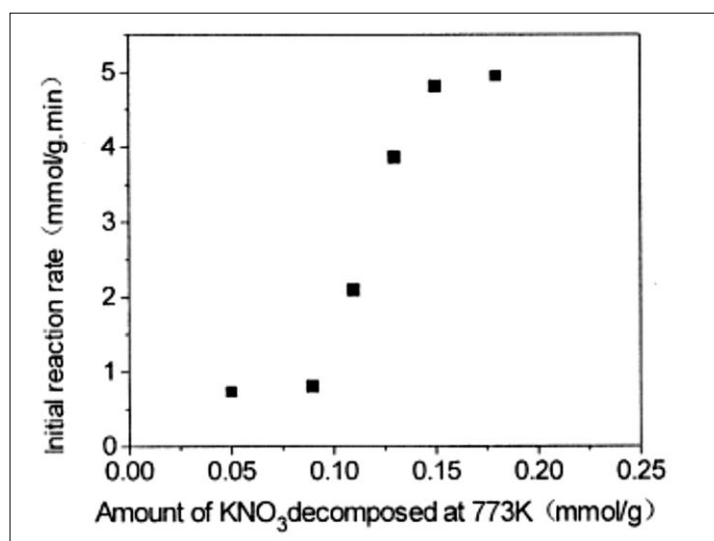
Fig. 4.17 Relationship between the initial reaction rate of KNO_3/ZrO_2 and the amount of KNO_3 decomposed at 500 °C in the isomerisation of *cis*-but-2-ene at 0 °C [67].

Thermal decomposition of KNO_3 yielded either K_2O ultra-fine particles [68] or K–O–Zr structures that are believed to be the main active sites.

There is a pronounced dependence of the catalytic activity of KNO_3 catalysts upon the nature of the support, with KNO_3/ZrO_2 materials generally being the most active. In contrast, KNO_3/TiO_2 and KNO_3/SiO_2 catalysts showed little activity while KNO_3/NaY and KNO_3/NaX zeolite were inactive [69, 70].

In this chapter, a study of the application of ZrO_2 derived catalyst for the acetone conversion reaction. Particular emphasis is placed upon modification, such as the inclusion of KNO_3 and Y_2O_3, which are anticipated to enhance basicity.

4.2 Results and discussion.

The aldol condensation reaction of acetone has been investigated in this thesis over a variety of zirconia related catalysts including ZrO_2, 14% KNO_3/ZrO_2, 36.5% KNO_3/ZrO_2, 14% $KNO_3/Zr(OH)_4$, 36.5% $KNO_3/Zr(OH)_4$, ZrO_2, and $Y-Zr(OH)_4$. The application and characterisation of each material is explained individually.

4.2.1 ZrO_2.

The XRD pattern of zirconia exhibited two crystal phases (Fig. 4.18). One is monoclinic baddeleyite with characteristic reflections at $2\theta = 24.2^o$, 28.2^o and 31.5^o and other is the metastable tetragonal form which contains characteristic reflections at $2\theta = 30.2^o$, 50.4^o and 60.2^o [66]. Calcination of the zirconia did not result in significant changes in its phase composition.

The volume fraction, V_m for the uncalcined zirconia sample was 98.0% monoclinic phase whereas the calcined zirconia sample comprises 97.5% (Table 3.3.2) and therefore essentially unchanged. As discussed in the introduction, the tetragonal form of zirconia may exist even at low temperatures depending on impurity and crystallite size effects [71, 72]. It is well known that the crystal phase of zirconia depends on the preparation and heating treatment of the precursor [73]. Previous studies have shown that the monoclinic ($m-ZrO_2$) and tetragonal ($t-ZrO_2$) modifications of ZrO_2 possess different acid/base properties [74, 75] and surface hydroxyl group concentrations [76].

The volume fraction of the monoclinic phase, V_m, of each sample was calculated using the following well-known relationship [77]:

$$V_m = 1.311X_m/(1 + 0.311X_m) \tag{4.1}$$

$$X_m=(I_m(111)+I_m(111`)/(I_m(111)+I_m(111`)+I_t(111)) \tag{4.2}$$

where $I_m(111)$ and $I_m(111`)$ are the line intensities of the (111) and (111`) peaks for m-$ZrO_2$ and It (111) is the intensity of the (111) peak for t-ZrO_2.
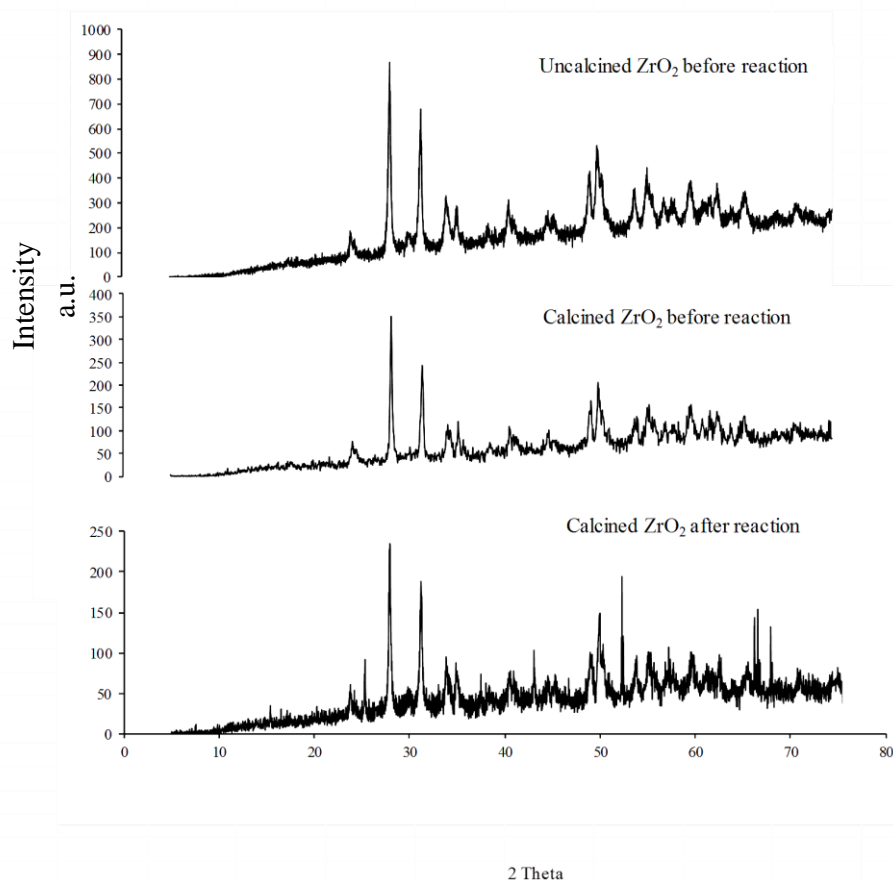
Fig. 4.18 X-ray diffraction patterns of ZrO_2.

Catalyst	Vm(%)
ZrO_2 (Commercial)	98.0
Calcined ZrO_2	97.5
Calcined ZrO_2 after reaction	96.0

Table 4.7 Volume fraction (V_m) of monoclinic phases of the various ZrO_2 samples used in this study.
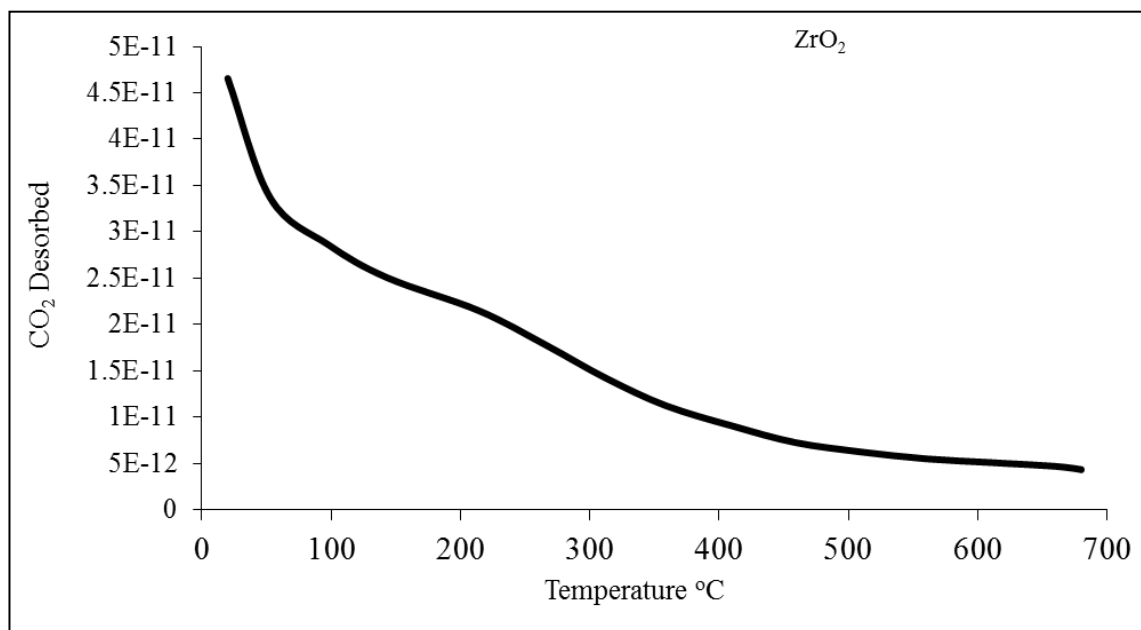
Fig. 4.19 Temperature programmed desorption of CO_2 on calcined ZrO_2 prior to reaction.

The base site strength of the calcined ZrO_2 sample prior to its application as a catalyst was evaluated by CO_2-TPDE and the results are presented in Figure 4.19. This result is consistent with previous work published by Li et al [78]. Both acidic and basic properties are present on the surface and their strengths are rather weak [79]. The curve levels off at about 600 ^{o}C.
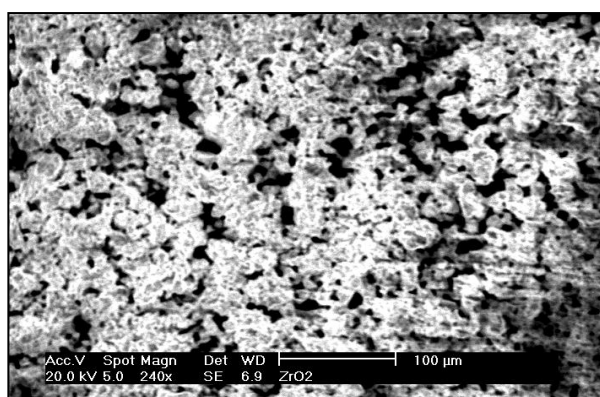
Fig. 4.20 Scanning electron microscope (SEM) image of calcined ZrO_2 prior to reaction.

SEM investigation of calcined ZrO_2 prior to reaction showed uniform dispersion of zirconia agglomerates with irregular shape and variable packing density of their primary particles (Fig. 4.20). According to the literature [80] these agglomerates can be classified

as 'soft' or 'hard', the hard agglomerates consisting of close-packed particles with high densities.

The BET surface area of ZrO_2 is 5% m^2/g which is rather low and consistent with the high phase fraction of the monoclinic polymorph.

Tempertaure ^{o}C	Conversion (%)	Selectivity (%)						
		DAA	MO	MIBK	Phor	Isoph	DH	MP
300	3	5.71	59.20	4.10	5.80	10.03	3.65	11.62
400	6	12.70	40.95	7.50	8.97	12.70	0.60	16.61

Table 4.8 Conversions and selectivities of aldol condensation of acetone over ZrO_2 catalyst as a function of temperature (300 ^{o}C and 400 ^{o}C, 5 bar H_2 pressure, TOS > 18 h).

The sample was investigated in the conversion of acetone as detailed in the experimental chapter. A conversion of 3% was obtained at 300 ^{o}C which was consequently increased to 6% by increasing reaction temperature to 400 ^{o}C, Table 4.8, in agreement with previous studies [81, 82] and normal expectation.

The rate of acetone conversion over zirconia catalyst significantly increases from 1.08×10^{-3} mol m^{-2} h^{-1} to 2.37×10^{-3} mol m^{-2} h^{-1} by increasing temperature from 300 ^{o}C to 400 ^{o}C (Fig. 4.21). It was also apparent that the conversion itself was a function of time on stream, sharply declining as a function of the time on stream during the early period of reaction, becoming stable beyond 21 h where the catalyst reached a steady state. The decrease of conversion was probably caused by a slow, progressive, deactivation by coke when highly unsaturated compounds, such as phorone, were formed and remained strongly adsorbed on the catalyst surface, yielding heavier oligomeric compounds which can block the active sites [83].
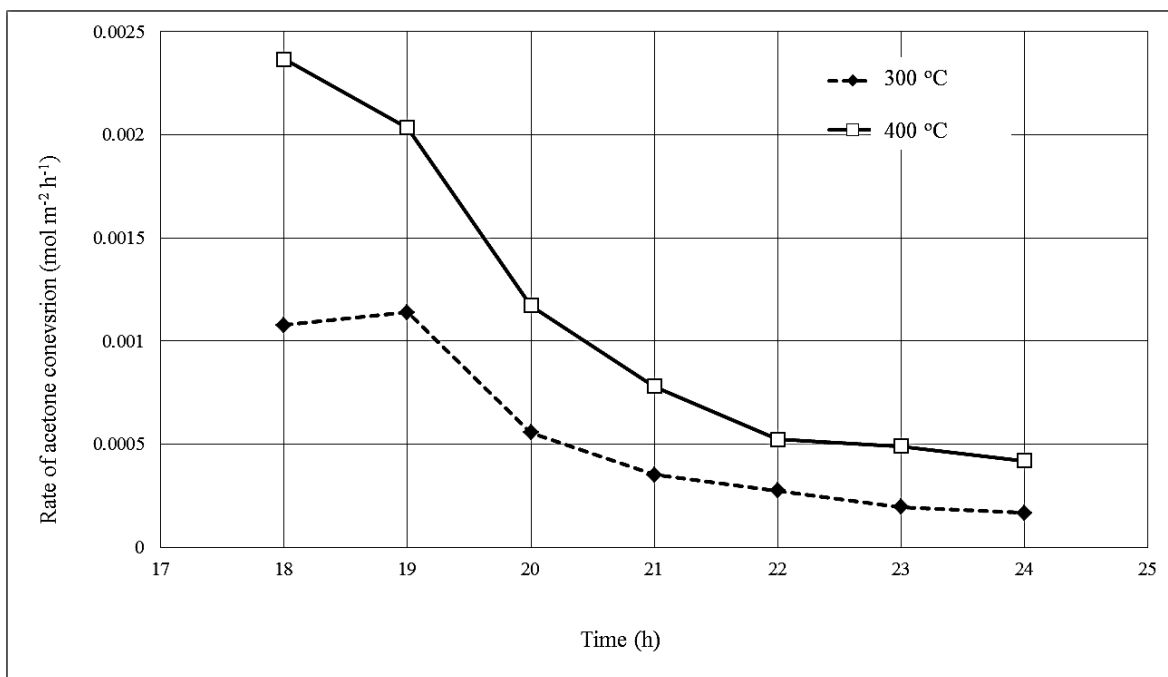
Fig. 4.21 Surface area normalised acetone conversions over ZrO_2 catalyst as a function of time on stream at 300 $^{\circ}$C, 400 $^{\circ}$C and 5 bar H_2 pressure, TOS > 18 h.

Product selectivities have also been determined for the reaction. The highest yield was observed for MO at 400 $^{\circ}$C (Fig. 4.22). When the hydrogenation activity is low, mesityl oxide (MO) produced by aldol condensation does not undergo further hydrogenation to MIBK. As a consequence, MO appeared as a main product. High MO concentrations, in turn, are accompanied by high selectivities to Isoph which was formed from MO and acetone in a secondary aldol condensation process.
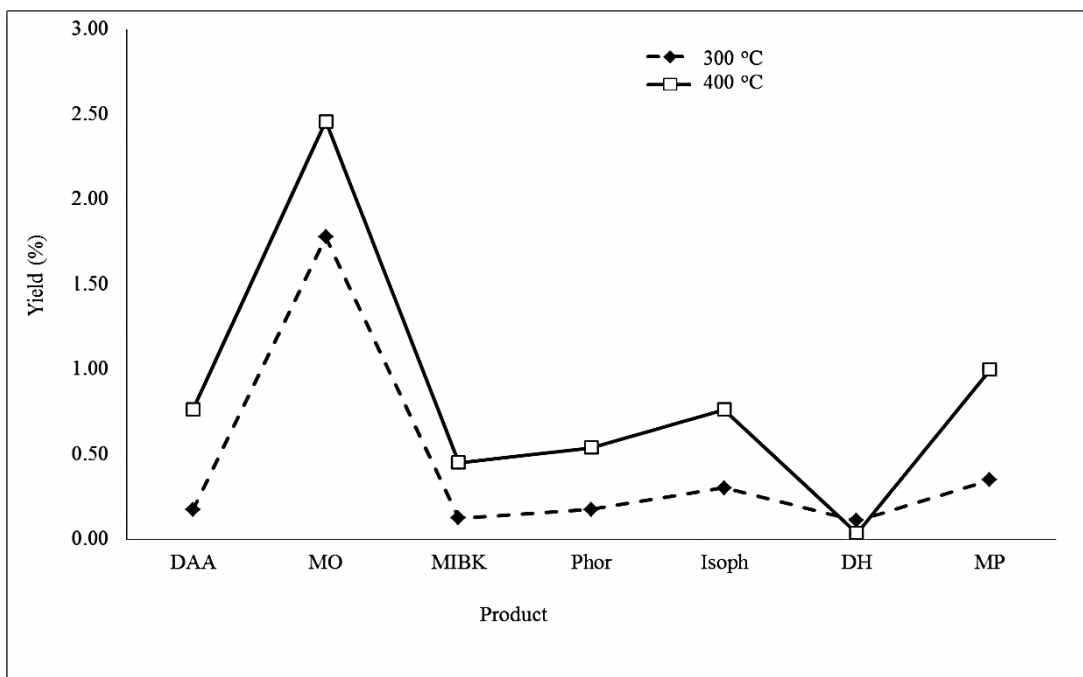
Fig. 4.22 Percentage yields of aldol condensation of acetone over ZrO_2 catalyst as a function of temperatures at 300 $^{\circ}$C, 400 $^{\circ}$C, 5 bar H_2 pressure, TOS > 18h.

The selectivity to all products except MO and DH was increased by increasing reaction temperature. A maximum selectivity of 59% for MO was obtained at 300 $^{\circ}$C which diminished to 41% by increasing reaction temperature to 400 $^{\circ}$C (Fig. 4.23). The production of MO was favoured via the dehydration of DAA. At higher conversion, the formation of high molecular weight compounds is significant. The catalyst also showed high selectivity toward 4-methyl-2-pentanol (MP) which is produced from hydrogenation of the MIBK.
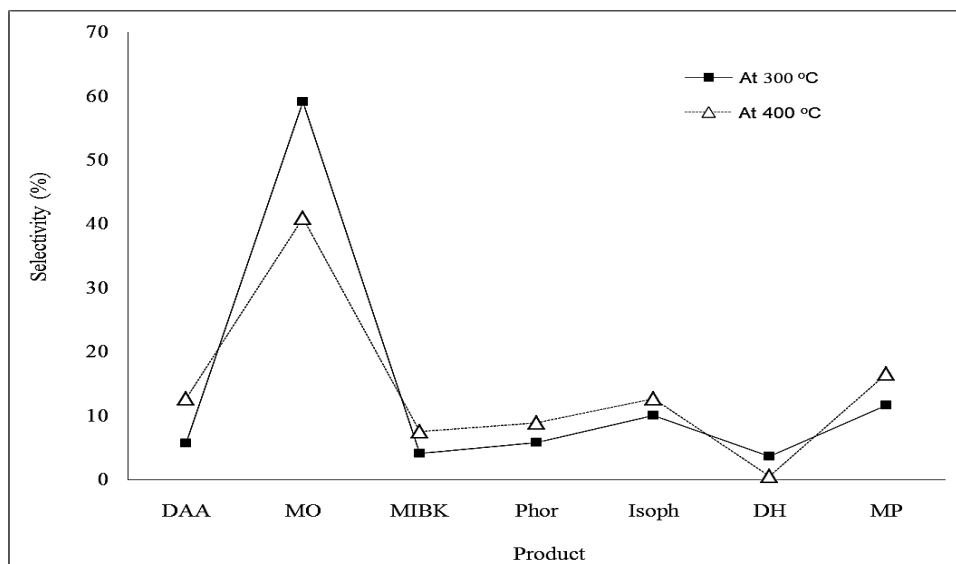
Fig. 4.23 Percentage selectivities of aldol condensation, after 18 h of the reaction time, over ZrO_2 catalyst at different temperatures (T = 300 ^{o}C, 400 ^{o}C, 5 bar H_2 pressure, TOS > 18 h).

4.2.2 KNO$_3$/ZrO$_2$.

The aldol condensation reaction of acetone has been studied over KNO_3/ZrO_2 materials with different loadings. XRD analysis has been undertaken.
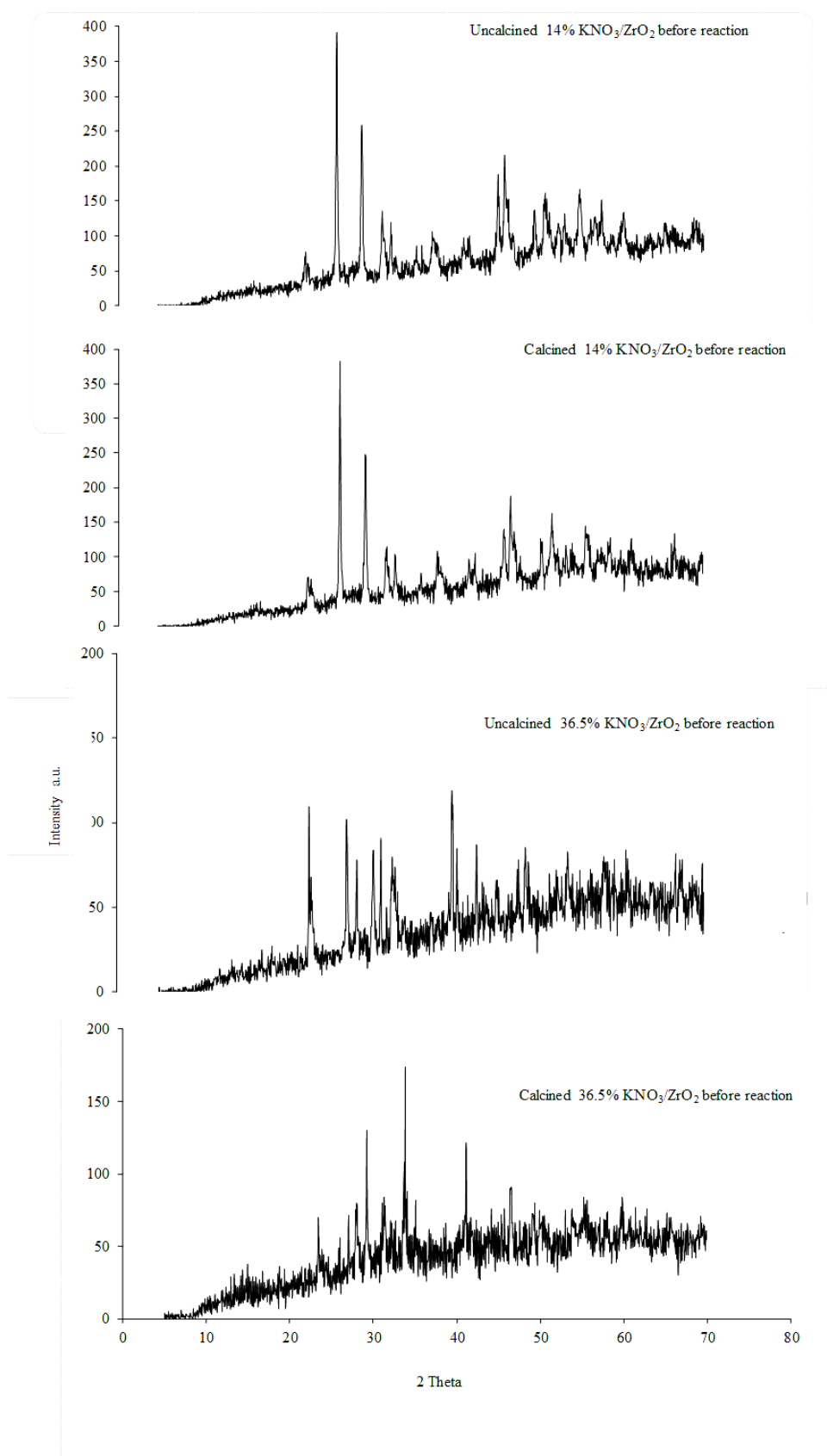
Fig. 4.24 X-ray diffractions pattern of KNO_3/ZrO_2 catalysts.

The XRD analysis (Fig. 4.24) reveals that the 5% KNO_3/ZrO_2 and 14% KNO_3/ZrO_2 patterns are similar to zirconia with peaks at $2\theta = 24.2^o$, 28.2^o, and 31.5^o characteristic of the monoclinic phase. The intensities of these peaks are relatively high and decline upon increasing the loaded amount of KNO_3, and by calcination. It is also found that the XRD peaks become gradually sharper with increasing temperature indicating a possible increase in crystal size.

The metastable tetragonal phase is also evident in these catalysts with characteristic reflections at $2\theta = 30.2^o$, 50.4^o, and 60.2^o although their intensity is weak compared to the monoclinic phase reflections.

When the loaded amount of KNO_3 on ZrO_2 is increased to 36.5% the overall intensities are reduced. The monoclinic phase is transformed to tetragonal. It is proposed that in this case the K^+ ions are incorporated in the vacant sites on the surface of zirconia and stabilise the tetragonal phase [84]. These XRD results are confirmed by calculation of the volume fraction of monoclinic phase from the XRD patterns as previously described. The 14% KNO_3/ZrO_2 catalyst contains 97.9% of monoclinic phase while for the 36.5% KNO_3/ZrO_2 catalyst it is only 69.4% which goes increases to 95.3% after calcination (Table 4.9). Loading KNO_3 on ZrO_2 below the spontaneous dispersion capacity such as in 5% KNO_3/ZrO_2 catalyst increases zirconia crystalline phases intensities. However, loading KNO_3 on ZrO_2 above the spontaneous capacity results in phase transformation and overall intensity reduction.

No additional phases such as K_2ZrO_3 were evident even for high loadings of KNO_3 Additional diffraction peaks were evident at 2θ values of 37°, 53°, 57°, and 62° related to K_2O. These peaks were clearly observed in the 14% KNO_3/ZrO_2 pattern which can be one of reasons for the high basicity and activity of this catalyst. The intensities of these peaks appeared to be reduced upon further calcination. On the other hand, the K_2O peaks were reduced and even disappeared in the 36.5% KNO_3/ZrO_2 patterns. These conclusions are in accordance with the literature [85].

Catalyst	Vm (%)
Calcined 14 % KNO_3/ZrO_2 before reaction	98.2
Calcined 36.5 % KNO_3/ZrO_2 before reaction	95.3
Uncalcined 14 % KNO_3/ZrO_2 before reaction	97.9
Uncalcined 36.5% KNO_3ZrO_2 before reaction	69.4

Table 4.9 Volume fractions (V_m) of monoclinic phase of KNO_3/ZrO_2 catalysts.

Catalyst	Surface area (m^2/g)
14% KNO_3/ZrO_2	8
36.5% KNO_3/ZrO_2	1

Table 4.10 BET surface areas of uncalcined 14% KNO_3/ZrO_2 and 36.5% KNO_3/ZrO_2 catalysts.

The 14% KNO_3/ZrO_2 catalyst has a larger surface area than the 36.5% KNO_3/ZrO_2 material as shown in Table 4.10. The exact reason for the decline in surface area with increased KNO_3 content is currently not clear, although it may relate to facilitated sintering and/or the presence of K_2O which covers the surface.
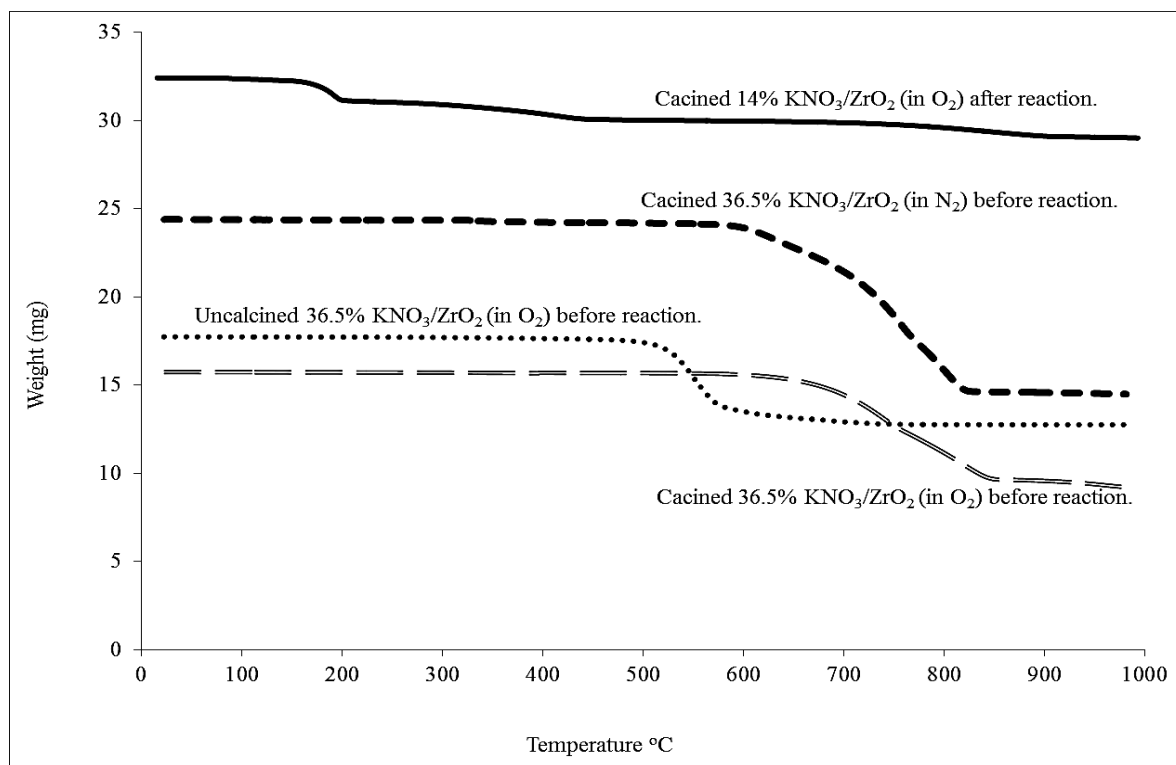
Fig. 4.25 Thermogravimetric analysis (TGA) of KNO_3/ZrO_2 catalysts.

TGA investigation (Fig. 4.25) of 14% KNO_3/ZrO_2, catalyst shows three weight losses. The earliest loss appears at 200 ^{o}C and may be attributed to the desorption of adsorbed water. The second loss at 420 ^{o}C could be associated with the formation of highly dispersed K^+ species which are believed to be responsible for the "superbasicity" [86] by decomposition. The last peak at 780 ^{o}C relates to the decomposition of bulk KNO_3 which does not participate in the generation of "superbasicity". However, the 36.5% KNO_3 on ZrO_2 sample requires a higher temperature for decomposition to occur. The conclusion therefore is that the decomposition of the 14% loaded of KNO_3 on ZrO_2 is more favourable than the 36.5% sample. Considering this result, it can be reported that the decomposition of KNO_3 on ZrO_2 is inhibited by increasing the loaded amount of KNO_3. These TGA results suggest that the spontaneous dispersion capacity of KNO_3 over the zirconia support is close to 14% wt as discussed previously in this chapter. The TGA pattern of the uncalcined 36.5% KNO_3/ZrO_2 catalyst shows a curve at 530 ^{o}C which may relate to the decomposition of KNO_3. For the calcined 36.5% KNO_3/ZrO_2 catalyst, the curve is observed at relatively higher temperatures in the range between 600 - 700 ^{o}C.
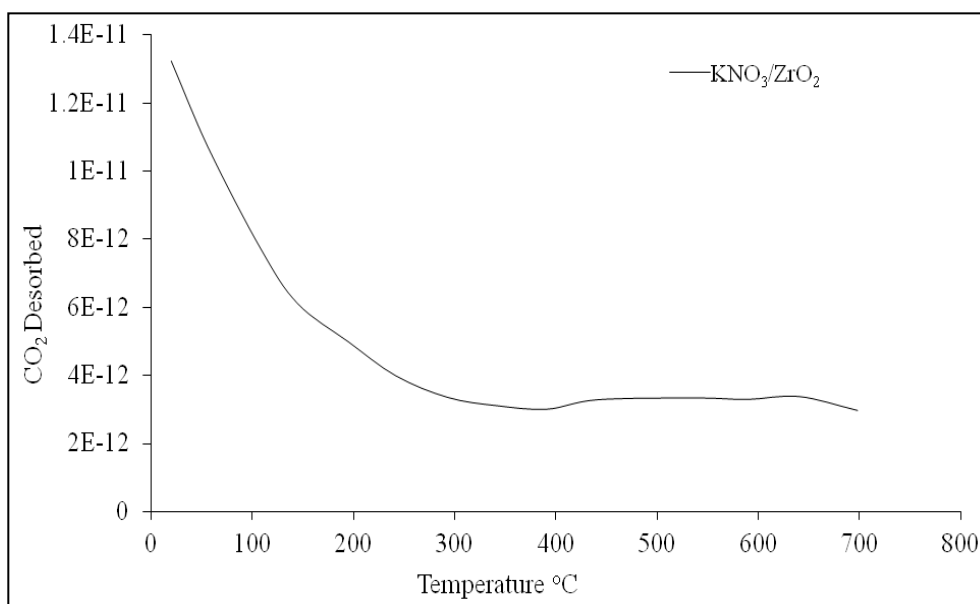
Fig. 4.26 CO_2 temperature programmed desorption (TPD) of uncalcined 36.5% KNO_3/ZrO_2 catalyst.

CO_2-TPD has been measured for the 36.5% KNO_3/ZrO_2 sample to determine its base site characteristics. There are three peaks observed at 200 ^{o}C, 410 ^{o}C, and 600 ^{o}C representing

the basicity of the KNO_3/ZrO_2 catalyst (Fig. 4.26). The increase of basicity upon increasing temperature may due to the formation of the highly active compounds such as K_2O extra-fine particles on the surfaces of ZrO_2 at high temperature. Since the obvious increase of basicity, due to mentioned active species, has noticeably occurred at ca. 410 ^{o}C, this strongly suggests the decomposition of KNO_3. Such a CO_2-TPD result is consistent with what TGA revealed and both conclusions are in agreement with Wang et al's [66] observation as they documented that KNO_3 starts to thermally decompose in the range of 340 – 416 ^{o}C after being supported on ZrO_2. Loading KNO_3 on ZrO_2 may produce strong basicity after activation at 410 ^{o}C.

a)   b)
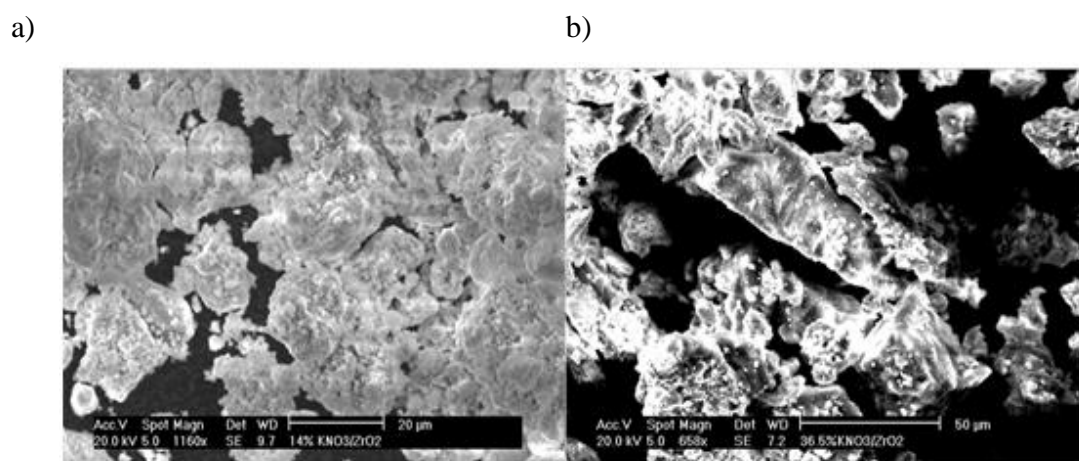
Fig. 4.27 Scanning electron microscopy (SEM) images of (a) 14% KNO_3/ZrO_2, and (b) 36.5% KNO_3/ZrO_2 catalysts.

The SEM images showed that the 14% loaded sample had a smaller particle size compared to the 36.5% loaded sample (Fig. 4.27) which resulted a much higher surface area (Table 4.10).

The catalytic behaviour of the KNO_3 loaded samples has been investigated and the influence of KNO_3 loadings determined. The 14% KNO_3/ZrO_2 catalyst gave yields and conversions higher than the 36.5% KNO_3/ZrO_2 catalyst. This result is consistent with Wang et al's results for the decomposition of 2-propanol at 400 ^{o}C, where they reported the highest yield was obtained with a 14% KNO_3/ZrO_2 catalyst [66]. This was interpreted in terms of the spontaneous dispersion capacity as discussed previously. It is also important

to take account of the higher surface area of the 14% sample which was 8 m^2/g whereas the 36.5% KNO_3/ZrO_2 catalyst exhibited only 1 m^2/g (Table 4.10).

The higher KNO_3 loading of 36.5 wt% (Fig. 4.28) presented a rate of acetone conversion of 11.81 x 10^{-3} mol m^{-2} h^{-1} after 18 h of reaction although just an hour later it appeared to be 0.56 x 10^{-3} mol m^{-2} h^{-1}. However, after the loaded of KNO_3 was reduced to 14 wt%, the rate was only 0.13 x 10^{-3} mol m^{-2} h^{-1} which was gradually and slightly increased during the following hours.

A conversion of 1% was achieved which then increased to a maximum of 7% over the 14% KNO_3/ZrO_2 (Table 4.11) and the highest selectivity was for MO which was 62.13%. However, the 36.5% KNO_3/ZrO_2 catalyst achieved 6% maximum conversion, which then gradually diminished, with MO selectivity of 38.03%. Furthermore, the 36.5% KNO_3/ZrO_2 catalyst deactivated more rapidly than its 14% KNO_3/ZrO_2 counterpart. The high loading of 36.5% KNO_3 on ZrO_2 catalyst covers the basic sites on the surface of the composite and decreases conversion. Conversion of the 14% loaded catalyst as a function of time on stream and starts from a very low value and suddenly goes up to reach its maximum value which is followed by a sharp decrease after 19 h due to catalyst deactivation (Fig. 4.28). This catalyst's tendency towards deactivation is probably caused by coke formation which reduces the reaction rate [87]. Both catalysts become stable after about 20 h on stream and remain relatively inactive until the end of the reaction.

Catalyst	Conversion (%)	Selectivity (%)						
		DAA	MO	MIBK	Phor	Isoph	DH	MP
14% KNO_3/ZrO_2	6	5.88	62.13	4.15	6.13	15.17	0.78	5.77
36.5% KNO_3/ZrO_2	1	13.01	38.03	8.27	8.73	16.94	0.15	14.88

Table 4.11 Percentage conversion of aldol condensation of acetone over 14% KNO_3/ZrO_2 and 36.5% KNO_3/ZrO_2 materials at 400 ^{o}C and 5 bar H_2 pressure, TOS > 18 h.
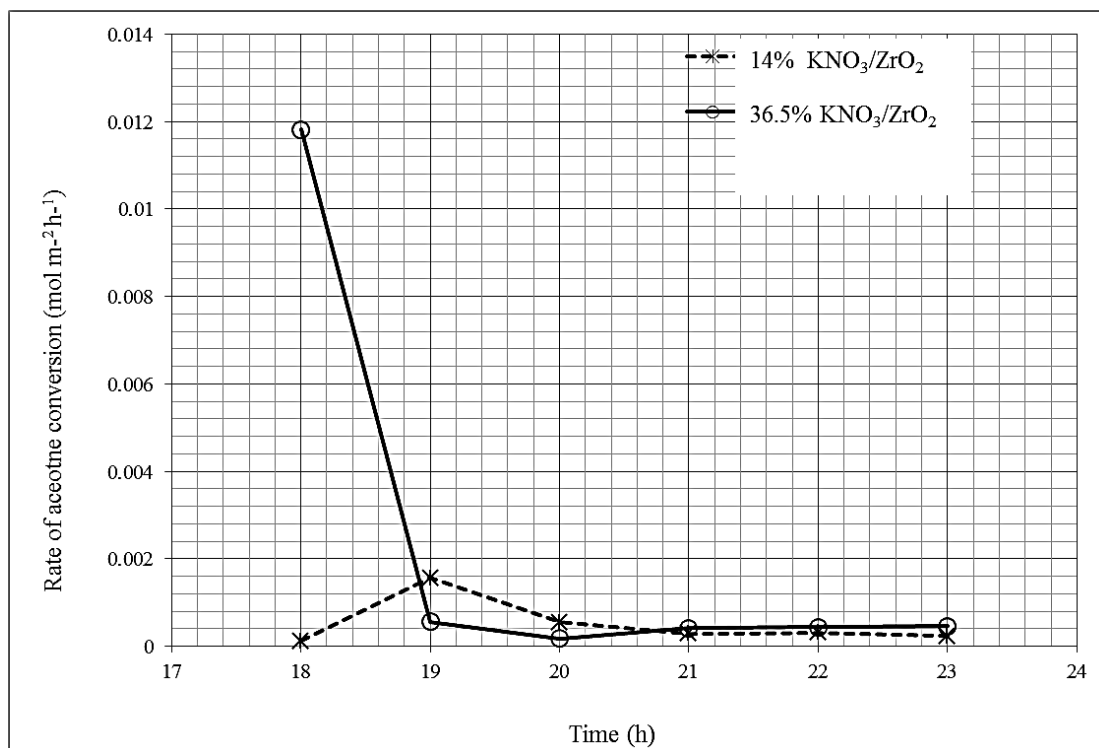
Fig. 4.28 Surface area normalised acetone conversions, after 18 h of the reaction time, over 14% KNO_3/ZrO_2 and 36.5% KNO_3/ZrO_2 catalysts at 400 ^{o}C and 5 bar H_2 pressure, TOS > 18 h.

The highest product yield is for the MO over both catalysts (Fig. 4.29). The MO yield over the 14% KNO_3/ZrO_2 catalyst is nearly twice as great as over 36.5% KNO_3/ZrO_2. Despite 14% KNO_3/ZrO_2 being the more active catalyst for the reaction, the 36.5% KNO_3/ZrO_2 shows higher yields of DAA and MP. Both catalysts exhibit small yields of Isoph.

Fig. 4.29 Percentage yields of aldol condensation of acetone, after 18 h of the reaction time, over 14% KNO_3/ZrO_2 and 36.5% KNO_3/ZrO_2 catalysts at 400 ^{o}C and 5 bar H_2 pressure, TOS > 18 h.

Both catalysts appeared to be selective toward the dehydration of DAA and thus the formation of MO. The MO selectivity over the 14 wt% KNO_3 catalyst was much larger than that over the 36.5 wt% sample.

Production of MP via the hydrogenation of the MIBK was slightly more favourable over 36.5% KNO_3/ZrO_2 catalyst compared with 14% KNO_3/ZrO_2. The production of Phor from the aldol condensation of MO occurred to a reasonable degree of selectivity (Fig. 4.30).

Fig. 4.30 Percentage selectivities of aldol condensation of acetone, after 18 h of the reaction time, over 14% KNO_3/ZrO_2 and 36.5% KNO_3/ZrO_2 catalysts at 400 ^oC and 5 bar H_2 pressure, TOS > 18 h.

4.2.3 $KNO_3/Zr(OH)_4$.

Since there may be residual OH group activity within materials, it was of interest to determine the behaviour of the non-calcined $KNO_3/Zr(OH)_4$ precursor materials, in addition to those produced following calcination.

Catalyst	Surface area (m^2g^{-1})
14% $KNO_3/Zr(OH)_4$	7
36.5% $KNO_3/Zr(OH)_4$	2

Table 4.12 BET surface areas of uncalcined 14% $KNO_3/Zr(OH)_4$, and 36.5% $KNO_3/Zr(OH)_4$ catalysts.

The 14% $KNO_3/Zr(OH)_4$ catalyst exhibited surface area of 7 m^2/g which diminished to 2 m^2/g as the loaded amount of KNO_3 increased to 36.5% (Table 4.12). Based on this result, it can be observed that the increased amount of KNO_3 on $Zr(OH)_4$ reduces surface area of the material.
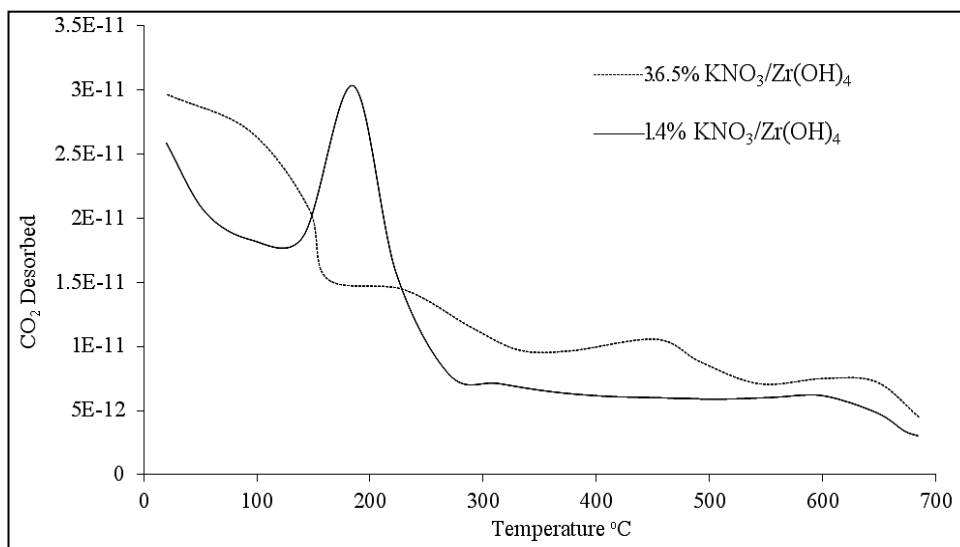
Fig. 4.31 CO_2 temperature programmed desorption (TPD) of 14% $KNO_3/Zr(OH)_4$ and 36.5% $KNO_3/Zr(OH)_4$ catalysts.

CO_2 TPD experiments were performed to determine the base site characteristics of the samples. The CO_2-TPD curve of the 14% $KNO_3/Zr(OH)_4$ catalyst was characterised by a large peak observed at 200 ^{o}C indicating the basicity of the catalyst, a second peak is detected at 315 ^{o}C followed by a further final peak at 600 ^{o}C whereas the 36.5% $KNO_3/Zr(OH)_4$ catalyst has four desorption peaks at 95 ^{o}C, 230 ^{o}C, 420 ^{o}C and 630 ^{o}C representing the basicity of this catalyst (Fig. 4.31). The result suggests that the 14% $KNO_3/Zr(OH)_4$ catalyst has a higher number of weak base sites than the 36.5% sample. The difference in the desorption patterns with respect to the calcined KNO_3/ZrO_2 samples (as shown in Fig. 4.26) is striking. CO_2 desorption at higher temperatures could be attributed to strong basic sites formed by K_2O extra-fine particles on the surface of ZrO_2 during decomposition. This has been reported by Zhu et al [68]. In the following work, $KNO_3/Zr(OH)_4$ catalysts were calcined prior to application, unlike in the previous section where materials were prepared by dispersion of KNO_3 upon pre-produced ZrO_2 following by calcination.
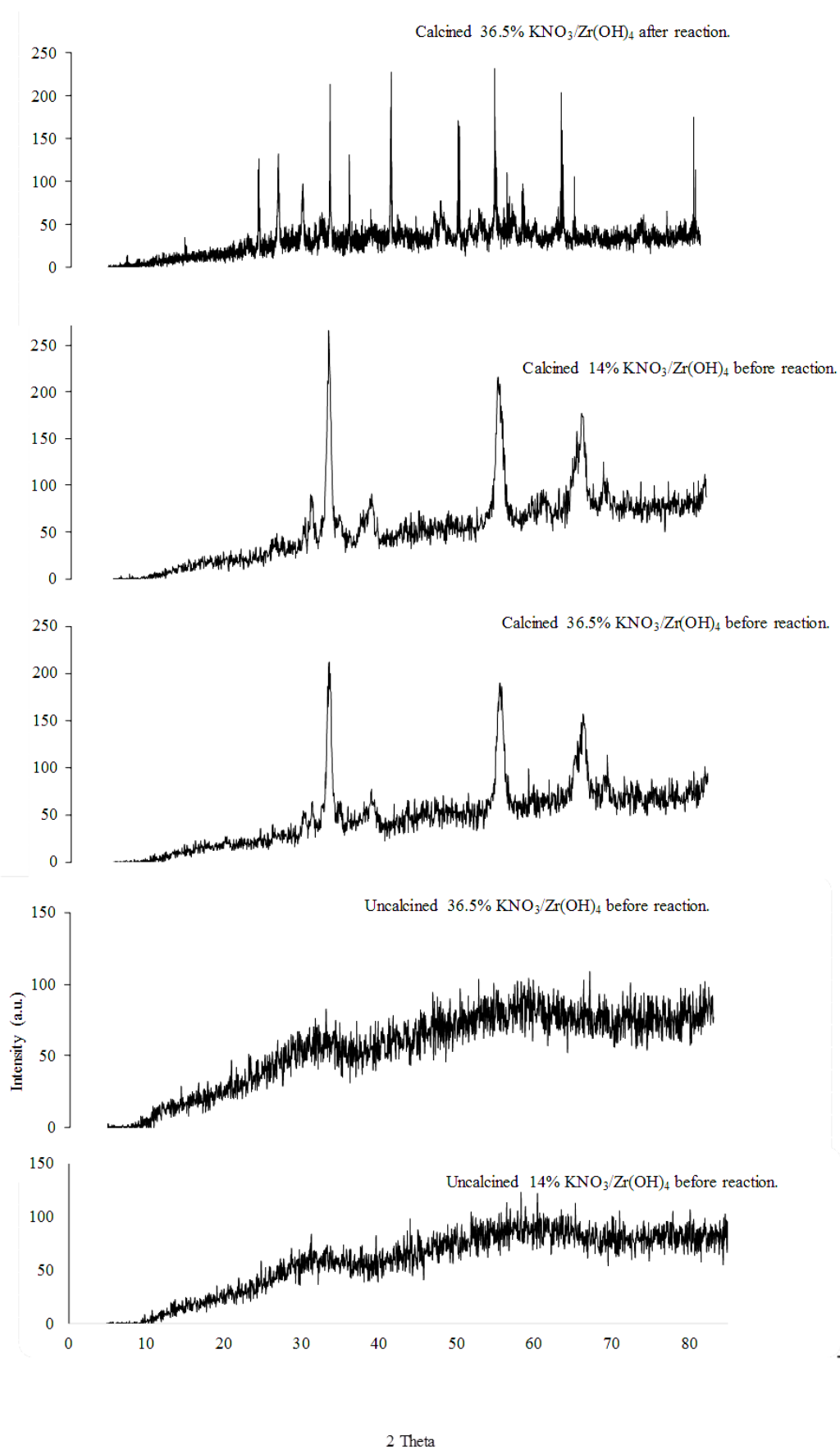
Fig. 4.32 X-ray diffraction patterns of $KNO_3/Zr(OH)_4$ catalysts.

The XRD patterns for various $KNO_3/Zr(OH)_4$ catalysts demonstrated that the main ZrO_2 phase is tetragonal for the all calcined samples as indicated by peaks at $2\theta = 30.2^o$, 50.4^o, and 60.2^o. However, the 14 wt% loaded amount of KNO_3 showed the monoclinic phase with weak intensity with characteristic reflections at $2\theta = 24.2^o$, 28.2^o, and 31.5^o (Fig. 4.32). The reflection intensities of the calcined 14% $KNO_3/Zr(OH)_4$ catalyst were stronger than those of the calcined 36.5% $KNO_3/Zr(OH)_4$. Further diffraction peaks appeared at 2θ values of 37°, 53°, 57°, and 62° in the same patterns which can be attributed to the active K_2O compounds which believed to be the responsible for the "superbase" catalytic activity enhancement. These active species were clearly present on the pattern of the post-reaction sample of 36.5% $KNO_3/Zr(OH)_4$ catalyst. New peaks emerged at $2\theta = 44^o$, 65°, 71°, and 84° of the post-reaction catalyst demonstrated that additional phase transformation occurred upon reaction.

The monoclinic phase volume fraction has been determined for the materials using the procedure detailed earlier.

Catalyst	Vm (%)
Calcined 14% $KNO_3/Zr(OH)_4$ before reaction	30.4
Calcined 36.5% $KNO_3/Zr(OH)_4$ before reaction	27.3
Calcined 14% $KNO_3/Zr(OH)_4$ after reaction	16.3

Table 4.13 Volume fraction (V_m) of monoclinic phase of the various $KNO_3/Zr(OH)_4$ materials.

The calcined 14% $KNO_3/Zr(OH)_4$ material contains 30.4% monoclinic phase which reduces to 16.3% for the post-reaction sample confirming it to be a metastable phase.
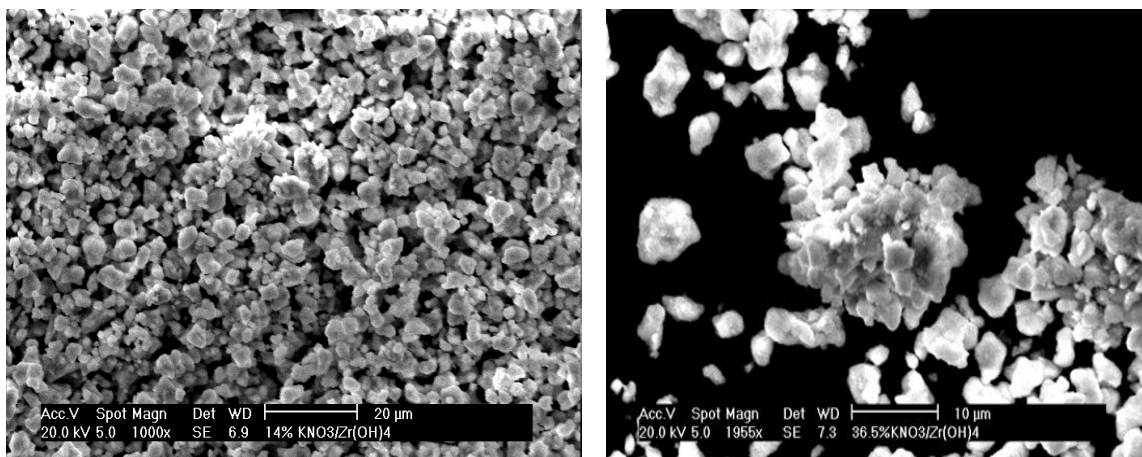
Fig. 4.33 Scanning electron microscope image of 14% $KNO_3/Zr(OH)_4$ and 36.5% $KNO_3/Zr(OH)_4$

Figure. 4.33 shows the SEM images for the 14 wt% and 36.5 wt% catalysts. A larger particle size of the 36.5 wt% was clearly observed which is results in a smaller surface area compared to the lower loaded amount (Table 4.12).

The aldol condensation reaction of acetone was investigated over calcined 14% $KNO_3/Zr(OH)_4$ and 36.5% $KNO_3/Zr(OH)_4$ catalysts at 400 ^{o}C reaction temperature and 5 bar pressure. Conversions (Fig. 4.34), yields (Fig. 4.35), and selectivities (Fig. 4.36) have been calculated and are discussed individually.
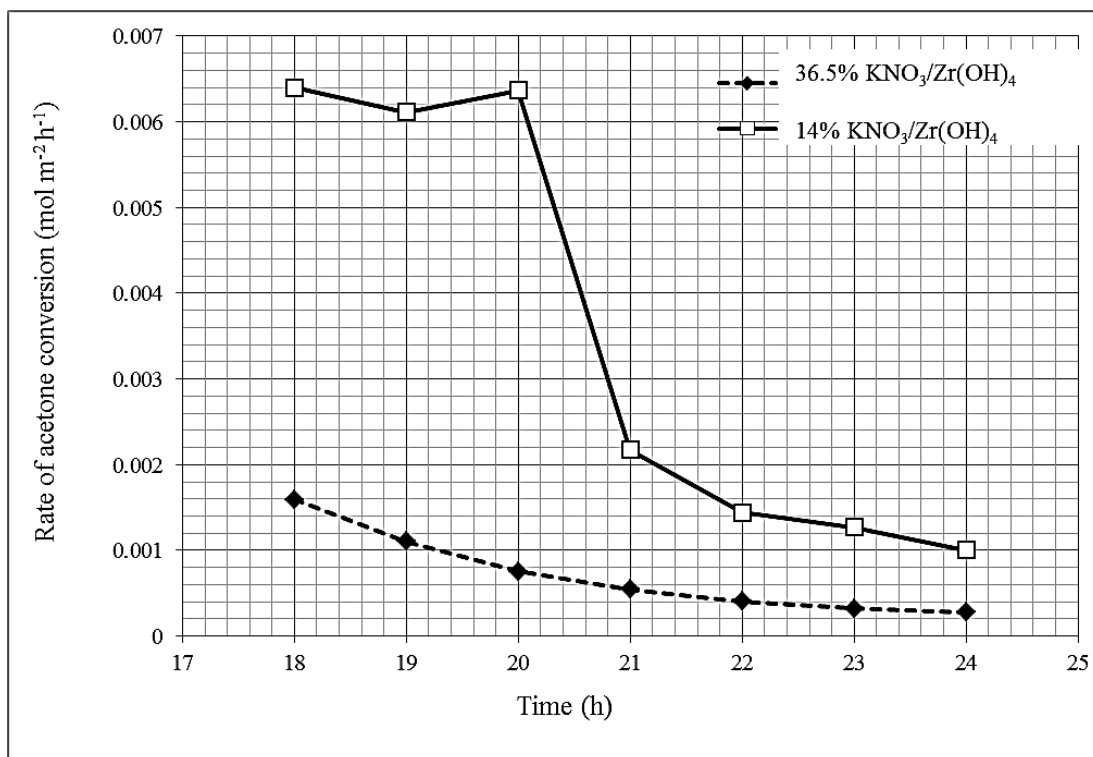
Fig. 4.34 Surface area normalised acetone conversions over 14% KNO$_3$/Zr(OH)$_4$ and 36.5% KNO$_3$/Zr(OH)$_4$ catalysts at 400 ^{o}C, 5 bar H$_2$ pressure, TOS > 18 h.

At first, both catalysts show relatively high catalytic activities followed by a decrease with time on stream.

A substantial difference was observed between the rates of acetone conversions over the two catalysts (Fig. 4.34). Acetone was converted at a rate almost four times higher over the 14 wt% catalyst with a rate of 6.39 x 10^{-3} mol m^{-2} h^{-1} compared to 1.60 x 10^{-3} mol m^{-2} h^{-1} achieved by the 36.5 wt% catalyst.

The 14% KNO$_3$/Zr(OH)$_4$ catalyst achieved almost 7% conversion, which is slightly greater than the 6% for the 36.5% KNO$_3$/Zr(OH)$_4$ catalyst (Fig. 4.34). This conversion result is in agreement with Wang et al's result for the decomposition of 2-propanol over KNO$_3$/ZrO$_2$ catalyst under similar conditions as they reported that the catalyst with 14 wt% loaded amount of KNO$_3$ on ZrO$_2$ was the optimal catalyst for that reaction [66] A similar trend was evident for the KNO$_3$/ZrO$_2$ catalyst, discussed previously in this chapter, which may be due to the decomposition of Zr(OH)$_4$ to ZrO$_2$ during heating. As tetragonal zirconia was the main phase observed in the diffraction pattern of the 14 wt% catalyst (Fig. 4.32), it is believed to be the active phase for the reaction.

Catalyst	Conversion (%)	Selectivity (%)						
		DAA	MO	MIBK	Phor	Isoph	DH	MP
14% KNO$_3$/Zr(OH)$_4$	7	6.15	39.21	4.06	5.32	35.48	0.48	9.30
36.5% KNO$_3$/Zr(OH)$_4$	6	6.88	43.71	5.25	5.52	27.82	0.22	10.61

Table 4.14 Percentage conversion and selectivities of aldol condensation of acetone, after 18 h of the reaction, over 14% KNO$_3$/Zr(OH)$_4$ and 36.5% KNO$_3$/Zr(OH)$_4$ materials at 400 ^{o}C and 5 bar H$_2$ pressure, TOS > 18 h.
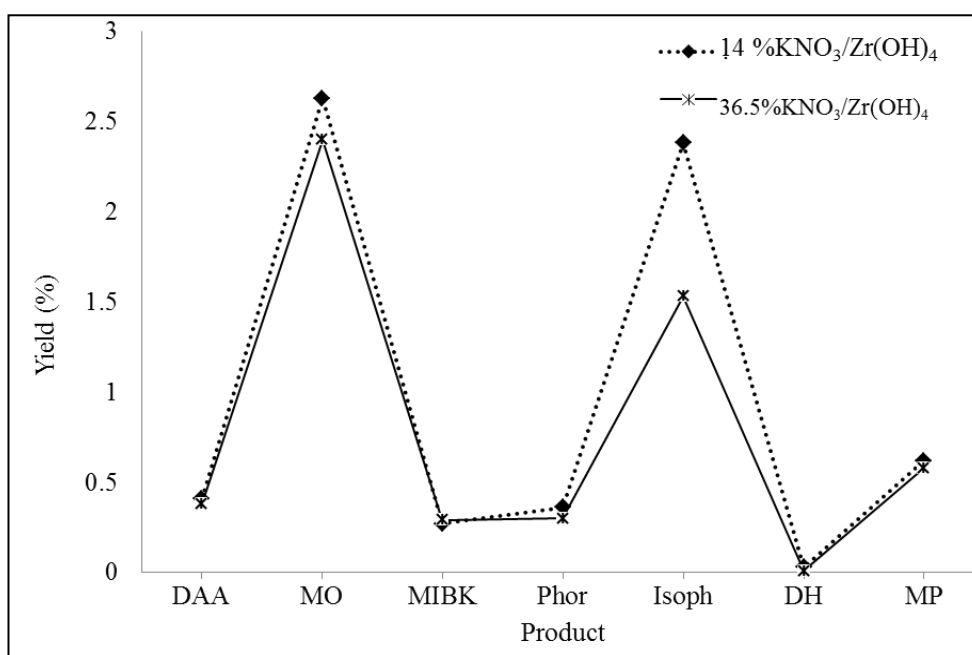
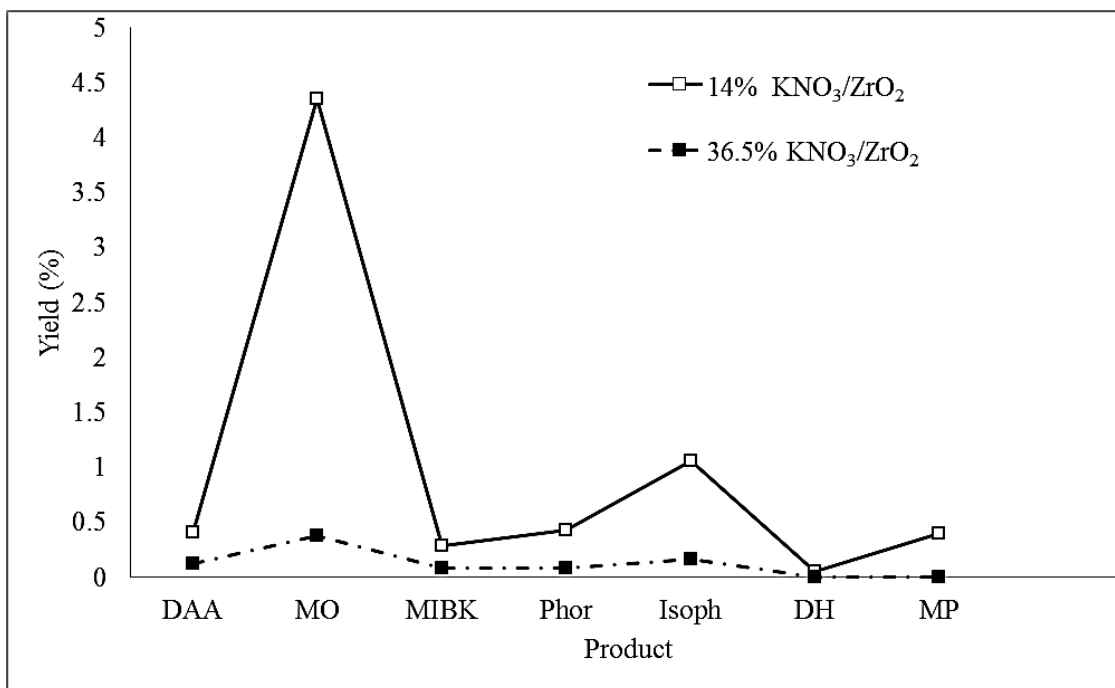Fig. 4.35 Percentage yields of aldol condensation of acetone, after 18 h of the reaction time, over 14% KNO$_3$/Zr(OH)$_4$ and 36.5% KNO$_3$/Zr(OH)$_4$ catalysts at 400 ^{o}C, 5 bar H$_2$ pressure, TOS > 18 h.

Yields of 2.63% and 2.40% have been produced for MO over the 14% and 36.5% KNO$_3$/Zr(OH)$_4$ materials respectively (Fig. 4.35) revealing little difference between the catalysts. Production of MP was apparent over both catalysts.
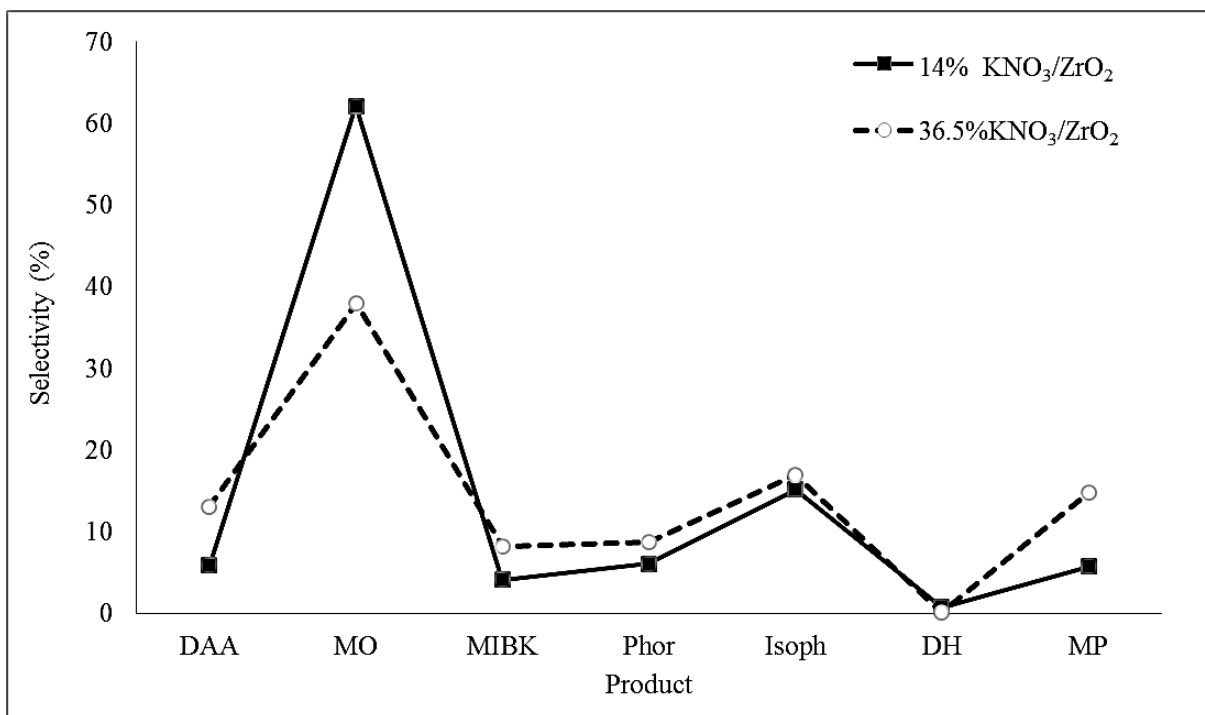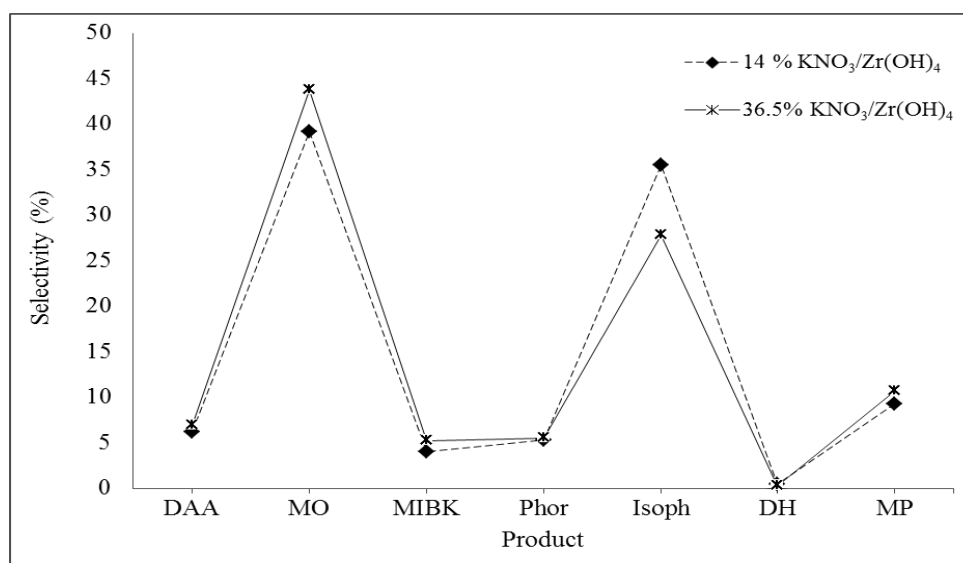
Fig. 4.36 Percentage selectivities of aldol condensation of acetone, after 18 h of the reaction time, over 14% KNO$_3$/Zr(OH)$_4$ and 36.5% KNO$_3$/Zr(OH)$_4$ catalysts at 400 $^{\circ}$C, 5 bar H$_2$ pressure, TOS > 18 h.

In spite of maximal selectivities being attained for the MO by both catalysts, the 36.5% KNO$_3$/Zr(OH)$_4$ was slightly more selective toward MO with 43.71% selectivity compared to the 14% KNO$_3$/Zr(OH)$_4$ catalyst which showed only 39.21% selectivity (Fig. 4.36). Isoph was also a major product over both of catalysts with selectivity of 35.48% over the 14% KNO$_3$/Zr(OH)$_4$ sample and 27.82% of selectivity for the 36.5% KNO$_3$/Zr(OH)$_4$. Production of MIBK did not occur due to the absence of a hydrogenation function.

4.2.4 Y-Zr(OH)$_4$.

Basicity can also be imparted by the presence of Y$_2$O$_3$ in ZrO$_2$. Accordingly, in this thesis the aldol condensation reaction of acetone was investigated over a calcined Y-Zr(OH)$_4$ catalyst at 400 $^{\circ}$C and 5 bar pressure.
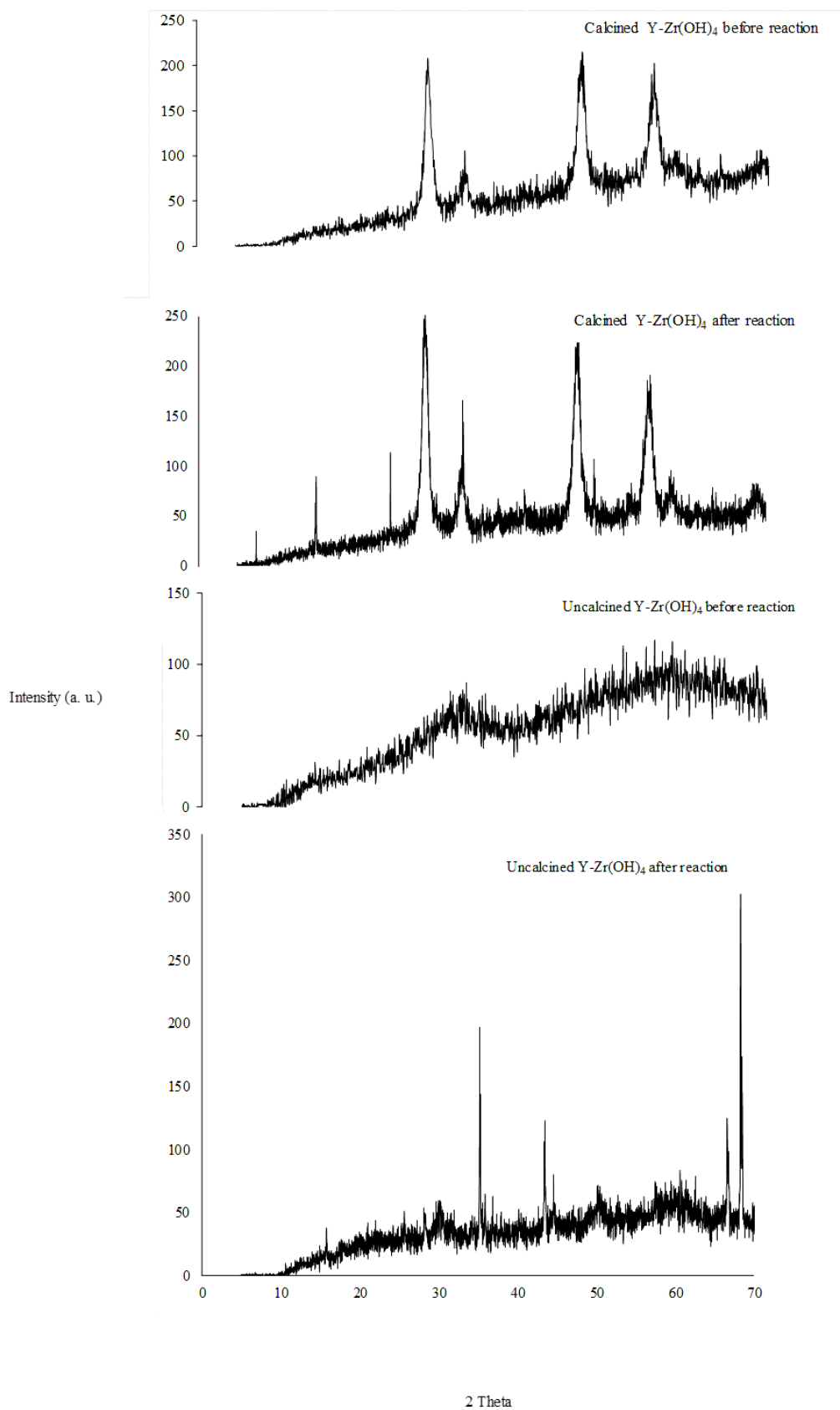
Fig. 4.37 X-ray diffraction patterns of Y-Zr(OH)₄ materials.

As for other materials investigated, XRD analysis has been undertaken. The XRD pattern of the calcined Y-Zr(OH)$_4$ showed high intensity peaks at $2\theta = 30.2$ ^{o}, 50.4 ^{o}, and 60.2 ^{o} attributed to the tetragonal phase of zirconia (Fig. 4.37). The monoclinic phase was also observed in the all samples in variable amounts (Table 4.15) at $2\theta = 24.2$ ^{o}, 28.2 ^{o} and 31.5 ^{o}. In the post-reaction Y-Zr(OH)$_4$ sample, intensities of these peaks were clearly enhanced. This result indicated that tetragonal zirconia was the main phase in the Y-Zr(OH)$_4$ catalyst and its intensity was increased by calcination. Since peaks of tetragonal phase remained in highest intensity after reaction, this demonstrates that the tetragonal phase was substantially stabilised by the yttrium dopant for the calcined samples. The monoclinic volume fraction was calculated as described previously and the results are presented in Table 4.15.

Catalyst	Vm (%)
Calcined Y-Zr(OH)$_4$ before reaction	22.3
Uncalcined Y-Zr(OH)$_4$ after reaction	61.5
Calcined Y-Zr(OH)$_4$ after reaction	19.1

Table 4.15 Volume fractions (V_m) of monoclinic phases of Y-Zr(OH)$_4$.

The BET surface area of the doped material was determined and the result is shown in Table 4.16. This area is very high which is consistent with the high fraction of tetragonal phase (associated with small crystallite size) and the broad reflections evident in the powder diffraction patterns.

Catalyst	Surface area (m^2/g)
Y-Zr(OH)$_4$	108

Table 4.16 BET surface area of Y-Zr(OH)$_4$ catalyst.
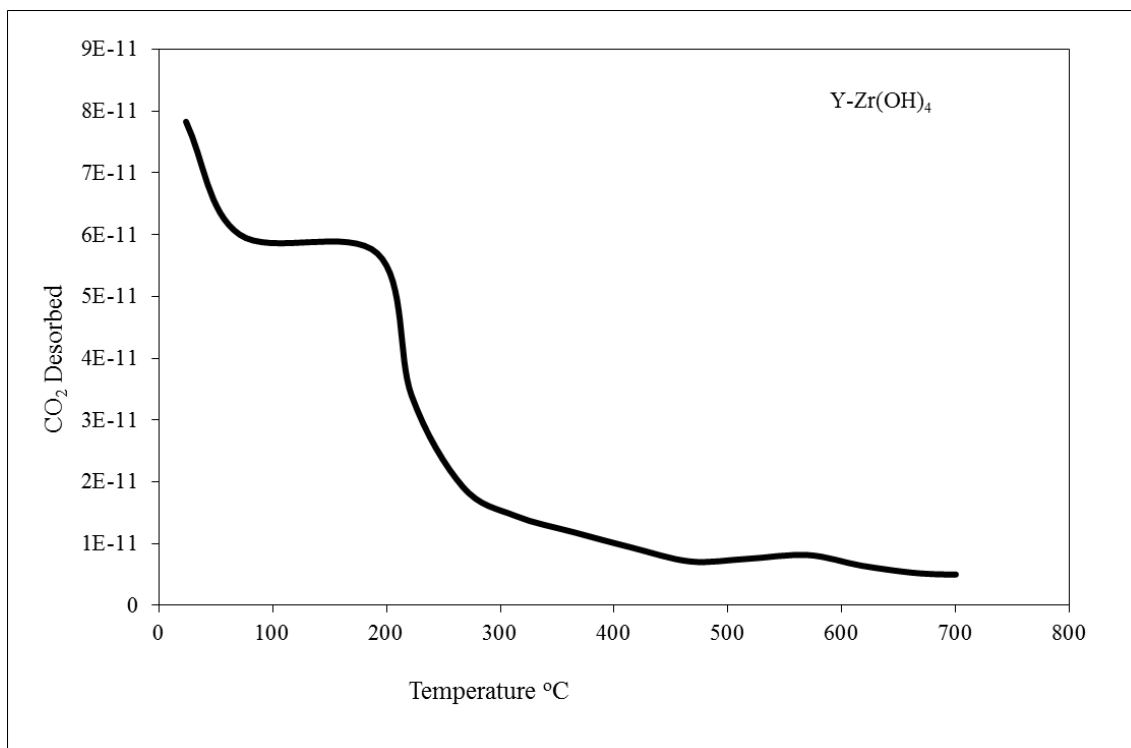
Fig. 4.38 CO_2 temperature programmed desorption (TPD) pattern of calcined Y-Zr(OH)$_4$ catalyst.

The CO_2-TPD was performed to determine the base site characteristic of the calcined Y-Zr(OH)$_4$ material.

The CO_2-TPD pattern at shows desorption peaks at 190 ^{o}C, 300 ^{o}C and 500 ^{o}C confirming the basicity of the catalyst (Fig. 4.38). Same peaks were detected in the CO_2-TPD curve of calcined ZrO_2 but in lower qualities. This result may indicate that yttria dopant promotes zirconia basicity.

Catalyst	C	H	N
Y-Zr(OH)$_4$	2.16/2.46	0.2	-

Table 4.17 CHN analysis of post-reaction Y-Zr(OH)$_4$ catalyst.

The CHN analysis for the post-reaction sample showed carbon and hydrogen were introduced to the sample with amounts of 2.16/2.46% and 0.2% respectively. These amounts of carbon and hydrogen were likely produced during the reaction via the adsorption of the hydrocarbon compounds onto the surface of the catalyst (Table 4.17).

Based on this result, it can be said that aldol condensation reaction of acetone was significant over Y-Zr(OH)$_4$ catalyst.

Catalytic activity data for the yttria stabilised catalyst is shown in Figure 4.41.

Catalyst	Conversion (%)	Selectivity (%)						
		DAA	MO	MIBK	Phor	Isoph	DH	MP
Y-Zr(OH)$_4$	8	6.42	26.29	5.14	3.84	33.79	18.47	6.06

Table 4.18 Conversions and selectivites of aldol condensation of acetone over Y-Zr(OH)$_4$ catalyst at 400 ^{o}C, 5 bar H$_2$ pressure, TOS > 18 h.

Acetone conversion occurred over Y-Zr(OH)$_4$ catalyst with a rate of 0.13 x 10^{-3} mol m^{-2} h^{-1} (Fig. 4.39), corresponding to a conversion of 8%. Initially, the catalyst had higher activity than the other ZrO$_2$ based materials due to the effect of dopant, and to the stabilisation of the active tetragonal phase and resulting high surface area. Deactivation took place beyond 19 h of time on stream. Catalyst deactivation was caused by coke probably formed from the non-volatile organic compounds Phoro and Isoph. The deposition of coke was determined by the CHN analysis data shown in Table 4.17. As the Isoph was produced in a large amount, the deactivation therefore expected to be significant.
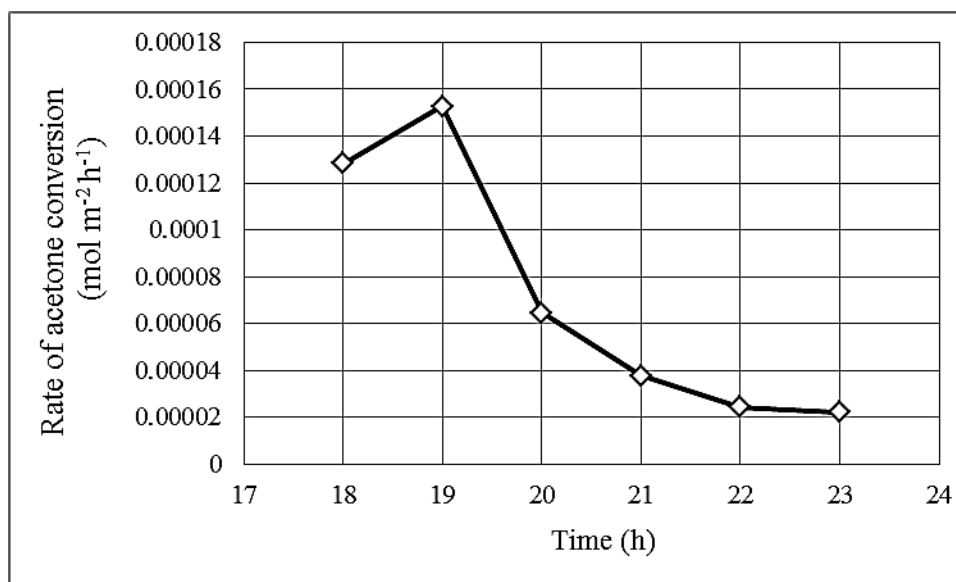
Fig. 4.39 Surface area normalised acetone conversions over Y-Zr(OH)$_4$ catalyst at 400 ^{o}C, 5 bar H$_2$ pressure, TOS > 18 h.

The main product was Isoph followed by MO, which is similar to Di Cosimo et al's work for the same reaction over Li-MgO catalyst (Fig 4.40) [88]. According to those workers,

the formation of Isoph was produced directly from Phor by an internal 1, 6-Michael addition. Stevens et al also observed that Isoph and MO were the major products in their study of the same reaction over Cs/NPC [19]. Since the production of Isoph requires very strong base sites, this indicates the high basicity of the Y-Zr(OH)$_4$ catalyst.
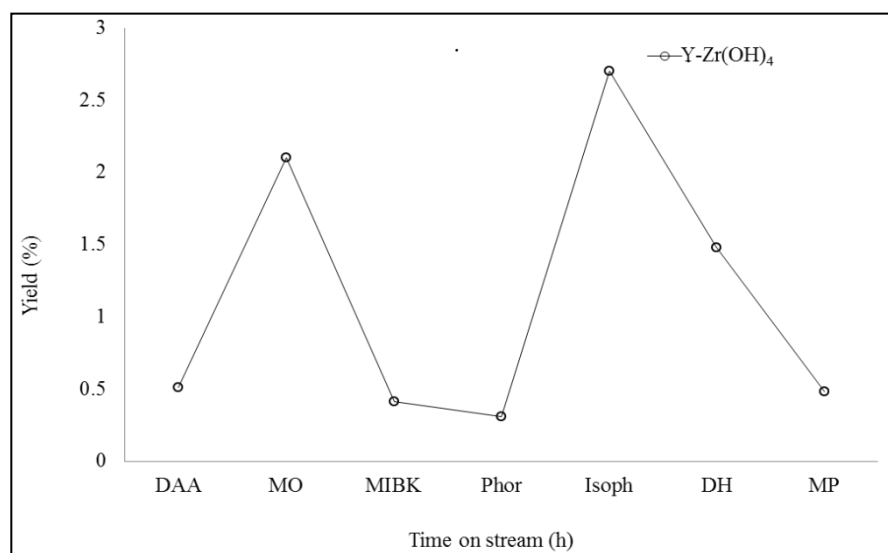
Fig. 4.40 Percentage yields of aldol condensation of acetone over Y- Zr(OH)$_4$ catalyst at 400 ^{o}C, 5 bar H$_2$ pressure, TOS > 18 h.
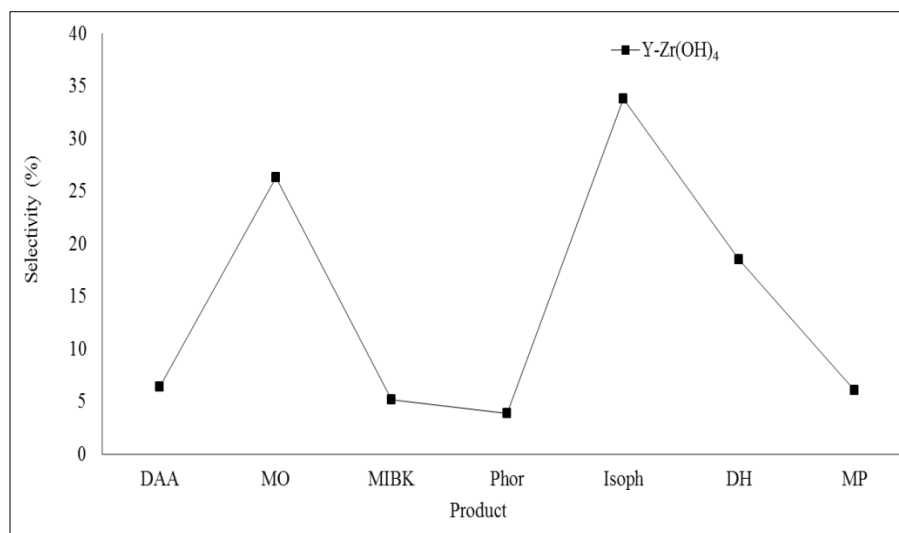
Fig. 4.41 Percentage selectivities of aldol condensation of acetone over Y-Zr(OH)$_4$ catalyst at 400 ^{o}C, 5 bar H$_2$ pressure, TOS > 18 h.

The catalyst was highly selective toward Isoph with 33.79%, MO with 26.29%, and for DH with 18.47%. In contrast, the lowest selectivity was observed for Phor and MIBK

respectively (Fig. 4.41). Based on this result, it can be reported that Y-Zr(OH)$_4$ catalyst promotes formation of heavier product in the aldol condensation reaction of acetone. The activity of this material is greater than that for all the other catalysts described in this chapter. In part this relates to the much higher surface area but the product distribution also suggests modified basicity.

4.3 Conclusion.

Comparative data for the various materials investgated in this chapter are shown below.
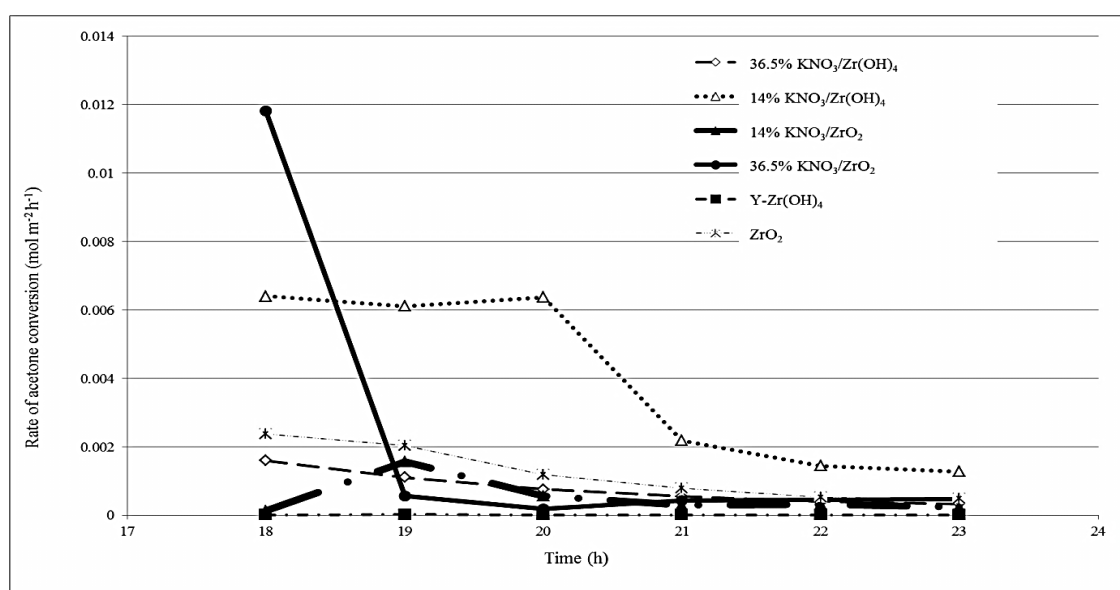
Fig. 4.42 Comparisons of catalytic activities of various zirconia catalysts, that were used in this thesis, on the aldol condensation reaction of acetone at 400 ^{o}C, 5 bar H$_2$, TOS > 18 h.

Catalyst	Conversion (%)	Rate of conversion (mol m^{-2}h^{-1})	Selectivity (%)							Surface area (m^2/g)	V$_m$(%)
			DAA	MO	MIBK	Phor	Isoph	DH	MP		
14% KNO$_3$/Zr(OH)$_4$	7	6.40E-03	6.15	39.21	4.06	5.32	35.48	0.48	9.30	2	16.30
36.5% KNO$_3$/Zr(OH)$_4$	6	1.60E-03	6.88	43.71	5.25	5.52	27.82	0.22	10.61	7	27.30
ZrO$_2$	6	2.37E-03	12.70	40.95	7.50	8.97	12.70	0.60	16.61	5	96.00
Y-Zr(OH)$_4$	8	1.19E-06	6.42	26.29	5.14	3.84	33.79	18.47	6.06	108	19.10
14% KNO$_3$/ZrO$_2$	7	1.25E-04	5.88	62.13	4.15	6.13	15.17	0.78	5.77	8	98.00
36.5% KNO$_3$/ZrO$_2$	1	1.18E-02	13.01	38.03	8.27	8.73	16.94	0.15	14.88	1	95.30

Table 4.19 Illustration of catalytic activity, surface area and volume fraction of monoclinic zirconia of different zirconia catalysts used in this thesis to catalyse the aldol condensation reaction of acetone at 400 ^{o}C, 5bar H$_2$ pressure, TOS > 18 h.

From Figure. 4.42 and Table 4.19 several significant points could be concluded:

- Utilisation of zirconia either as catalyst or as a catalytic support can catalyse the aldol condensation reaction of acetone.

- 14 wt% loaded KNO_3 on ZrO_2 was more active than the 36.5 wt% loading.

- Calcined KNO_3 supported on zirconia exhibited similar results to calcined KNO_3 supported on hydrous zirconia.

- The addition of 5 wt% and 14 wt% of KNO_3 to the support didn't apparently alter the structure of the support and high dispersions were achieved.

- KNO_3 decomposed at high temperatures to the highly active K_2O species which were responsible for the catalytic activity.

- The addition of yttria dopant improved the catalytic activity of zirconia. This is, in part, associated with the stabilisation of a much higher surface area for this sample and hence the proportion of tetragonal phase. However, the product distribution also indicates modified basicity.

4.4 References.

[1] T. Yamaguchi, *Catal. Today,* **20,**199 (1994).

[2] B-Q Xu, J-M Wei, Y-T Yu, Y Li, J-L Li, and Q-M Zhu, *J. Phys. Chem.* **107**, 5203 (2003).

[3] E. H. Kisi, and C. J. Howard, *Key Eng. Mater.* **153**, 1 (1998).

[4] O. Ruff, and F. Z. Ebert, *Anorg. Allgem. Chem.* **180**, 19 (1929).

[5] P. Murray, and E. B. Allison, *Trans. Brit. Ceram. Soc.* **53**, 335 (1954).

[6] C. T. Lynch, F. W. Bahldiek, and L. B. Robinson, *J. Am. Ceram. Soc.* **44**, 147 (1961).

[7] R. N. Patil, and E. C. Subba Rao, *Acta Crystallogr.* **26,** 555 (1970).

[8] H. S. Maiti, K. V. G. K. Gokhale, and E. C. Subba Rao, *J. Am. Ceram. Soc.* **55**, 317 (1972).

[9] A. H. Hueur, and M. Riihle, "Science and technology of zirconia", (Eds. N. Claussen, M. Riihle, and A. H. Hueur, *Am. Ceram. Soc.* ISBN 0916094642, 9780916094645 (1984).

[10] M. C. Muoz, S. Gallego, J. I. Beltr´an and J. Cerd´, *Surf. Sci. Rep.* 61 (2006).

[11] R. Suyama, T. Ashida, and S. Kume, *J. Am. Ceram. Soc.* **68**, 134 (1985).

[12] K. S. Mazdiyasni, C. T. Lynch, and J. S. Smith, *J. Am. Ceram. Soc.* **50**, 532 (1967).

[13] R. C. Garvie, R. H. J. Hannink, and R. T. Pascoe, *Ceram. Steel Natur.* **258**, 703 (1975).

[14] B. H. Davis, *J. Am. Ceram. Soc.* **67**, 168 (1984).

[15] R. Srinivasan, R.J. De Angelis, and B. H. Davis, *J. Mater. Res.* **1**, 583 (1986).

[16] R. Srinivasan, M. B. Harris, S. F. Simpson, R. J. De Angelis, and B. H. Davis, *J. Mater. Res.* **3**, 787 (1988).

[17] S. S. Jada, and N. G. Peletis, *J. Mater. Sci. Let.* **8**, 243 (1989).

[18] G. T. Mamott, P. Barnes, S. E. Tarling, S. L. Jones, and C. J. Norman, *Powder Diff.* **3**, 234 (1988.

[19] R. Stevens, "Zirconia and zirconia ceramics", Magnesium Elektron, Twickenham, UK, (1986).

[20] K. K. Srivastava, R. N. Patil, C. B. Choudhary, K. V. G. K. Gokhale, and E. C. Subba Rao, *Trans. Brit. Ceram. Soc.* **73**, 85 (1974).

[21] R. A. Miller, R. G. Garlick, and J. L. Smialek, *J. Am. Ceram. Soc. Bull.* **62**, 12 (1983).

[22] R. A. Miller, J. L. Smialek, and R. G. Garlick, *Adv. Ceram. Sci. Tech. Zircon.* (Eds. A. H. Hener and L. W. Hobbs, *Am. Ceram. Soc,* Columbus, 241(1981).

[23] N. Iwamoto, N. Umesaki, and S. Endo, *Trans.* JWRI, **41**, 89 (1985).

[24] V. S. Stubican, and J. R. Hellmann, *Adv. Ceram.* **3**, 25 (1981).

[25] E. Jaeger, and R. Nickell, *Plenum Press*, **5**, 163 (1971).

[26] E. C. Subbarao, *Adv. Ceram*, **3**, (1981).

[27] D. J. Green, P. S. Nicholson, and J. D. Embury, *J. Amer. Ceram. Soc.* **56**, 619 (1973).

[28] S. K. Saha, A. Pathak, and P. Pramanik, *J. Mater. Sci. Let.* **14**, 35 (1995).

[29] D.L. Porter, and A.H. Heuer , *J. Am. Ceram. Soc*. **62**, 298 (1997).

[30] M. Yoshimura, *Am. Ceram. Soc. Bull*. **67**, 1950 (1988).

[31] E. C. Subbarao, H. S. Maiti, and K. K. Srivastava, *Phys. Status Solid,*. **21**, 9 (1974).

[32] Y. Zhou, T-C Lei, and T. Sakuma, *J. Am. Ceram. Soc.* **74**, 633 (1991).

[33] R. N. Patil, and E. C. Subbarao, *J. Appl. Cryst.* **2**, 281 (1969).

[34] W. M. Hua, F. Zhang, Z. Ma, and Z. Gao, *Catal. Let.* **65**, 85 (2000).

[35] M. M. Rashad, and H. M. Baioum, *J. Mater. Process. Tech.* 195, 178 (2008).

[36] J. Liang, X. Jiang, G. Liu, Z. Deng, J. Zhuang, F. Li, and Y. Li, *Mater. Res. Bull.* **38**, 161 (2003).

[37] S. Roy, and J. Ghose, *Mater. Res. Bull.* 35, 1195 (2000).

[38] E. D. Banu´s, V. G. Milt, E. E. Miro´ , and M. A. Ulla, *Appl. Catal.* A: General **362**, 129 (2009).

[39] K. T. Jung, and A. T. Bell, *J. Mol. Catal.* A: Chem. **163**, 27 (2000).

[40] Y. V. Kolen'ko, V. D. Maximov, A. A. Burukhin, V. A. Muhanov, B. R. Churagulov, *Mater. Sci. Eng*. **23**, 1033 (2003).

[41] X-M Liu, and Z-F Yan, *Chinese J. Struct. Chem.,* **25**, 424 (2006).

[42] W. M. Hua, F. Zhang, Z. Ma, and Z. Gao, *Catal. Let.* **65**, 85 (2000).

[43] M. Hino, and K. Arata, *J. Chem. Soc. Chem. Commun.* 851 (1980).

[44] V. Quaschning, J. Deutsch, P. Druska, H. J. Niclas, and E. Kemnitz, *J. Catal.* **177**, 164 (1998).

[45] P. T. Patil, K. M. Malshe, P. Kumar, M. K. Dongare, and E. Kemnitz, *Catal. Commun*. **3**, 411 (2002).

[46] J. C. Yori, C. L. Pieck, and J. M. Parera, *Catal. Let.* **64**, 141 (2000).

[47] S. Sugiyama, K. Shimodan, H. Hayashi, N. Shigemoto, K. Miyaura, K. Saitoh, and J. B. Moffat, *J. Catal.* **141**, 279 (1993).

[48] B. M. Reddy, M. K. Patil, K. N. Rao, and G. K. Reddy. *J. Mol. Catal*. **258**, 302 (2006).

[49] Y. Nitta, O. Suwata, Y. Ikeda, Y. Okamoto, and T. Imanaka, *Catal. Let*. **26**, (1994).

[50] X. Chen, C. Chen, N. Xu, Song Han, and Chung-Yuan Mou, *Catal. Let*. **85**, 177 (2003)

[51] A. Sharma, *J. Envi. Eng*. **132**, 956 (2006).

[52] A. Indarto, H. Lee, J. Choi, and H. K. Song, *Utilize. Environ. Eff.*, **30**, 1628 (2008).

[53] A. Khodakov, J. Yang, S. Su, E. Iglesia, and A. T. Bell, *J. Catal*. **177**, 343 (1998).

[54] K. Tanabe, and T. Yamaguchi, *Catal. Today* **20**, 185 (1994).

[55] T. Yamaghuchi, and K. Tanabe, *Mater. Chem. Phys*. **16**, 67 (1986).

[56] G. Rinn, and H. Schmidt, in " Preparation of Y-doped zirconia by emulsion technique in Ceramic Powder Processing Science", Eds. H. Hausner, G. L. Messing, S. Hirano. Cologne, 221 (1989).

[57] J. D. A. Bellido, and E. M. Assaf, *Appl. Catal.* A: General **352**, 179 (2009).

[58] P. Marcos, and D. Gouvea, *Ceram.* **50**, 38 (2004).

[59] M. Labaki, J. F. Lemonier, S. Siffert, E.A. Zhilinskaya, and A. Aboukai, *Appl. Catal. B* **43**, 261 (2003).

[60] C. Yang, B. Hong, and J. Chen, Powder Tech. **89**, 149 (1996).

[61] J. C. Ray, C. R. Saha, and P. Pramanik, *J. Euro. Ceram. Soc*. **22**, 851 (2002).

[62] J. C. Ray, C. R. Saha, and P. Pramanik, *J. Euro. Ceram. Soc*. **30**, 649 (2010).

[63] C. Oelgardt, J. Anderson, J. G. Heinrich, and G. L. Messing, *Ceram. Inter.* **30**, 2 (2004).

[64] A. Mondal, and S. Ram, *Ceram. Inter.* **30**, 923 (2004).

[65] A. Carrascull, I. D. Lick, E. N. Ponzi, and M. I. Ponzi, *Catal. Commun.* **4**, 124 (2003).

[66] Y. Wang, W. Y. Huang, Z. Wu, Y. Chun, and J. H. Zhu, *Mater. Let.* **46**, 198 (2000).

[67] J. H. Zhu, Y. Chun, Y. Wang, Q. H. Xu, *Mater. Let.* **33**, 207 (1997).

[68] J. H. Zhu, Y. Wang, Y. Chun, X. S. Wang, *J. Chem. Soc*.,Faraday Trans. **94**, 1163 (1998).

[70] J. H. Zhu, Y. Chun, Y. Qin, Q. H. Xu, *Microprobe Mesopr. Mater.* **24**, 19 (1998).

[71] G. L. Clark and D. H. Reynolds, *Z. Kristallogr*. **98**, 299 (1937).

[72] E. D. Whitney, *Trans. Faraday Soc*. **61**, 1991 (1965).

[73] Y. Murase and E. Kato, *Nippon Kagaku Kaishi*, 367 (1978).

[74] C. Morterra, G. Cerrato, L. Ferronia, and L. Montanaro, *Mater. Chem. Phys.* **37**, 243 (1994).

[75] B. Bachiller-Baeza, I. Rodriguez-Ramos, and A. Guerrero-Ruiz, *Langmuir* **14**, 3556 (1998).

[76] K. Pokrovski, K. T. Jung, and A. T. Bell, *Langmuir* **17**, 4297 (2001).

[77] H. Toraya, M. Yashmura, and S. Somiya, *J. Am. Ceram. Soc*. **67**, 119 (1984).

[78] Z-J Li, H.A. Prescott, J. Deutsch, A. Trunschke, H. Lieske, and E. Kemnitz. *Catal. Let.* **92**,175 (2004).

[79] B-Q Xu, T. Yamaguchi, and K. Tanabe, *Chem. Let.* 1663 (1988).

[80] A. C. Dodd, and P. G. McCornick, *J. Metastable Nanocrytall. Mater.*, **312**, 221 (1999).

[81] Y. Watanabe, Y. Matsumura, Y. Izumi, and Y. Mizutani, *Bull. Chem. Soc.* **47**, 2922 (1974).

[82] S. Talwalkar, and S. Mahajani, *Appl. Catal.* 140, (2006).

[83] B. C. Gates, and H. Knözinger, *Adv. Catal.* **49**, 257 (2006).

[84] Z. Liu, W.J. Jie, L. Dong, Y. Chen, *J. Solid State Chem*. 138, **41** (1998).

[85] A. Khodakov, J. Yang, S. Su, E. Iglesia, and A. T. Bell, *J. Catal.* **177**, 343 (1998).

[86] D. G. Barton, S. L. Soled, G. D. Meitzner, G. A. Fuentes, and E. Iglesia, *J. Catal.* **181**, 57 (1999).

[87] W. Xie, and H. Li, *J. Mol. Catal.* **255** (2006).

[88] J. Cosimo, V. Díez, and C. Apesteguía, *Appl. Catal.* **137**, 149(1996).

Chapter 5

Alumina supported potassium nitrate derived catalysts for acetone conversion.

5. Alumina.

5.1 Introduction.

In order to make comparison with the KNO_3 doped ZrO_2 catalysts described in the previous chapter, KNO_3 doped γ-Al_2O_3 is considered in this short chapter. KNO_3 doped alumina has previously been investigated in the literature as outlined below:

Linbing et al [1] have studied the catalytic activity of KNO_3/Al_2O_3 for the methylation of cyclopentadiene. It was found that a base strength of (H_-) of 27.0 has been achieved for KNO_3/ZrO_2, KNO_3/γ-Al_2O_3, KNO_3/HT, and KNO_3/MgO catalysts which exhibited the characteristics of solid superbases, while SiO_2 and TiO_2 supported KNO_3 resulted in a lower strength (Table. 5.1).

Catalyst	Surface area of support (m²/g)	Base strength (H_-)
20%KNO_3/SiO_2	410.6	9.3
20%KNO_3/ZrO_2	120.0	27.0
20%KNO_3/TiO_2	51.8	9.3
26%KNO_3/γ-Al_2O_3	193.0	27.0
20%KNO_3/HT	244.6	27.0
26%KNO_3/MgO	151.1	27.0
23%MgO/γ-Al_2O_3	193.0	22.5
10%γ-Al_2O_3/MgO (mix)	151.1	22.5

Table. 5.1 Base strength of the solid bases and the surface area of the supports [1].

After being supported on γ-Al_2O_3, KNO_3 was completely decomposed after activation at 600 ^{o}C, and strongly basic sites emerged. It was believed that the potassium ions of KNO_3 inserted into octahedral vacant sites existing on the surface of γ-Al_2O_3 and lowered the decomposition temperature of KNO_3.

Activating KNO_3/TiO_2 at 600 ^{o}C resulted very weak residual peaks of KNO_3 being evident in the powder x-ray diffraction pattern. However, the appearance of new peaks 11.4^o and 29.1^o 2θ indicated the formation of $K_2Ti_8O_{17}$ that could be the responsible for the reduction of base strength to $H_- = 9.3$ on KNO_3/TiO_2 since KNO_3 was converted to $K_2Ti_8O_{17}$ with a lower basicity than K_2O. No vacant sites were available on SiO_2 and MgO for the insertion of potassium ions. As a result of the weak interaction between KNO_3 and the supports, two crystalline phases of KNO_3, denoted as A and B, were apparent in the XRD pattern of the KNO_3/SiO_2 sample. Conversion of the A phase into B took place upon increasing

temperature but with negligible decomposition of KNO_3. The XRD patterns of KNO_3/MgO before and after the activation at 600 ^{o}C suggested that some $Mg(OH)_2$ was present at room temperature which was subsequently converted to MgO upon thermal treatment (Fig. 5.1). The intensity of the KNO_3 peaks were weakened to a small extent by activation, suggesting that only a minor amount of KNO_3 supported on MgO has been decomposed. The decomposition of KNO_3 over both SiO_2 and MgO was limited. SiO_2 favourably reacted with K_2O derived from KNO_3 decomposition and produced K_2SiO_3 species with low base strength. However, only a small quantity of K_2O that formed from the KNO_3 decomposition was able to generate basic sites with high strength ($H_- = 27.0$) on KNO_3/MgO. The characteristic peaks of hydrotalcite (HT) disappeared and the MgO crystal phase was observed at 2θ of 43.2^o and 62.7^o on KNO_3/HT after thermal treatment at 600 ^{o}C. This indicated the conversion of HT to a mixture of MgO and Al_2O_3. The diffraction peaks at 23.5^o and 29.5^o corresponding to crystal phase A of KNO_3 almost disappeared, which was accompanied by the development of new diffraction peaks at 27.3^o, 29.8^o, 32.7^o, and 39.3^o resulting from crystal phase B of KNO_3. Therefore, it was proposed that part of the KNO_3 supported on HT was decomposed to K_2O and the rest was transformed to phase B. The HT support possessed a base strength (H_-) of over 18.4, and the decomposition of KNO_3 could create basic sites with high strength ($H_- = 27.0$) on KNO_3/HT. The conversion of the two crystal phases of KNO_3 showed various trends after thermal treatment on different oxide supports.

Crystal phase A was predominant on KNO_3/TiO_2, KNO_3/HT, and KNO_3/MgO. After activation, all or only some KNO_3 was converted to crystal phase B. However, for KNO_3 loaded on SiO_2, both crystal phases existed.
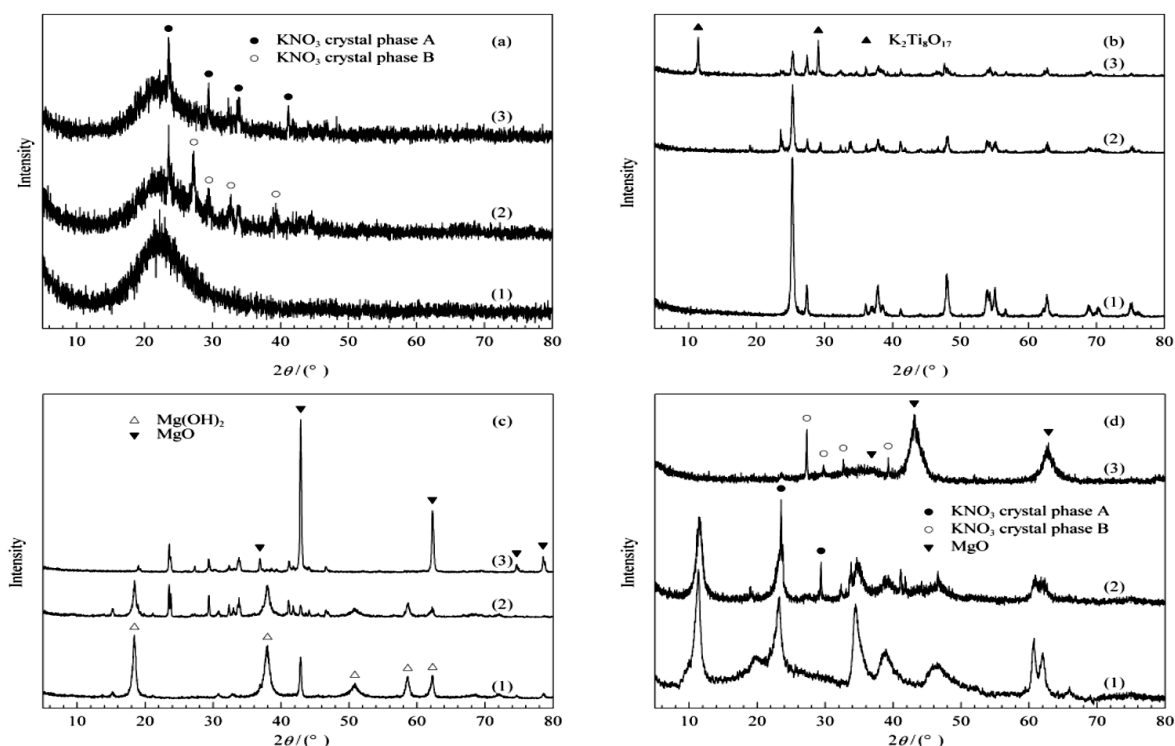
Fig. 5.1 XRD patterns of catalysts 20% KNO_3/SiO_2 (a), 20% KNO_3/TiO_2 (b), 26% KNO_3/MgO (c), and 20% KNO_3/HT (d), (1) The support, (2) As prepared, (3) Pre-treated at 600 ^{o}C for 1 h [1].

Among the supports, SiO_2 has the largest surface area of 410.6 m^2/g but TiO_2 possessed the smallest area of only 51.8 m^2/g (Table. 5.1). The difference in the surface areas was also responsible for the difference in the basic properties of the KNO_3 modified solid bases. It was known that iso-propanol is dehydrogenated to acetone over basic sites and dehydrated over acidic sites to propene. In contrast to KNO_3/ZrO_2 and KNO_3/MgO, the samples of $KNO_3/\gamma-Al_2O_3$ and KNO_3/HT promote more conversion to acetone. A larger yield of propene has been attained over KNO_3/HT than that over the other composites owing to the additional acidic sites on KNO_3/HT. Generally, these solids exhibited major basic properties along with minor acidic properties as observed from the results of the reaction. Extensive enhancement of the catalytic activity of the oxide supports for cyclopentadiene (CPD) methylation has been noted after loading KNO_3. The composites of $KNO_3/\gamma-Al_2O_3$ and KNO_3/HT exhibited the highest activity and about 32% of CPD was converted with a methylcyclopentadiene selectivity of about 86% at 450 ^{o}C.

Despite the strong basicity of KNO_3/ZrO_2 and KNO_3/MgO ($H_- = 27.0$) their catalytic activity of CPD methylation was very low, and only 9.4% and 13.5% CPD was converted, respectively. Their catalytic activity was much worse than that of KNO_3/γ-Al_2O_3 and KNO_3/HT. The conversion of CPD was reduced but the selectivity for methylcyclopentadienes was dramatically increased over γ-Al_2O_3 by loading 23% MgO. A mechanical mixture of 10% γ-Al_2O_3 and 90% MgO achieved a higher conversion and selectivity than MgO. All samples showed optimum catalytic activity at 450 ^{o}C excluding the KNO_3/SiO_2 and MgO-related composites as their maximum activities raised at 500 ^{o}C. TiO_2 and γ-Al_2O_3 were acidic, whereas SiO_2 and ZrO_2 exhibited weak acidity as well as basicity thus these oxides were ineffective for the methylation of CPD. The catalytic activity of CaO was worse than MgO especially at 500 ^{o}C, although the CaO was more basic. The significant difference in the surface area of CaO (8.4 m^2/g) and that of MgO (151.1 m^2/g) could account for this.

The higher activity of KNO_3/γ-Al_2O_3, KNO_3/HT, and KNO_3/ZrO_2 were attributed to them being solid superbases. Since a weak base strength (H_-) of only 9.3 has been measured on KNO_3/SiO_2 and KNO_3/TiO_2, such basic sites were not strong enough to catalyse the methylation of CPD.

The base strength of MgO was relatively strong ($H_- = 22.5$), and the increase in the base strength was modest after modifying with KNO_3 that was associated with the reasonable improvement of the catalytic activity for CPD methylation. For this reason, solids with strong basicity were of assistance for the methylation of CPD. The activities of KNO_3/ZrO_2 and KNO_3/MgO was lower than that of KNO_3/γ-Al_2O_3 and KNO_3/HT in spite of base strength of $H_- = 27.0$. One of the possible reasons was that γ-Al_2O_3 and HT have greater surface areas than ZrO_2 and MgO. However, the limited variation in the surface area of the oxides may not give a definitive explanation for the considerable difference in their catalytic performance. The results of isopropanol decomposition showed that the yield of acetone over KNO_3/γ-Al_2O_3 and KNO_3/HT was much higher than that over KNO_3/ZrO_2 and KNO_3/MgO even with the similarity of base strength which had been verified by their activity for CPD methylation. Therefore, the basicity of the catalysts could be ascribed as a dominant factor for CPD methylation. Analogous amounts of CPD were converted over KNO_3/γ-Al_2O_3 and KNO_3/HT while more acetone was yielded over KNO_3/γ-Al_2O_3. A

higher yield of propene over KNO_3/HT might be used to illustrate this phenomenon since a synergistic effect of the basic and acidic sites was beneficial for the CPD methylation.

Another study of KNO_3 supported on alumina was reported by Xie et al [2]. The base strength measurement of a series of KNO_3/Al_2O_3 catalysts calcined at high temperature (Table. 5.2) showed that the parent alumina was acidic and converted the colour of dimethylaminoazobenzene (H_- = 3.3) from yellow to red.

Sample	T_p (K)	Basic strength (H_-)
15% KNO_3/Al_2O_3	773	$15.0 < H_- < 18.4$
20% KNO_3/Al_2O_3	773	$15.0 < H_- < 18.4$
25% KNO_3/Al_2O_3	773	$15.0 < H_- < 18.4$
30% KNO_3/Al_2O_3	773	$15.0 < H_- < 18.4$
35% KNO_3/Al_2O_3	773	$15.0 < H_- < 18.4$
40% KNO_3/Al_2O_3	773	$15.0 < H_- < 18.4$
45% KNO_3/Al_2O_3	773	$15.0 < H_- < 18.4$
35% KNO_3/Al_2O_3	573	$3.9 < H_- < 7.2$
35% KNO_3/Al_2O_3	673	$9.3 < H_- < 15.0$
35% KNO_3/Al_2O_3	723	$15.0 < H_- < 18.4$
35% KNO_3/Al_2O_3	823	$15.0 < H_- < 18.4$
35% KNO_3/Al_2O_3	873	$15.0 < H_- < 18.4$
35% KNO_3/Al_2O_3	973	$15.0 < H_- < 18.4$

Table. 5.2 Basic strengths of different KNO_3/Al_2O_3 catalysts calcined at high temperature [2].

After loading potassium nitrate and calcination at temperatures higher than 500 ^{o}C, the modified alumina samples demonstrated a high base strength unlike 35% KNO_3/Al_2O_3 samples calcined at temperatures lower than 450 ^{o}C. They could change the colour of 2, 4-dinitroaniline (H_- = 15) from yellow to mauve very quickly, but failed to convert 4-nitroaniline (H_- = 18.4) to its conjugate base form, and therefore, their base strength could be tentatively ranged between (H_- = 15 -18.4) and they could be regarded as strong bases. The basicity of the catalysts with different amounts of loaded KNO_3 was measured by Hammett titration (Fig. 5.2).
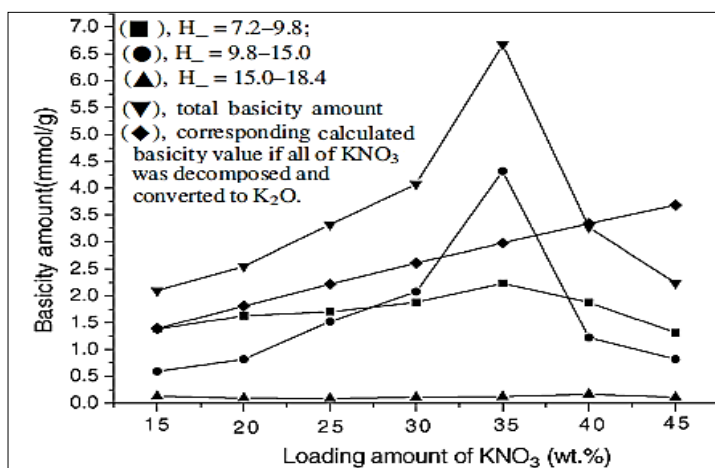
Fig. 5.2 Basicity of 35% KNO_3/Al_2O_3 sample calcined at different temperatures [2].

When the amount of loaded KNO_3 increased to 35 wt% the catalyst basicity was markedly improved and the basicity became the highest. Although the basic strengths of various KNO_3/Al_2O_3 samples calcined at 500 ^{o}C were the same (Table. 5.2) the basicities of the samples of 40% KNO_3/Al_2O_3 and 45% KNO_3/Al_2O_3 were lower than that of 35% KNO_3/Al_2O_3 which resulted in a drop of the catalytic activity towards the methanolysis reaction (Fig. 5.3).
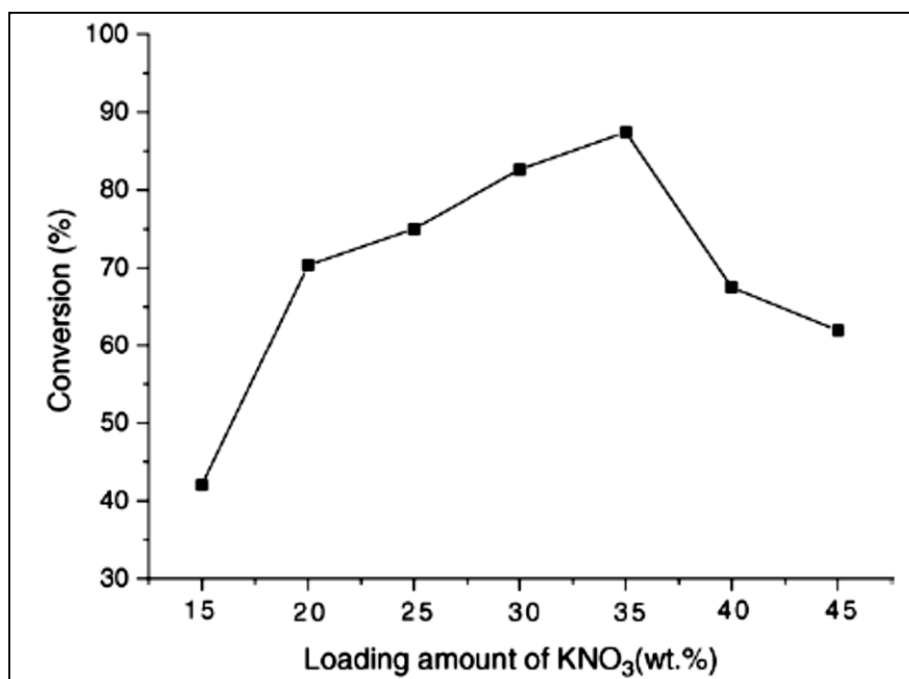
Fig. 5.3 Influence of loading amount of KNO_3 on the conversion. Reaction conditions: methanol/oil molar ratio 15:1, catalyst amount 6.5% after 7h on stream, methanol reflux temperature [2].

This was probably due to the coverage of surface basic sites by the excess KNO_3. The sites are, thus, not accessible to incoming reactants when the amount of loaded KNO_3 exceeded 35 wt%. Moreover, the basicity of 35% KNO_3/Al_2O_3 sample calcined at different temperatures was measured by the same method (Fig. 5.4).
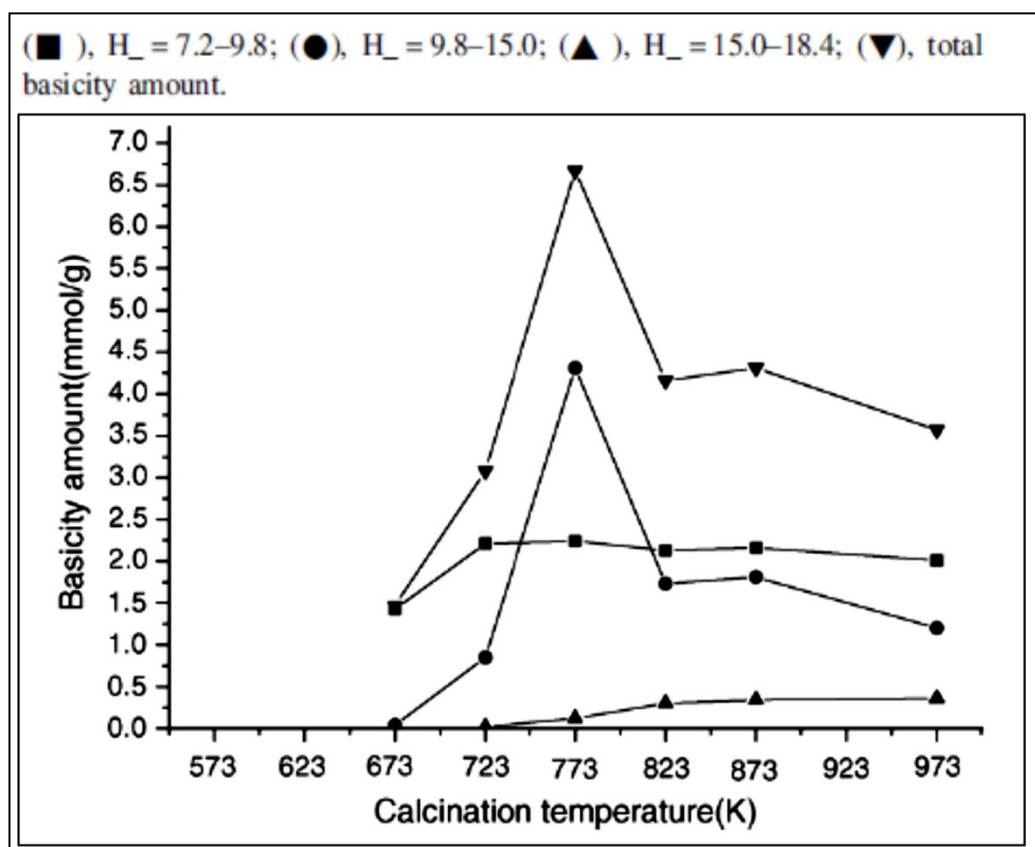
Fig. 5.4 Basicity of 35% KNO_3/Al_2O_3 sample calcined at different temperatures [2].

The result established that the 35% KNO_3/Al_2O_3 sample calcined at 500 ^{o}C had the highest basicity, reaching 6.67 mmol/g. When the calcination temperature was greater than 500 ^{o}C, the basicity decreased. The basicity change with calcination temperature paralleled the change in the catalytic activity for the methanolysis of soybean oil (Fig. 5.5).
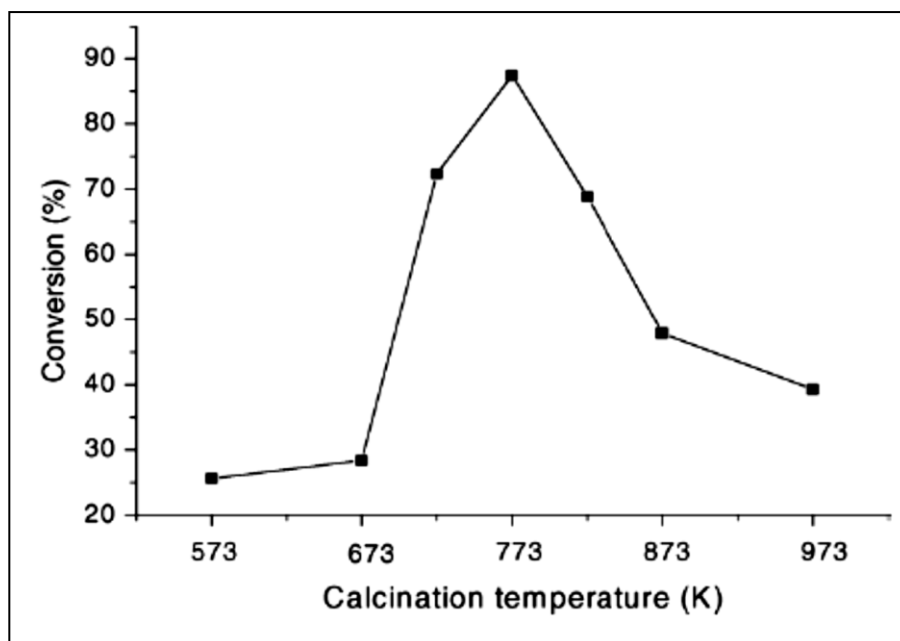
Fig. 5.5 Influence of calcination temperature on the conversion. Reaction conditions: methanol/oil molar ratio 15:1 on 6.5% amount of catalyst after 7 h reaction time, methanol reflux temperature [2].

5.2 Results and discussion.

Since it has been documented that the basicity, and hence catalytic activity, of KNO_3/Al_2O_3 catalysts is strongly dependent upon loading, a range of KNO_3 loadings has been studied in this chapter. XRD patterns of the various resultant samples are shown in Figure 5.6.
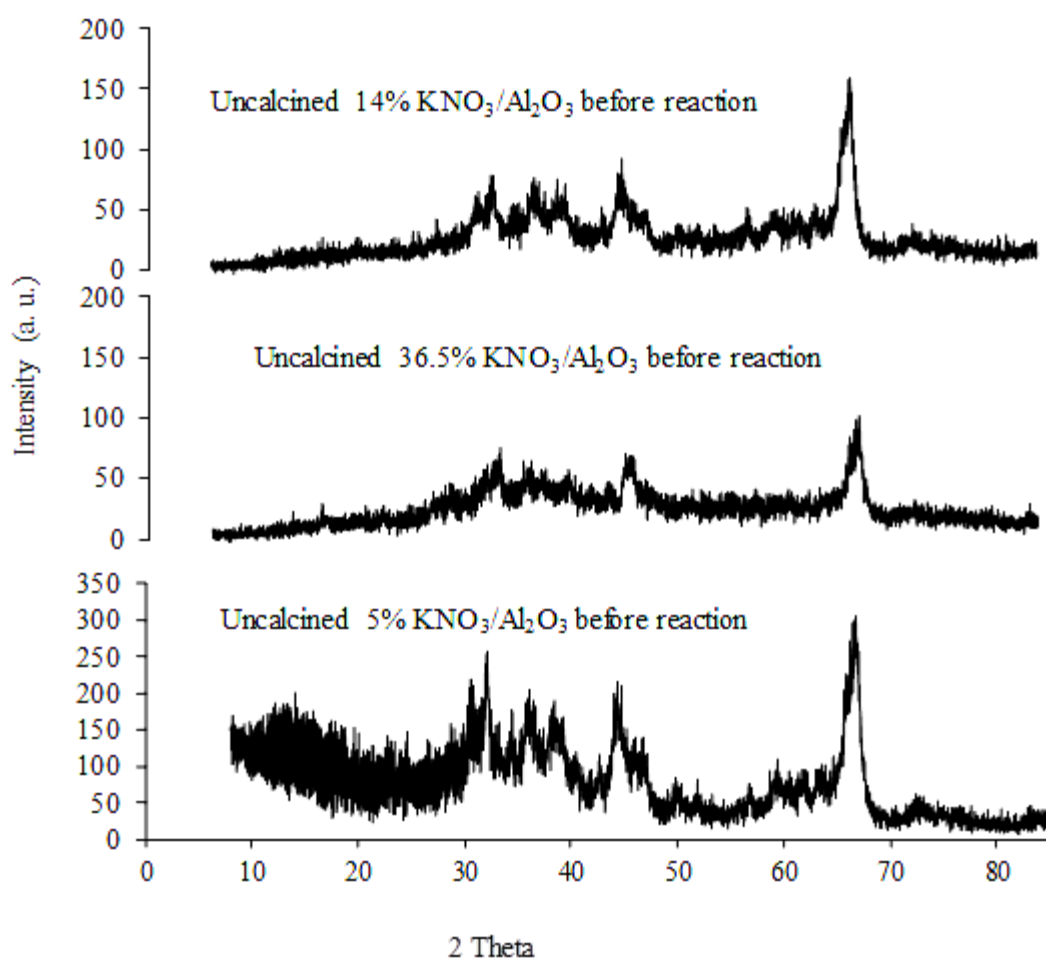
Fig. 5.6 XRD patterns of KNO_3/Al_2O_3 catalyst with various loading of KNO_3.

The XRD patterns of the KNO_3/Al_2O_3 samples revealed that for samples with loaded KNO_3 less than the dispersion threshold (12–25%), the XRD pattern is almost identical to Al_2O_3 with the (440), (400), (222), (311) and (111) refelctions being observed at $2\theta = 67$ ^{o}, 46 ^{o}, 39 ^{o}, 37 ^{o}, and 19.2 ^{o} respectively [3]. It was reported that these peaks are particularly related to cubic γ-Al_2O_3 [(JCPD No. 04-0858)]. The XRD pattern also revealed that no other compounds such as $KAlO_2$ were detected which is similar to Stork and Pott's XRD result for the K_2CO_3 on alumina [4]. The XRD result in Fig. 5.6 also agrees with those of Zhu and Wang [5] who reported that by increasing the amount of KNO_3 to 13 wt%, KNO_3 reflections became apparent at $2\theta = 19.0$ ^{o}, 23.6 ^{o}, 29.4 ^{o}, and 33.8 ^{o} indicating that KNO_3 may not be well dispersed and its residual phase remained. Compounds which were formed by interaction between KNO_3 and the surface of alumina [6] appeared at

$2\theta = 27.2$ ^{o} and 32.7 ^{o} [7] although the nature of the interaction is not clearly understood. Accordingly, it is reasonable to surmise that only part of the loaded KNO_3 could be decomposed under the activation conditions, depending on the interaction of KNO_3 with the surface of support. This XRD result is consistent with what Xie et al [2] reported in their work over KNO_3 on alumina. It is proposed that high basicity is generated by inserting K^+ ions in the vacant sites of alumina, accelerating dispersion and decomposition of KNO_3 to form strong basic sites associated with K_2O during the activation process. Further peaks attributed to a compound containing K and Al appeared at $2\theta = 10$ ^{o} and 36 ^{o} which may possibly be one of the reasons for the reduction and even loss of KNO_3 and K_2O peaks, hence possibly lowering the basicity and hence catalytic activity. Furthermore, since some diffraction peaks related to the nitrate salt still remained on the catalysts even after calcination, it appears that calcination of KNO_3/Al_2O_3 at 400 ^{o}C did not sufficiently convert the corresponding nitrate precursors into the active oxide forms which is consistent with the study reported by Benjapornkulaphong and Ngamcharussrivichai for $NaNO_3/Al_2O_3$ and KNO_3/Al_2O_3 calcined at 450 ^{o}C [8]. This XRD result is also in agreement with Zhu and Wang's study for KNO_3/Al_2O_3 as they found that the KNO_3 peaks intensities were not obviously affected by calcination at 773 K in air for 4 h [5].

Some samples displayed a nearly identical diffraction pattern to that of the catalyst calcined at 400 ^{o}C suggesting that KNO_3 can be preserved in the composite structure at such high temperature. Thermal stability of KNO_3 up to 600 ^{o}C has been previously reported on La_2O_3 [9], V_2O_5 and CeO_2 [10].

Catalyst	Surface area ($m^2 g^{-1}$)
5% KNO_3/Al_2O_3	89
14% KNO_3/Al_2O_3	71
36.5% KNO_3/Al_2O_3	1

Table. 5.3 Surface area for KNO_3/Al_2O_3 catalysts.

The BET surface area results (Table. 5.3) show that the surface area of KNO_3/Al_2O_3 catalysts decreased when the loading amount of KNO_3 increased, in agreement with results for KOH/Al_2O_3 and KOH/NaY catalysts [11]. As described later, the 14% KNO_3/Al_2O_3 catalyst exhibited higher conversion and selectivity than 36.5% KNO_3/Al_2O_3, although not

when surface area was account. A larger surface area of support may be beneficial for a faster decomposition of KNO_3 [12].
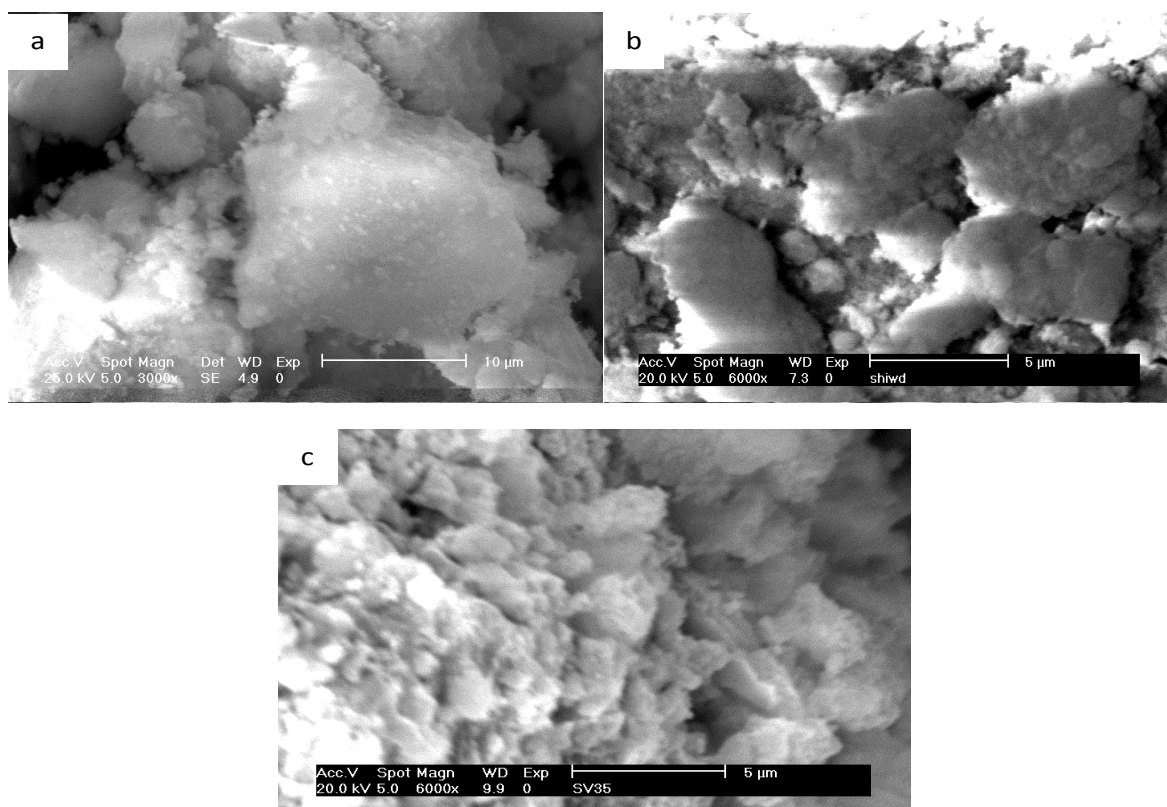
Fig. 5.7 SEM images for a) 5% KNO_3/Al_2O_3, b) 14% KNO_3/Al_2O_3 and c) 36.5% KNO_3/Al_2O_3.

The SEM images show that a range of morphologies is present which may influence the catalyst performance. It can be observed that the 14 wt% KNO_3 is well dispersed over alumina compared to the 5 wt% and 36.5 wt% samples. Particles were irregularly dispersed within the structure.

The catalytic activity of 14% KNO_3/Al_2O_3 and 36.5% KNO_3/Al_2O_3 samples has been investigated. A high acetone conversion rate of 147×10^{-3} mol m^{-2} h^{-1} after 18 h on stream was apparent over the 36.5 wt% catalyst compared to only 2.11×10^{-3} mol m^{-2} h^{-1} for its 14 wt% counterpart, demonstrating that catalytic behaviour is a strong function of loading.
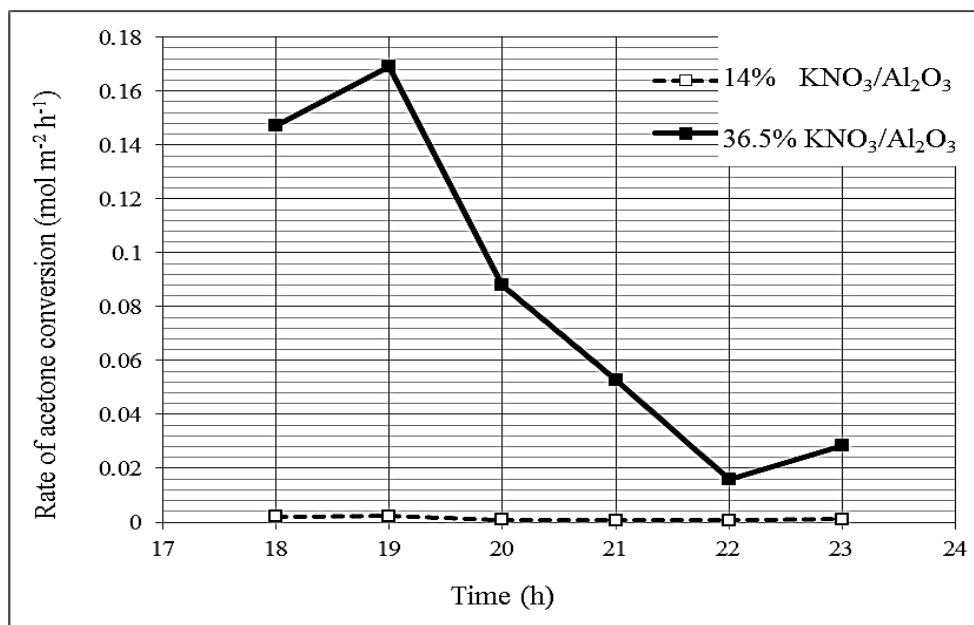
Fig. 5.8 Surface area normalised acetone conversion as a function of time over 14% KNO_3/Al_2O_3 and 36.5% KNO_3/Al_2O_3 catalysts at 400 ^{o}C, 5 bar H_2 pressure, TOS > 18 h.

Yields were reasonably high for both 14% and 36.5% loaded samples. The 14% sample achieved a much greater yield than the 36.5% catalyst since it showed a maximum yield of about 60 % for MO while the 36.5% achieved only around 30% (Fig. 5.9). These results are in agreement with the work of Noiroj and Intarapong who reported that the yield for biodiesel over KOH/Al_2O_3 was increased by increasing the loading of KOH on Al_2O_3 from 1% - 25%, beyond which, the yield began to decrease [11]. It is very likely that dispersion of KNO_3 on Al_2O_3 support weakens the interaction between K^+ and NO_3^- ions due to the interaction between KNO_3 and the surface of support, assisting the decomposition of KNO_3. At low loadings of KNO_3, the active base sites are more dispersed on the alumina surface leading to a strong adsorption of reactant at unreactive surface sites. But, with the higher loading of KNO_3, the KNO_3 cannot be well dispersed and only part of the loaded KNO_3 could be decomposed. Therefore, KNO_3 may cover the basic sites on the surface of the composite material and reduce catalytic activity. Based on this result, the catalytic activity seems to relate to the amount of decomposed KNO_3 instead of the total amount of KNO_3 loaded.
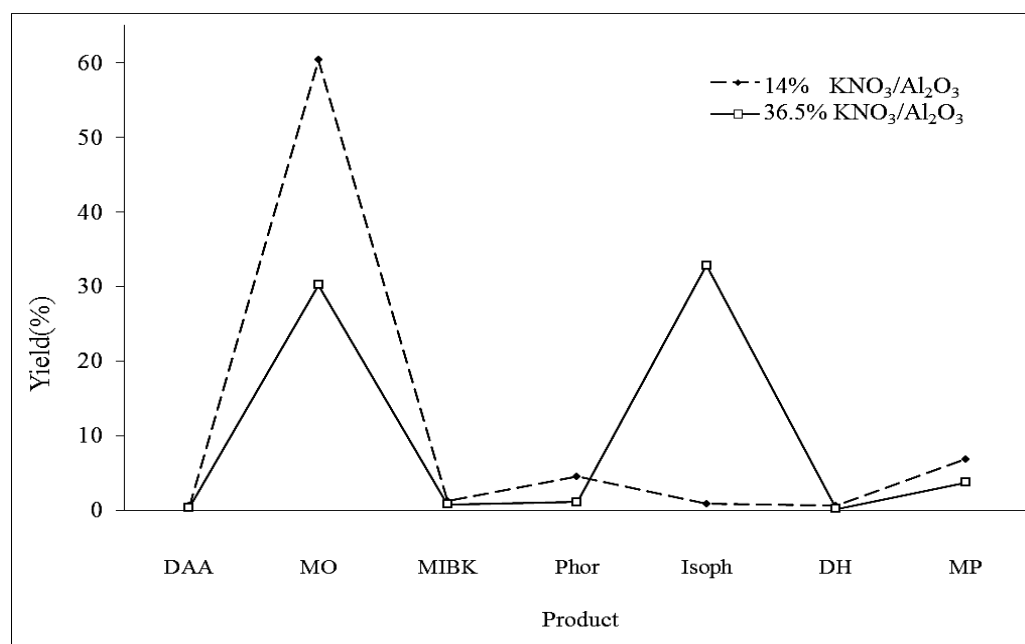
Fig. 5.9 Percentage yields of the condensation and hydrogenation products of acetone as a function of temperature over 14% KNO_3/Al_2O_3, and 36.5% KNO_3/Al_2O_3 catalysts at 400 ^{o}C and 5 bar H_2 pressure, TOS > 18 h.

Catalyst	Conversion (%)	Selectivity (%)						
		DAA	MO	MIBK	Phor	Isoph	DH	MP
14% KNO_3/Al_2O_3	75	0.70	80.80	1.60	6.00	1.10	0.80	9.10
36.5% KNO_3/Al_2O_3	70	0.50	43.70	1.10	1.60	47.50	0.20	5.40

Table. 5.4 Conversions and selectivities for the aldol condensation reaction over 14% KNO_3/Al_2O_3 and 36.5% KNO_3/Al_2O_3 catalysts at 400 ^{o}C and 5 bar H_2 pressure ,TOS > 18 h.

Both catalysts exhibited high selectivity for MO of 80.80% and 43.70% for the 14% KNO_3/Al_2O_3 and 36.5% KNO_3/Al_2O_3 catalysts respectively. However, the 36.5% KNO_3/Al_2O_3 catalyst showed a considerable selectivity for isophorone (Table 5.4). A significant selectivity of isophorone has been previously reported over Mg-Al mixed oxides [13].
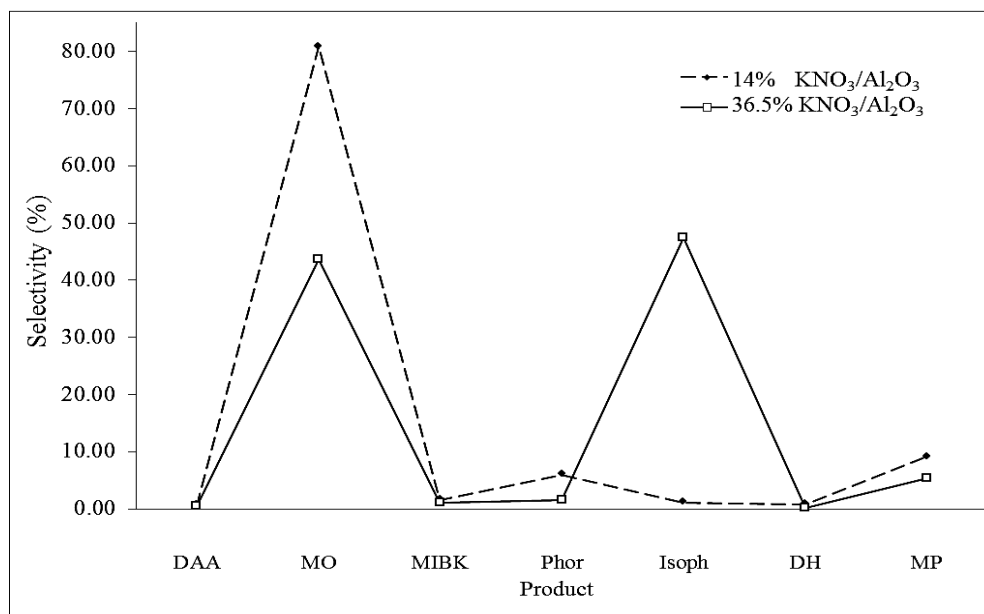
Fig. 5.10 Percentage selectivities of the condensation and hydrogenation products of acetone as a function of temperature over 14% KNO_3/Al_2O_3 and 36.5% KNO_3/Al_2O_3 catalysts at 400 ^{o}C, 5 bar H_2 pressure, TOS > 18 h.

It is therefore clear that it is possible to study the selectivity of the acetone condensation reaction by varying the KNO_3 loading. Since the overall conversions are not significantly different between the two loadings studied, the selectivity differences are intrinsic. At this point, it is useful to draw comparison with the results of the KNO_3/ZrO_2 and $KNO_3/Zr(OH)_4$ catalysts since they were less active and presented much lower conversion and selectivity.

5.3 Conclusion.

In this very brief study, a few conclusions can be drawn:

- the surface area of KNO_3/Al_2O_3 catalyst is reduced by increasing the loading of KNO_3.

- KNO_3/Al_2O_3 is an effective catalyst for the aldol condensation reaction of acetone.

- The aldol condensation reaction of acetone over KNO_3/Al_2O_3 catalyst is a dependent upon KNO_3 loading.

- There is a strong relation between product selectivities and the loading of KNO$_3$ on alumina.

5.4 References.

[1] S. Linbing, W. Zhengying, K. Jiahui, C. Yuan, W. Ying, Z. Jianhua and Z. Zhigang, *Chinese J. and Catal.* **27**, 8 (2006).

[2] W. Xie, H. Peng and L. Chen, *Appl. Catal. A: General* **300**, 67 (2006).

[3] R. M. Leuy, and D. J. Bauer, *J. Catal.* **9**, 76 (1967).

[4] W. H. J. Stork, and G. T. Pott, *J. Phys. Chem.* **78**, 2496 (1974).

[5] J. Zhu, Y. Wang, Y. Chun and X. Wang*, J. Chem. Soc.,* Faraday Trans. **94**, 1163 (1998).

[6] T. Yamaguchi, J. H. Zhu, Y. Wang, M. Komatsu, and M. Ookawa, *Chem. Let.* 989 (1997).

[7] Powder Diffraction File, Alphabetical Index. International Center for Diffraction Data, JCPDS (1988).

[8] S. Benjapornkulaphong, C. Ngamcharussrivichai, and K. Bunyakiat, *Chem. Eng. J.* **145**, 468 (2009).

[9] V. Milt, C. Querini, and E. Mir´o, *Thermochim. Acta* **404**, 177 (2003).

[10] Y. Zhang, X. Zou, and L. Sui, *Catal. Commun.* **7**, 855 (2006

[11] K. Noiroj , P. Intarapong , A. Luengnaruemitcha,i and S. Jai-In , *Rene. Ener.* **34**, 1145 (2009).

[12] B. Shen, Y. Chun, J. Zhu,Y. Wang, Z. Wu, J. Xia, and Q. Xu, *Phys. Chem. Comm.* 3, (1999).

[13] C. Ma, G. Liu, Z. Wang, Y. Li, J. Zheng, W. Zhang and M. Jia, *React. Kinetic. and Catal. Let.* **98**, 149 (2009).

Chapter 6

Silica supported metal oxide catalysts for acetone conversion.

6. Introduction.

6.1 Silica.

Silica is a common chemical compound with a general formula SiO_2 or $SiO_2.xH_2O$. It can be found in an amorphous state and also in a crystalline state. It exists in crystalline phase and various phases can be formed depending on temperature, pressure and degree of hydration. These forms include quartz, cristobalite and trydimite. It is relatively inert, slightly soluble in alkali, and soluble in dilute hydrofluoric acid, it often has a large surface area, and has a high melting point due to the strength of the bonds between the atoms. Amorphous silica occurs in various forms, which can be prepared depending upon its the application, such as sheets, sols, and gels.

Silicas are covalent network structures in which each Si atom is covalently bound to four oxygen atoms. Each oxygen atom is shared between two Si atoms, yielding the formula SiO_2 (ie Si + (½ O)). Surface silanol groups (—Si—OH) occur on silicas and can impart reactivity. The silanol groups act as centres for molecular adsorption by interacting with adsorbates capable of forming hydrogen bonds or by donating or accepting electrons. There are various types of silanol groups [1].

These active silanol groups can be formed by two main processes. Firstly, via polymerisation condensation of silicic acid during the preparation of silica gel. Upon drying, the hydrogel becomes xerogel leaving some residual hydroxyls on the surface [2]. The second process is the reaction of the siloxane (Si-O-Si) surface with water under ambient conditions. The concentration of the silanol groups on the surfaces is dependent on the thermal history of the substrate, method of synthesis and on the immediate environment such as temperature and pH [3].

These silanol active sites are dependent upon the pH of the solution from which the silica is synthesised, their concentration increasing as the pH decreases. When dissolved in water, SiO_2 depolymerises and then hydrolyses to form around 40% partially hydrated (meta) silicic acid at pH = 6 with a medium surface area and high pore volume. At pH = 2 a fully hydrated (ortho) model silicic acid is formed which generally has a high surface area and low pore volume. At neutral pH, the ionization of silicic acid depends on the concentration of hydrogen ions. Silicate ion is present at a pH greater than 10 [4-6]. A schematic of these various inter-conversions is presented in Fig. 6.1:

$$(SiO_2)_n + nH_2O \longrightarrow \quad n \left[\begin{array}{c} HO \qquad OH \\ \diagdown \qquad \diagup \\ Si \\ \diagup \qquad \diagdown \\ HO \qquad OH \end{array} \right] \quad \text{Ortho silicic acid}$$

$$\boxed{\textbf{pH = 2}}$$

$$\left[\begin{array}{c} HO \qquad O^- \\ \diagdown \quad \diagup \\ Si \\ \diagup \quad \diagdown \\ HO \qquad OH \end{array} \right] \longleftarrow \left[\begin{array}{c} OH \\ \diagup \\ O = Si \\ \diagdown \\ OH \end{array} \right]$$

Silicate Ion   Meta silicic acid

$$\boxed{\textbf{pH > 10}} \qquad \boxed{\textbf{pH = 6}}$$
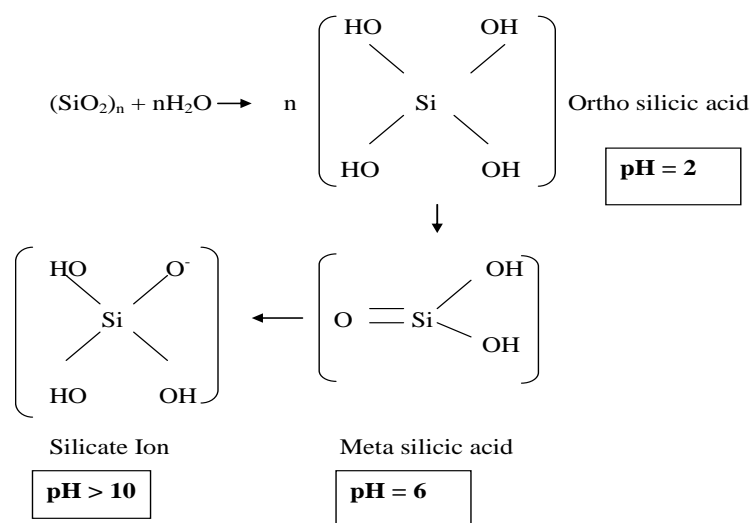
Fig. 6.1 Silica solubility in H_2O [5, 6].

As pH is lowered, a polymerization and a condensation process occurs which can be visualized starting with silicic acid [$Si(OH)_4$]. This polymerises with condensation of silane groups (SiOH) to generate an ill-defined polymer having siloxane type (Si-O-Si) bonds. This precipitates as a gel or as a colloid and its properties depend on mixing procedures, presence of electrolytes, temperature and aging, etc. Hydrogels consisting of small micelles that are roughly spherical can be obtained under certain conditions. Upon drying, the combination of micelles is appreciably weak especially if the liquid is removed at critical temperature and pressure. Under these conditions, no interface forms that may collapse the structure by the forces of surface tension. The tiny size of the micelles and use of procedures to inhibit coalescence lead to production of a high surface area material. Commercial silica gel usually has a large surface area of about 700 m^2/g. The average pore diameter is correspondingly very low, typically in the range of 2.5 to 5 nm, but is larger than those in zeolites and is substantially greater than the most reactant molecules of interest. By changing manufacturing and aging procedures, silica gels can be made with considerably larger pore diameters and correspondingly lower surface areas, perhaps as low as ca. 100 m^2/g. A fully hydroxylated silica is preferable for many applications since it improves hydrolytic stability and enhances mechanical strength.

The term silica gel is commonly used although the final dry product has to be strictly referred to xerogel or porous silica. At ambient temperature the surface comprises of a

layer of silanol groups (SiOH) in addition to the physically adsorbed water. Most of the water is removed upon drying in air at 150 to 200 °C leaving silanol groups on the surface which can be lost with increased temperature. Some siloxane groups may also be present on the surface [7]. A basic knowledge of the surface structure is of great assistance in understanding the adsorption behaviour and the chemical reactivity of silica in a variety of processes. Hydroxyl groups that exist on the surface of crystalline silicas are either free or isolated hydroxyl groups (Scheme 6.2). In contrast, the surface structure of amorphous silica is highly disordered and such regularity of the hydroxyl groups arrangement is not highly predictable [8].
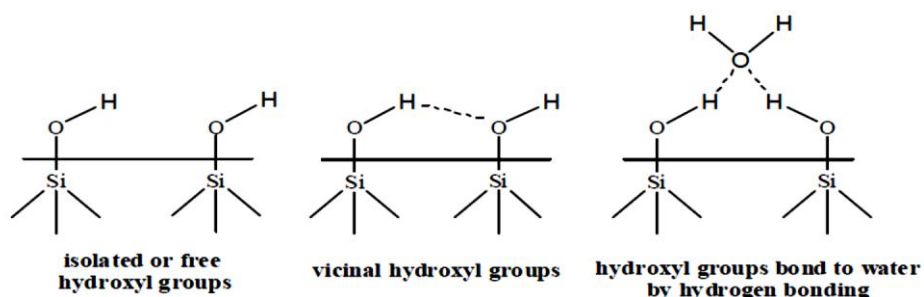
Fig. 6.2 Arrangement of hydroxyl groups on a silica surface [8].

The preparation of silica can be tailored with respect to the chemical and physical behaviour such as surface area, pore size, pore volume and particle size. The most common method for the preparation of silica is the sol-gel route [9]. The method involves condensation of $Si(OH)_4$ molecules to form a siloxane network. Soluble silicate (usually sodium silicate) is used as a starting compound although alkoxysilanes $Si(OR)_4$ can be alternatively used. Hydrolysis of the alkoxy-group and condensation with neighbouring silonal simultaneously occur in the aqueous alkoxide solution. The formation of silica sols then occurs by mixing the silicate salt of the liquid alkoxide with water or an acid. Stable particles can be obtained via condensation. Continuous condensation leads to the formation of a small three-dimensional siloxane network. The condensation process is controlled by the addition of electrolyte or by the pH. As the viscosity increases the sol can then undergo condensation process to yield a gel. Further forms of silica can be then produced by changing temperature and pH.

Silica gel is a partially hydrated form of silica. It is an amorphous and highly porous material. Silica gel powder is commonly used as a catalyst support, as an adsorbent, as a

dehydrating agent, and as a buffering medium.

Silica gel is an inorganic polymer composed of siloxane groups (Si-O-Si) with silanol groups (Si-OH) distributed on the surface. The modification of silica gel using inorganic or organic functional groups has been a subject of high interest. Surface modifications are commonly accomplished through silanisation by using an appropriate organosilane agent.

The chemical and adsorption properties of silica gel are dependent upon the number and reactivity of the surface silanol groups. Two forms of adsorption centre possibly exist on the surface of silica gel: (i) hydroxyl groups; (ii) co-ordinatively unsaturated atoms of silicon.

A wide range of catalytic processes were performed over silica on its own or as a support for another active phase. It can be used as a catalyst itself but most of the studies use silica as a support due to several inherent advantages. It is chemically inert towards many reactants since it has no pronounced surface acidity which would induce secondary reactions. Silica also has surface hydroxyl groups which allow for ligand bonding to present high specific surface areas as well as having good thermal and mechanical stabilities.

The first use of the preparation of coherent expanded aerogels was reported by Kistler et al in 1931[10]. The study clearly observed that the inorganic gel, after dehydration under normal conditions, collapses into a powder as a result of the disruption in the pore structure of the gel. However, when the gel was dehydrated under super-critical conditions of temperature and pressure, the gel did not collapse on drying and the liquid-vapour boundary within the pores of the gel no longer existed. The description of silica gel formation has been documented. Silica gel chemistry is performed either with an inorganic precursor such as ''water-glass'' or with organic precursors like silicon alkoxides, tetramethoxysilane (TMOS) of formula $Si(OCH_3)_4$, or tetraethoxysilane (TEOS) of formula $Si(OC_2H_5)_4$, which are usually applied in monomer forms. Partially condensed silica or pre-polymers (oligomers) are occasionally used. Preparation of silica gel is commonly achieved by hydrolysis using acid, generally hydrochloric acid, with a solution of "water glass" that consists of orthosilicates (Na_4SiO_4), metasilicates (Na_2SiO_3), and related compounds. The resultant material undergoes washing to remove chloride.

In the following, a number of illustrative examples to demonstrate the effects of applying SiO_2 as a support are described. Examples are taken from a range of different reactions and are not intended to be a comprehensive reference list.

Catalytic activity and characterisation of CaO/SiO_2 catalyst has been previously investigated for the oxidative dehydrogenation (OD) of ethylbenzene (EB) [11]. The samples denoted as $xCaO/SiO_2$ and $yP/xCaO/SiO_2$ (where x = 0.5 - 4.5 and y = 1.0 - 8.0 wt.%) were dried at 373-383 K and calcined at 773 - 823 K for 5 - 6 h. The results showed that the activity of silica gels slightly increased after their modification with CaO. The values of EB conversion, selectivity on styrene and CD quantity in steady state over catalysts $xCaO/SiO_2$ prepared using a macroporous silica denoted as SiO_2-V are presented in Table 6.1.

Catalysts	Conversion of ethylbenzene (%)	Selectivity on styrene (%)	CD^b (%)
SiO_2-V	47.4	76	17.5
0.5% CaO/SiO_2	52.2	80	10.0
1.0% CaO/SiO_2	59.6	83	8.5
1.9% CaO/SiO_2	42.8	80	5.5
2.9% CaO/SiO_2	35.4	64	3.0
4.5% CaO/SiO_2	25.2	55	1.0

Table 6.1 The influence of CaO quantity (wt.%) in $xCaO/SiO_2$ composition on OD of ethylbenzene. 760 K, PEB = 0.14 atm, PO_2 = 0.l7 atm, space velocity = 0.5 h^{-1}.b CD in steady state (wt.%) [11].

As can be seen from the table, with increasing of CaO quantity up to 1%, EB conversion rose from 47.4 to 59.6% beyond this loading, EB conversion and CD quantity strongly reduced. It was proposed that the amount of CaO induces a more significant influence on the activation of oxygen than on the activation of ethylbenzene. It has been shown by EPR that modification of silica gels by small quantities of CaO results formation of anion vacancies. Upon increasing CaO from 0.5 up to 4.5% the activity of catalysts in dehydration of iso-propanol declined (used as an acidity measurement) but is increased for the dehydrogenation of iso-propanol into acetone (used as a measure of basicity test reaction) (Fig. 6.3).
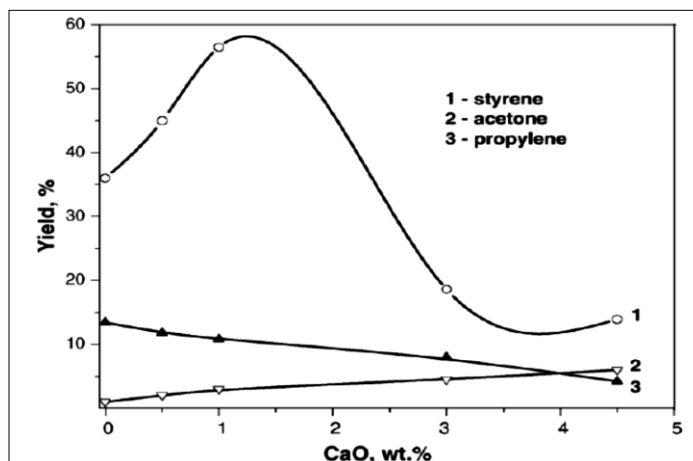
Fig. 6.3 The dependence of styrene (1), acetone (2) and propylene (3) yields upon the CaO content of CaO/SiO_2 catalyst [11].

It was notable that only iso-propanol dehydration occurred over SiO_2 treated by hydrochloric acid and 7% P/SiO_2. The strong dependence of styrene yield and selectivity upon calcium oxide concentration could be associated with presence of optimal ratio of base and acid centres taking part in activation of EB and oxygen which resulted in formation of catalytically active CD. With increasing average pore radius of silica gel from 1.1 up to 7.0 nm styrene conversion rose (Table 6.2).

The texture characteristics and catalytic properties of silica gels at OD of ethylbenzene[a]							
Samples of silica gel	Average radius of pores (nm)	Specific surface (cm^2/g)	Total volume of pores (cm^3/g)	Conversion of ethylbenzene (%)	Yields (%)		CD^b (%)
					Styrene	CO_2	
SiO_2-I	1.1	527	0.29	23.2	18.5	2.3	5.0
SiO_2-II	1.6	715	0.57	31.4	23.0	4.5	8.5
SiO_2-III	3.5	522	0.92	39.1	30.0	5.5	13.0
SiO_2-IV	5.2	376	0.97	42.7	33.0	6.9	16.0
SiO_2-V	7.0	333	1.19	47.0	36.3	7.0	17.5
SiO_2-VI	8.5	300	1.10	39.9	32.0	6.8	16.5

Table. 6.2 The texture characteristics and catalytic properties of silica gels at OD of ethylbenzene [11].

Likewise, an analogous dependence was observed also for CaO/SiO_2, prepared using different silica gels. It can be seen in Fig. 6.4 that the larger the average pore radius, the higher the impact of calcium oxide exerted on EB conversion.

In addition, the general increase in conversion with time on stream can be seen to occur for the 1% $CaO-SiO_2$-V catalyst but not the 1% $CaO-SiO_2$-I material.
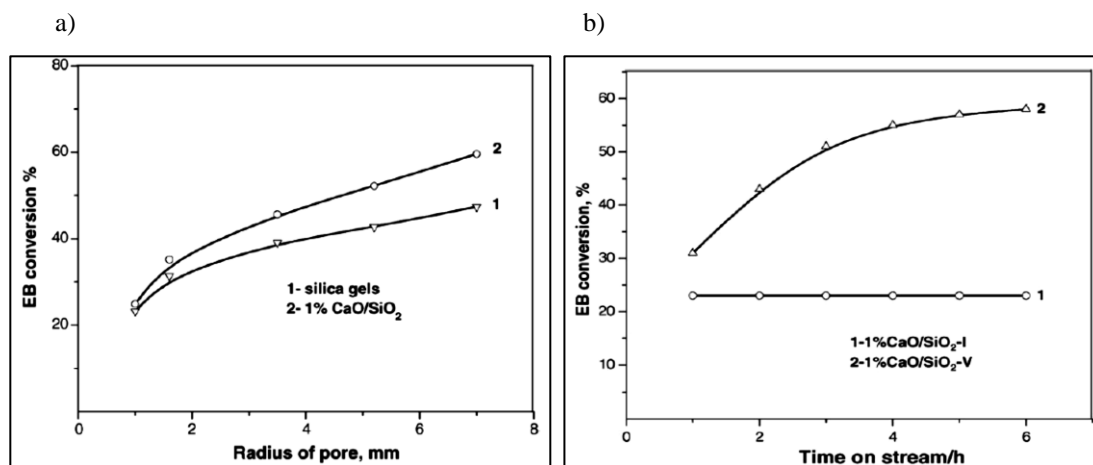
Fig. 6.4 a) The dependence of EB conversion from average radius of silica gels (1) and 1% CaO/SiO_2 pores (2) (temperature = 487 ^{o}C, space velocity = 0.5 h^{-1}). b) The dependence of EB conversion from time on stream (temperature = 487 ^{o}C, space velocity = 0.5 h^{-1}) [11].

In the thermal analysis of the l% CaO/SiO_2 catalyst only an exothermic peak with a maximum at 773 K was detected. The treatment of SiO_2 and $xCaO/SiO_2$ with phosphoric acid caused an increase of conversion of EB and selectivity of styrene (Table 6.3).

Catalyst	Conversion of ethyl-benzene (%)	Selectivity on styrene (%)	CD (%)
SiO_2-V	47.4	76	17.5
6% P/SiO_2	55.8	82	19.5
1% CaO/SiO_2	59.6	83	8.5
3% $P/1\%$ CaO/SiO_2	72.1	91	17.0
6% $P/4.5\%$ CaO/SiO_2	64.0	92	14.0

Table. 6.3 OD of ethylbenzene over silica gel (sample V) modified by calcium and/or phosphorus [11].

The dependence of styrene yield upon content of phosphorus in yP/SiO_2 samples passed through a weak maximum corresponding to 6-7% of phosphorus. Thermal analysis showed that the quantity of CD in the case of 7% P/SiO_2 was greater than for SiO_2. High conversion of EB was observed in the case of $yP/xCaO/SiO_2$ catalysts. The introduction of phosphorus into $xCaO/SiO_2$ diminished the yield of CO_2, the time required to achieve steady state and increased selectivity to styrene. The optimal quantity of phosphorus for

this series of catalysts depended upon the content of CaO (Fig. 6.5). Maximum conversion of EB was observed for 1% CaO/SiO_2 and 4.5% CaO/SiO_2 at 3 and 6% content of phosphorus respectively.
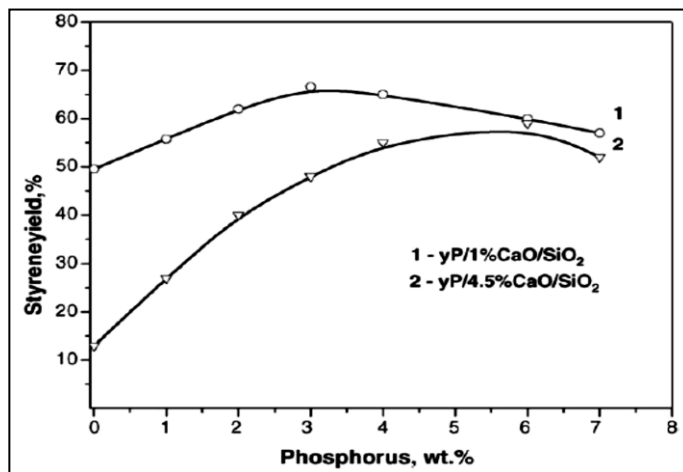
Fig. 6.5 The dependence of styrene yield from quantity of phosphorus in catalysts yP/l% CaO/SiO_2 (1) and yP/4.5% CaO/SiO_2 (2) (temperature = 487 ^{o}C, space velocity = 0.5 h^{-1}) [11].

The comparative thermogravimetric analysis of SiO_2 and $xCaO/SiO_2$ did not reveal a significant variation in the thermal behaviour of these samples apart from the change of concentration of surface hydroxyl groups. The decomposition process of silica gel impregnated by calcium nitrate was completed at 300–500 ^{o}C and the adsorption of cations was initiated. The nature of the calcium cation interaction with the surface was complicated and led to an alteration of the pore structure and the concentration of hydroxyl groups over the modified sample. The surface of silica gel has a weak acidity and many ions were rather strongly and even irreversibly held. The surface of silica gel became more effective for activation of reacting molecules. The characteristic feature of the given series of catalysts was a presence of a non-steady-state period at the beginning of reaction related to the formation and accumulation of CD which was accompanied by increase of EB conversion up to a maximum and a relatively constant value. Catalysts entirely regenerated by air at 773 K as well as fresh samples possessed low starting activity, however, after some time on stream conversion of EB reached the maximal value. For various types of SiO_2 (quartz glasses, Aerosils) only the macroporous silica gels showed good activity in the EB OD reaction. After treatment by acid, the activity of silica gel was increased,

however it was accompanied by excessive accumulation of CD leading to further reduction of styrene yield. EPR spectra showed that concentration of the paramagnetic centres in CD was increased with the rise of CD quantity and continued to grow after establishing steady state reaction. The concentration of the paramagnetic centres after 2 h was $1.7 - 10^{17}$ spin g^{-1}, but after 20 h it increased to $3.4 \cdot 10^{19}$ spin g^{-1}. The accumulation process of excessive CD may be slowed down by modification of SiO_2 with different oxides. In fact, the introduction of 0.5–1% CaO into the silica gel composition changes the acid–base properties and texture characteristics. Conversion of EB over 1% CaO/SiO_2 was higher than over SiO_2 with a lower rate of CD accumulation in the steady state reaction period. Calcium atoms appear to impact favourably on the formation of anionic vacancies, which make the surface of SiO_2 more open for activation of EB molecules with participation of co-ordinately unsaturated Si^{IV}, which are electron-acceptor centres [12]. In the activation of EB the surface hydroxyl groups can participate also. The activation of oxygen occur out on the electron-donor centres representing the lattice oxygen and anionic vacancies, the concentrations of which, according to EPR spectra, increased when CaO was introduced into silica gel composition. The continuous increase of EB conversion and selectivity to styrene in the case of $yP/xCaO/SiO_2$ appeared to be related to several factors. So, upon the impregnation of phosphoric acid on silica gel new hydroxyl groups were likely to be characterised by a higher electron-acceptor ability [13]. The thermal treatment caused formation of surface groups which were reversibly re-hydroxylated into acid groups partly covering the surface [14]. Investigation of texture characteristics of phosphorus-containing silica gels showed that at the introduction of phosphoric acid, the specific surface area was decreased but the total pore volume remained constant with increasing average pore radius. In contrast, phosphoric acid neutralised a fraction of the strongly basic centres, and decreased the yield of CO_2 and thereby improved selectivity of styrene. The presence of maxima in the dependence of styrene yield on phosphorus content in $yP/xCaO/SiO_2$ samples was proposed to be connected with the optimal ratio of the concentrations of the centres activating EB and oxygen. The duration of steady-state activity was determined by the ratio of consumption and resumption rates of oxygen-containing groups in the CD composition. On the $3\%P/1\%CaO/SiO_2$ catalyst a slow decrease of styrene yield was observed only after 8–10 hours on stream. However, aerating the catalyst for 30–40 min practically restored maximal conversion of EB. Furthermore, calcium- and phosphorus-containing catalysts were characterised by high accumulation rate of CD in the initial

reaction period (63– 68 mg g^{-1} h^{-1}) and a drastic decrease of this value during steady-state operation. Thus, the promoting influence of optimal quantities of CaO and phosphorus on the activity of silica gels appeared to be linked to creating and balancing of acid and base centres of definite force activating EB and oxygen molecules that further resulted in formation of catalytically active CD in optimal quantity. Excessive CD accumulation on the catalyst surface and its highly condensed character promoted deactivation of catalytic system in EB OD.

The above summary illustrates some of the effects of the application of a SiO_2 support reported in the literature. Particular focus was placed upon the study involving CaO/SiO_2, as this material is closest to those applied for the work described in the following section.

6.2 Results and discussion.

6.2.1 5% CaO/SiO$_2$.

5% CaO/SiO_2 and $Pd/MgO/SiO_2$ catalysts were used to catalyse the vapour phase aldol condensation reaction of acetone at different temperatures (200 ^{o}C, 300 ^{o}C, and 400 ^{o}C). Using the SiO_2 support has two potential major advantages: (i) enhanced the mechanical stability of the active CaO phase, and (ii) increased dispersion of CaO which can be anticipated to increase the relative proportion of the lowest co-ordinated O^{2-} sites (3 co-ordinate sites) which are anticipated to exhibit the highest base strength. Conversions, selectivities and yields were calculated, analysed and compared with other studies.
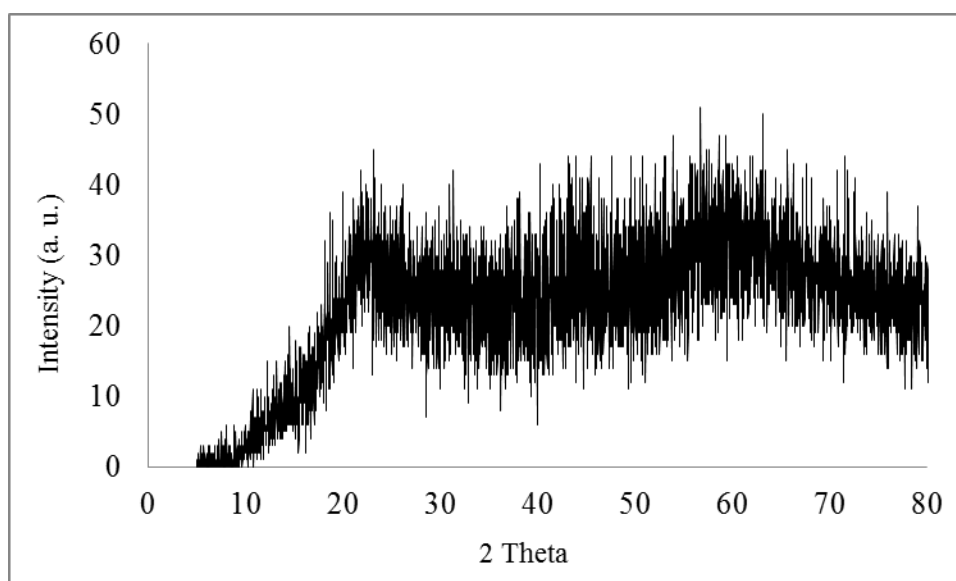
Fig. 6.6 The XRD pattern for 5% CaO/SiO_2 catalyst before at 400 ^{o}C for 24 h.

The X-ray diffraction pattern of the 5% CaO/SiO_2 material is shown in Figure 6.6. The pattern is highly amorphous, and so little information can be obtained. The relative quantity of CaO in the material is low, and possibly below detection limits, and the XRD pattern is consistent with amorphous SiO_2.

Scanning electron micrographic investigation of the 5% CaO/SiO_2 sample revealed that features, possibly CaO, randomly distributed on the silica surface with irregular particle size (Fig. 6.7).
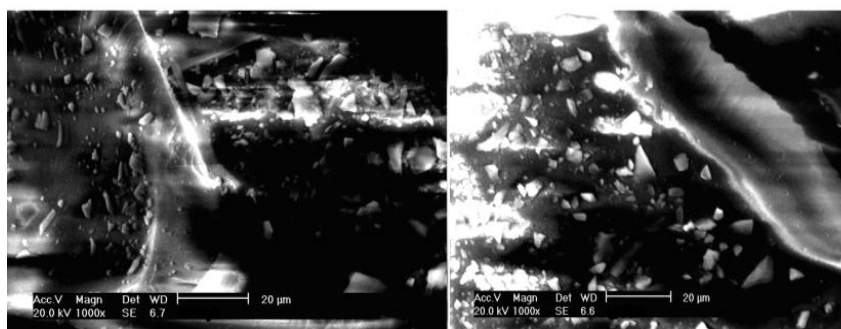
Fig. 6.7 Scanning electron microscopy (SEM) images for 5% CaO/SiO_2 catalyst.

CHN analysis has been applied to the 5% CaO/SiO_2 catalyst before and after reaction at 400 ^{o}C for 24 h (Table. 6.4). The sample prior to reaction contained 0.74/0.59 wt% of hydrogen and 2.13/2.10 wt% nitrogen but no carbon was detected. The small amount of hydrogen was believed to originate from water during the preparation process and surface hydroxyl groups. Nitrogen was introduced from the $Ca(NO_3)_2$ precursor that was used as a source of CaO in the preparation. In comparison, the post-reaction sample comprised of 7.51/7.99 wt% carbon and 1.03/1.13 wt% hydrogen. The absence of nitrogen in the post-reaction sample is noteworthy and indicates that decomposition of the nitrate has occurred.

	C	H	N
Pre-reaction sample	-	0.74/0.59	2.13/2.10
Post-reaction samlpe	7.51/7.99	1.03/1.13	-

Table. 6.4 CHN analysis (wt%) for 5% CaO/SiO_2 before reaction and after reaction at 400 ^{o}C for 24 h.
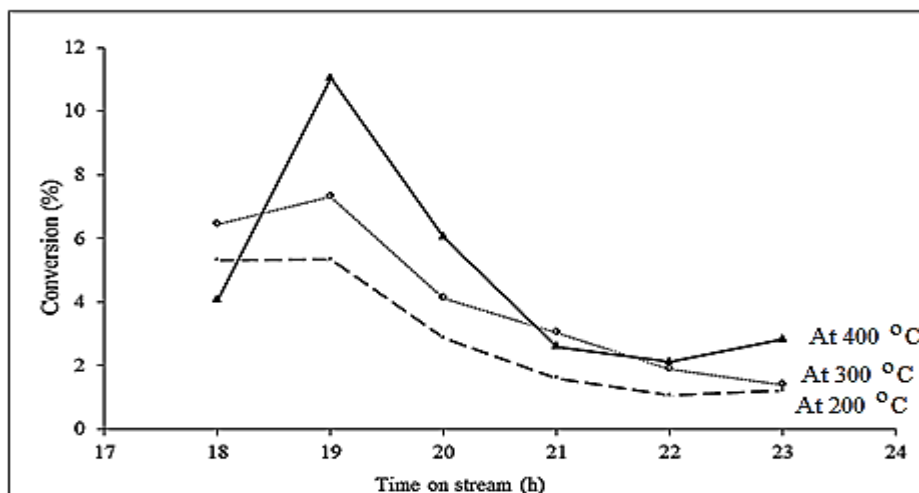
Fig. 6.8 Percentage conversions of acetone over 5% CaO/SiO$_2$ catalyst, after 18 h of reaction, as a function of time on stream at 200 ^{o}C, 300 ^{o}C, and 400 ^{o}C, 5 bar H$_2$ pressure, TOS > 18h.

The conversion of acetone is observed to increase with increase in reaction temperature (Table. 6.5) and decrease as reaction time increases (Fig. 6.8). No product was formed within the initial period of reaction; this is probably due to the period of time for carbon to lay down onto the catalyst and possible modification of the catalyst surface. The modified catalyst was then subjected to a period of reaction from 18-20 h which leads to more stable behaviour of the catalyst. It can be observed from Table 6.5 that by increasing reaction temperature within the range (200-400 ^{o}C) the DAA selectivity is slightly decreased from 7.30% to 3.04%, which can be attributed to the increase of dehydration capacity of DAA to MO with increasing temperature indicating that the catalyst has a hydrogenation capacity to form MIBK and this capacity increases with increasing temperature under a hydrogen atmosphere. This result is agreement with Kelly and Jackson's [15] work since they did not report the formation of DAA in their product stream.

The catalytic activity is generally fairly stable beyond 20 h of reaction (Fig. 6.8). The result is in agreement with work by Canning and Jackson [16] who studied the same reaction on a CsOH/SiO$_2$ catalyst at reaction temperatures between 100 and 400 ^{o}C and who reported the highest yield for MO at 300 ^{o}C and the highest selectivity of MO at 200 ^{o}C. Another study reported a yield of 25% for isophorone in the temperature range (350-400 °C) using CaO or Ca(OH)$_2$ catalyst prepared by the deposition of a calcium salt on certian alumina supports followed by calcination [17]. Moreover, acetone conversions in the present study

are between 4-6% and are strongly dependent on the reaction temperature (Fig. 6.8) and the maximum value observed at 300 °C was 6%. The conversions observed are generally greater than those reported by Kelly and Jackson [15] (1.2-3.0%) under similar conditions. The highest selectivity of 60.72% observed at 200 °C for the MO is considerably different than that obtained by Canning and Jackson [16] which was 85% (observed at 200 °C). This may indicate that alkaline earth oxide catalysts are more active for the aldol condensation reaction of acetone than the alkali metal oxides whereas the latter are more selective for MO.
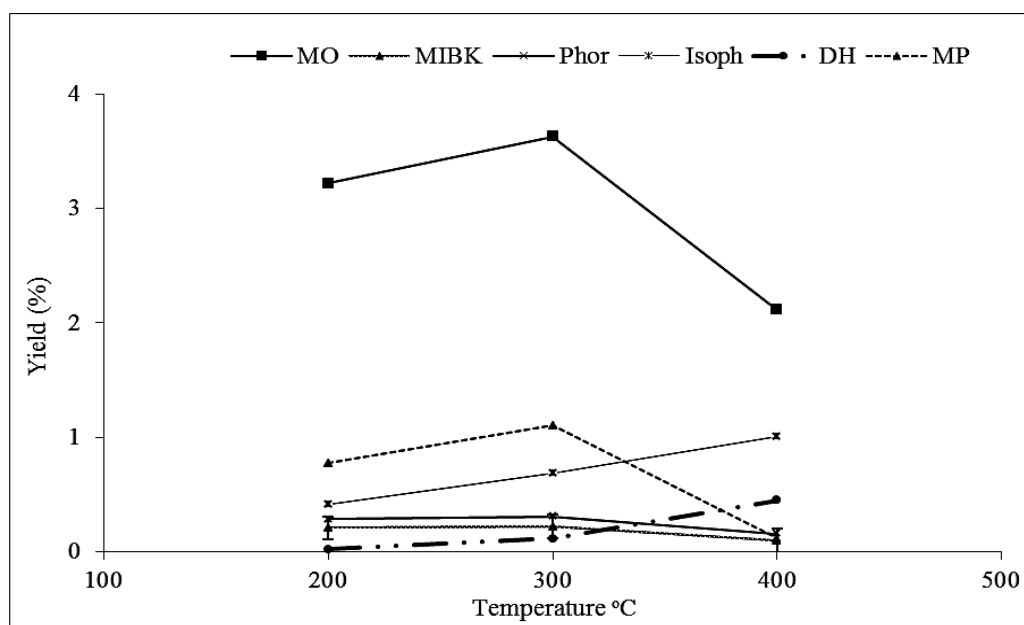
Fig. 6.9 Percentage yields of the condensation and hydrogenation products of acetone as a function of temperature over 5% CaO/SiO$_2$ catalyst (At 200 °C, 300 °C and 400 °C, 5 bar H$_2$ pressure, TOS > 18 h).

Yields are relatively low and are increased by raising reaction temperature to reach a maximum value at 300 °C for MO of 3.63%. Subsequently, the yield is strongly decreased (Fig. 6.9). It also can be observed from that above 300 °C the yield of MO is decreased due to the sequential formation of higher molecular weight molecules from the aldol condensation of MO with an additional acetone molecule. The formation of these heavy products is consistent with number of previous studies such as that by Di Cosimo et al [18]. In that study, phorone and isophorone formation as precursors to non-volatile organic compounds that caused coke formation and deactivation of an MgO catalyst for the aldol

condensation of acetone was studied. It was concluded that the isophorone was formed from a direct internal 1,6-Michael addition of phorone. Further heavier molecules are formed such as 4-methyl-2-pentanol from the hydrogenation of the MIBK. Aldol condensation of MIBK and acetone yields 2,6-dimethylheptan-4-one.

Temperature ^{o}C	Conversion (%)	Selectivity (%)						
		DAA	MO	MIBK	Ph	Isoph	DH	MP
200	5	7.30	60.72	3.91	5.33	7.80	0.44	14.60
300	6	6.03	56.24	3.40	4.80	10.70	1.81	17.10
400	4	3.04	52.00	2.43	3.90	24.80	11.10	2.84

Table. 6.5 Conversions and selectivities as a function of temperature for the aldol condensation reaction over 5% CaO/SiO$_2$ catalyst (200 ^{o}C, 300 ^{o}C and 400 ^{o}C, 5 bar H$_2$ pressure, TOS > 8 h).

The catalyst shows a high selectivity for MO (mesityl oxide) of ca. 61% at 200 ^{o}C illustrating that MO is clearly the main product (Fig. 6.10) in agreement with a number of studies [19]. This indicates that the hydrogenation process of MO to MIBK is not favoured which can be expected due to absence of a metal hydrogenation function. However, the inclusion of a Pd metal dopant, as discussed later, would be expected to assist the hydrogenation of MO to MIBK. The selectivity for isophorone is significant particularly at 400 ^{o}C where it is 25% which is in agreement with Lippert et al [20]. In that study, the same reaction over a non-supported Ca(OH)$_2$ catalyst between 200-400 ^{o}C showed a high selectivity for isophorone. However, the acetone conversion (4-6%) is much lower than that achieved by Lippert et al [20] which was 43%. This difference may relate to the presence of silica support, indicating that silica support may negatively influence the performance of calcium oxide catalyst. However, this suggestion is not proved.
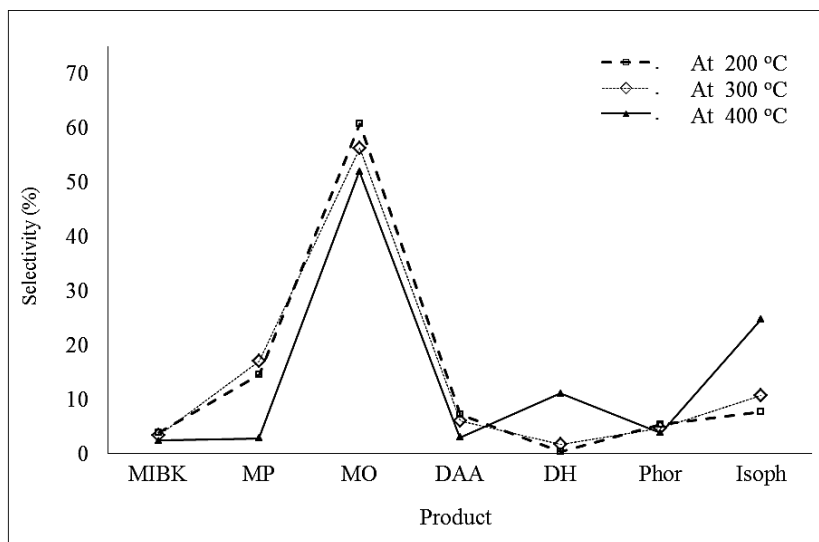
Fig. 6.10 Percentage selectivities, after 18 h of reaction, as a function of temperature for the aldol condensation reaction over 5% CaO/SiO$_2$ catalyst at 200 ^{o}C, 300 ^{o}C and 400 ^{o}C, 5 bar H$_2$ pressure, TOS > 18 h.
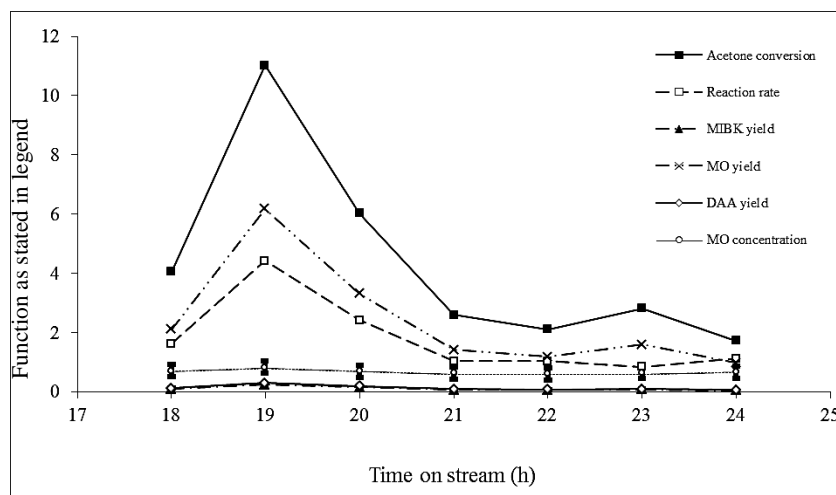
Fig. 6.11 Reaction rate and conversion for the aldol condensation reaction of acetone over 5% CaO/SiO$_2$ catalyst as a function of temperature (T = 400 ^{o}C, P = 5 bar H$_2$ pressure).

Figure 6.11 demonstrates that the rate of mesityl oxide formation is very low even at low conversion levels. The production of MO from DAA is an eqiluibrium limition as discussed early in this thesis. Bases on this, the simultaneous hydrogenation of mesityl oxide may help in shifting the reaction in the forward direction by keeping the mesityl oxide concentration at low level at any given time within the reaction period. However,

Winter et al [21] showed that 100% conversion mesityl oxide in liquid phase could be achieved on a Pd/CNF catalyst.

6.2.2 1%Pd5%MgO/SiO$_2$.

In order to assess whether the "one pot" conversion of acetone to MIBK was possible a Pd/MgO/SiO$_2$ catalyst has been screened. This is a bifunctional system in that a base component (MgO) and a hydrogenation component (Pd) are present.
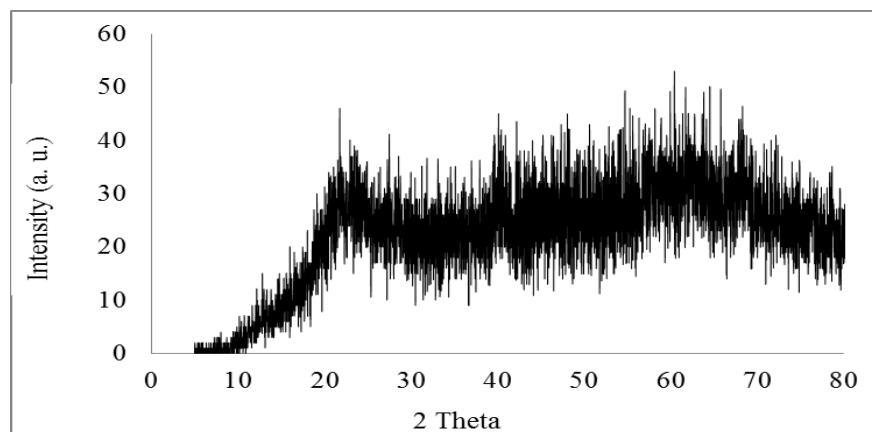
Fig. 6.12 X-ray diffraction (XRD) pattern for 1%Pd5%MgO/SiO$_2$ catalyst after reaction at 400 ^{o}C for 24 h.

The post-reaction XRD pattern shown in Fig. 6.12 is amorphous and it is not possible to discern features associated with the MgO and Pd components.

The SEM images of 1%Pd5%MgO/SiO$_2$ catalyst showed that there is a high dispertion of the catalyst over the silica support Fig. 6.13.
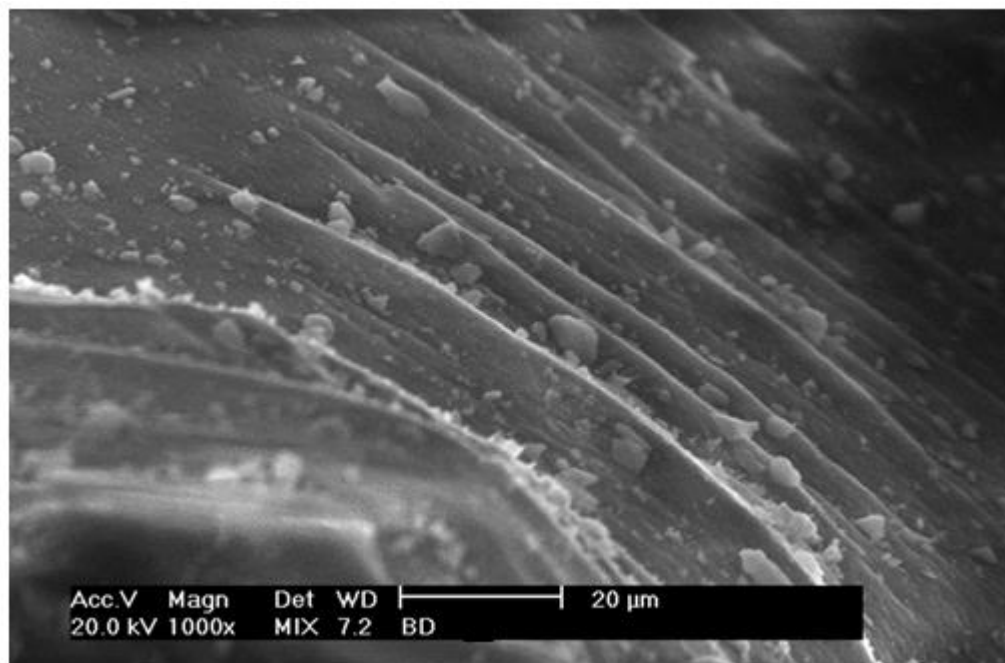
Fig. 6.13 SEM image of the 1%Pd5%MgO/SiO$_2$ catalyst.

The CHN analysis for the post-reaction 1%Pd5%MgO/SiO$_2$ catalyst showed that carbon was present on the post-reaction catalyst with a high amount of 5.31/5.11% with small amount of 0.91/0.82% of hydrogen were produced during the reaction Table. 6.6. However, nitrogen was not detected within the catalyst.

	C	H	N
Pos-reaction	5.31/5.11	0.91/0.82	-

Table. 6.6 CHN analysis for 1%Pd5%MgO/SiO$_2$ catalys post-reaction reaction at 400 ^{o}C for 24 h.

The aldol condensation reaction of acetone was performed over a 1%Pd5%MgO/SiO$_2$ catalyst in the temperature range of 100–400 ^{o}C. The catalyst was pre-treated at 450 ^{o}C under N$_2$ for 2 h to convert the Mg(NO$_3$)$_2$ and Pd(NO$_3$)$_2$ to NO$_2$ and subsequently oxidise to MgO, PdO and Pd. However, under H$_2$ gas the following reaction occurs on SiO$_2$ surface:

$$MgO + H_2O \longrightarrow Mg(OH)_2$$

$$PdO + H_2 \longrightarrow Pd + H_2O$$
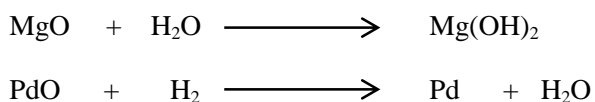
Average conversions of 7–23% were obtained after 18 h of the reaction and the catalyst was highly selective to MIBK with 73.92% at 200 ^{o}C due to the presence of the hydrogenation site (Table. 6.7). This result is consistent with previous studies including that of Rodrigues and Monteiro [22] who studied the same reaction on Pd/NaX catalyst at 250 ^{o}C and revealed that MIBK was the most selective product being 80%, Nikolopoulos and Jang [23] have also achieved similar results for MIBK synthesis over Pd supported on hydrotalcite (HT)-derived Mg–Al mixed-oxide catalyst at 99–153 ^{o}C.

Temperature ^{o}C	Conversion (%)	Selectivity(%)						
		DAA	MO	MIBK	Phorone	Isophorone	26DMH	4MP
100	7	6.46	10.69	54.45	4.07	6.37	8.18	9.77
200	20	2.18	2.33	73.92	1.36	1.90	6.56	11.76
300	23	1.95	1.61	72.18	1.22	1.61	12.65	8.73
400	10	3.11	28.68	47.94	1.96	6.66	8.50	3.20

Table. 6.7 Conversions and selectivities as a function of temperature for the aldol condensation reaction over 1%Pd5%MgO/SiO$_2$ at 400 ^{o}C, 5 bar H$_2$ pressure, TOS > 18 h.
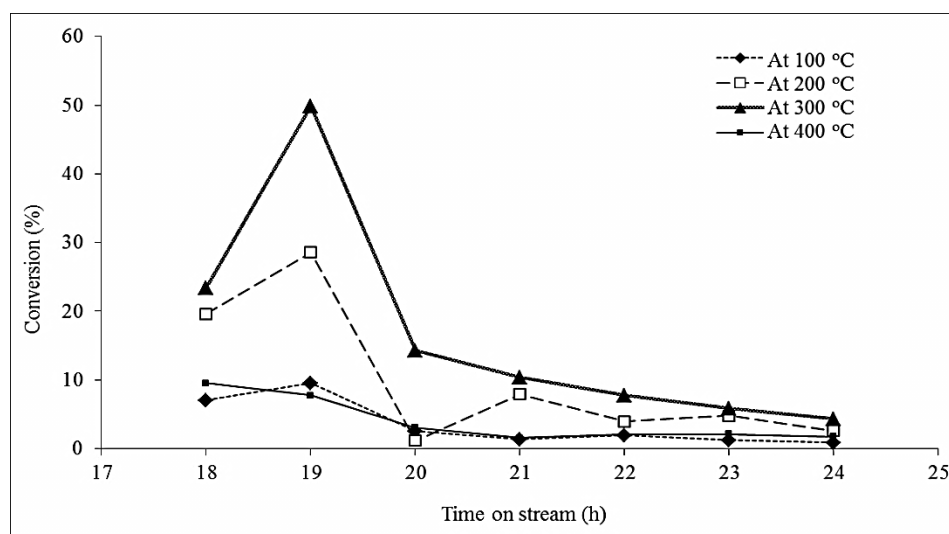
Fig. 6.14 Percentage conversions of aldol condensation, after 18 h of reaction, over 1%Pd5%MgO/SiO$_2$ as a function of time on stream at (100 ^{o}C, 200 ^{o}C, 300 ^{o}C, and 400 ^{o}C, 5 bar H$_2$ pressure, TOS > 18).

The conversion is less than 10% at 100 ^{o}C which is similar to previous work reported by Mattos et al on Pd/X zeolite [24] and Chen et al on Pd/SiO$_2$ and Pd/CaO–Al$_2$O$_3$ [23]. By in creasing reaction temperature (100–300 ^{o}C) there is a large increase of conversion. The catalyst shows high performance during the first period of reaction before it reaches a more

stable state after 20 h reaction time (Fig. 6.14). At 400 ^{o}C, the conversion is lower which may be due to accelerated deactivation either by coking or by sintering. MO was formed in all experiments which indicates that the quantity/activity of the metal phase is insufficient to carry out total hydrogenation.
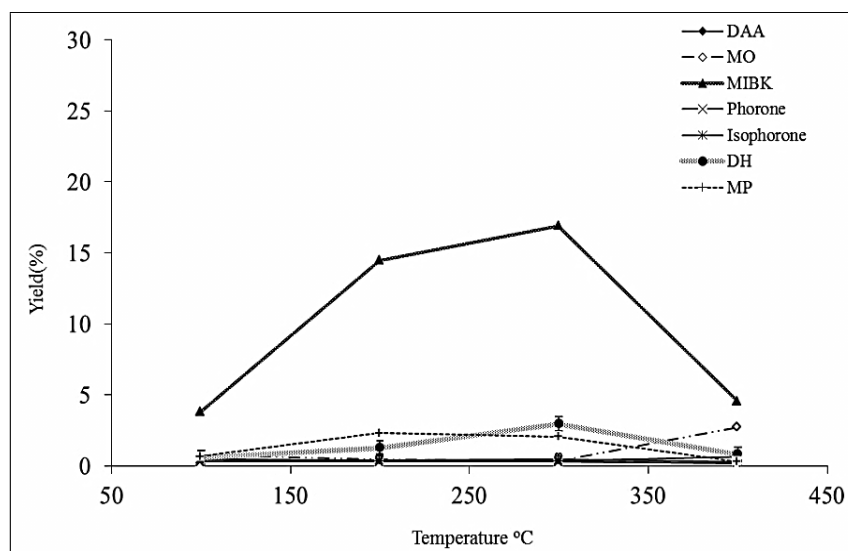
Fig. 6.15 Percentage yields of the condensation and hydrogenation products of acetone as a function of temperature on 1%Pd5%MgO/SiO$_2$ catalyst at 100 ^{o}C, 200 ^{o}C, 300 ^{o}C and 400 ^{o}C, 5 bar H$_2$ pressure, TOS > 18 h.

It can be observed from Fig. 6.15 that the MIBK yield over 1%Pd5%MgO/SiO$_2$ is relatively high. It increases with increasing temperature to reach a maximum of ca. 17% at 300 ^{o}C followed by a sharp decrease due to the formation of heavier by-products. The hydrogenation of MO to MIBK over palladium metal is obviously fast.
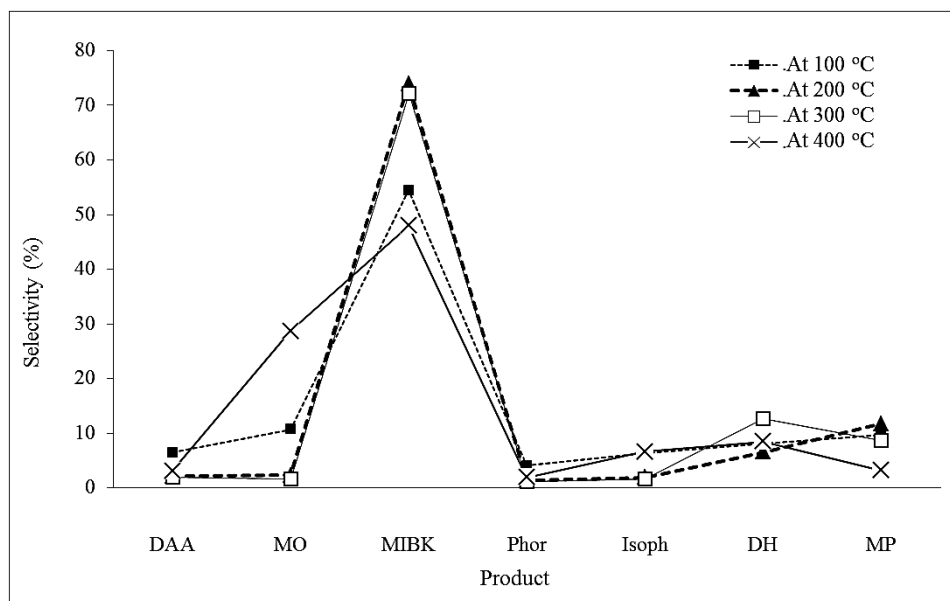
Fig. 6.16 Percentage selectivities as a function of temperature for the aldol condensation reaction over 1%Pd5%MgO/SiO$_2$ catalyst at 100 ^{o}C, 200 ^{o}C, 300 ^{o}C and 400 ^{o}C, 5 bar H$_2$ pressure, TOS > 18 h.

MIBK selectivity increases from ca. 54% to ca. 74% by increasing temperature from 100-200 ^{o}C and then it decreases dramatically to 48% at 400 ^{o}C due to the formation of heavier molecules (Fig. 6.16). The optimal performance was obtained at 300 ^{o}C. This is consistent with the work of Chen et al who found similar MIBK selectivity over Pd/KHZSM-5 catalyst at 250 ^{o}C [25]. Olson et al also reported similar MIBK selectivity 70–80% at 20 ^{o}C on a Ni/MgO catalyst [26].

6.3 Conclusion.

The aldol condensation reaction of acetone has been investigated in this chapter over 5%CaO/SiO$_2$ and 1%Pd5%MgO/SiO$_2$. The two catalysts showed significant activity for the reaction but they behaved differently (Fig. 6.17). The 5% CaO/SiO$_2$ catalyst exhibited high selectivity (ca. 52%) toward the MO but on the catalyst that contained palladium, some of MO was hydrogenated to MIBK (Fig. 6.18). It is believed that the presence of palladium metal is responsible for the hydrogenation process. Thus the MIBK has achieved a high selectivity of ca. 48% on this catalyst. The palladium catalyst is highly active for MIBK synthesis while the CaO/SiO$_2$ is better for the production of MO.
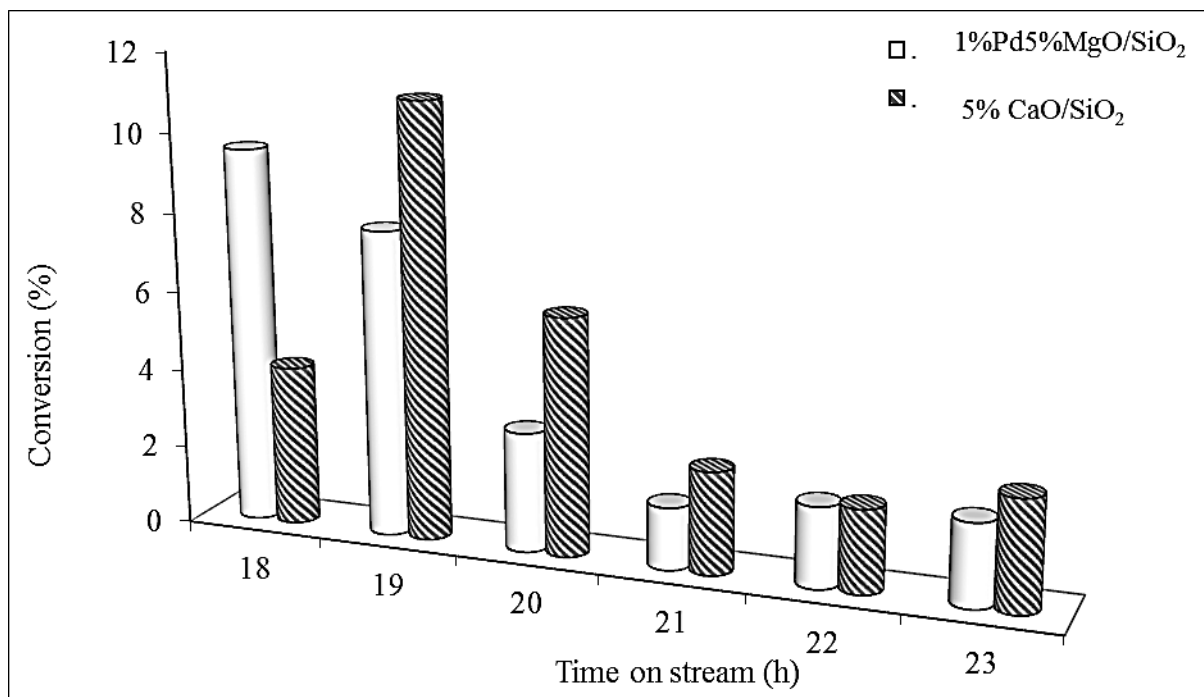
Fig. 6.17 Comparison of conversions between 5% CaO/SiO$_2$ and 1%Pd5%MgO/SiO$_2$ catalysts at 400 ^{o}C, 5 bar H$_2$ pressure, TOS > 18 h.
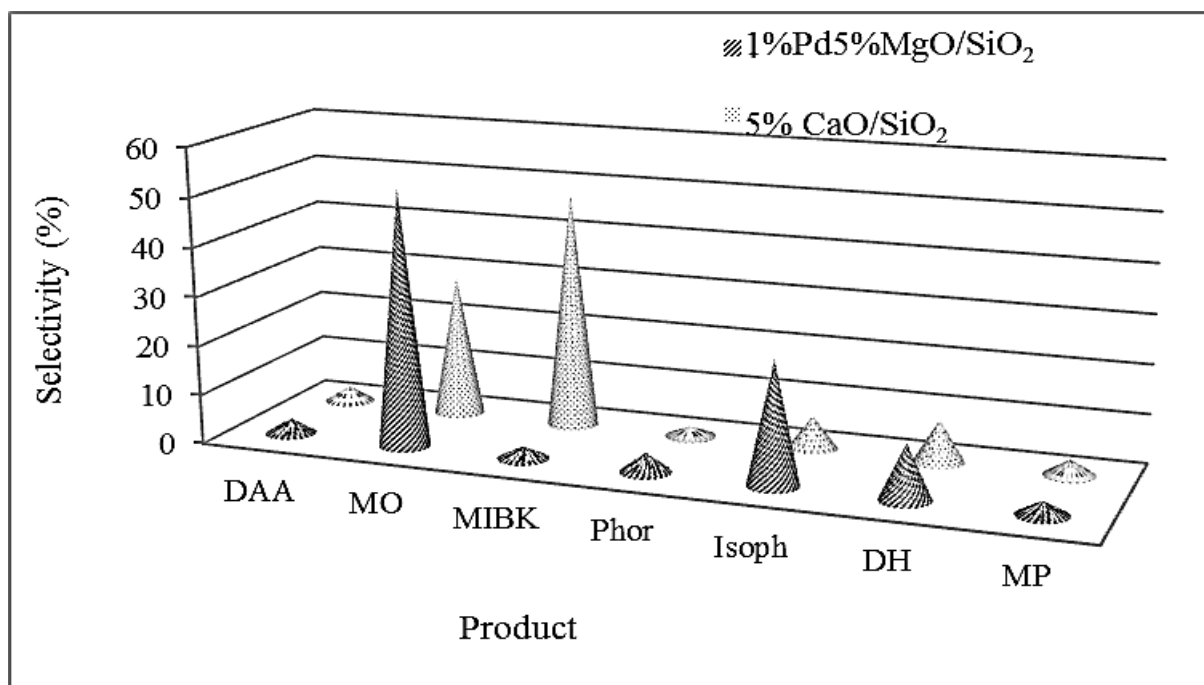
Fig. 6.18 Illustration of products selectivities over 5% CaO/SiO$_2$ and 1%Pd5%MgO/SiO$_2$ catalysts at 400 ^{o}C, 5 bar H$_2$ pressure, TOS > 18 h.

6.4 References.

[1] R. T. Yang, "Adsorbents: fundamentals and applications", John Wiley and Sons, ISBN: 0471297410, 9780471297413 (2003).

[2] J-E Otterstedt, and D. A. Brandreth, "Small particles technology", Springer, ISBN: 0306459353, 9780306459351 (1998).

[3] A. Dabrowski, and V. A. Tertykh, "Adsorption on new and modified inorganic sorbents", Elsevier, ISBN: 0444821791, 9780444821799 (1996).

[4] V. Ponec, *Appl. Catal.* **222**, 31 (2001).

[5] S. I. Lerman, and C. C. Scheerer, "Instrumentation –The chemical behavior of silica", Ultrapure Water, **24** (1988).

[6] L. F. Comb, *Ultrapure Water*, **41** (1996).

[7] C. N. Satterfield in "Heterogeneous catalysis in industrial practice", 2nd ed., Eds: McGraw-Hill (1991).

[8] K. K. Unger, *J. Chromato.* (1988).

[9] E. F. Vansant, P. Voort, and K. C. Vrancken, "Characterization and chemical modification of the silica surface", 2nd ed., Elsevier, ISBN: 0444819282, 9780444819284 (1995).

[10] S. S. Kistler, *Nature* **127**, 741 (1931).

[11] D. B. Tagiyev , G. O. Gasimov, and M. I. Rustamov, *Catal. Today* **102**, 197 (2005).

[12] H. Noller, and J. M. Pearo, *J. Res. Inst. Catal.* **29**, 95 (1981).

[13] M. L. Hair, W. Hertle, *J. Phys. Chem.* **74**, 91 (1970).

[14] M. J. D. Low, and P. Ramamatry, *J. Phys. Chem.* **72**, 3161 (1968).

[15] G. J. Kelly, "Catalysis in Application", Eds S. D. Jackson, J. S. J. Hargreaves, and D. Lennon, RSC, Cambridge, ISBN: 0854046089, 9780854046089 (2003).

[16] A. Canning, S. Jackson, E. McLeod, and E. Vass, *Appl. Catal.* **289**, 59 (2005).

[17] T. H. Vaughn, D. R. Jackson, US Patent, 2183127 (1939).

[18] J. Cosimo, V. Díez, and C. Apesteguía, *Appl. Catal.* **137**, 149(1996).

[19] K.H. Lin, and A.N. Ko, *Appl. Catal.* **147**, 259 (1996).

[20] S. Lippert, W. Baumann, and K. Thomke, *J. Mol. Catal.* **69**, 199 (1991).

[21] F. Winter, A. van Dillen, and K. de Jong, *J. Mol. Catal.* **219**, 273 (2004).

[22] A. C. C. Rodrigues,and J. L .F. Monteiro, *Stud. Surf. Sci. Catal.* **154**, 2395 (2004).

[23] A.A. Nikolopoulos, B.W. Jang and J. J. Spivey, *Appl. Catal.* **296**, 128 (2005)

[24] L. V. Mattos, F. B. Noronha, and J. L. F. Monteiro, *J. Catal.* **209,** 166 (2002).

[25] Y. Z. Chen, B. J. Liaw, H. R. Tan, and K. L. Shen, *Appl. Catal..*, **205**, 61, (2001).

[26] K. D. Olson, *U.S. Pat*. 4704478 (1987).

[27] H. V. Fajardo, E. Longo, D. Z. Mezalira, G. B. Nuernberg, G. I. Almerindo, A. Collasiol, L. F. D. Probst, I. T. S. Garcia, and N. L. V. Carren`o, *Environ. Chem. Let.* **8**, 79 (2010).

Chapter 7
Conclusions and future work.

Conclusions and future work.

Catalyst	Surface area (m^{2}g^{-1})	Conversion (%)	Surface area normalised conversion (mol m^{-2} h^{-1})	Major product selectivity (%)
1%Pd5%MgO/SiO$_2$	-	10	-	48 (MIBK)
5% CaO/SiO$_2$	-	4	-	52 (MO)
36.5% KNO$_3$/Al$_2$O$_3$	89	70	1.47E-01	44 (MO)
Li-MgO	3	65	5.04E-02	74 (MO)
36.5% KNO$_3$/ZrO$_2$	1	1	1.18E-02	38 (MO)
36.5% KNO$_3$/Zr(OH)$_4$	7	6	6.40E-03	44 (MO)
MgO derived from Mg(OH)$_2$.3MgCO$_3$	36	85	4.80E-03	88 (MO)
14% KNO$_3$/Al$_2$O$_3$	71	75	2.10E-03	81 (MO)
MgO derived from Mg(OH)$_2$	61	60	1.96E-03	82 (MO)
14% KNO$_3$/Zr(OH)$_4$	2	7	1.60E-03	39 (MO)
ZrO$_2$	5	6	1.10E-03	41 (MO)
14% KNO$_3$/ZrO$_2$	8	7	1.00E-04	62 (MO)
Y-Zr(OH)$_4$	108	8	1.19E-06	34 (Isoph)

Table 7.1 A comparison of conversions and selectivities of aldol condensation reaction of acetone over the all base catalysts used in this thesis at 400 ^{o}C, 5 bar H$_2$ pressure, TOS > 18 h.

A wide range of diverse materials has been screened for activity for acetone conversion. Taking 18 h on stream as a standard reaction time, comparisons can be made in terms of catalytic activity. The catalytic data is summarised in Table 7.1, where surface area normalised conversion data is also presented in order to give an indication of the intrinsic activity of the diverse set of materials screened. Total surface areas are used instead of specific surface area of active compononets. However, caution must be applied to this means of comparison in the cases of CaO/SiO$_2$ and Pd/MgO/SiO$_2$ where the BET surface area is dominated by the inactive SiO$_2$ support.

When the influence of surface area is taken into account, it can be seen that many of the materials have similar intrinsic activity, which is perhaps surprising although it must be recognised that the range of materials surveyed are basic metal oxides which are expected to exhibit activity for the reaction. Against this backdrop, the relatively high activities of Li/MgO and, in particular, KNO$_3$/Al$_2$O$_3$ should be noted. Whilst it may be tempting to ascribe this to a possible role of alkali metal ions, the comparatively low specific activities of the other K$^+$ doped materials suggests otherwise, and currently, there is no simple explanation for the enhanced intrinsic behaviour of Li/MgO and KNO$_3$/Al$_2$O$_3$.

MO was the major product observed over the all catalysts except 1%Pd5%MgO/SiO$_2$ since it was highly selective toward MIBK due to inclusion of the strongly hydrogenation component. General comparison between the all catalysts used in this study showed

maximum conversion of 85% achieved over MgO derived from $Mg(OH)_2.3MgCO_3$ while the minimum conversion of 1% was over the 36.5% $KNO_3/Zr(OH)_4$ catalyst. Therefore, it can be concluded that the most active catalyst for the aldol condensation reaction of acetone was MgO whereas the 36.5% $KNO_3/Zr(OH)_4$ revealed the weakest catalytic activity. Upon the catalysts that yielded MO as the main product, Y-$Zr(OH)_4$ catalyst accomplished the lowest selectivity of MO.

The influence of the nature of dopants/additional catalyst components is illustrated in the following comparison, Y-$Zr(OH)_4$ achieved 8% conversion and the catalyst was significantly selective to Isoph with 34%. In contrast, $1\%Pd5\%MgO/SiO_2$ catalyst exhibited a slightly higher conversion of 10% and the main product was MIBK with 48% selectivity. However, Li/MgO catalyst obtained, comparatively, the highest conversion of 65% and a maximum selectivity of 74% for MO. Li/MgO is highly active catalyst for aldol condensation reaction of acetone compared to Y-$Zr(OH)_4$, and $1\%Pd5\%MgO/SiO_2$. Since production of Isoph requires strong basic sites, this suggests that Y-$Zr(OH)_4$ possesses strong basicity. Production of MIBK is considerably favoured over $1\%Pd5\%MgO/SiO_2$ catalyst which is due to the well documented ability of palladium for hydrogenation.

Non-doped catalysts including 5% CaO/SiO_2, ZrO_2 and MgO derived from $Mg(OH)_2$ and $Mg(OH)_2.3MgCO_3$ have shown different behaviour for the aldol condensation reaction of acetone. Differences are also apparent for the same phase prepared by different routes. MgO derived from $Mg(OH)_2$, and $Mg(OH)_2.3MgCO_3$ precursors were active catalysts. They exhibited conversion of 60%, and 85% respectively. Maximum selectivities of 88% over MgO derived from $Mg(OH)_2.3MgCO_3$ and 82% by MgO derived from $Mg(OH)_2$ were also achieved for MO. When surface area is taken into consideration, it can be seen that the basic carbonate precursor leads to the most active catalyst. This can be ascribed to the role of morphology and/or different impurity catalysts. However, the 5% CaO/SiO_2 catalyst exhibited a low conversion of 4% and selectivity of 52%, lower than magnesia but greater than that obtained by zirconia. Although zirconia showed higher activity than 5% CaO/SiO_2 catalyst since it achieved slightly greater conversion of 6%, it was moderately less selective to MO product with only 41%. The remarkable difference between the results obtained by these three base catalysts may be attributed to various factors including crystalline phases, basicity, and surface area. The results also reveal variable basicity of the three catalysts as shown the figure below.
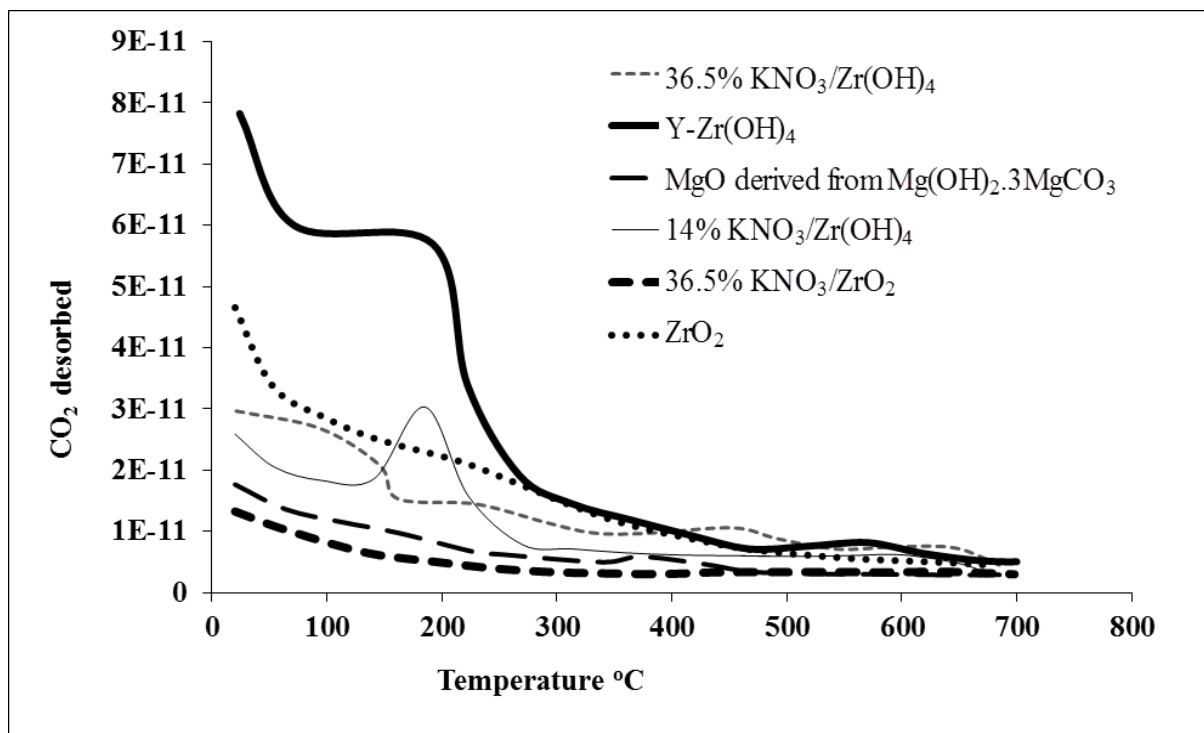
Figure 7.1 CO_2-TPD data for various catalysts tested.

The basis of this thesis has been a comparison of solid bases for acetone conversion, a base catalysed reaction. Accordingly, it would be of importance to determine the base site strengths and base site numbers for each of the materials screened. However, as outlined in Chapter 1, this is not trivial. CO_2-TPD has been applied for this purpose. Unfortunately, due to experimental problems, it did not prove possible to apply this method to all the materials screened. CO_2-TPD data for the materials which were successfully investigated are presented in Figure 7.1. It should be noted that since 700 ^{o}C was the upper desorption temperature which could be applied, due to experimental limitations, the spectra possoibly do not probe very strong base sites.

From the CO_2-TPD study it can be concluded that Y-Zr(OH)$_4$ catalyst comprised maximum numbers of weak to intermediate strength basic sites whereas the 36.5% KNO$_3$/ZrO$_2$ had the fewest. Yttria dopant increased the number of basic sites on hydrous zirconia while loading of KNO$_3$ on zirconia inhibited its basicity. When comparing activity and surface area and based on these CO_2-TPD results, it can be concluded that there is a proportional relation between the number of basic sites and surface area in which both can be accounted as important driving forces of catalytic activity of those catalysts for acetone conversions. The number of basic sites on ZrO$_2$ was also considerable. The 14wt% KNO$_3$

loaded $Zr(OH)_4$ appeared to possess a greater number of base sites of relatively well defined strength than its 36.5 wt% loaded counterpart.

Overall, it is clear that the materials tested in this thesis exhibited appreciable activity towards acetone conversion after 18 hours on stream under a H_2 containing atmosphere. This suggests that it may be possible, by suitable addition of a hydrogenation function, to develop single phase one-stage catalytic systems for the conversion of acetone to MIBK. The possibility of this approach has been exemplified by the $Pd/MgO/SiO_2$ system investigated in the present study, as well as others reported in the literature outlined in the introduction to this thesis. Based solely upon per pass conversion 14% KNO_3/Al_2O_3 and MgO derived from $Mg(OH)_2.3MgCO_3$ appear to be the best candidate systems, although attention should be directed towards the overall stability of the system in operation, as well as any effect (whether good or bad) induced by the introduction of the hydrogenation component. The optimum hydrogenation component, its loading and method of introduction, will also be crucial consedrations.

Injection Date: 10/20/2005 6:35 PM   Calculation Date: 10/20/2005 6:55 PM

Operator   : khalaf   Detector Type: ADCB (10 Volts)
Workstation: Bus Address : 18
Instrument : GC 2   Sample Rate : 10.00 Hz
Channel   : A = A   Run Time   : 20.002 min

** Star Chromatography Workstation Version 5.51 ** 01657-37c8-82a-2631 **

Chart Speed =   0.98 cm/min   Attenuation = 9916   Zero Offset = 2%
Start Time =   0.000   min   End Time   = 20.002 min Min / Tick = 1

Injection Date: 10/12/2005 3:56 PM   Calculation Date: 10/12/2005 4:16 PM

Operator   : Khalaf   Detector Type: ADCB (10 Volts)
Workstation: Storage Disc   Bus Address : 18
Instrument : GC 2   Sample Rate : 10.00 Hz
Channel   : A = A   Run Time   : 20.002 min

** Star Chromatography Workstation Version 5.51 ** 01657-37c8-82a-2631 **

Chart Speed =   0.98 cm/min   Attenuation = 9916   Zero Offset = 2%
Start Time =   0.000 min   End Time   = 20.002 min   Min / Tick = 1

Injection Date: 10/12/2005 3:56 PM   Calculation Date: 10/12/2005 4:16 PM

Operator   : Khalaf   Detector Type: ADCB (10 Volts)
Workstation: Storage Disc   Bus Address : 18
Instrument : GC 2   Sample Rate : 10.00 Hz
Channel   : A = A   Run Time   : 20.002 min

** Star Chromatography Workstation Version 5.51 ** 01657-37c8-82a-2631 **

Chart Speed =   0.98 cm/min   Attenuation = 9916   Zero Offset = 2%
Start Time =   0.000   min   End Time   = 20.002 min   Min / Tick = 1

Injection Date: 10/19/2005 1:29 PM   Calculation Date: 10/19/2005 1:49 PM

Operator   : khalaf   Detector Type: ADCB (10 Volts)
Workstation: Bus Address   : 18
Instrument : GC 2   Sample Rate   : 10.00 Hz
Channel   : A = A   Run Time   : 20.002 min

** Star Chromatography Workstation Version 5.51 ** 01657-37c8-82a-2631 **

Chart Speed =   0.98 cm/min   Attenuation = 9916   Zero Offset = 2%
Start Time =   0.000   min   End Time   = 20.002 min   Min / Tick = 1

Injection Date: 1/22/2008 12:50 PM   Calculation Date: 1/22/2008 1:10 PM

Operator   : Ron   Detector Type: ADCB (10 Volts)
Workstation: Bus Address : 18
Instrument : GC 2   Sample Rate : 10.00 Hz
Channel   : A = A   Run Time   : 20.002 min

** Star Chromatography Workstation Version 5.51 ** 01657-37c8-82a-2631 **

Chart Speed =   0.98 cm/min   Attenuation = 777   Zero Offset = 7%
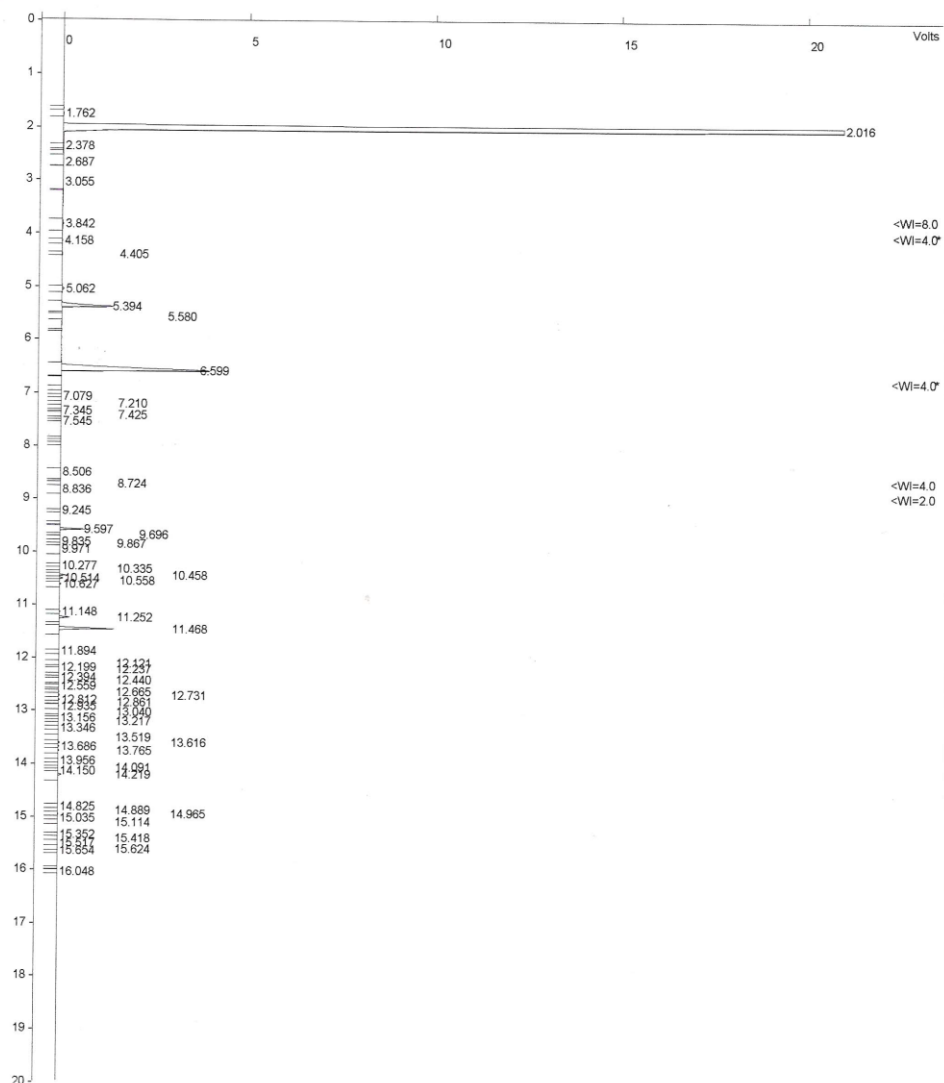Start Time =   0.000   min   End Time   = 20.002   min Min / Tick = 1

Injection Date: 10/19/2005 1:00 PM   Calculation Date: 10/19/2005 1:20 PM

Operator   : khalaf   Detector Type: ADCB (10 Volts)
Workstation: Bus Address : 18
Instrument : GC 2   Sample Rate : 10.00 Hz
Channel   : A = A   Run Time   : 20.002 min

** Star Chromatography Workstation Version 5.51 ** 01657-37c8-82a-2631 **

Chart Speed =   0.98 cm/min   Attenuation = 9916   Zero Offset = 2%
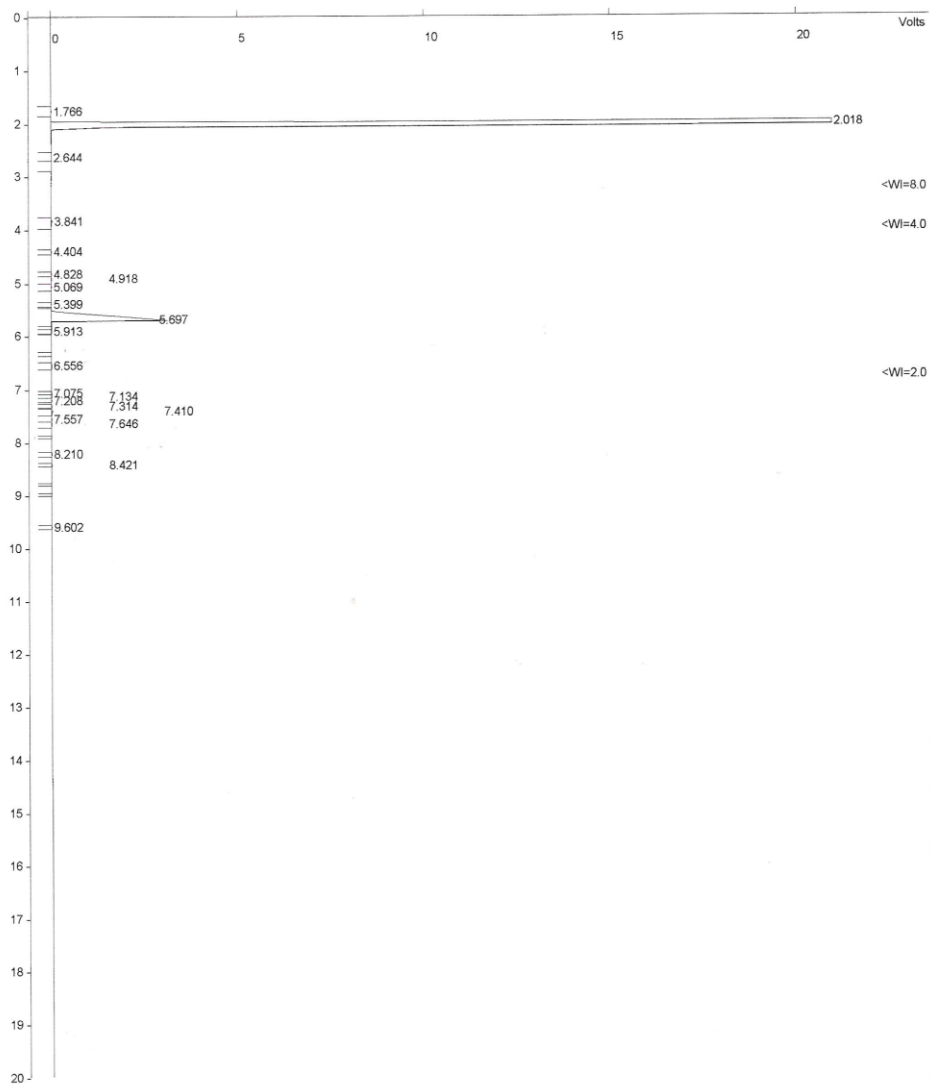Start Time =   0.000   min   End Time   = 20.002 min   Min / Tick = 1

Injection Date: 2/18/2008 12:55 PM   Calculation Date: 2/18/2008 1:16 PM

Operator   : Ron   Detector Type: ADCB (10 Volts)
Workstation: Bus Address : 18
Instrument : GC 2   Sample Rate : 10.00 Hz
Channel   : A = A   Run Time   : 20.002 min

** Star Chromatography Workstation Version 5.51 ** 01657-37c8-82a-2631 **

Chart Speed =   0.98 cm/min   Attenuation = 288   Zero Offset = 2%
Start Time =   0.000 min   End Time   = 20.002 min   Min / Tick = 1